The complex nature of the ISM in the SMC: an HI and infrared study

Snežana Stanimirović

A thesis
submitted for the degree of
Doctor of Philosophy
at the
University of Western Sydney Nepean

July, 1999

PLEASE NOTE

The greatest amount of care has been taken while scanning this thesis,

and the best possible result has been obtained.

Abstract

This thesis presents the results of a combination of new observations with the Parkes telescope of neutral hydrogen (HI) in the Small Magellanic Cloud (SMC) with an Australia Telescope Compact Array (ATCA) aperture synthesis mosaic. The new data consists of a set of images sensitive to all angular (spatial) scales between 98 arcsec (30 pc) and 4° (4 kpc). The data are used to study the HI distribution and mass, the velocity field and rotation curve of the SMC, as well as to probe the 3-D structure of the SMC. A kinematic study of the HI data reveals the existence of three supergiant shells which were previously undetectable in the ATCA data alone. The HI spatial power spectrum has been investigated over a range of contiguous scale sizes wider than those previously achieved in any other galaxy, including our own. It closely obeys the relation, $P(k) \propto k^{\gamma}$, suggesting an alternative model for the interstellar medium (ISM) of the SMC, having fractal nature and consisting of a hierarchy of HI cloud structures.

This thesis also demonstrates that the infrared data obtained with the Infrared Astronomical Satellite (IRAS) for the SMC can be successfully reconstructed with much higher resolution using the Pyramid Maximum Entropy algorithm. The new infrared (IR) data are used to study the integrated IR spectrum, the dust temperature and dust column density in the SMC. The high resolution HI and IR data enable an investigation of the spatial correlation of dust and gas and the assumption of the dust and gas being well-mixed in the ISM. The spatial power spectrum of the dust column density shows that, as with the HI power spectrum, there is no preferred scale size for dust clouds. The remarkable similarity of the spatial power spectra for the HI and dust column density distributions suggests a unique and ubiquitous hierarchical structure organisation for the ISM in the SMC. Such an organisation is likely to be governed by the Kolmogorov type turbulence and could be described by the fractal nature with the volume fractal dimension of 2.4.

Acknowledgements

My deepest and warmest thanks go to my four supervisors: Dr Lister Staveley-Smith (ATNF*), Dr Paul Jones (UWSN), Dr Raymond Haynes (ATNF) and Assoc. Prof. Graeme White (UWSN), for a continuous scientific guidance and personal support over last three and an half years. I own so much to Lister for providing a brilliant scientific input and for knowing always what is the best to do next. Paul helped extremely on very early and very late stages of my PhD, with amazingly quick reading and debugging of previous versions of my chapters. I am very grateful to Raymond for being there all the time to talk about both scientific and personal problems, and to Graeme for providing financial support for my student fees in very hard times for the Centre for Astronomy at the UWSN.

Another person who influenced my research tremendously, although not being my official supervisor, is Prof. John Dickey from University of Minnesota. I show my deepest appreciation for all enormously inspiring conversations about the Magellanic Clouds we had, which indirectly led my thesis through various fascinating research islands.

I want to thank the University of Western Sydney Nepean for having me as an overseas postgraduate student and showing understanding with the constant problem of my student fees. I am grateful to all people in the Astronomy Group at the Faculty of Mathematics in Belgrade who encouraged me to do my PhD in Australia. Thanks also go to Dr Miroslav Filipović for helping me to come here and start a very different life on this completely 'new planet', and to all students and staff at the Centre for Astronomy at the UWSN.

During my whole PhD I highly enjoyed and appreciated being an ATNF student, using the ATNF observing facilities and interacting with a lot of wonderful people in Epping, Narrabri and Parkes. I thank all ATNF scientists and stuff for enabling this thesis get through.

I wish to thank Prof. Thijs van der Hulst from the Kapteyn Astronomical Institute, Dr Romke Bontekoe from the Bontekoe Data Consultancy and the Astronomical Institute 'Anton Pannekoek' at the University of Amsterdam, and Do Kester from Laboratorium voor Ruimteonderzoek, SRON in the Netherlands, for kindly hosting me at the Kapteyn Astronomical Institute and providing an inspiring collaboration.

During the third year of my PhD I received the financial support of a Nepean Postgraduate Research Award. I also acknowledge travel support by: a UWS Nepean travel grant, an Astronomical Society of Australia travel grant, an International Astronomical Union 190 travel grant and an ATNF travel grant, which enabled me to attend the IAU Symposium 190 and present my research.

*The Australia Telescope is funded by the Commonwealth of Australia for operation as a National Facility managed by CSIRO.

Finally, I wish to thank all my friends back in Serbia, and all the friends I made while being in Australia, for heaps of support, help and fun. Guys, you are all wonderful and thank you so much! Yes, Natalija and Slavica, it's finally 'gotovo'! Thank you dear Shirley for wonderful energetic sparks of life at the Adelaide Hills.

I am indebted to my parents and my brother for having so much understanding for my various 'astronomical missions', the latest of them being coming to Down Under from Serbia. Thank you so much for all your endless love and encouragement! And, at the end, as my Kiwi-Aussie Significant Other, Matthew Wyndham, usually says: 'short and sweet', I'll just say that all this work would simply not be possible without his precious love and support.

Statement of originality

This thesis describes work carried out in the Centre for Astronomy at the University of Western Sydney Nepean and at CSIRO's Australia Telescope National Facility between 1996 and 1999. Sections: 2.2 and 2.3 in Chapter 2; 3.2 and 3.4.1 in Chapter 3; 4.1, 4.2 and 4.3 in Chapter 4; 6.2.1 and 6.3 in Chapter 6; and 8.3.1 and 8.3.2 in Chapter 8, appeared in a slightly modified version as a paper in Monthly Notices of the Royal Astronomical Society, 1999, 302, 417, on which I am the first author. Except where otherwise acknowledged, the work presented in this thesis is my own. Significant contributions from other people are as follows:

- Chapter 2: Lister Staveley-Smith carried out the most of data reduction of the ATCA and Parkes SMC data. Steve Snowden helped with Parkes observations. Bob Sault was involved in the ATCA data processing.
- Chapter 3: Lister Staveley-Smith, John Dickey and Bob Sault provided useful comments on data combination methods. The idea about the relationship between the calibration scaling factor and the single-dish beam was suggested to me by John Dickey (Section 3.2.1). Bob Sault implemented the 'joint' deconvolution method for data combination in MIRIAD.
- Chapter 4: John Dickey performed the analysis of the HI self absorption in Section 4.2.1.
- Chapter 6: The catalogue of previously found shells in the SMC by Lister Staveley-Smith was used.
- Chapter 7 and Chapter 8: The most of these two chapters will be submitted in a slightly modified version for publication by Monthly Notices of the Royal Astronomical Society, on which I will be the first author. Romke Bontekoe and Do Kester performed complete processing of the old IRAS SMC data. They also contributed to the text of Section 7.2. Lister Staveley-Smith, Thijs van der Hulst and Paul Jones helped to improve the text for the future publication.

Snežana Stanimirović
Sydney, Australia
July 1999

Contents

List of Tables

List of Figures

Chapter 1

Introduction

1.1 The interstellar medium (ISM)

The interstellar medium (ISM) is the matter which occupies the enormous volume between the stars. Why is it important? At the IAU Symposium 75 on star formation, Herbig (1977) said: 'Let me say at first, rather naively, how struck I am by the delicate symbiosis that exists between the stars and the interstellar medium, how each is nourished by the other, and how the Galaxy as we know is entirely a consequence of that balance and interplay'. It is this fascinating interplay in the system stars-ISM that is responsible for the evolution of any galaxy, initially created entirely from the interstellar gas. As the ISM carries embedded signatures of these complex and delicate interactions, it can tell us the story about the past, present and future of any galaxy.

1.1.1 The composition of the ISM

The ISM consists of gas and dust particles, permeated by magnetic fields and bathed by energetic cosmic rays (energetic protons, electrons and gamma rays) (Spitzer 1978).

The most dominant constituent of the gas component is hydrogen, with $\sim$ 90% by number; helium atoms contribute only $\lesssim$ 10%, while atoms of carbon, nitrogen or oxygen contribute a further 0.1% (Dyson & Williams 1980; Brinks 1990). The interstellar gas exists in the ISM with an extremely wide range of physical properties, commonly grouped into the following five different phases: the molecular medium (MM), the cold neutral medium (CNM), the warm neutral medium (WNM), the warm ionised medium (WIM) and the hot ionised medium (HIM). Table 1.1, compiled from Dyson & Williams (1980), Kulkarni & Heiles (1988), Brinks (1990), Knapp (1990) and Dyson & Williams (1997), summarises some of the main

characteristics of these phases, such as the kinetic temperature and density, as well as ways of probing these phases.

Table 1.1 . Five different regimes or phases of the interstellar gas, compiled from: Dyson & Williams (1980); Kulkarni & Heiles (1988); Brinks (1990); Knapp (1990) and Dyson & Williams (1997).

Component	$\langle n \rangle$ (cm^{-3})	T (K)	Probes
Molecular Medium (MM)	$10^3 - 10^4$	$5 - 30$	CO
Cold Neutral Medium (CNM)	$10 - 10^3$	$10 - 10^2$	HI
Warm Neutral Medium (WNM)	0.3	$\sim 6{\times}10^3$	HI, Hα
Warm Ionised Medium (WIM)	0.3	$\gtrsim 8{\times}10^3$	HI, Hα
Hot Ionised Medium (HIM)	$< 10^{-2}$	$\sim 10^6$	X-rays, UV, O^{5+}

The molecular gas is found mainly in clumpy and dense regions, which are held together by gravity. Molecular clouds mainly contain H_2 and CO molecules, and more complex molecules inside their dense cores. The usual way of probing the MM is using the rotational transitions of CO. The CNM has been observed mainly in absorption of neutral hydrogen (HI). Many observations suggested that this medium occupies a small fraction of the volume, being concentrated in separate regions or so called 'standard clouds' (Spitzer 1978), whose parameters greatly vary in the ISM.

Another flavour of neutral gas is the WNM, visible only in emission, it reaches temperatures up to 8×10^3 K and fills in a large fraction of the interstellar space around cool and cold neutral clouds, forming therefore a so-called inter-cloud medium. Our knowledge about the WNM has mainly resulted from observations of the HI atom emission at 21 cm. The 21 cm line of the HI atom results from the hyperfine splitting of its ground state; the transition often referred to as the 'spin-flip' transition. Due to radio emission at 21 cm, the HI atom is one of the best tracers of the ISM. It is easy to detect, since its 'spin-flip' transition belongs to the 'radio window' of the atmospheric transparency, and it provides extremely valuable information in the optically-thin regime, being a direct measure of the HI column density.

The WIM has been observed mainly within HII regions using hydrogen recombination lines (such as Hα), but observations by Reynolds (1988) showed that the considerable fraction of the ISM is filled with ionised gas. Finally, the HIM, or 'coronal gas' with temperatures reaching $\sim 10^6$ K, is observed in X-rays and lines of multiply-ionised oxygen. It is a product of supernova explosions and stellar winds, and appears to be also widely distributed (Dyson & Williams 1980).

The interstellar dust particles are small pieces of solid material in the ISM, composed of graphite, silicate, carbon and ices. Their sizes range from ~ 0.001 to 0.1 μm. The dust grains absorb the starlight at visible and ultraviolet wavelengths and then re-emit the energy, mainly in the infrared (IR). The dust grains appear to be ubiquitous

in the ISM and it is believed that they are well mixed with the gas on all scales (Cox & Mezger 1989; Knapp 1990; Dyson & Williams 1997). The condensation of dust grains from the interstellar gas appears to be a very slow process. One of the places, observationally confirmed, where the grain formation is believed to take place, is in gas outflows from cool stars. Recent studies have shown that novae and type II supernovae are also very important sources for the dust formation (Dwek 1998). On the other hand, fast supernovae shocks are capable of shrinking or even completely disintegrating grains, in the process called sputtering, when incident atoms manage to knock atoms out of a grain skeleton. However, the origin of dust grains, and their formation and destruction mechanisms are, in general, still not well enough understood (Draine 1989; Knapp 1990). Although dust grains comprise less than 1% of the ISM (by mass), the role they play in the ISM is extremely important. As well as being a source of coupling between the neutral and ionised gas (see Section 1.1.2), dust grains enable the creation of molecules in denser regions (Dyson & Williams 1980). In this chemical process grains act as catalysts, facilitating contact between reacting molecules (Wynn-Williams 1992).

The role of magnetic fields in the ISM is to constrain motion of the highly energetic cosmic 'visitors' (cosmic and gamma rays). The magnetic fields are also responsible for the alignment of dust grains (Spitzer 1978).

1.1.2 The energy balance in the ISM

The energy balance in the ISM, responsible for the existence of different interstellar phases, is mostly determined by the cooling and heating processes on a microscopic level. These processes, in turn, control the bulk (macroscopic) properties of the ISM and hence determine its evolution (Dyson & Williams 1997).

A summary of the main cooling mechanisms in the ISM is shown in Table 1.2, taken from Dyson & Williams (1980). As shown, cooling of the molecular gas occurs mainly through the rotational transitions of CO. The most important coolant of the cold neutral gas is C^+. The combination of the collisional excitation of C^+ ions and their spontaneous return to the ground state, results in the emission of photons, which escape from the gas causing its cooling. The second choice for cooling of the cold neutral gas is H_2 with its electric dipole transitions. At a temperature of $\sim 10^3$ K, ions such Fe^+ and Si^+ can get excited by collisions to the long-lived metastable states, which act as new ground states from which the collisions occur (Dyson & Williams 1980). The cooling of a very hot gas at $\sim 10^4$ K is maintained through the recombination process, whereby the resultant neutral atom after recombination is in excited state and cascades through the energy levels emitting a photon at each level.

The main heating mechanism in the ISM is photoionisation by starlight, supernovae and/or energetic cosmic rays and X-rays (Kulkarni & Heiles 1988). The photoion-

Table 1.2 . Main cooling mechanisms of the interstellar gas at different temperatures (from Dyson & Williams 1980): the rotational transitions of CO, the collisional transitions of C^+, the electric dipole transitions of H_2, the collisional transitions of the metastable states and the recombination.

Temperature (K)	~ 10	$\sim 10^2$	$\sim 10^3$	$\gtrsim 10^4$
Main coolant	CO	C^+, H_2	Metastable ions	H, H^++e, O^{2+}

isation in cool molecular clouds occurs mainly on C, Si and Fe atoms. The photodissociation of H_2 molecules, a process similar to the photoionisation, but with the resultant particles being atoms instead of ions, can also contribute significantly. The photoionisation in the neutral gas occurs mainly on C atoms, while the ionisation of H atoms is the most important contribution to the heating of HII regions (Dyson & Williams 1980). The most dominant of all starlight mechanisms appears to be heating by photoelectric emission from dust grains (Draine 1989). This is essentially a photoionisation of a dust grain by a photon, resulting in an ejection of a fast energetic electron from its surface whose kinetic energy is then available for heating the gas. However, at the same time, grains are also good coolants, since they are well mixed with the gas but usually have much lower temperature. The photoionisation by supernovae and/or energetic ionising particles is capable of dumping even larger amounts of energy into a relatively small fraction of gas, causing HII regions and regions with coronal gas (Knapp 1990).

1.1.3 Structure of the ISM

For many years there have been theoretical and observational support for structures in the ISM on scales from $\sim$ 1 pc to 1 kpc (Dickey & Lockman 1990), while structures on scales smaller than 1 pc were not believed to have a significant role. Studies of HI in galaxies of different morphological types, and gas-rich galaxies in particular, have shown that features like shells, filaments, arcs, worms and chimneys are, most likely, general phenomena of the ISM (Heiles 1984; Brinks & Bajaja 1986; Braun 1997). Statistical studies of the ISM have revealed a power-law behaviour of the spatial power spectrum for the HI emission fluctuations in the Galaxy (Crovisier & Dickey 1983; Green 1993) and for the cool dust in the Galaxy, traced by the infrared intensity at 100 μm (Gautier et al. 1992; Schlegel, Finkbeiner, & Davis 1998). Such statistical descriptions point out the hierarchy of scales on which structure is present in the ISM, placing therefore some constraints on the topology of the ISM.

Many surveys of molecular clouds have shown a power-law scaling relation for the cloud mass ($10^1 - 10^7$ $M_\odot$) and size ($10^{-1} - 10^2$ pc) distribution functions (Elmegreen & Falgarone 1996). Dickey & Garwood (1989) extended the study of the cloud mass spectrum further for diffuse atomic clouds (having masses of 1–100 $M_\odot$) and have

shown that there probably exists a single mass spectrum for all interstellar clouds, suggesting again a hierarchical structure organisation within the neutral gas.

Recent observations of the tiny (AU-scale) structure in the atomic gas at 5–100 AU and $\sim 10^3$ AU (Dieter, Welch, & Romney 1976; Diamond et al. 1989; Frail et al. 1994; Davis, Diamond, & Goss 1996; Faison et al. 1998), in the molecular gas at $<$ 10 AU (Marscher, Moore, & Bania 1993; Moore & Marscher 1995) and in ionised gas at $\sim$ 20 AU (Fiedler et al. 1994), seem to be introducing a new dimension to the studies of the ISM. It seems that the tiny-scale structure has been found in all different phases of the ISM, which suggests that it is more likely to be a general property of the ISM than the effect of some more local phenomena, although its origin is still not understood (Heiles 1997; Walker & Wardle 1998).

1.1.4 The 'jigsaw puzzle' of the ISM

Observations of the ISM have shown that the gaseous component exists in various phases, with a wide range of physical parameters. An important conclusion from observations is that much of the neutral gas mass is seen only in absorption, suggesting that this matter must be cold, while much of the volume appears to be observable only in emission, suggesting that this matter must be warm (McKee 1995). Different models for the ISM try to put the 'jigsaw puzzle' of the ISM together in a coherent fashion. Questions these models must answer include: why do the different phases of the interstellar gas exist at all? Are these phases static, or does the interstellar gas cycle through the different phases? What is the relationship between different phases, and how do they affect each other?

In answering all these questions, one of the usual assumptions is that all phases of the interstellar gas are in pressure equilibrium, an idea first proposed by Spitzer (1956). The problem then becomes searching for the thermally stable phases of interstellar gas, under conditions governed by main heating/cooling processes at work in the ISM. The first idea about the relationship between cold and warm phases in the ISM was introduced by Spitzer (1954). Later, the two-phase model by Field, Goldsmith, & Habing (1969) and the three-phase model by McKee & Ostriker (1977), were introduced.

1. **Spitzer's 'standard cloud' model**
   In his pioneering paper 'Behaviour of matter in space', Spitzer (1954) presents a picture of the ISM with HI clouds having typical temperature of $\sim$ 100 K being surrounded by a rarefied medium of much lower density but higher temperature. According to Spitzer this picture was consistent with the suggestion that the pressure in the interstellar gas tends to be uniform. This paper also made the first venture into understanding the intrinsic topology of the ISM, viewing the ISM as a two-level hierarchical system with the neutral gas being present mainly in a form of clouds, not for example sheets or filaments.

Interestingly, many later and current models of the ISM, are still tied to this idea.

2. **The two-phase model of a quiescent ISM**
   The two-phase model by Field, Goldsmith, & Habing (1969) shows that two thermally stable phases can co-exist in the ISM at the same pressure, provided that a thermally unstable phase occurs at the intermediate temperature (McKee 1995). Two stable phases are: the CNM, confined in clouds and occupying a small fraction of the ISM volume, and the WNM, or 'intercloud' phase, which fills almost the entire ISM volume (Kulkarni & Heiles 1988). The two-phase model assumes that the ISM has a quiescent nature and is not disturbed by any of the violent events in the ISM, such as supernovae explosions or stellar winds.
3. **The three-phase model of a violent ISM**
   The powerful impact of supernovae explosions on the surrounding ISM was first recognised by Cox & Smith (1974). The vigorous stirring of the ISM by the supernovae highlighted the fact that the ISM is in general very violent, and led to the three-phase model of McKee & Ostriker (1977). In this model, the supernovae play the main role: they produce a third interstellar phase – the hot ionised medium (HIM), expanding and merging together to form an interconnecting network of tunnels containing hot gas. The hot phase occupies $\sim 60\%$ of the volume, while cold clouds are uniformly interspersed in it, being created at the peripheries of expanding supernova shells (Kulkarni & Heiles 1988). These clouds have an 'onion-skin' structure, with HIM, WIM, WNM and CNM phases forming different levels (skins). All phases are in pressure equilibrium.

Although these models explain some observational constraints, several problems are still waiting to be solved. Firstly, observations show that the topology of the ISM is far more complex than assumed in these models. HI observations suggest shells, filaments and arcs, rather than the 'onion-skin' clouds. The discovery of the hierarchical organisation of structure and the tiny-scale structure in the ISM suggests that the ISM is likely to have more than two levels of hierarchy. Secondly, the three-phase model assumes a uniform distribution of supernova explosions, which is not observed. Supernovae appear to be mainly confined to galaxy disks and they tend to cluster (Brinks 1990). Thirdly, the observed volume filling factor of the hot gas in galaxies appears to be much smaller than 60% predicted by McKee & Ostriker (1977) (Brinks & Bajaja 1986; Brinks 1990; for discussion see Slavin & Cox 1993). Furthermore, the observed volume filling factor of the WNM seems to be much larger than the predicted 2% (Kulkarni & Heiles 1988).

In order to overcome some discrepancies between the models and the observations, several alternatives have been proposed. First of all, in the case of the Galaxy, a combined model, with the two-phase model being applied for the inner Galaxy and the three-phase model being applied for the outer Galaxy, would fit the observations

better (Kulkarni & Heiles 1988). Norman & Ikeuchi (1989) suggest the 'chimney' model of the ISM which allows the ISM to cycle between the two–phase and the three–phase models, relative to the SN rate and the total gas density. This model suggests that the galactic disk and halo are connected by chimneys of hot gas, which result from superbubble breakouts from the disk. Another alternative, highly inhomogeneous model, is the fractal model of the ISM (Elmegreen & Falgarone 1996), originating in the interstellar turbulence (Elmegreen 1998). It consists of a hierarchy of clouds, having smaller clumps inside bigger ones, and so on until the smallest, 'atomic' clumps are reached. The dense regions are made of clusters of small and dense 'atomic' clumps, while the bulk of the ISM matter has very low density (Elmegreen 1989). Such a model would thus imply different density functions for many physical processes, starting with the theory of radiative excitation and transfer.

1.2 The Small Magellanic Cloud (SMC)

The Small Magellanic Cloud (SMC) is a nearby dwarf irregular galaxy. Throughout this thesis a distance to the SMC of 60 kpc is assumed from the most recent review of the Magellanic Clouds by Westerlund (1997). The SMC is the third member of an interacting threesome of galaxies (Murai & Fujimoto 1980), the other members of which are the Large Magellanic Cloud (LMC) and the Galaxy. It is generally believed that both the SMC and the LMC have been bound to our Galaxy for at least 7 Gyr (Westerlund 1997). Being of the lowest mass in the SMC-LMC-Galaxy system, the SMC is the most disrupted by the apparently gravitational nature of the interactions (Putman et al. 1998), and its large-scale morphology is complex and not fully understood. An encounter with the LMC some 200 Myr ago is widely believed to be responsible for its present appearance (Gardiner, Sawa, & Fujimoto 1994), resulting in a bridge and a stream, mainly of gas: the Magellanic Bridge which connects the SMC and the LMC; and the Magellanic Stream which extends behind the SMC and the LMC for about 100° (Mathewson, Cleary, & Murray 1974).

The general morphology of the SMC, seen by radio and optical observations, consists of an elongated bar, with the position angle of $\sim 45°$, and an eastern wing (Westerlund 1997). From many radio observations of HI, the SMC appears to be extremely rich and with complex morphology in neutral atomic gas (Staveley-Smith et al. 1998). The observed splitting of the HI line has caused a lot of controversy in the past, and was variously interpreted as expanding shells of gas or spatially separate systems (Hindman 1967; Mathewson, Ford, & Visvanathan 1988; Martin, Maurice, & Lequeux 1989; Staveley-Smith et al. 1997). Hindman (1967) was the first to acknowledge the influence of powerful expanding shells of gas on the surrounding ISM suggesting the presence of three such features in the SMC. He also derived the rotation curve of the SMC. The most recent high resolution HI survey by

Staveley-Smith et al. (1997) revealed a great variety of the small-scale HI structure, with numerous giant shells, filaments, knots and arcs.

The SMC is also the site of several giant HII regions, observed in Hα by Davies, Elliot, & Meaburn (1976). Recent observations by Kennicutt et al. (1995) found the extended network of filaments, pointing out that the diffuse Hα is quite significant. Numerous molecular clouds have been found in the SMC, primarily in small dense cores of massive HI regions (Rubio, Lequeux, & Boulanger 1993).

Early studies of the dust properties in the SMC, undertaken with ground based instruments, covered only a negligible fraction of the SMC area. A new dimension in the understanding of its dust properties, was added with the advent of the Infrared Astronomical Satellite in 1983, enabling the first infrared maps of the SMC to be made (Schwering 1988). As a result of an almost primordial interstellar medium with low heavy element abundance (Sauvage & Vigroux 1991), and very high UV-bright interstellar radiation field (Lequeux 1989), the dust in the SMC appears to be hotter than in the LMC or in the Galaxy.

But what makes the SMC so attractive for studies of the ISM? There are several very good reasons. First, the SMC is a dwarf, very gas-rich galaxy with a low metallicity. As such galaxies in general have undergone fewer generations of star formation, they can help us to understand what triggers star formation, whether there is a threshold density of gas necessary for the star burst, what is the aftermath of the star formation on the ISM and how the metallicity evolves with time (Knapp 1990). Second, the SMC is nearby. Hence, high resolution observations at different wavelengths can reach structure down to parsec and sub-parsec scales. This allows different ISM phases to be probed and their filling factor and topology to be estimated, enabling us to test different models of the ISM. Nearby galaxies have an advantage relative to the Galaxy for such studies, since observers have an unfavourable position in the Galaxy, being located within the Galaxy disk (Brinks 1990). Third, although nearby, the SMC is far enough away so that all its objects can be treated as having the same distance, unlike in the Galaxy, where distance determination is relatively uncertain. And finally, as a young, less-evolved galaxy, the SMC is an excellent laboratory to test whether and how the phase-mix of the ISM differs from that in the well-evolved galaxies, such as our Galaxy.

1.3 Aim and outline of this thesis

This thesis aims to investigate the following main scientific questions.

1. What are the inventories of HI and dust contents of the ISM in the SMC? What are dominant structures, their characteristics, distributions and organisations? What can we learn about the intrinsic topologies of HI and dust contents of

the ISM? In particular, as the supergiant shells are common features in the ISM, what role they have in the multi-phase ISM of the SMC? What causes their creation and evolution?

2. What is the kinematics of the SMC? Which is more responsible for its velocity field: random or gravitational motions? Can the SMC be interpreted as a rotationally supported system? If so, what is its rotation curve? Does the SMC have a dynamically significant halo of dark matter as some other dwarfs? Can the 3-D structure of the SMC be probed? Does the SMC have a significant line-of-sight depth?

3. What is the relationship between dust and gaseous contents in the SMC? Are gas and dust well correlated spatially? Is the dust-to-gas mass ratio constant, or does it vary across the SMC? What could cause the variation of the dust-to-gas mass ratio? What is the relationship between the intrinsic topologies of both dust and HI content? What can this tell us about the global model of the ISM?

The main emphasis in this work will be put on probing the current models of the ISM, their topological aspects and the interplay of dominant processes at work. In order to address all the above scientific questions, the high resolution HI spectral line and infrared observations were used, and both qualitative and quantitative approaches for data analyses were employed.

The high resolution Australia Telescope Compact Array (ATCA) HI spectral line data, used in this thesis, and their observations and data reduction are described in Chapter 2. The same chapter also describes observations and processing of the Parkes telescope HI spectral line data, which complement the ATCA data with the structures having sizes up to the physical size of the SMC ($\sim$ 4 kpc). The process of combination of both data sets is analysed and applied in Chapter 3. The combined HI data are then presented in Chapter 4, and the HI total mass is derived and discussed. Chapter 5 is devoted to kinematics and dynamics of the SMC. As the main gaseous body of the SMC suggests circular rotation, the rotation curve is modelled here using both the gaseous and stellar content of the SMC. Models for the 3-D structure are reviewed and compared with the new data. The aftermath of star formation on the ISM is discussed in Chapter 6, together with the estimate of the filling factor for the hot gas and its consequences for the models of the ISM. The statistical description of shell properties is further employed, and results are compared with the ones for several other galaxies.

The IRAS IR observations of the SMC, re-processed to high resolution to match the resolution of the HI data, are discussed and presented in Chapter 7. The main properties of the dust content of the SMC are analysed here and compared with previous studies. Chapter 8 concerns the relationship between gas and dust in the SMC, using both qualitative and quantitative methods. The qualitative approach challenges the view of the well mixed gas and dust model of the ISM and draws out a

few ideas about the molecular gas and very cool dust content. As an alternative, the reason for an intrinsic variation of the dust-to-gas mass ratio is investigated. The second part of this chapter employs several statistical descriptors (the spatial power spectrum and the coherency spectrum) in order to probe the structure organisation of both gas and dust content in the SMC, as well as the statistical correlation between the two. An alternative, fractal model of the ISM is also briefly presented. Finally, the overview of results and the future directions are outlined in Chapter 9.

Chapter 2

HI observations and data reduction

2.1 Introduction

Radio emission in the 21 cm line, in the optically-thin regime, is a direct measure of the HI column density, providing valuable information about the structure and evolution of the ISM, as well as the relationship between star formation and the surrounding interstellar environment. Hence a long history of HI observations in the SMC.

The first detection of 21 cm line emission in the SMC was reported by Kerr, Hindman, & Robinson (1954), followed by Hindman, Kerr, & McGee (1963) and Hindman et al. (1963). The resolution of these pioneering observations was quite poor, being only $1.^\circ5 - 2.^\circ2$. In 1966, Hindman (1967) used the 64 m Parkes telescope to survey a region, approximately of 30 deg^2, covering the SMC and having the much better angular resolution of 15 arcmin. McGee & Newton (1981) used a new Parkes receiver, an order of magnitude better in sensitivity than used in the previous survey, to map HI with the same angular resolution of 15 arcmin and a velocity resolution of 8.2 km s^{-1}. Slightly lower angular resolution (30 arcmin) but better velocity resolution (2 km s^{-1}) was obtained in the survey undertaken with the IAR 30 m dish (Bajaja & Loiseau 1982). High velocity resolution (1.6 km s^{-1}) observations with the Parkes 64 m telescope were performed by Mathewson, Ford, & Visvanathan (1988). During a long period between 1966 and 1997, the angular resolution of HI observations was dictated by the Parkes telescope, resulting in the limited spatial resolution of 260 pc.

However, advances in optical, infrared and millimetre studies have managed to push down the spatial resolution to $\lesssim 1$ pc, $\lesssim 100$ pc and $\lesssim 13$ pc, respectively (Staveley-Smith et al. 1997). The advent of the Australia Telescope Compact Array (ATCA)

has made a big step forward in matching the spatial resolution of the radio data with those from optical, infrared and millimetre studies.

This chapter summarises the ATCA HI data observations and the data reduction procedure from Staveley-Smith et al. 1997, which enabled Staveley-Smith et al. to investigate HI structures in the SMC on scales from 28 pc to $\sim$ 600 pc. Some additional data processing, applied here, is explained, and some consideration of the mosaic theory in interferometry is provided. Since these interferometric data do not contain information about the large-scale HI structure, new Parkes telescope observations of the SMC were undertaken. The motivation is to complement the ATCA data with the information about structure on all scales up to the physical size of the SMC ($\sim$ 4 kpc). These new Parkes observations and their data reduction procedure is outlined here as well.

2.2 The ATCA HI observations and reduction

2.2.1 Mosaicing observations

The Australia Telescope Compact Array (ATCA) was used to observe the SMC in 1992 October 6 – 14 (ATCA project C159, investigators: Staveley-Smith L., Sault R.J., Kesteven M., McConnell D., Hazidimitriou D., Cote S., Freeman K. & te Lintel-Hekkert P.). The ATCA is an east-west radio interferometer located in Narrabri, Australia. It consists of 5 movable antennas spread over 3 km of rail track and an additional antenna fixed 3 km further west. Each antenna has a diameter of 22 m and the FWHP antenna primary beamwidth of 34 arcmin at 21 cm.

The 375-m configuration of the ATCA was chosen due to its relatively uniform (compact) $u-v$ coverage. It consists of 10 baselines which are all multiples (2, 4, 6, 8, 12, 14, 16, 18, 22 and 30) of the basic ATCA increment 15.3 m. The central observing frequency was 1420 MHz and the bandwidth of 4 MHz was divided into 1024 channels, resulting in the velocity resolution of 0.82 km s^{-1}. During data reduction, the data was boxcar-averaged into 78 $\times$ 1.6 km s^{-1}channels, covering a heliocentric velocity range from 88 to 216 km s^{-1}. The final velocity resolution is therefore 1.6 km s^{-1}.

To cover the area containing the SMC and similar to previous surveys (Hindman 1967; McGee & Newton 1981), the observations of multiple pointings were required. This technique is known as mosaicing (Sault & Killeen 1998). Hence, 320 different pointing centres were observed by Staveley-Smith et al. (1997) in total, placed on a hexagonal grid. The Nyquist sampling theorem requires a maximum side of a hexagonal grid to be:

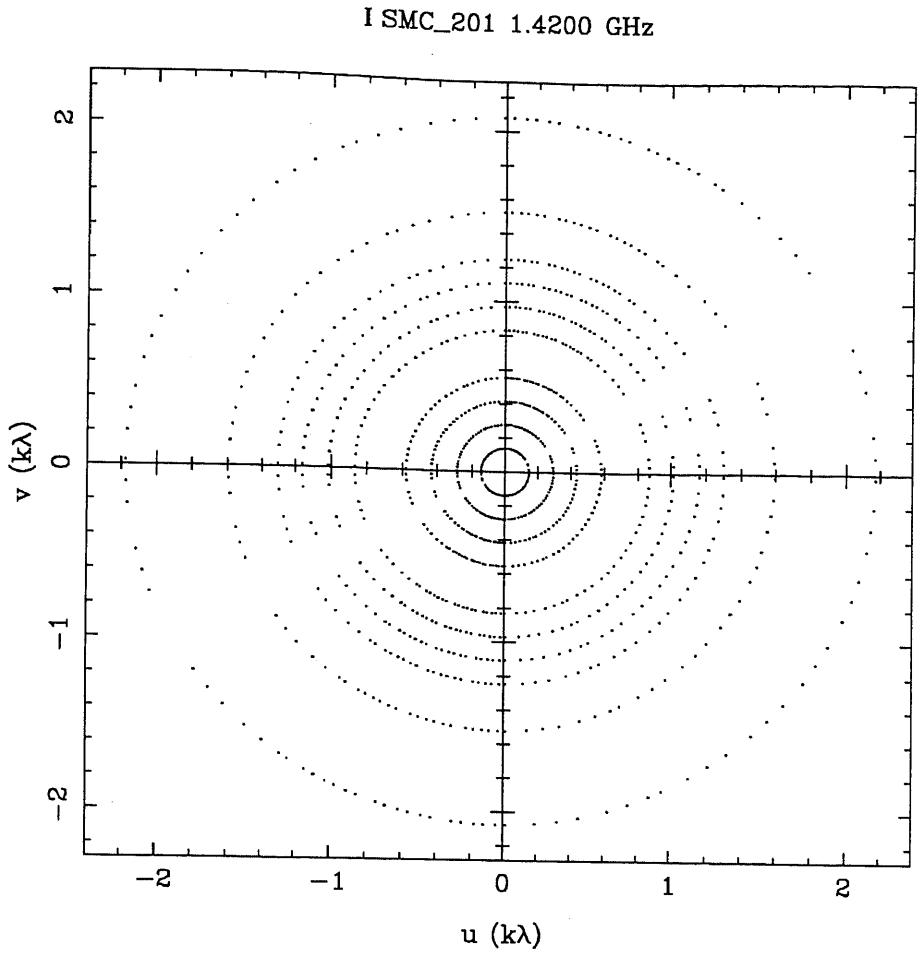

Figure 2.1 . The $u-v$ coverage of the pointing 201, the closest one to the centre of the covered area, at RA $01^h01^m46^s$, Dec $-72°49'34''$ (J2000).

$$\theta_{\rm hex} = \frac{2}{\sqrt{3}} \frac{\lambda}{2D} \approx 19 \text{ arcmin} \tag{2.1}$$

in order to retrieve all available information, with λ being a wavelength of the observation and D being a diameter of a single antenna. The grid side of 15 arcmin was chosen to help with the simultaneous observations at 13cm which are not reported here. In mosaicing observations, antennas dwell on one pointing centre for some time, and then move to another position, repeating the whole cycle for 12 or more hours. The aim is to visit each pointing frequently enough, in order to obtain as full $u-v$ coverage as possible, and also dwell on each pointing long enough, so that time lost for driving from one position to another is not too long. The maximum dwell time (in seconds) hence can be calculated from (Sault & Killeen 1998):

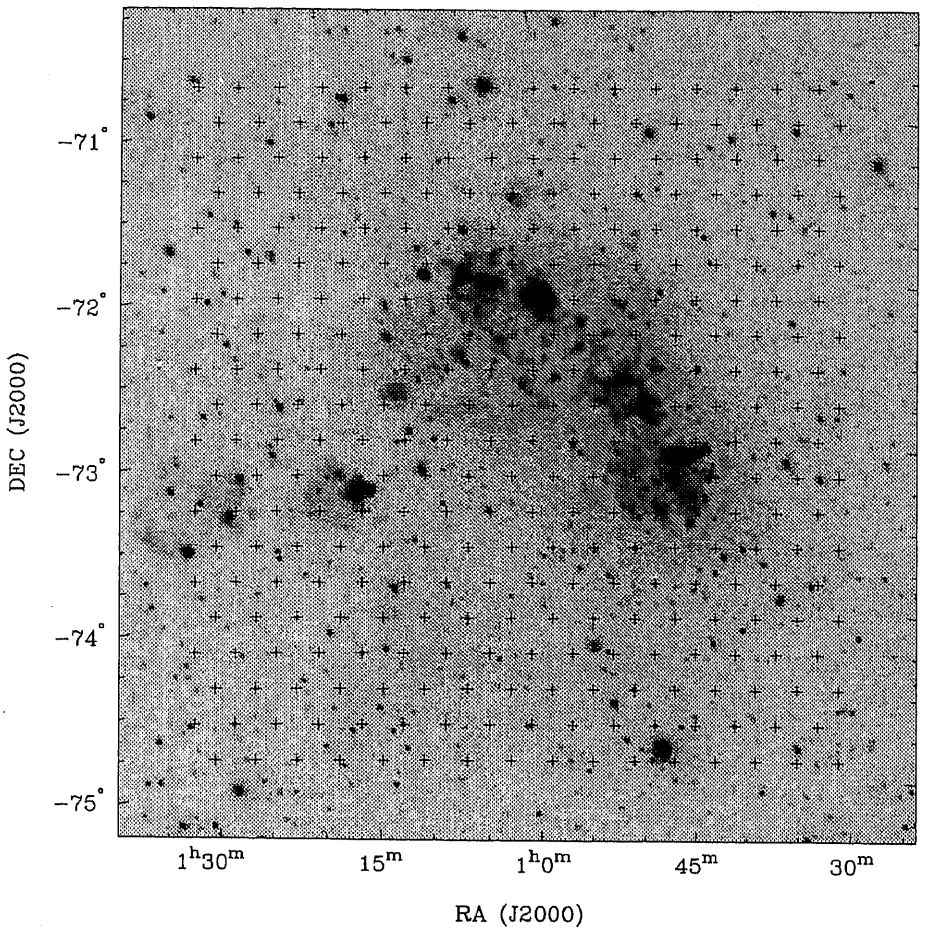

Figure 2.2 . The distribution of observed pointing centres observed with the ATCA (+) and superimposed on an Hα image of the SMC from Kennicutt et al. (1995).

$$\tau = \frac{86400}{2\pi} \frac{2D}{L} \tag{2.2}$$

where L is the maximum baseline for a given array configuration. The determined time τ is then shared between N different pointing centres, having spent $\tau/2N$ seconds on each pointing. During each observing day, the array was cycled around 40 adjacent pointings in a raster pattern, spending 16.1 sec on each pointing, and losing 3.9 sec to drive from one pointing to another. During 12–14 hours every day, each pointing was visited $\sim$ 50 times, which resulted in $\sim$ 800 sec of total integration time. The resultant $u - v$ coverage for pointing 201, which is very close to the centre of observed area, is shown in Fig. 2.1. After each third cycle, the secondary calibrator (PKS B0252-712) was observed for $\sim$ 100 sec. The primary calibrator (PKS B1934-638) was observed each day for the purposes of obtaining an absolute flux density scale and bandpass calibration.

The total area covered is 4°.5 × 4°.5 and is centred on RA 01^h01^m, Dec $-72°56'$ (J2000). Fig. 2.2 shows the distribution of all 320 pointing centres superimposed on the Hα image of the SMC from Kennicutt et al. (1995).

2.2.2 Calibration and data editing

Initial data reduction in Staveley-Smith et al. (1997) was done using the NRAO's AIPS imaging package. The small amount of bad data was flagged out. Amplitude and phase calibration was done using 0252-712, while the primary calibrator, 1934-638, was used for the bandpass calibration. For the original continuum subtraction, three ranges of channels were chosen to avoid HI emission from the Galaxy and the SMC: -89 to -32 km s^{-1}, 51 to 92 km s^{-1}and 207 to 306 km s^{-1}. The final images show, though, that this range of line-free emission was underestimated, since some SMC emission is present above 207 km s^{-1}. This resulted in the four low-level 'shadows' in the north-east, as is shown in the top panel of Fig. 2.3. The same panel shows the effects of solar interference during the first day of observations. Horizontal stripes are visible on the south-west part of the image.

To correct for these effects, some additional processing was performed here using the MIRIAD imaging package (Sault, Teuben, & Wright 1995). In particular, all daytime data taken during October 6 were removed to reduce solar interference. Also, continuum subtraction was redone using a higher velocity for the assumed third range of line-free channels (230 to 306 km s^{-1}). The same velocity channel after these extra steps is shown in the bottom panel of Fig. 2.3, with the successfully removed north-east and south-west artifacts.

2.2.3 Mosaic imaging and deconvolution

To create an image of the whole SMC, data from all different pointing centres need to be mosaiced. An early approach (the 'individual' approach) in the mosaicing technique, was to make separate images of all pointings, deconvolve them individually and then put together. Cornwell (1988) has shown that the linear mosaicing before deconvolution (the 'joint' approach), gives much better results, since it recovers some missing information in the $u-v$ plane which is not accessible to a single pointing. The idea of 'rebuilding' the $u-v$ coverage in interferometric observations is relatively old. Making an analogy between a single dish and an interferometer, Ekers & Rots (1979) showed that each interferometric baseline (d) measures not only one spatial frequency, but a range of spatial frequencies between $d-D$ and $d+D$ (where D is diameter of an antenna). To retrieve this extra information, they suggested scanning across an object. Cornwell (1988) presented a practical mosaicing algorithm, which combines data from all pointing centres before deconvolution, and showed that it has the same effect as scanning, if the pointing sample grid is

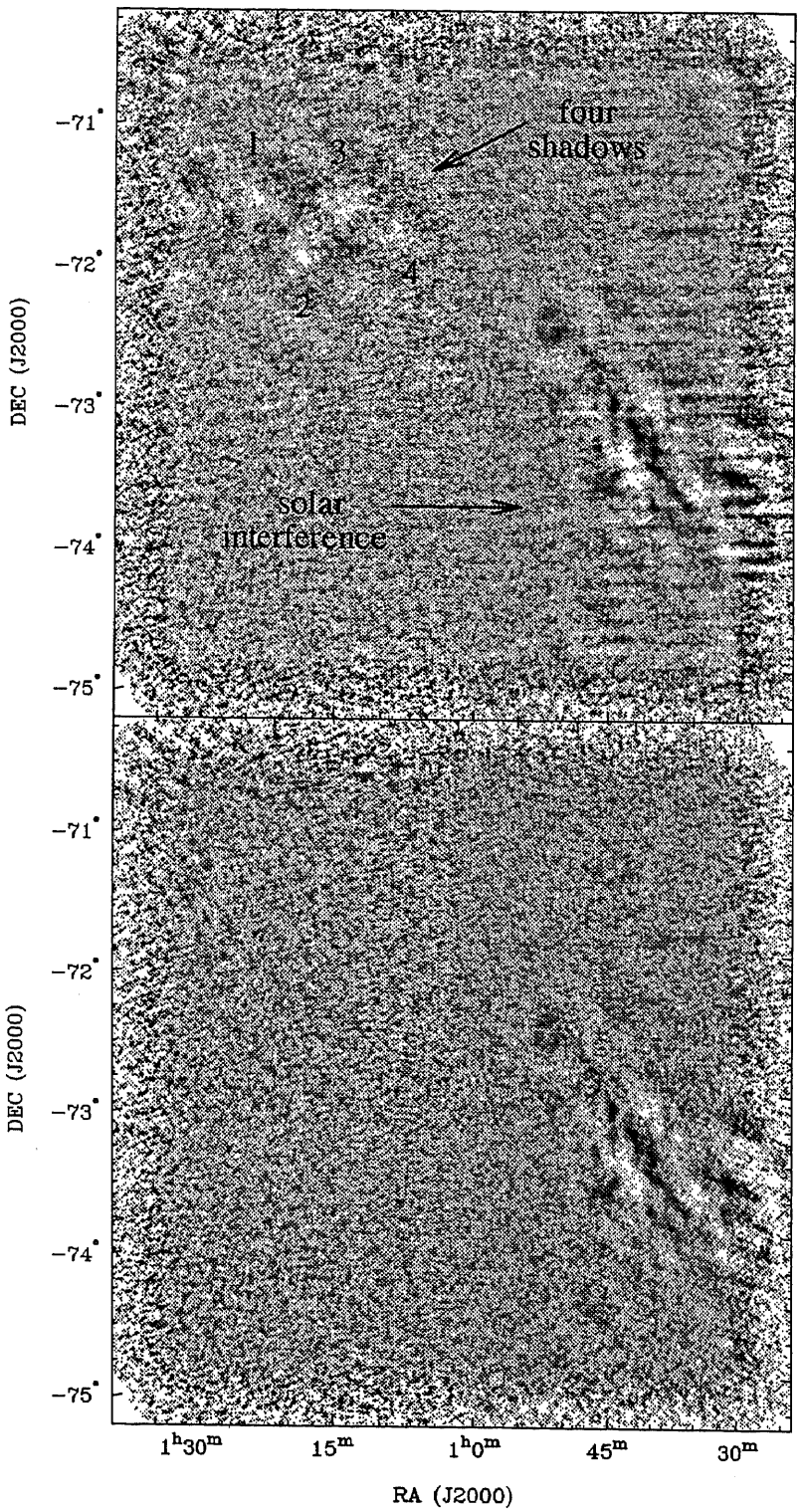

Figure 2.3 . The ATCA HI image of the SMC at heliocentric velocity 90 km s^{-1}, before (top panel) and after (bottom panel) additional data editing. The grey-scale intensity range is 0 to 13 K with a linear transfer function, for both images. Low-level artifacts around RA 01^h15^m, Dec $-72°50'$ (J2000) due to the underestimated line-free velocity range, as well as horizontal stripes on the south-west, due to solar interference are labelled on the top panel.

sufficiently fine.

The mosaicing algorithm applied here on the SMC ATCA data, following Staveley-Smith et al. (1997), is implemented in MIRIAD (Sault, Teuben, & Wright 1995). It consists of three steps, and only a short summary is given here. For more details see Sault, Staveley-Smith, & Brouw (1996) and Staveley-Smith et al. (1997).

1. **The imaging step**
   Dirty sub-images were first made for all pointing centres separately by gridding and Fourier transforming visibility data for each velocity channel. During this process, visibilities were robustly weighted (Briggs 1995) with a robust parameter equal to zero in order to provide a compromise between minimising sidelobes and the noise level. Sub-images (I_p) were then linearly mosaiced together into a 'dirty' spectral data cube $I_{\rm LM}$:

$$I_{\rm LM}(l) = W(l)\,\frac{\sum_p A(l-l_p)I_p(l)/\sigma_p^2}{\sum_p A(l-l_p)^2/\sigma_p^2}. \qquad (2.3)$$

   Note that this equation (from Sault, Staveley-Smith, & Brouw 1996) is written in only one dimension for simplicity, and assuming that the primary beam, $A(l)$, is the same for all pointings. Weighting by the noise variance of a sub-image, σ_p^2, causes the noise variance in the resultant mosaiced image to be minimised. The weighting factor $W(l)$ is determined so it partially corrects for the primary beam attenuation and also suppresses noise amplification at the edge of the mosaic.

   The imaging task (INVERT) also outputs a beam data set. It consists of the synthesised beams for each pointing (B_p) and the primary beam model ($A(l)$), and is therefore a cube of 320 planes in this case. As the point-spread-function (PSF, $B_{\rm LM}$) is position-dependent in the case of mosaicing (Cornwell, Holdaway, & Uson 1993), it can be computed at each position l_0 from the linear mosaic of individual synthesised beams (Sault, Staveley-Smith, & Brouw 1996), using:

$$B_{\rm LM}(l;l_0) = W(l)\,\frac{\sum_p A(l_0-l_p)B_p(l-l_0)A(l-l_p)/\sigma_p^2}{\sum_p A(l-l_p)^2/\sigma_p^2}. \qquad (2.4)$$

   It is interesting to note the difference between a synthesised beam and a PSF at the same position in the case of mosaicing (Fig. 2.4). The PSF looks much cleaner because of the noise suppression during linear mosaicing. Also, summing up different synthesised beam patterns in a linear mosaic (Eq. 2.4), makes the PSF having much fuller $u-v$ coverage (Sault, Staveley-Smith, & Brouw 1996).

2. **The deconvolution step**
   The 'dirty' data set, $I_{\rm LM}$, the position dependent PSF, $B_{\rm LM}$, and the true sky

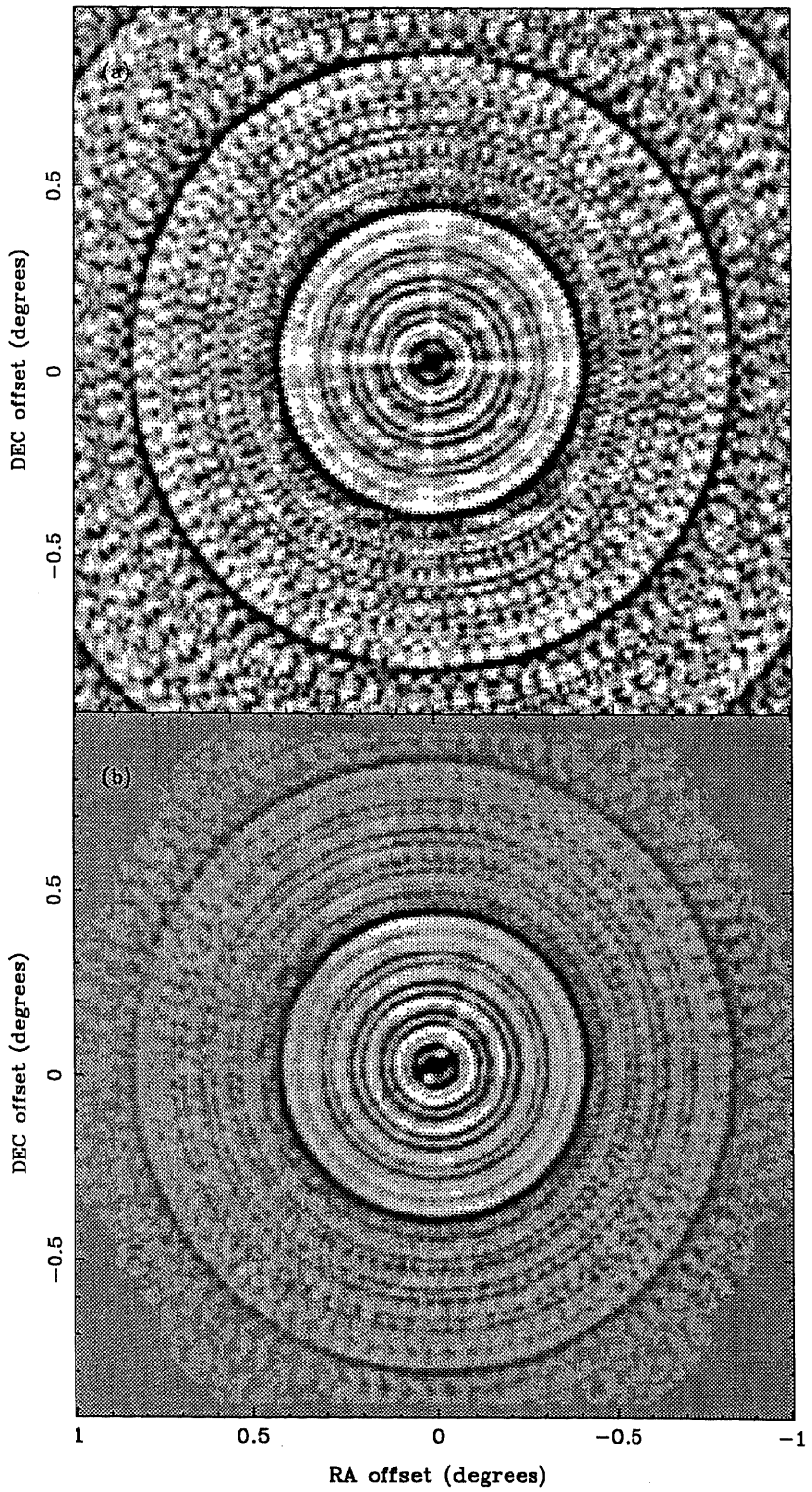

Figure 2.4 . The synthesised beam (a) and the mosaic point-spread-function (b) for pointing 201, centred at RA $01^h01^m46^s$, Dec $-72°49'34''$ (J2000). The grey-scale range is -2 to 6 K with a linear transfer function.

brightness distribution, I, still obey the convolution relationship (Cornwell, Holdaway, & Uson 1993) given by:

$$I_{\rm LM} \approx B_{\rm LM} * I. \tag{2.5}$$

The 'dirty' data cube was hence spatially deconvolved for each velocity channel, using a non-linear maximum entropy algorithm (MEM). This algorithm is discussed in more detail in the next chapter. Like all other deconvolution algorithms, MEM interpolates missing information in the $u-v$ plane between adjacent spacings. It also tries to extrapolate the missing information within the central hole in the $u-v$ plane, determined by the shortest spacing (see Chapter 3), but with limited success. Therefore, all angular scales corresponding to the spacings shorter than the shortest measured spacing, will be unreliable on the final images. In practice, mosaicing reduces the shortest spacing to $d - D/2$, which corresponds to the angular size of $\lambda/(d - D/2) = 0°.6$. Angular scales larger than $0°.6$ cannot be reliably reproduced on the resultant images.

3. **The image restoration**
The deconvolution model was further convolved with a 98 arcsec FWHM Gaussian function and the residuals of the deconvolution process were added back in.

The final data cube has a size of 578 × 610 × 78 pixels, in RA, Dec and velocity, respectively. The rms noise, measured in line-free parts of the cube, is 22 mJy beam^{-1}. This corresponds to a 1-σ brightness temperature sensitivity of 1.4 K, or a column density sensitivity of 4.2×10^{18}cm^{-2} per 1.65 km s^{-1} channel.

As an example, the deconvolved and restored ATCA SMC image at heliocentric velocity 169 km s^{-1} is presented in Fig. 2.5. The image shows a lot of negative bowls and sidelobes (shown in white colour) around emission regions (in grey or black colour). These are the artifacts due to the missing information about the large-scale structure. The Fourier transform of the 'dirty' data cube at the same velocity is shown in Fig. 2.6. Comparison of this figure with an example of the $u-v$ coverage for an individual pointing (Fig. 2.1), demonstrates nicely that it is not a deconvolution that enables some 'missing information' in the $u-v$ plane to be recovered, but a linear mosaic of many different pointing centres.

2.2.3.1 Probing different weighting schemes

As well as the robust weighting, a number of other weighting schemes were explored.

Natural weighting gives constant weight $D_k = 1$ to all visibilities, hence it optimises point-source sensitivity in an image but gives a poor synthesised beam-shape and higher sidelobes levels (Sramek & Schwab 1989).

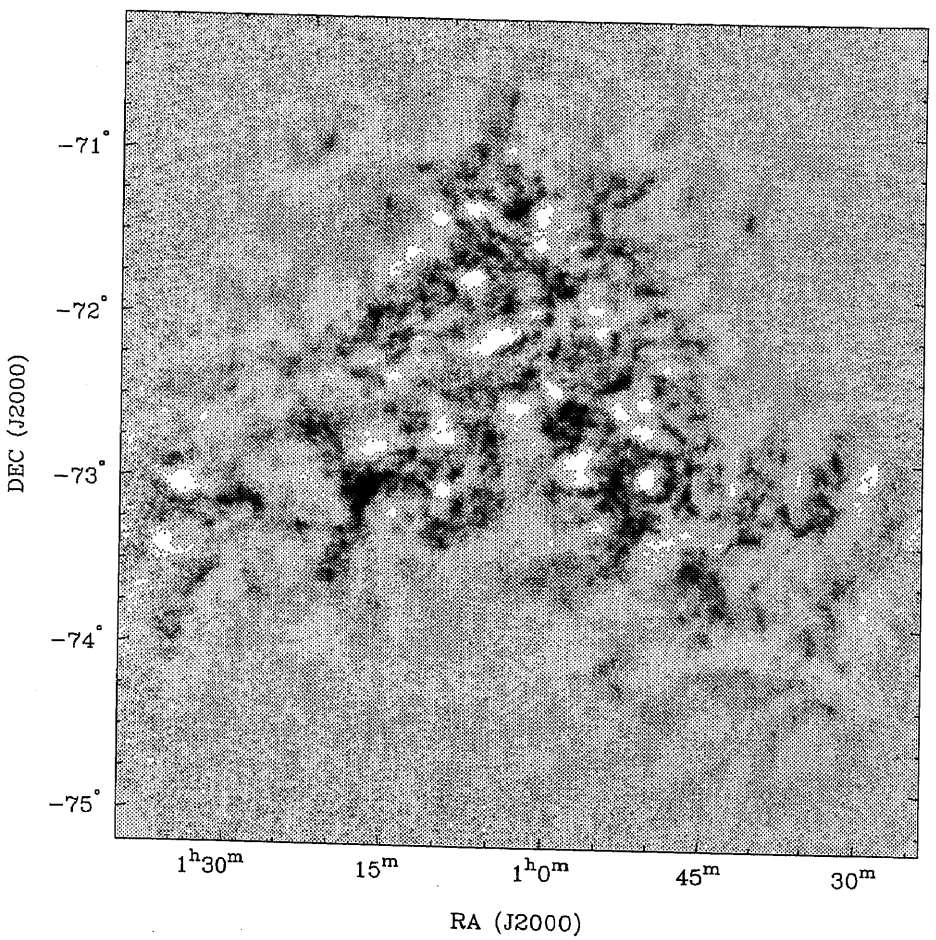

Figure 2.5 . The ATCA HI image of the SMC at heliocentric velocity 169 km s^{-1}. The grey-scale intensity range is −11 to 76 K with a linear transfer function. The beam size is 98 arcsec. The maximum HI brightness temperature, 95 K, is at position RA $01^h13^m10^s$, Dec −73°14′43″ and the minimum brightness temperature, −16 K, is at RA $01^h04^m10^s$, Dec −72°00′00″ (J2000). Bowls of negative flux density (in white colour) around emission regions (shown in black or grey colour) are not real, these are artifacts of the missing short spacings.

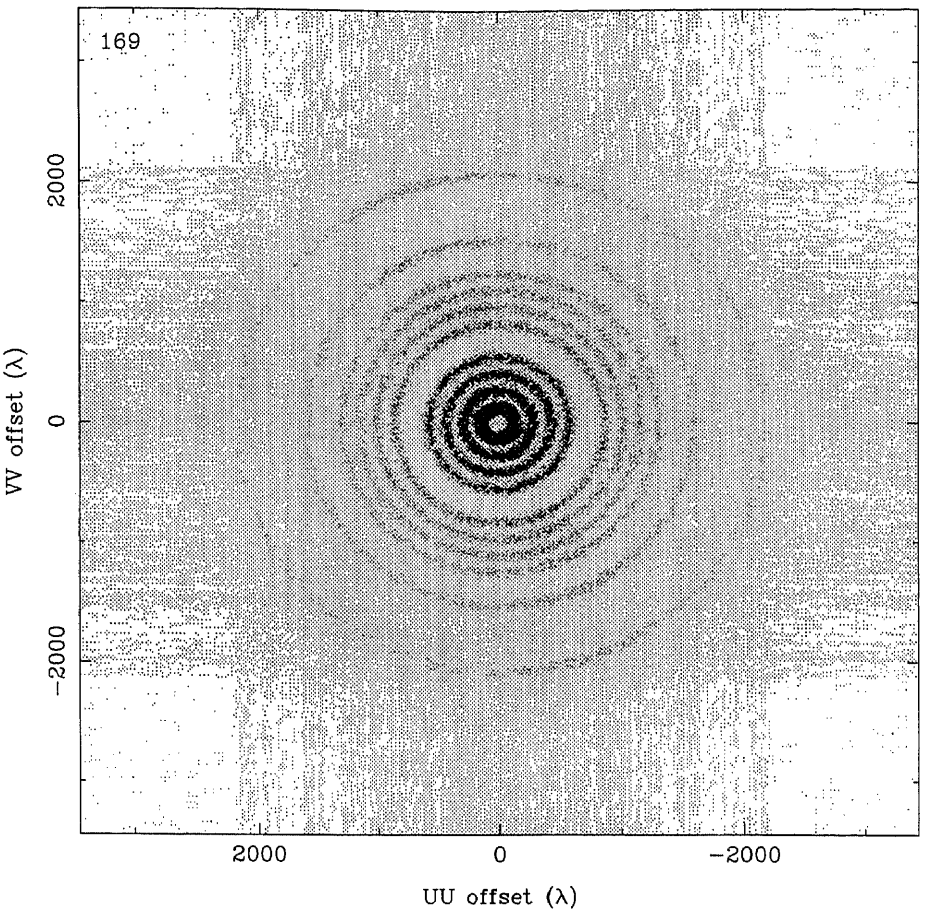

Figure 2.6 . The Fourier transform of the SMC 'dirty' mosaic at heliocentric velocity 169 km s^{-1}. The grey-scale range is 0 to 32 K. Ten baselines are visible with extended coverage due to the mosaicing. The central hole corresponds to missing information about the large-scale structure.

Uniform weighting gives a weight inversely proportional to the sampling density function, $D_k = 1/N_s(k)$, where $N_s(k)$ is the number of data points within a symmetric region in the $u - v$ plane having a characteristic width s and being centred on the k^{th} data point (Sramek & Schwab 1989). This type of weighting usually minimises sidelobe level but increases the noise level. This weighting was originally applied on the data by Staveley-Smith et al. (1997) and had resulted in the rms noise of 22 mJy $beam^{-1}$ of the final data cube. This corresponds to the brightness temperature sensitivity of 1.3 K.

Robust weighting can provide a compromise between natural weighting (which minimises the noise level) and uniform weighting (which minimises sidelobes). The robust parameter (Sault & Killeen 1998) ranges between $-\infty$ and ∞, with values less than -2 minimising sidelobes and values greater than 2 minimising the noise level. To provide a compromise between the noise level and sidelobes, the robust

parameter was set to zero. This resulted in the rms noise, measured in line-free parts of the final data cube, of 22 mJy beam^{-1}, as already mentioned.

However, Sault, Staveley-Smith, & Brouw (1996) argue that none of the robust, natural and uniform weightings give optimum sidelobe suppression for mosaics. The use of a large size for sub-images (115 × 115 pixels each of size 30 arcsec, see Staveley-Smith et al. 1997 for details), which is constrained by the FWHP of the primary beam, results in a very fine $u-v$ grid and $N_s(k) \approx 1$ for all data points. Therefore, all three weighting schemes become identical. Better sidelobe suppression (and resolution) can be achieved using 'super-uniform' weighting (Sault 1984; Sault, Staveley-Smith, & Brouw 1996). Applying this weighting scheme with the 'sup' parameter in INVERT equal to the antenna primary beamwidth ($\sim$ 2000 arcsec), resulted in the final resolution of 77 arcsec, but higher rms of 26 mJy beam^{-1}. The corresponding brightness temperature sensitivity is 2.7 K.

For further data analysis, the data cube obtained using robust weighting will be used, since it has a lower noise level (1.3 K) than the one produced with the 'super-uniform' weighting, but not much deeper sidelobes.

2.3 Parkes HI observations and reduction

2.3.1 Observations and data calibration

Observations of the SMC were made with the Parkes telescope on 1996 March 14 – 17 and August 2 – 3 (Parkes project P194, investigators: Staveley-Smith L., Kesteven M., Sault R.J., Snowden S.L. & Dickey J.M.). The Parkes telescope is a 64 m single-dish situated near Parkes, Australia. The telescope has a FWHP beamwidth of approximately 14.7 arcmin at 21 cm when the single beam 'H/OH' feed is used.

A single-beam, cooled, 21-cm receiver was used to observe a total of 1540 pointings centred on RA 01^h01^m, Dec $-72°56'$ (J2000) and covering a total area of 4°.5×4°.5 (which matches the ATCA coverage). The pointings were spaced by 7.5 arcmin, half of the telescope FWHP beamwidth. Fig. 2.7 shows the distribution of all 1540 pointings superimposed on the Hα image of the SMC from Kennicutt et al. (1995). An observing bandwidth of 8 MHz (1688 km s^{-1}) was used, and the AT correlator was configured to give 2048 channels on each of the two (linear) polarisations. This gives a channel spacing of 0.82 km s^{-1}, though consecutive channels were later averaged to give a channel spacing of 1.65 km s^{-1} to match the ATCA data. Although the results are not presented here, Galactic HI was also observed during the observations.

Data were taken by scanning the telescope in 35 tracks in declination (more strictly – the tangent plane y–axis), stopping at 44 discrete positions along each track,

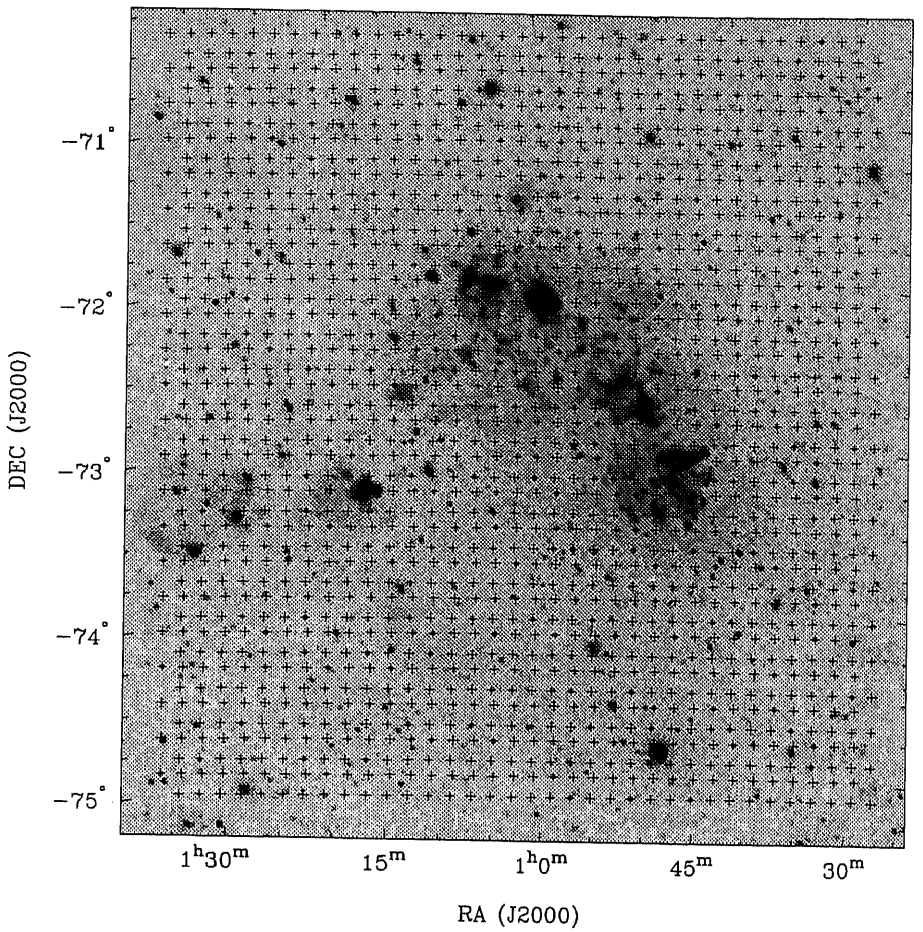

Figure 2.7 . The distribution of the observed pointing centres with the Parkes telescope (+) and superimposed on an Hα image of the SMC from Kennicutt et al. (1995).

and integrating for 30 s at each position. After each declination track, a line-free calibration region at RA 00^h10^m, Dec $-60°00'$ (J2000) was observed. This was used for bandpass-removal. For calibration purposes, the highest brightness-temperature region in the SMC (pointing 416 at RA $00^h47^m52.6^s$, Dec $-73°02'19.8''$, J2000) was observed after each track. This was used to establish accurate relative calibration for the data on each day and in each polarisation. Absolute calibration was based on observations of PKS B1934-638 which was assumed to have a flux density of 14.9 Jy at the observing frequency. With this calibration, pointing 416 has a peak flux density of 147.4 Jy, with an rms calibration accuracy of $\sim$ 0.7 per cent. This flux density is telescope- and feed-dependent, but contemporaneous observations of the Galactic calibration source S9 (T_B = 85 K, Williams 1973) gave a conversion factor to brightness temperature of 0.93 K Jy^{-1}, resulting in an estimated peak brightness temperature of 137 K for pointing 416*. This is also the position of maximum HI

*The theoretical conversion factor, based on a main-lobe beam area of 2.07×10^{-5} sr, is 0.78 K

column density in the SMC, for which a value of 1.14×10^{22} atoms cm^{-2} is measured. This corresponds to the extraordinarily high value, for any galaxy, of 91 M$_\odot$ pc^{-2} for the projected surface density of neutral hydrogen alone. Results in Section 4.2.1 suggest that correction for self-absorption may increase this by a factor ~ 1.44. For comparison with our results, Hindman (1967) quotes a peak brightness temperature of 150 K and his maps show a maximum HI column density of 1.28×10^{22} cm^{-2}. The spectra of McGee & Newton (1982) show a peak of 130 K, and a summation of their Gaussian decomposition gives a peak column density of 1.08×10^{22} cm^{-2}. The peak brightness temperature measured by Mathewson, Ford, & Visvanathan (1986) is ~ 150 K. All these temperatures and column densities appear to be within 15 per cent of our new values.

Observations of the continuum source PKS B0252-712 were also made after each declination scan. The average flux density of this was found to be 5.43 Jy, close to the 1992 ATCA value of 5.48 Jy. Observations of Hydra A gave flux densities almost identical to the Baars et al. (1977) value of 43.5 Jy (to which the 1934-638 flux-density scale is ultimately tied), if a beam-dilution factor of 1.08 is used to account for its non-compact nature (J.E. Reynolds, private communication).

2.3.2 Gridding spectra

In order to combine single-dish with interferometer data in the next chapter, both Parkes and the ATCA data sets must have the same coordinate system.

Therefore, the 2×1540 Parkes spectra were subsequently convolved onto a sky grid using a Gaussian convolving function with a FWHM of 12 arcmin. A North Celestial Pole (NCP) projection was used to match the ATCA projection. Originally, a larger pixel size than the one for the ATCA data set was used for the Parkes data, since gridding with smaller pixel size requires much longer computing time. The cube was then re-gridded to match the coordinate system of the ATCA data, using the AIPS's task HGEOM which applies polynomial interpolation. Since the HGEOM result was not satisfactory (due to artifacts in the Fourier domain), the gridder was performed again specifying a pixel size of 30 arcsec as for the ATCA data.

After the gridding by convolution the effective beam became equal to $\sqrt{12^2 + 14.7^2}$, which means that the angular resolution was broadened to 18.8 arcmin. A gridding correction factor (Sramek & Schwab 1989) of 1.63, equal to the ratio of new and old beam areas, was applied to account for the new beam size. This ensures that, as with the ATCA cube, a point source has a peak flux density equal to its true flux density.

As an example, the Parkes HI image of the SMC, at heliocentric velocity of 169 km s^{-1} is presented in Fig. 2.8.

Jy^{-1}. The ratio represents a main-beam efficiency of ~ 0.84.

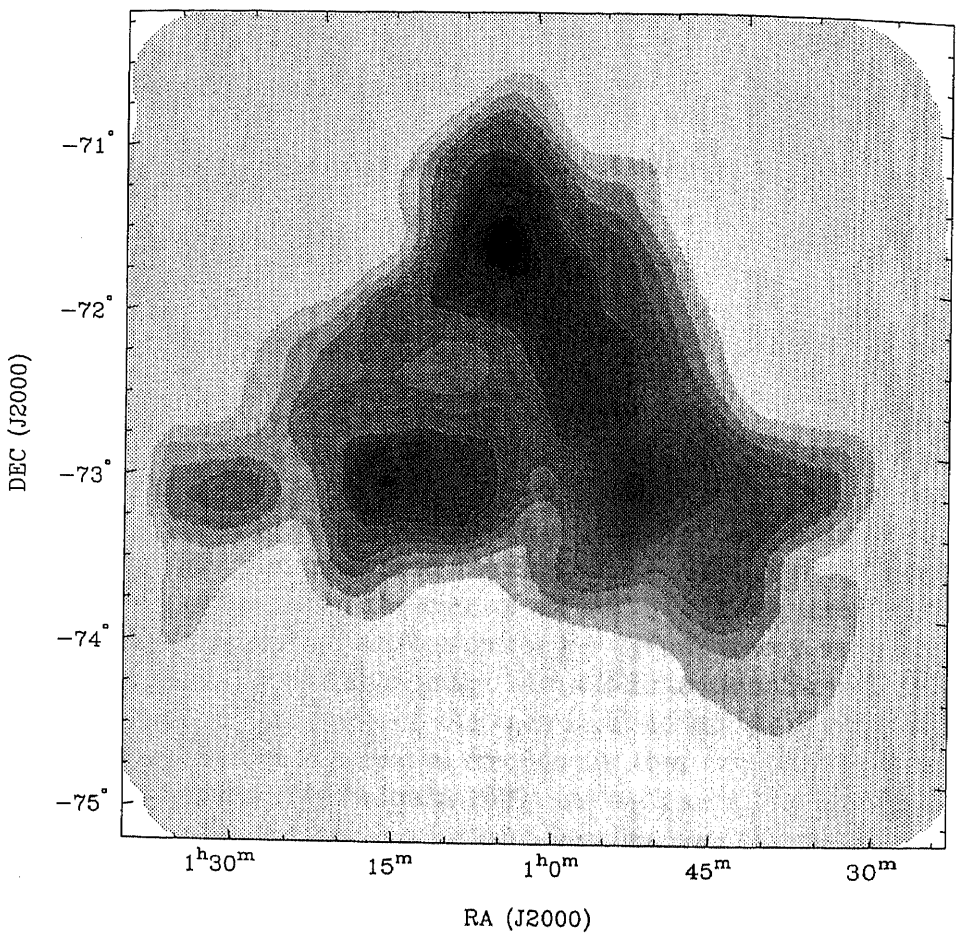

Figure 2.8 . The Parkes HI image of the SMC at heliocentric velocity 169 km s^{-1}. The grey-scale intensity range is 0 to 77 K with a linear transfer function. The beam size is 18.8 arcmin. The maximum HI brightness temperature, 76 K, is at position RA $01^h02^m48^s$, Dec $-71°49'11''$ and the minimum brightness temperature, 0 K, is at RA $00^h37^m18^s$, Dec $-70°39'51''$ (J2000).

Chapter 3

Combining single-dish and interferometer data

3.1 Introduction

Any interferometer, for a given configuration of antennas, has a limited range of baselines, including the minimum* and maximum baselines, and a discontinuous range of baselines in between. In the case of an Earth tracking interferometer, as the Earth rotates the baseline projections on the $u-v$ plane trace a series of ellipses. All ellipses are concentric for a linear array. For a 2-dimensional array, the ellipses are not concentric and so can intersect. As each baseline has a different ellipse, the ensemble of ellipses indicates the spatial frequencies that can be measured by the array (see Thompson, Moran, & Swenson 1986). At each sampling interval, the correlator measures the visibility function for each baseline over elliptical tracks in the $u-v$ plane, thus resulting in a discrete number of samples being measured. Hence, the resultant interferometer's $u-v$ coverage will be always, more or less, incomplete, having: a hole in the centre of the $u-v$ plane with a diameter corresponding to the minimum baseline; gaps between measured elliptical tracks; and gaps between each two adjacent samples on each elliptical track.

When imaging, an incomplete $u-v$ coverage leads to artifacts, such as negative 'bowls' around emission regions and negative and positive sidelobes (Cornwell & Braun 1989). The deconvolution process is able to partially overcome these problems by interpolating/extrapolating missing information in the $u-v$ plane (Cornwell & Braun 1989). This process works well when a compact configuration of antennas is used and when the source is small enough, $\theta \leq 2\lambda/b_{\min}$ (Bajaja & van Albada 1979), where θ is an angular extent of the object, λ is an observational wavelength and $b_{\min}$

*The shortest baseline that can be achieved is constrained by the physical limitations in placing two dishes together and a shadowing effect of one dish by another one.

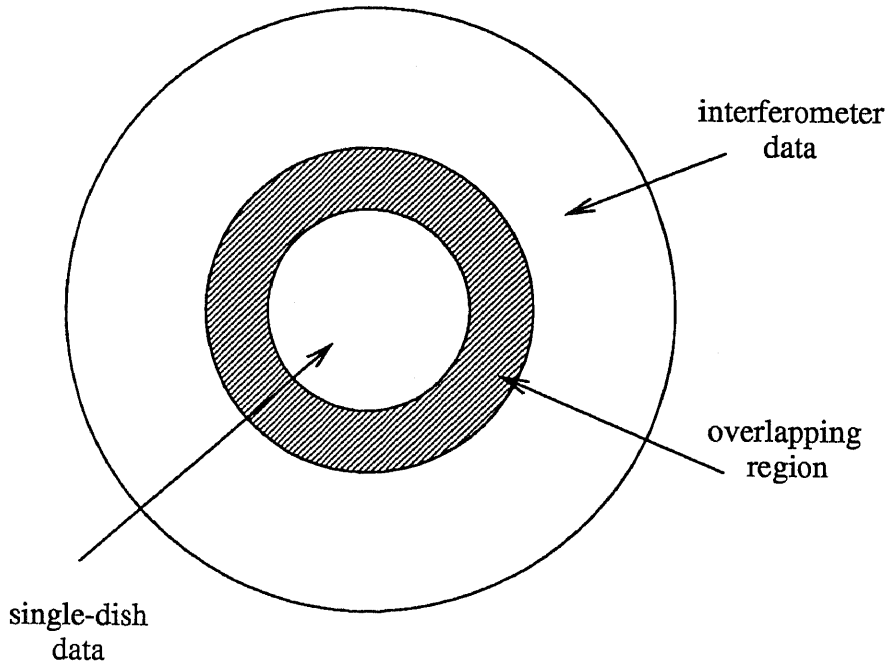

Figure 3.1 . The $u-v$ coverage of an image in a heterogeneous scheme for providing missing short-spacings: the inner part comes from a single-dish only, the outer part comes from an interferometer only, while the overlapping region contains spacings to which both the single-dish and interferometer are sensitive.

is the shortest baseline. The lack of information on very low spatial frequencies (around the centre of the $u-v$ coverage) in an interferometric observation is usually referred to as the 'short-spacings problem'.

Larger objects with $\theta > \lambda/b_{\rm min}$ can be observed with a single-dish. If a single-dish scans across an object on the sky, it measures not only a single spatial frequency, but a whole range of continuous spatial frequencies all the way up to a maximum one, which corresponds to the baseline equal to the diameter of a dish, $D_{\rm sd}$. Hence, a single-dish behaves as an interferometer having a continuous range of baselines, from zero up to $D_{\rm sd}$. An analogy of a scanning single-dish in interferometry, led to the foundations of a new observing technique for large objects – mosaicing (Ekers & Rots 1979; Sault, Staveley-Smith, & Brouw 1996). Mosaicing many different pointing centres together enables a large object to be observed with an interferometer, but at the same time rebuilds the interferometer's $u-v$ coverage, making it more complete. However, this still leaves the central hole corresponding to the shortest spacings.

Hence, interferometers provide, in general, high resolution observations for imaging

the small-scale structure (corresponding to high spatial frequencies), while single-dishes provide the data from the largest spatial scales (corresponding to the lowest spatial frequencies), including the total power (corresponding to the zero spacing). However, for many astrophysical studies, it is essential to bring 'both worlds' together by combining information about both small and large scale structure.

There are two main questions concerning the short-spacings problem:

1. how to provide (observe) missing short-spacings; and
2. how to combine them with interferometric data containing longer spacings.

In answering the first question, all solutions can be grouped into two array schemes: homogeneous, having all antennas of the same size, and heterogeneous, based on observations obtained with different-sized antennas. There are many possibilities concerning the heterogeneous arrays, such as using smaller arrays and even a hierarchy of smaller arrays. The simplest option, though, is a large single-dish telescope with a diameter ($D_{\rm sd}$) larger that the interferometer's minimum baseline, since a single dish will measure all baselines between zero and $D_{\rm sd}$, as shown in Fig. 3.1. Holdaway (1998) argues that it is hard to provide a large single-dish which would have the sensitivity equivalent to the interferometer's. Also, single-dish observations are very difficult (they require a lot of separate pointing centres to cover a large object) and very sensitive to systematic errors. Using theoretical analysis, numerical simulations and observational tests, Cornwell, Holdaway, & Uson (1993) show that a homogeneous array in which the short-spacings are obtained from single antennas in the array, allow high quality imaging. They find that a key advantage over a large single-dish scheme is pure simplicity, which is an important factor for the complex interferometric systems.

In answering the second question, methods for the combination of interferometer and single-dish data can be grouped in two approaches: data combination in the Fourier domain (Bajaja & van Albada 1979; Volgel et al. 1984; Roger et al. 1984; Wilner & Welch 1994; Zhou, Evans, & Wang 1996), and data combination in the image domain (Ye & Turtle 1991; Stewart et al. 1993; Schwarz & Wakker 1991; Holdaway 1998). Each approach can be realised through a number of different methods.

This chapter discusses theory and applications of both approaches for the combination of single-dish and interferometer data. The relative calibration for the flux-density scales of both data sets, is also considered. Four different methods for data combination were applied on the HI spectral line observations of the SMC, obtained with the ATCA and Parkes telescope, and the results compared. Therefore, the heterogeneous scheme for providing missing short-spacings has been used. The shortest ATCA baseline is 31 m, while the Parkes dish has a diameter of 64 m. However, using the mosaicing technique for the ATCA observations (Section 2.2), resulted in the shortest spacing being 25 m. This provided a large overlap of the spatial frequencies, which was used to determine the relative calibration of the ATCA and

Parkes flux density scales.

3.2 The calibration scaling factor ($f_{\rm cal}$)

Before combination, an estimate of the relative calibration of the flux-density scales for the interferometer and the single-dish data is required. The relationship between flux density S (in Jy) of a source and its brightness temperature $T_{\rm B}$ (in units of K) or brightness distribution I (in units of Jy sr^{-1}), is given by:

$$S = \int \frac{2kT_{\rm B}}{\lambda^2} d\Omega = \int I d\Omega \tag{3.1}$$

(Kraus 1966), where k is the Bolzmann constant, λ is the wavelength of observation (21 cm) and $d\Omega$ is an infinitesimal solid angle of sky (in rad^2).

For a point source, this gives:

$$S = \frac{2kT_{\rm B,peak}}{\lambda^2}\Omega = I_{\rm peak}\Omega \tag{3.2}$$

with $T_{\rm B,peak}$ being the peak brightness temperature, Ω being the main beam area and $I_{\rm peak}$ being the peak brightness. Although the single dish and interferometer have different beams, $S_{\rm sd} = S_{\rm int}$ if the data sets are properly calibrated. However, calibration is never perfect and the calibration differences between the two data sets can be significant in some cases (e.g. observations spread over long period of time, different data quality, use of different flux scales for calibration, quality of calibrators, etc.). This results then in the difference of the measured flux-densities.

Hence, we define the relative calibration factor of the flux-density scales for the interferometer and the single-dish data ($f_{\rm cal}$) as the ratio of the flux densities of an unresolved, compact source:

$$f_{\rm cal} = \frac{S_{\rm int}}{S_{\rm sd}}. \tag{3.3}$$

In the case of a perfect calibration $f_{\rm cal} = 1$, but $f_{\rm cal} \neq 1$ otherwise, and needs to be determined very accurately.

Unfortunately, no suitable compact HI sources exist to directly determine $f_{\rm cal}$. Hence, the best way to estimate $f_{\rm cal}$ is to compare surface brightness of the observed object in the region of overlap in the $u - v$ plane. This region should correspond to angular sizes to which both telescopes are sensitive. For a source of brightness I

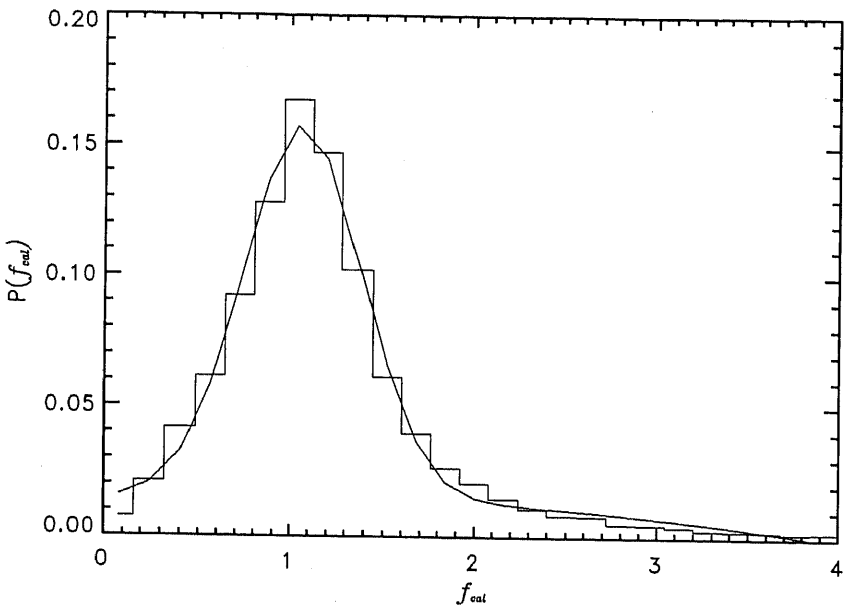

Figure 3.2 . The probability distribution of the ratios of the amplitudes of the ATCA and Parkes visibilities at all positions in the overlapping range of spatial frequencies and for all velocity planes. The mean of distribution has value of 1.28, while the modal value is 1.05 ± 0.05.

which fills the beams, both the interferometer and single dish should measure within this region the same, $I_{sd} = I_{int}$, and calibration errors will appear as:

$$f_{cal} = \frac{I_{int}}{I_{sd}}. \tag{3.4}$$

I_{int} and I_{sd} are often, for convenience, expressed in units of Jy beam^{-1} not Jy sr^{-1}, and so will be different numbers because of different beams considered (with beam areas Ω_{int} and Ω_{sd}, respectively). For this purpose, an estimate of the resolution difference between two data sets ($\alpha = \Omega_{int}/\Omega_{sd}$) is also needed. A value $\alpha = 7.5 \times 10^{-3}$ was estimated from the square of the ratio of the assumed Gaussian ATCA beam with FWHM of 98 arcsec (see Section 2.2) and the convolved Gaussian Parkes beam of 18.8 arcmin (Section 2.3). The following procedure was further applied.

1. Both the Parkes and ATCA images (in units Jy beam^{-1}) were tapered by multiplying by a function which smoothly decreased the image intensities to zero near the edges. This is a necessary step, since the Parkes image in particular has non-zero emission observed everywhere and hence sharp image edges where the data end. The sharp edges produce strong horizontal and vertical ringing (spikes) in the centre of the Fourier plane (Bracewell 1978) after

Fourier transforming (an effect caused by the Gibbs phenomenon and referred to as the edge-effect).

2. The Parkes cube was multiplied by the beam area ratio, α, to account for the resolution difference.

3. Both dirty cubes were Fourier transformed. The Fourier transform of the Parkes dirty cube was then divided by the Fourier transform of the Parkes beam (which is equivalent to the deconvolution of the single-dish data).

4. The ratio of the amplitudes of the ATCA and Parkes visibilities was calculated at all positions in the overlapping range of spatial frequencies (120–170λ, corresponding to 25–35 m baselines where good sensitivity data is provided by both the ATCA and Parkes) and for each velocity plane separately.

5. The modal value from a histogram of ratios for all velocity planes (see Fig. 3.2) was then estimated. The probability distribution of the measured $f_{\rm cal}$ seems to be well approximated with a Rayleigh distribution

$$P(f_{\rm cal}) = \frac{f_{\rm cal}}{\sigma^2} \exp - \frac{f_{\rm cal}^2}{2\sigma^2} \tag{3.5}$$

(Crane & Napier 1989) and a long tail in the distribution is the result of noise in the data. The mean value of the distribution is hence a biased estimate of $f_{\rm cal}$ and is equal to 1.28, while $\sigma = 1.03$.

The modal value gives a better estimate for $f_{\rm cal}$ (Crane & Napier 1989), of:

$$f_{\rm cal} = 1.05 \pm 0.05, \tag{3.6}$$

which is consistent with the relative calibration accuracy of both data sets.

Since $f_{\rm cal}$ represents the calibration accuracy of both data sets it must not vary for velocity channels with sufficient signal. Fig. 3.3 shows the total flux density and $f_{\rm cal}$ plotted versus heliocentric velocity. The very high values of $f_{\rm cal}$ for the velocity range $80 - 110$ km s^{-1} correspond to very noisy channels. $f_{\rm cal}$ is approximately constant for the velocity range $130 - 200$ km s^{-1}, which corresponds to velocity channels with the most HI emission. This proves the calibration accuracy of both interferometer and single-dish data. The values for $f_{\rm cal}$ on this plot are slightly higher than the final deduced value since they represent mean values in each velocity channel and are therefore slightly biased by noise.

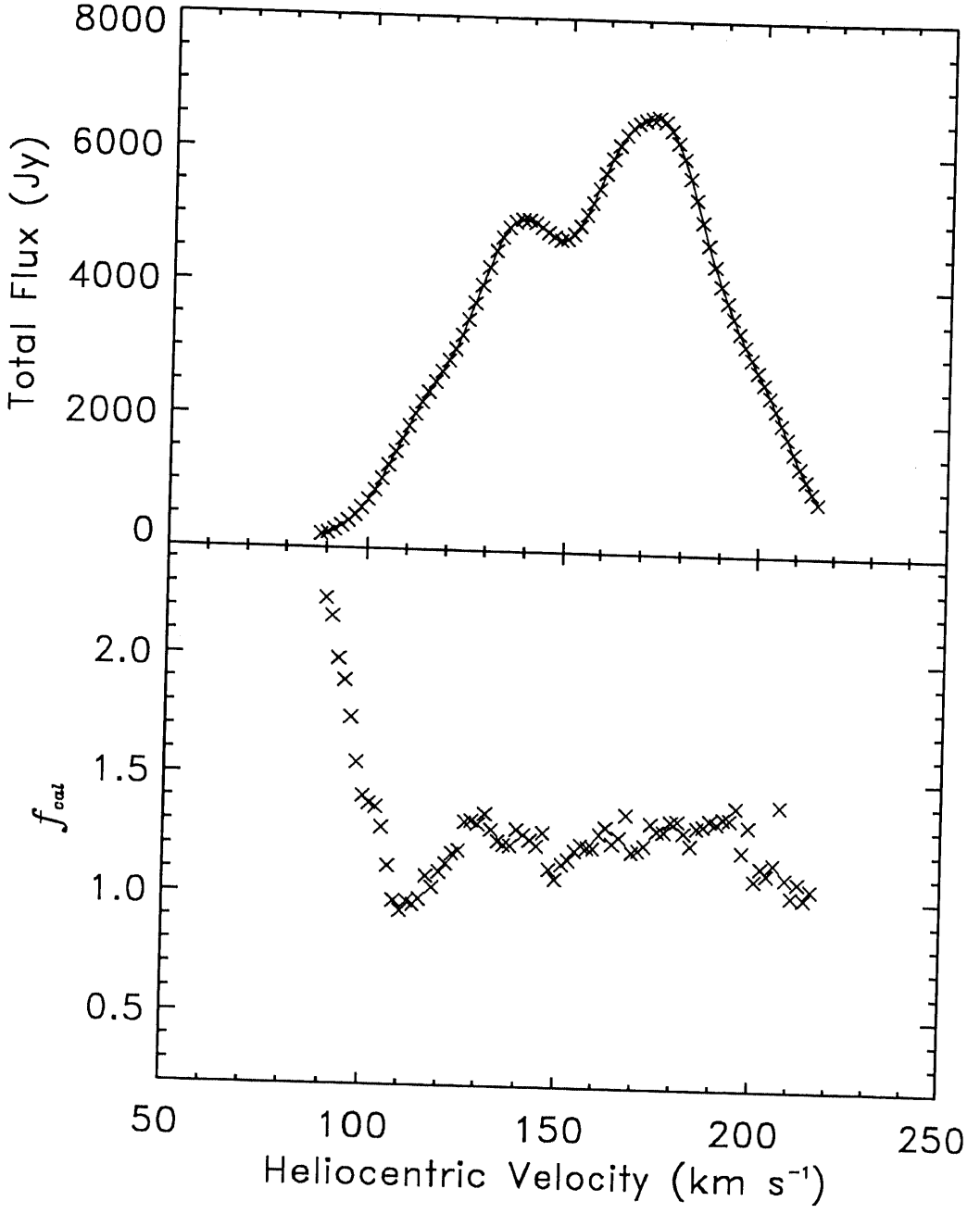

Figure 3.3 . The total flux density in Jy (top) and the dimensionless calibration scaling factor f_{cal} (bottom) of the SMC data plotted as a function of heliocentric velocity. The values for f_{cal} are estimated as mean values in the overlapping annulus for each velocity channel, and are therefore slightly biased by noise.

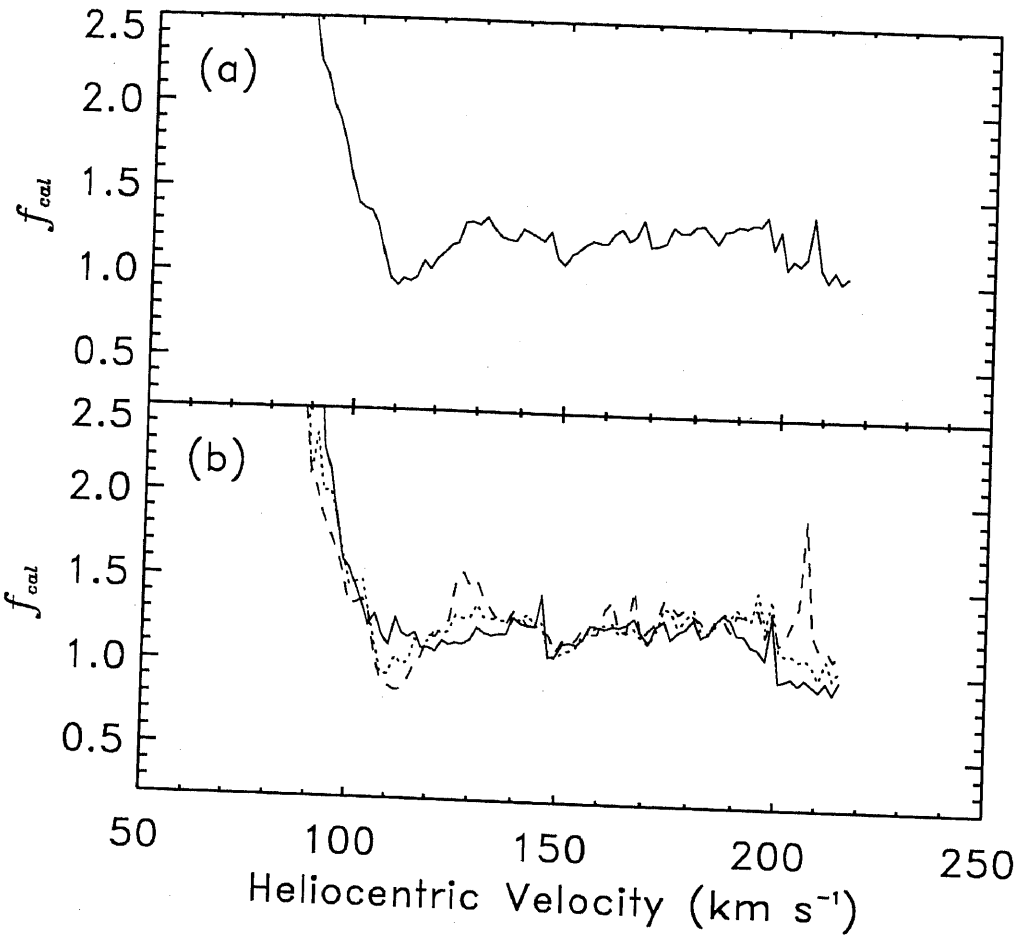

Figure 3.4 . The calibration scaling factor as a function of heliocentric velocity determined within: (a) 0.12 - 0.17 kλ and (b) 0.11 - 0.13 kλ (solid line), 0.13 - 0.15 kλ (dotted line) and 0.14 - 0.16 kλ (dashed line).

3.2.1 The relationship between the calibration scaling factor ($f_{\rm cal}$) and the single-dish beam

The deconvolution of the single-dish data (step 3) requires very good knowledge of the single-dish beam. The calibration scaling factor should not vary with the spatial frequency within the overlapping annulus, since it is a result of the calibration differences between two data sets only. But, an error in the single-dish beam model has the same effect in the overlapping region as an error in the flux scale (Sault & Killeen 1998), resulting in a different value for the calibration scaling factor. Therefore, the single-dish beamwidth and the calibration scaling factor are highly coupled. Unfortunately, in most cases, they can not be determined simultaneously, since the overlap of spatial frequencies is usually not wide enough and S/N ratio is often not great. However, a variation of $f_{\rm cal}$ in the overlapping annulus of spatial frequencies, for different single-dish beamwidths, can be iteratively used to check or

approximate the single-dish beam size.

The Fourier transform of a single-dish dirty map gives:

$$V'_{\rm sd}(k) = V(k) \times b_o(k) \tag{3.7}$$

where k is a distance from the centre of the Fourier plane, $V(k)$ and $V'(k)$ are the Fourier transforms of the true and observed sky brightness distribution, respectively, and $b_o(k)$ is the Fourier transform of a single-dish beam. If a Gaussian beam is assumed, with FWHM being θ_o, for a true single-dish beam, its Fourier transform is given by:

$$b_o(k) = \frac{1}{\sqrt{2\pi}} \exp\left(-\frac{\theta_0^2 k^2}{4\ln 2}\right) \tag{3.8}$$

If a Gaussian beam with the different FWHM (θ), is used for deconvolution, where $\theta = \theta_0 + \Delta\theta$, the ratio of amplitudes of the interferometer and single-dish Fourier transforms will be:

$$\frac{V_{\rm int}}{V_{\rm sd}} = \exp\left(-\frac{\Delta\theta(2\theta_0 + \Delta\theta)k^2}{4\ln 2}\right) \tag{3.9}$$

In the case when assumed beamwidth is close to the true one, $|\Delta\theta| \ll \theta_o$, this simplifies to a quadratic equation:

$$f_{\rm cal} \approx \left[1 + \frac{\Delta\theta(2\theta_0 + \Delta\theta)}{4\ln 2} k^2\right]. \tag{3.10}$$

Hence, in the case when a FWHM of the Gaussian single-dish beam is not known well enough, $f_{\rm cal}$ will be a quadratic function of a distance k in the Fourier plane:

$$f_{\rm cal} = M + Nk^2. \tag{3.11}$$

One can iteratively determine coefficients M and N for different assumed FWHM finding values for $f_{\rm cal}$ for different annuli within the overlapping region. The real value of FWHM can be then interpolated so that it corresponds to $N = 0$.

Fig. 3.4 shows $f_{\rm cal}$, determined in three smaller rings within the overlapping range of spatial frequencies (bottom plot), as a function of heliocentric velocity and in comparison with $f_{\rm cal}$ determined within the whole overlapping region (top plot). All graphs are very similar, showing that $f_{\rm cal}$ does not vary with spatial frequencies for adopted Gaussian Parkes beam of 18.8 arcmin, which confirms our assumed value for α.

3.3 Data combination in the Fourier domain

3.3.1 Theory

Visibilities measured by an interferometer ($V'_{\rm int}$) are given by:

$$V'_{\rm int}(u,v) = (V(u,v) * a_{\rm int}(u',v')) \times b_{\rm int}(u,v), \tag{3.12}$$

where u and v are baseline coordinates projected in the plane of the sky and measured in units of wavelength, V and $a_{\rm int}$ are Fourier transforms of the true sky brightness distribution I and the primary beam pattern $A_{\rm int}$, respectively, and $b_{\rm int}$ is the interferometer sampling function. $b_{\rm int}$ is usually representable by a collection of δ-functions, between the lowest and the highest spatial frequency sampled by the interferometer (corresponding to the shortest and the longest baselines, respectively). The Fourier transform of this relationship gives the observed sky brightness distribution $I^{\rm D}_{\rm int}$ ('dirty' image):

$$I^{\rm D}_{\rm int}(x,y) = (I(x,y) \times A_{\rm int}(x,y)) * B_{\rm int}(x',y') \tag{3.13}$$

with x and y being coordinates on the sky and $B_{\rm int}$ being the synthesis beam or the point source response of the interferometer. The determination of I from $I^{\rm D}_{\rm int}$ in the deconvolution process (Cornwell & Braun 1989), involves interpolation and extrapolation of $V'_{\rm int}$ for missing data due to the discontinuous nature of $b_{\rm int}$ (see Section 3.1). The modified sky brightness, $I(x,y) \times A_{\rm int}(x,y)$, can be trivially corrected for the primary beam at the final stage of data processing (Sramek & Schwab 1989). Hence, the distinction between the true and modified sky brightness will not be made from now on.

In the case of observations with a single-dish, the observed sky brightness distribution $I^{\rm D}_{\rm sd}$ is given by:

$$I^{\rm D}_{\rm sd}(x,y) = I(x,y) * B_{\rm sd}(x',y'), \tag{3.14}$$

with $B_{\rm sd}$ being the single-dish beam pattern. The Fourier transform of this relationship gives observed single-dish visibilities, $V'_{\rm sd}$:

$$V'_{\rm sd}(u,v) = V(u,v) \times b_{\rm sd}(u,v) \tag{3.15}$$

where $b_{\rm sd}$ is the Fourier transform of the single-dish beam pattern, which is a continuous function between zero and the highest spatial frequency sampled by the

single-dish (corresponding to the diameter of the single-dish), contrary to $b_{\rm int}$. Determination of I from $I^{\rm D}_{\rm sd}$ (called deconvolution) is different than the one in Eq. 3.13. It does not require interpolation and extrapolation since $V'_{\rm sd}$ is a continuous function. Note that both $V'_{\rm int}$ and $V'_{\rm sd}$ have a finite extent in the $u-v$ plane, which limits the final resolution of I.

Bajaja & van Albada (1979) show that the true missing short-spacing visibilities can be provided in the Fourier domain from the function $V(u,v)$ in Eq. 3.15, if the single-dish is large enough to cover the whole central gap in the interferometer's $u-v$ coverage. The deconvolution of the single-dish data gives the true single-dish visibilities, where $b_{\rm sd}(u,v) \neq 0$, by:

$$V(u,v) = \frac{V'_{\rm sd}(u,v)}{b_{\rm sd}(u,v)}. \tag{3.16}$$

Function $V(u,v)$ can be then substituted in Eq. 3.12, after rescaling by $f_{\rm cal}$, everywhere in the $u-v$ plane where Eq. 3.16 holds. This would provide the resultant $u-v$ coverage having the inner visibilities from the single-dish data only (rescaled to match interferometer's flux density scale due to the calibration differences), and the outer visibilities from the interferometer data only. The region of overlapping spatial frequencies, if present, can be represented by the weighted mean of both single-dish and the interferometer visibilities, or data can be complementary filtered (Roger et al. 1984). To produce the final (corrected for the short-spacings) image, the deconvolution with $b_{\rm int}$ and a correction for the primary beam attenuation are required at the end.

An alternative to this method is to extract circular visibility tracks from $V_{\rm sd}$ (Volgel et al. 1984; Wilner & Welch 1994; Zhou, Evans, & Wang 1996), instead of using the whole data provided by the single-dish. Wilner & Welch (1994) have generated a set of (u,v) points randomly distributed within the missing central gap of the interferometer's Fourier plane, taking care that the density of points is equal to that in the inner (u,v) range sampled by the interferometer. Another slight variation would be to use a clean interferometer map as an input, so that the combined map does not require deconvolution with $b_{\rm int}$ at the end. This is implemented in the AIPS image analysis package as a task called IMERG.

In all cases, for a good data combination, the single-dish data set should fulfill several of the following conditions.

- The diameter of the single-dish should be greater or equal to the central hole in the interferometer's $u-v$ plane in order to fill in all missing spacings. The region of overlapping spatial frequencies is required in order to determine the scaling factor.
- A sufficiently fine sampling of the single-dish data at the Nyquist rate (twice per beamwidth) is required to avoid aliasing during deconvolution (Volgel et al.

1984). Single-dish data also must have the same coordinate system as the interferometer data. Therefore, it is sometimes necessary to re-grid single-dish images.

- Both methods require a Fourier transform of the single-dish data. This can suffer from the strong edge-effects when the observed object is very extended and has significant column densities at the edges of the surveyed region. To avoid edge-effects, the observed single-dish field must be therefore sufficiently large, usually larger than the field covered by an interferometer.
- Visibilities derived from the single-dish should have a signal-to-noise ratio comparable to those of the interferometer in the overlapping region in order not to degrade the combined map (Volgel et al. 1984).
- The deconvolution of the single-dish data is necessary in both methods. This can amplify the edge-effect errors and the systematic errors which may be present in the data (such as varying baselines, etc.) (Schwarz & Wakker 1991), and is very sensitive to the knowledge of the single-dish beam. It is therefore essential to have the best information possible of the single-dish beam.

3.3.2 Application

One application of the data combination in the Fourier domain, investigated here, is implemented in the MIRIAD image analysis package as task IMMERGE (Sault & Killeen 1998). In order to compare this method later with other ones, we will call it 'method A'. IMMERGE works with the clean, high resolution and non-deconvolved, low resolution, images. The input images are Fourier transformed (labelled as $V(k)$ and $V'_{\rm sd}$) and combined in the Fourier domain applying tapering functions, $w'(k)$ and $w''(k)$, such that their sum is equal to the Gaussian function having a FWHM of the interferometer, $\theta_{\rm int}$:

$$V_{\rm comb}(k) = w'(k)V(k) + f_{\rm cal}w''(k)V'_{\rm sd}(k) \tag{3.17}$$

$$w'(k) + w''(k) = \frac{1}{\sqrt{2\pi}} \exp\left(-\frac{\theta^2_{\rm int}k^2}{4\ln 2}\right). \tag{3.18}$$

Function $w''(k)$ is a Gaussian with the FWHM of the single dish. The low resolution visibilities are multiplied by $f_{\rm cal}$ to account for the calibration differences. The final resolution is that of the interferometer image. The sampling (tapering) functions are shown in Fig. 3.5, together with the sampling function of the merged data set.

The data combination using IMMERGE was applied on the SMC ATCA and Parkes HI spectral line observations. For simplicity, we consider only one velocity channel at 169 km s^{-1}. The Parkes image was first multiplied by the gain function of the

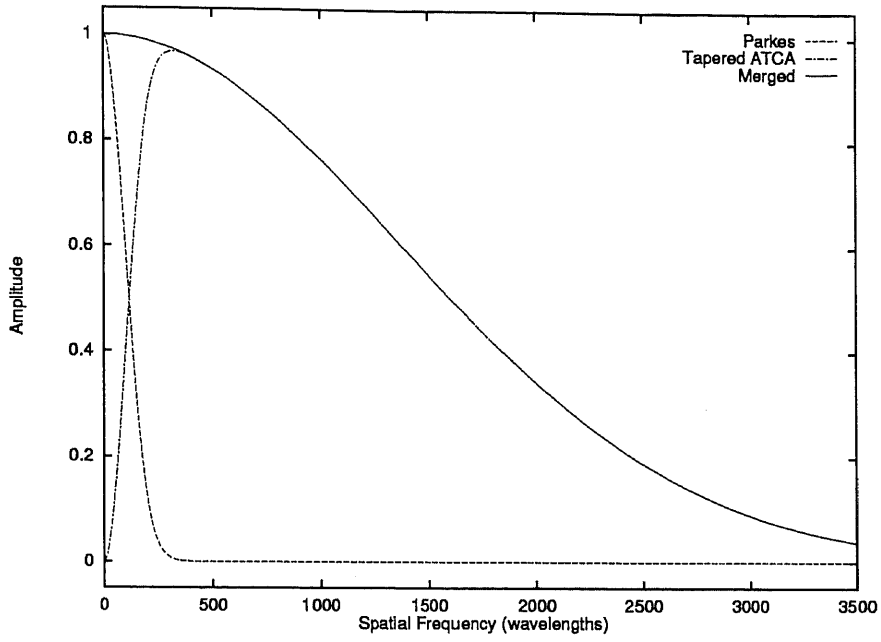

Figure 3.5 . The spatial frequencies sampled by the low resolution Parkes image, the tapered high resolution ATCA image, and by the image produced by IMMERGE.

ATCA image to smoothly taper down image intensity towards the edges, in order to avoid edge-effects. The already determined calibration scaling factor of 1.05 was assumed, together with the Gaussian Parkes and ATCA beams having the FWHM of 18.8 arcmin and 98 arcsec, respectively. The resultant combined image is shown in Fig. 3.6.

3.3.3 $f_{\rm cal}$ from IMMERGE

An alternative method for the determination of the calibration scaling factor, different from the method explained in Section 3.2, can be performed by IMMERGE. A clean interferometer image is convolved with a single-dish beam and Fourier transformed ($V \times b_{\rm sd}$). A single-dish image is Fourier transformed ($V'_{\rm sd} = V \times b_{\rm sd}$), and functions $V \times b_{\rm sd}$ and $V'_{\rm sd}$ are then compared in the region of the overlapping spatial frequencies, pixel by pixel, including both real and imaginary values. A linear function is then fitted between them, to estimate $f_{\rm cal}$. In this way, the deconvolution of the single-dish data, which is dependent on a good knowledge of the single-dish beam, is avoided.

The method was tested on the same ATCA and Parkes SMC HI spectral line data cubes. Parkes images, for all velocity planes, were tapered by the ATCA gain function to avoid edge-effects, and the calibration scaling factor ($f_{\rm cal}$) was derived

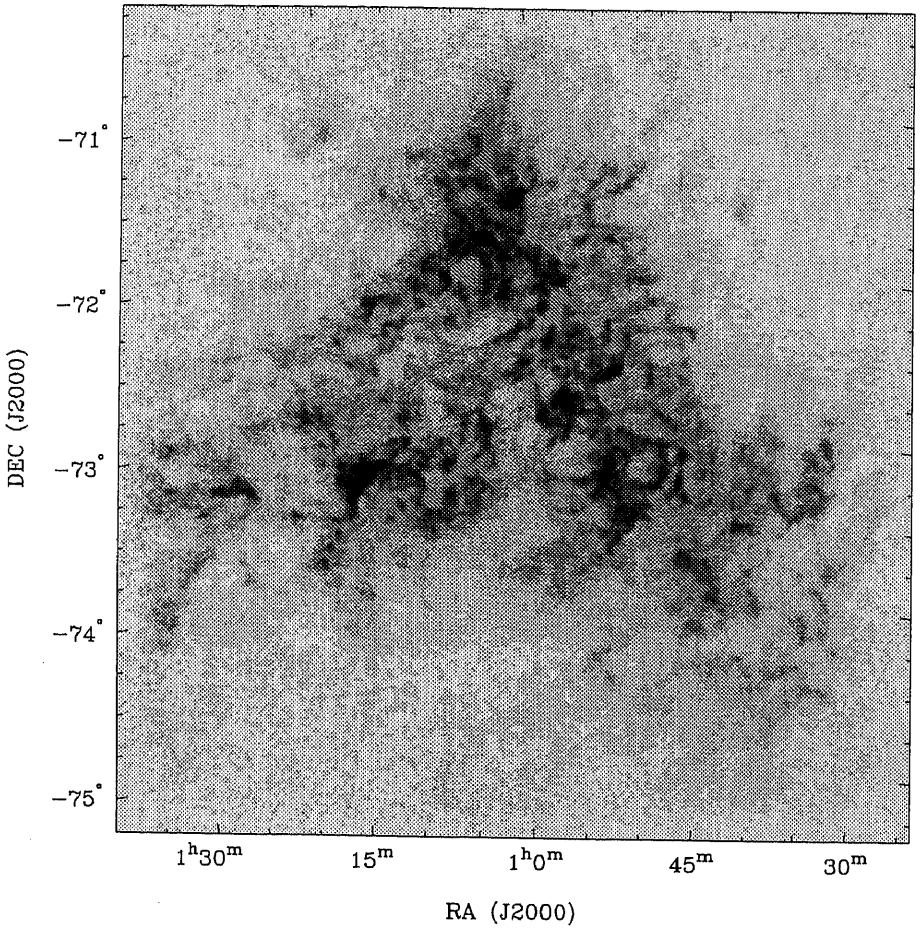

Figure 3.6 . The HI image of the SMC at heliocentric velocity 169 km s^{-1} after adding the Parkes short-spacings data using IMMERGE (method A). The grey-scale intensity range is −11 to 101 K with a linear transfer function. The beam size is 98 arcsec. The maximum HI brightness temperature of 124 K, is at position RA $01^h13^m10^s$, Dec −73°14′43″ (J2000) and the minimum brightness temperature, −15 K, is at RA $01^h34^m33^s$, Dec −73°18′37″ (J2000).

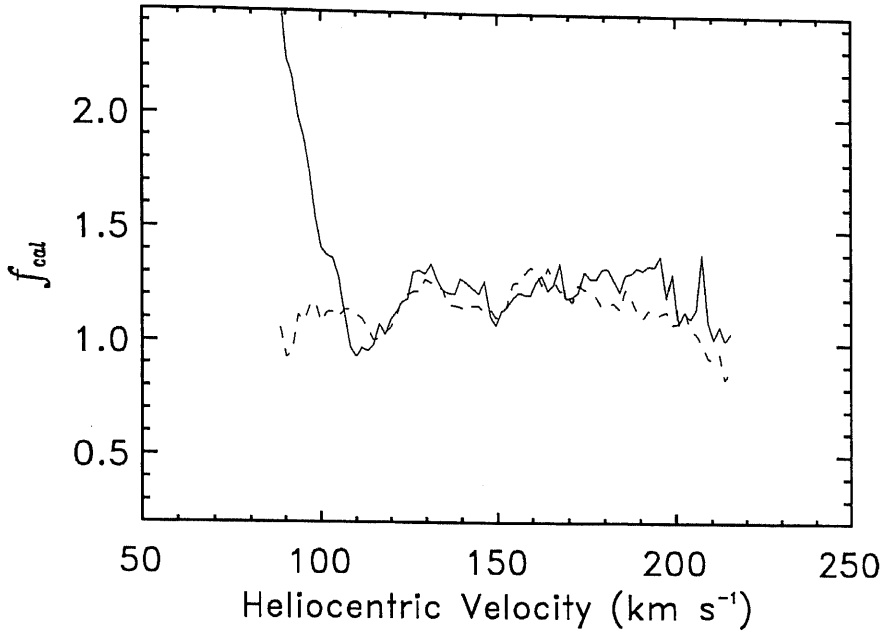

Figure 3.7 . The relative calibration factor f_{cal} as a function of heliocentric velocity. Values from Section 3.2 are shown with a solid line, while dashed line represents values derived using IMMERGE. All plotted values were estimated as a mean of the overlapping annulus of spatial frequencies, and are hence slightly biased by noise.

for each of the two ATCA and Parkes planes respectively. The region of overlapping spatial frequencies corresponds to 120–170 λ. For comparison with the calibration scaling factor determined in Section 3.2, values for f_{cal} determined for each velocity plane in both methods are plotted in Fig. 3.7. In the case of velocity channels with significant emission, both methods give very similar values for f_{cal}. For more noisy channels, IMMERGE seems to work better by including both real and imaginary parts in the analysis, while the previous method used amplitudes only, which increased noise for velocities < 110 km s^{-1}. However, all values plotted in Fig. 3.7 are slightly biased for noise, since f_{cal} is estimated by the mean value of the overlapping annulus.

Using simultaneously all data from velocity channels with significant emission, in the velocity range 130–200 km s^{-1}, the mean value of $f_{cal} = 1.20$ was estimated by IMMERGE, by fitting a linear function between the high and low resolution data (see Fig. 3.8). This is slightly higher than the value found in Section 3.2 where $f_{cal} = 1.05 \pm 0.05$. Since values determined by both methods for individual velocity channels agree well (Fig. 3.7), the mean value of $f_{cal} = 1.20$ is most likely slightly biased by noise, as suggested from Fig. 3.8. The residual difference between the high and the scaled low resolution data within the overlapping region, defined as:

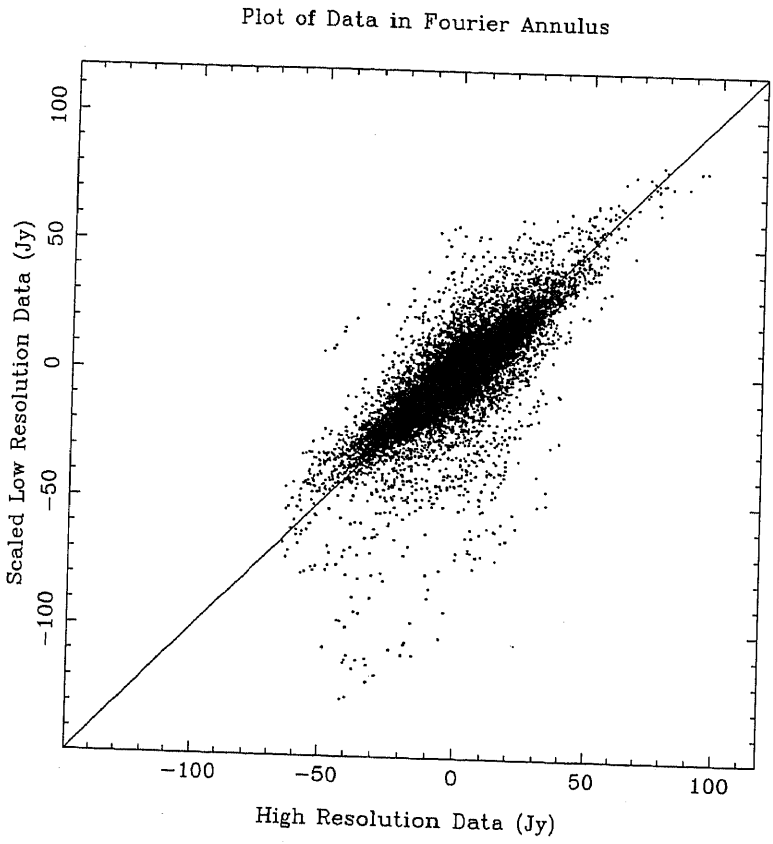

Figure 3.8 . A pixel-to-pixel comparison of the ATCA (x-axis) and the Parkes SMC (HI) data scaled by 1.2 (y-axis), for the heliocentric velocity range 130–200 km s^{-1}, between 120λ and 170λ in the Fourier plane. The data follows a $y = x$ line, although some scatter is present due to noise.

$$R(k) = V(k) \times b_{\rm sd}(k) - f_{\rm cal} V'_{\rm sd}(k), \tag{3.19}$$

can be also a good diagnostic for a quality of the single-dish beam parameters, similarly as discussed in Section 3.2.1. A trend in $R(k)$ might suggest that the single-dish beam parameters are grossly wrong (Sault & Killeen 1998). In Fig. 3.9, R is plotted as a function of spatial frequency k. All values $R(k)$ are close to zero and no systematic features as suggested in Section 3.2.1, which may be due to a poor model of the single-dish beam, are visible in the plot.

However, the normalised histogram of all data points, shown in Fig. 3.10, could explain the difference between the values for $f_{\rm cal}$ estimated here and in Section 3.2. This histogram can be fitted with a Gaussian function having the mean value $m = 0.1$ and the standard deviation $\sigma = 3.3$. As the beam parameters have been already tested, this slight displacement of $R(k)$ from zero is most likely a result of the value used for $f_{\rm cal}$. Using $f_{\rm cal} = 1.05$ in Eq. 3.19, results in a Gaussian fit with $m = 0.0$

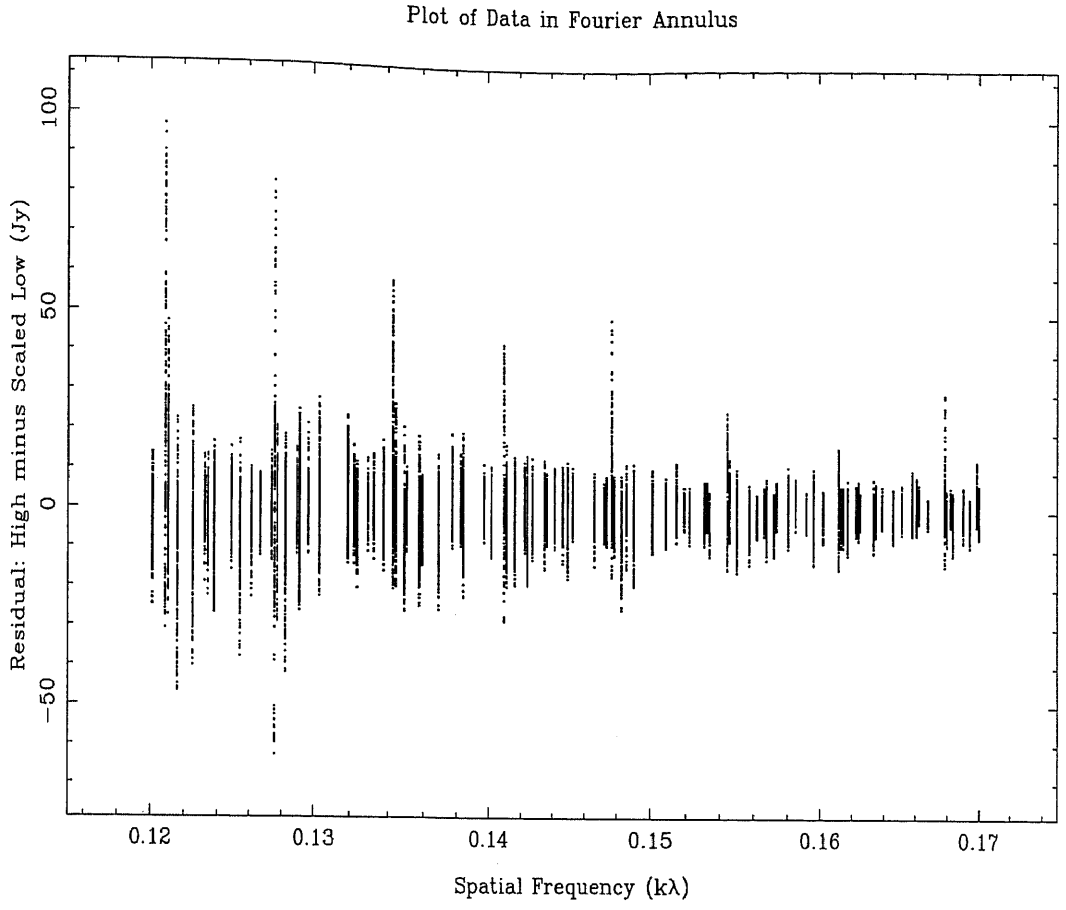

Figure 3.9 . The difference between the ATCA and the scaled Parkes SMC data for heliocentric velocities 130–200 km s^{-1}, as a function of spatial frequency in the Fourier plane.

and $\sigma = 3.2$. This proves that the value $f_{\rm cal} = 1.20$ is higher than the real scaling factor due to noise, and that method used in Section 3.2 provides more accurate estimate of $f_{\rm cal}$.

3.4 Data combination in the image domain

All methods for the data combination in the image domain can be divided into merging before and merging during a deconvolution process.

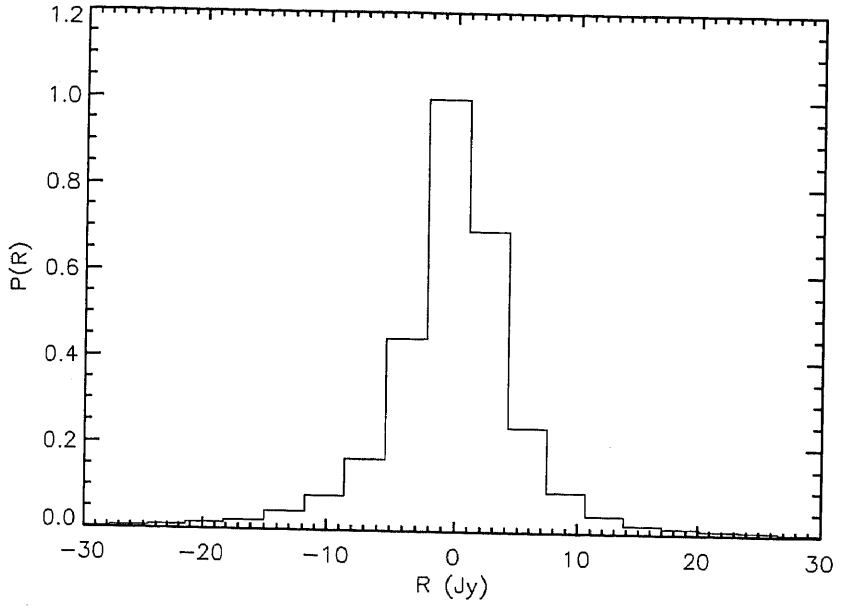

Figure 3.10 . The probability distribution of the difference between the ATCA and the scaled Parkes SMC data for velocity range 130–200 km s^{-1}.

3.4.1 Merging before deconvolution

The theoretical basis for merging before deconvolution is the linear property of the Fourier transform: a Fourier transform of a sum of two functions is equal to the sum of the Fourier transforms of both functions individually:

$$F(f_1 + f_2) = F(f_1) + F(f_2). \tag{3.20}$$

Therefore, instead of adding two maps in the Fourier domain and Fourier transforming the combined map to the image domain, one can produce the same effect (fill in missing short-spacings in an interferometer's $u - v$ coverage) by adding maps in the image domain. This method was applied by Ye & Turtle (1991), and Stewart et al. (1993).

The interferometer and single-dish data obey the convolution relationship:

$$I^{\rm D}_{\rm int} = I * B_{\rm int} \tag{3.21}$$
$$I^{\rm D}_{\rm sd} = I * B_{\rm sd} \tag{3.22}$$

where $I^{\rm D}_{\rm int}$ is a dirty high resolution image, $B_{\rm int}$ is a interferometer synthesised beam, $I^{\rm D}_{\rm sd}$ is a low resolution image and $B_{\rm sd}$ is a single-dish beam. $I^{\rm D}_{\rm int}$ and $I^{\rm D}_{\rm sd}$ are in units

Jy beam^{-1}, and therefore have different HI brightness scales since their beams and calibrations are different. The brightness scale of $I^{\rm D}_{\rm sd}$ is higher by a factor of $1/\alpha$, relative to the brightness scale of $I^{\rm D}_{\rm int}$ due to the resolution difference.

The dirty images and beams can be combined to form the composite dirty image ($I^D_{\rm comb}$) and the composite beam ($B_{\rm comb}$) with the following weighting:

$$I^D_{\rm comb} = (I^D_{\rm int} + \alpha f_{\rm cal} I^{\rm D}_{\rm sd})/(1+\alpha) \tag{3.23}$$

$$B_{\rm comb} = (B_{\rm int} + \alpha B_{\rm sd})/(1+\alpha). \tag{3.24}$$

The single-dish beam pattern was rescaled to match the interferometer beam pattern due to the resolution difference, and then normalised to have a maximum of 1. Effectively the same was done with the dirty images, since $\alpha I^D_{\rm sd}$ has a brightness different than $I^D_{\rm int}$ by a factor $1/f_{\rm cal}$ due to the calibration differences.

The convolution relationship, $I^D_{\rm comb} = B_{\rm comb} * I$, still exists between the composite dirty image, $I^D_{\rm comb}$, and the true sky brightness distribution, I, since:

$$I^D_{\rm int} + \alpha I^{\rm D}_{\rm sd} = (B_{\rm int} + \alpha B_{\rm sd}) * I. \tag{3.25}$$

Deconvolving the composite dirty image with the composite beam solves for I. Since any deconvolution algorithm implicitly applies certain weighting (Cornwell & Braun 1989), no *a priori* re-weighting of the interferometer and single-dish data is necessary (Ye & Turtle 1991). No data filtering in the region of the overlapping spatial frequencies is required, either. As much the same procedure is applied on both the combined dirty image and the combined beam, this is all the deconvolver needs. For example, in the region of the spatial overlap, true visibilities are obtained during deconvolution from:

$$V = \frac{V'_{\rm int} + \alpha V'_{\rm sd}}{b_{\rm int} + \alpha b_{\rm sd}} \approx \frac{2V'_{\rm int}}{2b'_{\rm int}} \tag{3.26}$$

which shows that the method does not simply double the power within this region.

Merging before deconvolution, hereafter 'method B', was applied on the 169 km s^{-1} velocity channel of the HI spectral line ATCA and Parkes observations of the SMC. The Parkes image was tapered to avoid edge-effects in the usual way. Dirty images and beams were combined according to Eq. 3.23 using the previously determined values for α and $f_{\rm cal}$ (Section 3.2). Note that $B_{\rm int}$ in this case represents a cube of beams (see Section 2.2.3). The combined dirty image was then deconvolved using MIRIAD's maximum entropy algorithm (Sault, Staveley-Smith, & Brouw 1996), which implicitly applies uniform weighting. The model was restored with a 98 arcsec Gaussian function, and the resultant image is shown in Fig. 3.11.

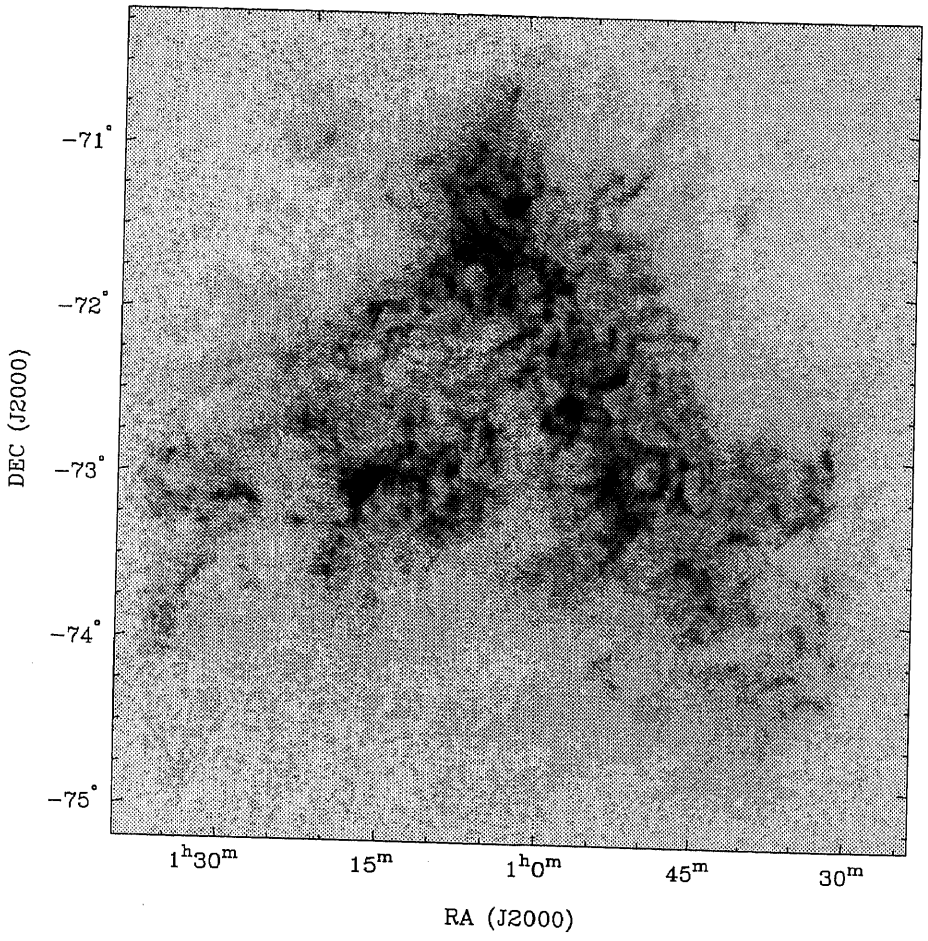

Figure 3.11 . The HI image of the SMC at heliocentric velocity 169 km s^{-1} after adding the Parkes short-spacings data in the image domain before deconvolution (method B). The grey-scale intensity range is −11 to 101 K with a linear transfer function. The beam size is 98 arcsec. The maximum HI brightness temperature, 136 K, is at position RA $01^h13^m11^s$, Dec −73°14′43″ and the minimum brightness temperature, −13 K, is at RA $01^h17^m7^s$, Dec −75°23′49″ (J2000).

3.4.2 Merging during deconvolution

3.4.2.1 Theory

Besides the missing information in the centre of the $u-v$ plane, an interferometer's $u-v$ coverage suffers from spatial frequency gaps. Since the missing information can be introduced in an infinite number of ways, the convolution equation ($I^D = I * B$) has a non-unique solution. Hence, the deconvolution has the task to select the 'best' image from many possible ones (Cornwell 1988). Since deconvolution has to estimate missing information, a non-linear algorithm must be employed (Cornwell 1988; Sault, Staveley-Smith, & Brouw 1996). Cornwell (1988) and Sault, Staveley-Smith, & Brouw (1996) showed that the algorithms implementing the 'joint' deconvolution scheme produce superior results in the case of mosaicing, since more information is provided to the deconvolver. We expect that the same argument might apply to the single dish data, resulting in the merging before and during deconvolution being more successful than the merging of clean images in the Fourier plane.

The maximum entropy method (MEM) is one of the non-linear deconvolution algorithms. It selects the deconvolution solution so it fits the data and, at the same time, has a maximum 'entropy'. Cornwell (1988) explains this entropy as something which when maximised produces a positive image with a compressed range in pixel values. The compression criterion forces the final solution (image) to be smooth, while the positivity criterion forces interpolation of unmeasured Fourier components. One of the commonly used definitions of entropy is:

$$\aleph = -\sum_i I_i \ln\left(\frac{I_i}{M_i e}\right) \tag{3.27}$$

where I_i is the brightness of i'th pixel of the MEM image and M_i is the brightness of i'th pixel of a 'default' image incorporated to allow *a priori* knowledge to be used (e is base of natural logarithm). The requirement that the final image fits the data is usually incorporated in a constraint such that the fit $\chi^2_{\rm int}$ of the predicted visibility to that observed (Cornwell, Holdaway, & Uson 1993) is close to the expected value:

$$\chi^2_{\rm int} \leq N\sigma^2_{\rm int} \tag{3.28}$$

with N being a number of independent pixels in the map and $\sigma^2_{\rm int}$ being a noise variance of interferometer data.

The single-dish data can be incorporated during the maximum-entropy deconvolution process in two ways.

1. The easiest way is to use single-dish data as a 'default' image in Eq. 3.27, since, in the absence of any other information or constraints, this forces the

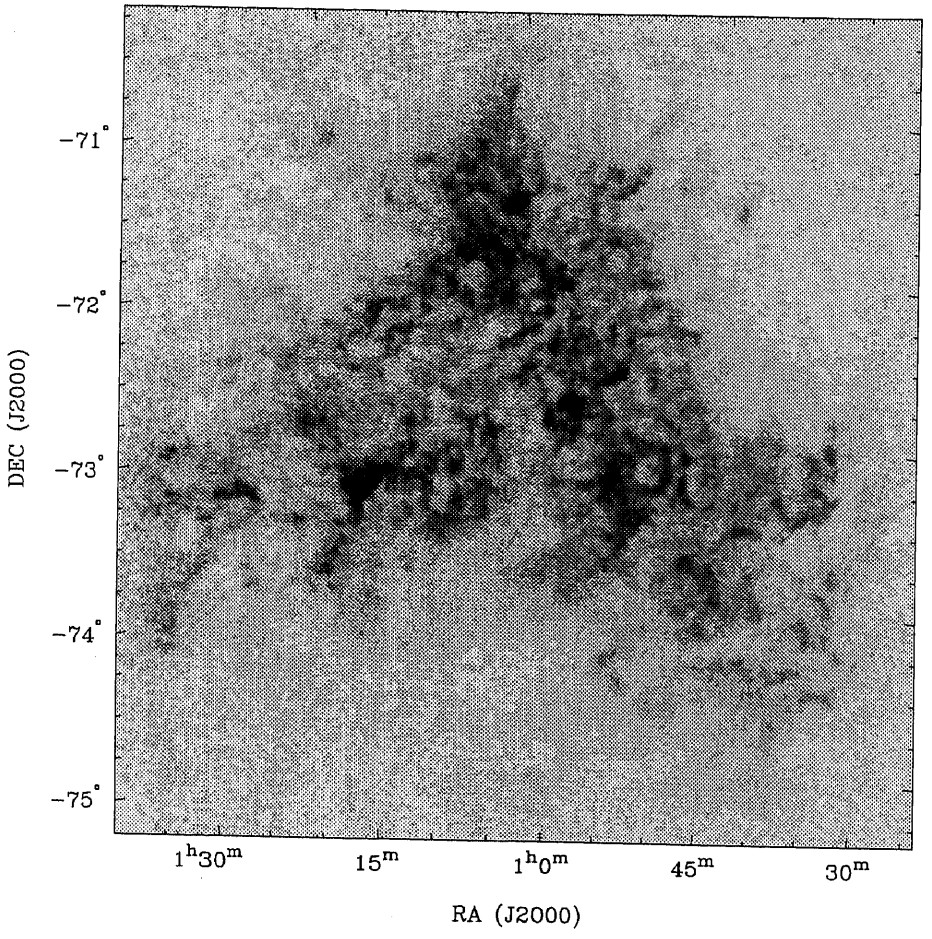

Figure 3.12 . The HI image of the SMC at heliocentric velocity 169 km s^{-1} after adding the Parkes short-spacings data in the image domain during deconvolution using the single-dish image as a 'default' information (method C). The grey-scale intensity range is −11 to 101 K with a linear transfer function. The beam size is 98 arcsec. The maximum HI brightness temperature, 126 K, is at position RA $01^h13^m10^s$, Dec $-73°14'43''$ and the minimum brightness temperature, −13 K, is at RA $01^h16^m51^s$, Dec $-73°23'52''$ (J2000).

deconvolved image to resemble the single-dish image in the spatial frequency domain where the interferometer data contribute no information. Since this method puts more weight to the interferometer data, wherever it exists, the size of the overlapping region plays a very important role (Holdaway 1998). As large an overlap of spatial frequencies as possible is required to provide good quality interferometer and single-dish data within this region, in order to retain the same sensitivity over the image. We label this method as 'method C' hereafter.

2. The final method (labelled as 'method D') maximises the entropy while being a subject to constraints of fitting both data sets simultaneously:

$$\aleph = -\sum_i I_i \ln\left(\frac{I_i}{e}\right) \tag{3.29}$$

$$\sum_i \left\{I^D_{\rm int} - B_{\rm int} * I\right\}^2_i < N\sigma^2_{\rm int} \tag{3.30}$$

$$\sum_i \left\{I^D_{\rm sd} - \frac{B_{\rm sd} * I}{f_{\rm cal}}\right\}^2_i < M\sigma^2_{\rm sd} \tag{3.31}$$

where: $I^D_{\rm int}$ and $I^D_{\rm sd}$ are dirty interferometer and single-dish images; $B_{\rm int}$ and $B_{\rm sd}$ are interferometer and single-dish beams; N and M are the numbers of independent pixels in the interferometer and single-dish map; $\sigma^2_{\rm int}$ and $\sigma^2_{\rm sd}$ are the noise variances of interferometer and single-dish data; and $f_{\rm cal}$ is the calibration scaling factor. The sum is taken over image pixels in all equations. To solve for I, the method of Lagrange multipliers can be employed which requires an iterative procedure. The method seems to be highly dependent on estimates of the noise variance of the interferometer and single-dish data.

The 'joint' deconvolution method, method D, provides also an alternative way, completely performed in the image domain, for determining the calibration scaling factor. Maximising the entropy while fitting both data sets, a 'joint' deconvolution algorithm, MOSMEM, can iteratively solve for I and $f_{\rm cal}$, simultaneously. However, the current performance of MOSMEM is still not satisfactory. Firstly, when performed on the spectral line observations, it handles only one velocity channel at the time, requiring some additional statistical method at the end for the estimate of the final value of $f_{\rm cal}$. Secondly, the convergence of $f_{\rm cal}$, for each velocity channel, appears to be dependent on $\sigma_{\rm sd}$. Future algorithm improvements are necessary in this direction.

3.4.2.2 Applications

Both methods for data combination during deconvolution are implemented in MIRIAD through the non-linear deconvolution algorithm MOSMEM. To test their performance, the same ATCA and Parkes HI spectral line observations of the SMC at

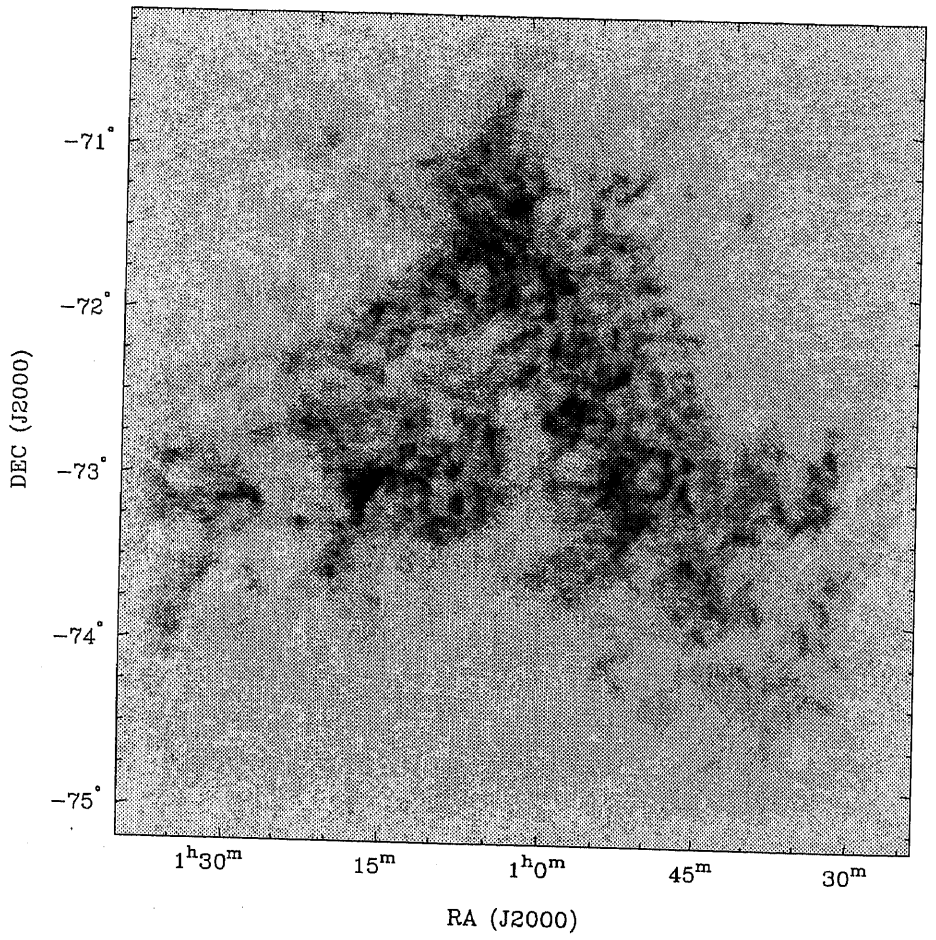

Figure 3.13 . The HI image of the SMC at heliocentric velocity 169 km s^{-1} after adding the Parkes short-spacings data in the image domain during the 'joint' deconvolution of both single-dish and interferometer data (method D). The grey-scale intensity range is −11 to 101 K with a linear transfer function. The beam size is 98 arcsec. The maximum HI brightness temperature, 126 K, is at position RA $01^h13^m10^s$, Dec $-73°14'43''$ and the minimum brightness temperature, −19 K, is at RA $01^h33^m17^s$, Dec $-72°45'09''$ (J2000).

velocity 169 km s^{-1} were used. The Parkes image was tapered in the usual way to avoid edge-effects.

1. For method C, the Parkes image (in units Jy $pixel^{-1}$) was multiplied by the previously determined value for αf_{cal} in order to match the ATCA flux density scale. The dirty ATCA image and beam were used as input parameters, while the rescaled Parkes image was used as a 'default' image, during the deconvolution process. The deconvolution model was then restored with a 98 arcsec Gaussian function and the result is shown in Fig. 3.12.

2. To apply the 'joint' deconvolution (method D) for final imaging, the calibration scaling factor $f_{cal} = 1.05$ was assumed, as well as σ_{sd}=0.1 Jy $beam^{-1}$. The deconvolution model (the result of MOSMEM) was then restored with a 98 arcsec Gaussian function and the resulting image is shown in Fig. 3.13.

3.5 Comparison of different methods

The qualitative comparison of all four methods for the short-spacings correction addressed here, labelled as methods A–D, is shown in Fig. 3.14 for the 169 km s^{-1} velocity channel of the SMC data. All four images have the same grey-scale range (−11 to 107 K) and are remarkably similar. They all have the same resolution and show the same small and large scale features with only slightly different flux scales. No signs of the interferometric artifacts are visible on any of the images. This shows that all four methods for the short-spacings correction, give satisfactory results in the first approximation, when an *a priori* determined calibration scaling factor is used.

Table 3.1 . Total flux, minimum, maximum and noise of the SMC ATCA image at 169 km s^{-1} corrected for Parkes short-spacings. Results of four different methods are shown: data combination in the Fourier domain using IMMERGE (method A), data combination before deconvolution (method B), data combination during deconvolution using Parkes data as a 'default' image (method C) and the 'joint' deconvolution of both Parkes and ATCA data (method D). The total flux of the Parkes image alone is 6100 Jy.

Method	Total Flux (Jy)	Min (Jy $beam^{-1}$)	Max (Jy $beam^{-1}$)	Noise (mJy $beam^{-1}$)
A	5600	−0.24	1.97	30
B	6500	−0.21	2.16	32
C	6300	−0.21	2.00	28
D	5900	−0.30	2.00	29

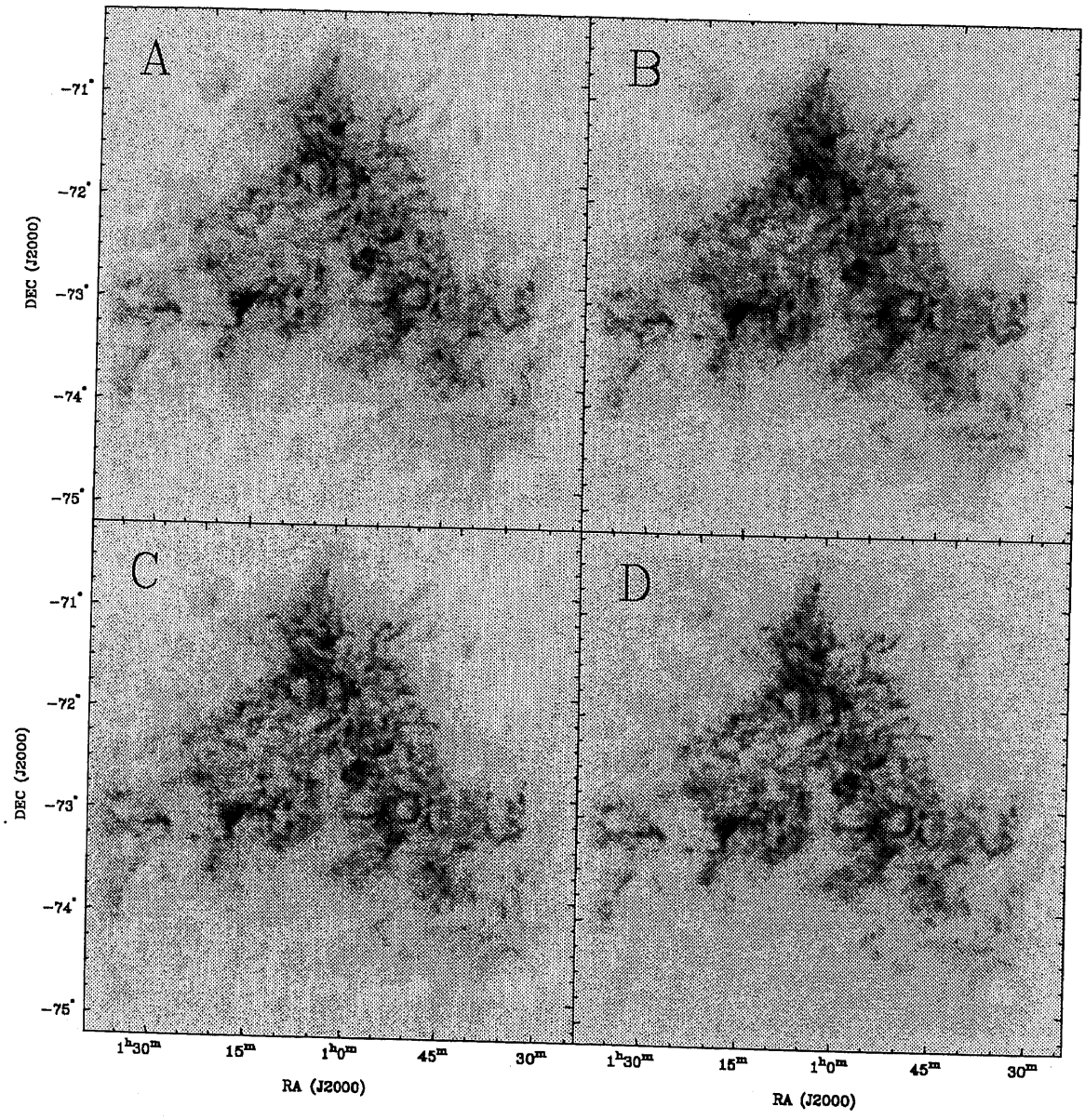

Figure 3.14 . The result of adding Parkes short-spacings into an ATCA HI mosaic of the SMC at heliocentric velocity 169 km s^{-1}. Four different methods are shown from top-left to bottom-right: data combination in the Fourier domain using IMMERGE (method A), data combination before deconvolution (method B), data combination during deconvolution using Parkes data as a 'default' image (method C) and the 'joint' deconvolution of both Parkes and ATCA data (method D). All images have the grey-scale range −11 to 107 K with a linear transfer function. Images A–D are the same ones as shown in Fig. 3.6, Fig. 3.11, Fig. 3.12 and Fig. 3.13, respectively.

The quantification of the quality of an image depends on the scientific questions we want to address (Cornwell, Holdaway, & Uson 1993) and is therefore case specific. Something that any short-spacings correction must fulfill, though, is that the resolution of the final image should be the same as for interferometer data alone, while the integrated flux of the final image should be the same as measured from single-dish data alone. Table 3.1 shows measurements of the total flux density, minimum/maximum values and noise level in the four resultant images.

All four images have very comparable noise levels, minimum values and maximum values. The last two images also have very comparable (within 3%) total flux, relative to the Parkes flux alone, while the first two have lower (within 8%) and higher (within 7%) flux, respectively. The differences come, most likely, from the different weighting of single-dish data employed by different methods. Method A (IMMERGE) over-weights very short interferometer spatial frequencies, by including them into the final Fourier plane (see Section 3.3), instead of taking only spatial frequencies from the single-dish data set. This is responsible for the lowest total flux of the image produced with method A. Method B gives the same weight to both interferometer and single-dish data within the region of overlapping spatial frequencies, over-weighting slightly single-dish data. This might result in a slightly higher total flux of the combined image, relative to Parkes flux alone. However, Sault & Killeen (1998) suggest that a slightly broader single dish beam (B_{sd}) should be used when applying method B (Eq. 3.23), if B_{int} is the synthesised mosaic beam. This could then decrease the total flux for up to 10% (R.J. Sault, private communication).

The only noticeable things on the difference maps taken for each two combined images, are slightly deeper sidelobes on the image produced with method A. As an example, the difference map between the results of methods B and A is shown in Fig. 3.15. After taking a Fourier transform of this difference map, a profile of the Fourier amplitudes at position angle of 45°, was plotted in Fig. 3.16. Prominent sidelobes between baselines 31 and 61m, 61 and 92 m, 92 and 122m, 122 and 184 m, respectively, are visible. Method A is the only one which requires a clean interferometer image as an input parameter. Residual sidelobes could be a sign that the deconvolution before data combination is less successful, since the full $u-v$ information is not available to the deconvolver (Holdaway 1998). However, since the sidelobes are present on several spatial scales, we believe that they are not a consequence of the short-spacings correction method employed, but show that the interferometer data could be cleaned better (using, for example, more iterations in the MEM). It is therefore more likely that the cleaning before adding short spacings requires more care. The same profile on Fig. 3.16 shows a prominent bump at the region of overlapping spatial frequencies, emphasising a difference between methods A and B.

Method A is the fastest way to add short-spacings. It is also the most robust way, relative to the other three methods which require a non-linear deconvolution at the end which requires all data to satisfy certain assumptions. Surprisingly, the

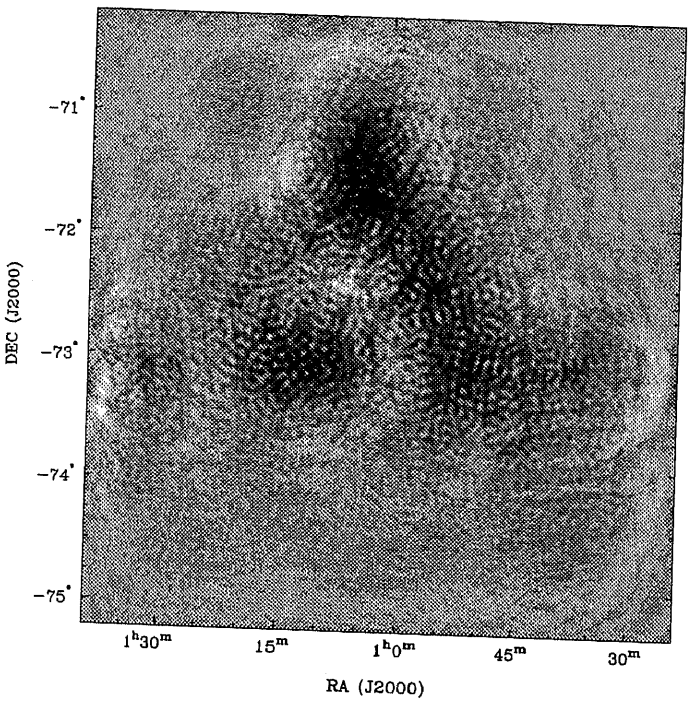

Figure 3.15 . The difference map between the SMC combined images using methods B and A. The grey-scale range is −5 to 16 K, with a linear transfer function.

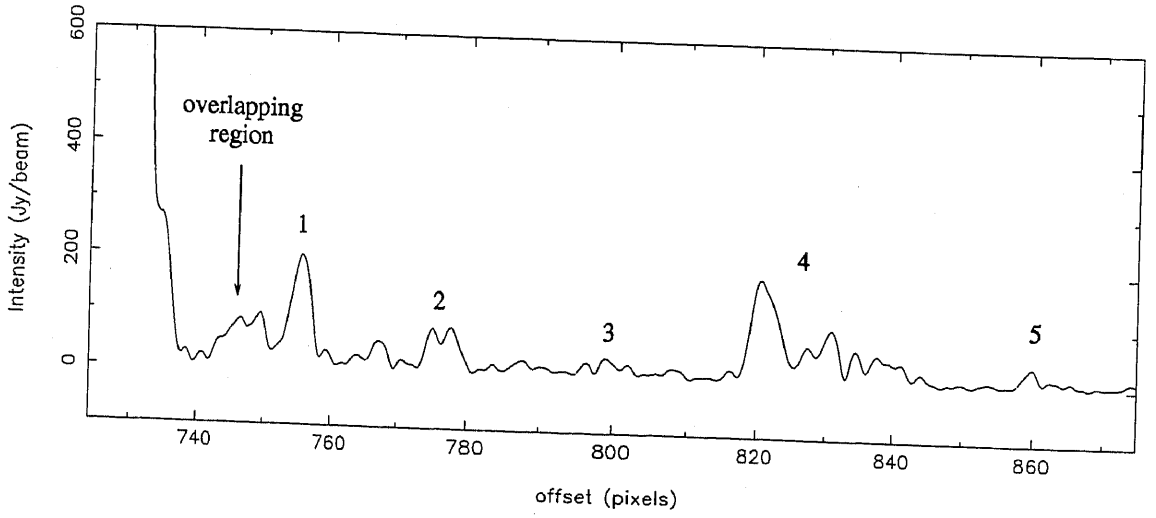

Figure 3.16 . The profile of the amplitudes, at position angle 45°, of the Fourier transform of the difference map between the SMC image (at 169 km s^{-1}) corrected for short-spacings using methods B and A. For pixel conversion into metres, use: $x_m = |724 - i| \times 0.99$. The overlapping region of spatial frequencies and sidelobes between baselines: 31 and 61 m (1), 61 and 92 m (2), 92 and 122 m (3), 122 and 184 m (4), are labelled.

fastest way to combine data in the image domain, performed by method C, proves to be very reliable in the case when a significant overlap in the spatial frequencies is present (this is the case with the ATCA and Parkes telescopes). Method D provides, theoretically, the best way to add short-spacing data into an interferometer map, since it finds the solution which fits both data sets simultaneously. However, this method depends very much on a good estimate of the interferometer and single-dish noise variances, which can be a quite tedious job.

The determination of the calibration scaling factor for the relative calibration of single-dish and interferometer data, seems to work well in the Fourier plane. Method A provides a faster way to determine the calibration scaling factor since it is implemented in MIRIAD's IMMERGE, relative to the method explained in Section 3.2. The derived value is however, slightly biased by noise, and requires more robust statistics, as shown in Section 3.2. The determination of the calibration scaling factor in the image domain, employed by method D, is still not fully explored.

For further analysis of all four methods for data combination, data simulations over a wide range of spatial frequencies are necessary, as well as applications of all four methods on observations of various types of astrophysical objects.

3.6 Summary

- To determine the calibration scaling factor necessary for matching flux density scales of the interferometer and single-dish data sets, both data sets need to be compared in the Fourier plane. This process is very sensitive to edge-effects and deconvolution of the single-dish data and requires a good statistical method. The method explained in Section 3.2 shows superior results relative to the method performed by IMMERGE (method A). The 'joint' deconvolution with MOSMEM (method D) still has not been explored enough for this purpose.
- Four different methods, two linear and two non-linear, for the short-spacings correction have been discussed and applied on the ATCA and Parkes HI spectral line observations of the SMC. Linear methods are: data combination in the Fourier domain (method A); and data combination before deconvolution (method B), while non-linear methods are: data combination during deconvolution using single-dish data as 'default' information (method C); and the 'joint' deconvolution of both interferometer and single-dish data (method D). All four methods show satisfactory results when the same *a-priori*-determined calibration scaling factor is used. The resultant short-spacing corrected images are very similar. Since all methods are independent of each other, this gives confidence in the final solution.
- All methods are sensitive to edge-effects. Sufficient tapering of the single-dish images with the gain function of the interferometer, solves this problem in

both approaches for data combination. Both approaches also require a very good knowledge of the single-dish beam. Analysing differences between the four methods discussed we find that:

1. method A, based on data combination in the Fourier domain, proves to be equally reliable as methods B, C and D, based on data combination before or during a deconvolution process, although it requires slightly more careful *a priori* cleaning of the interferometer data ;
2. method B slightly over-weights single-dish data within the region of spatial overlap, resulting most likely in the slightly higher total flux of the combined image;
3. method C slightly over-weights interferometer data for very short spatial frequencies and its performance depends very much on the size of the overlapping region; and
4. method D provides theoretically the best fit to both data sets, but it is very sensitive to the noise variances of both single-dish and interferometer data, and therefore is the least robust method of all four.

All four methods give very comparable results. We will hereafter use the result of method B for the whole spectral data cube of the SMC ATCA and Parkes observations for further data analysis.

Chapter 4

The HI distribution and mass

4.1 HI distribution

The ATCA observations of the SMC, corrected for Parkes short spacings, are presented as isovelocity images in Fig. 4.1. The cube was averaged for this purpose into 24 velocity planes, each of width 4.95 km s^{-1}. The figures have a grey-scale range from -0.18 to 2.0 Jy $beam^{-1}$ which corresponds to -11 to 126 K.* A slightly different view of the data, as a sequence of RA-velocity and Dec-velocity slices through the data cube, is shown in Fig. 4.2 and Fig. 4.3, respectively. The maximum brightness temperature of the whole cube is 179 K at position RA $00^h48^m42^s$, Dec $-73°05'36''$ (J2000). This is the same position as, but 42 K brighter than, the maximum in the low-resolution Parkes data alone (Section 2.3), and 53 K brighter than the maximum in the ATCA data alone (Staveley-Smith et al. 1997). At this position, the HI column density is 1.43×10^{22} atoms cm^{-2}, corresponding to 114 $M_\odot$ pc^{-2}, without correction for self-absorption. This is 25 per cent higher than that in the Parkes data alone.

The main difference between these data and those in previous single-dish studies is the complexity and variety of the small-scale structure. Much of this structure appears to be in the form of filaments, arcs, knots, and shells. Contrary to Hindman's description of a 'smooth HI distribution,' we see strong variation of the HI distribution spatially, and in velocity. At low velocities ($\sim$ 130 km s^{-1}), the 'bar' is prominent but, unlike the stellar bar, the HI bar is more extended and broken up into giant shells and supershells resulting from the interaction of the gas and the HII regions (see Chapter 6). An interesting drop of the total HI flux is present between 140 and 160 km s^{-1} (see also Fig. 8.6). At these velocities, the SMC appears to take on a 'wispy' morphology. A general velocity increase from west to east, seen

*The conversion factor between flux density and brightness temperature is 63.07 K (Jy $beam^{-1})^{-1}$, the same as for the ATCA data alone.

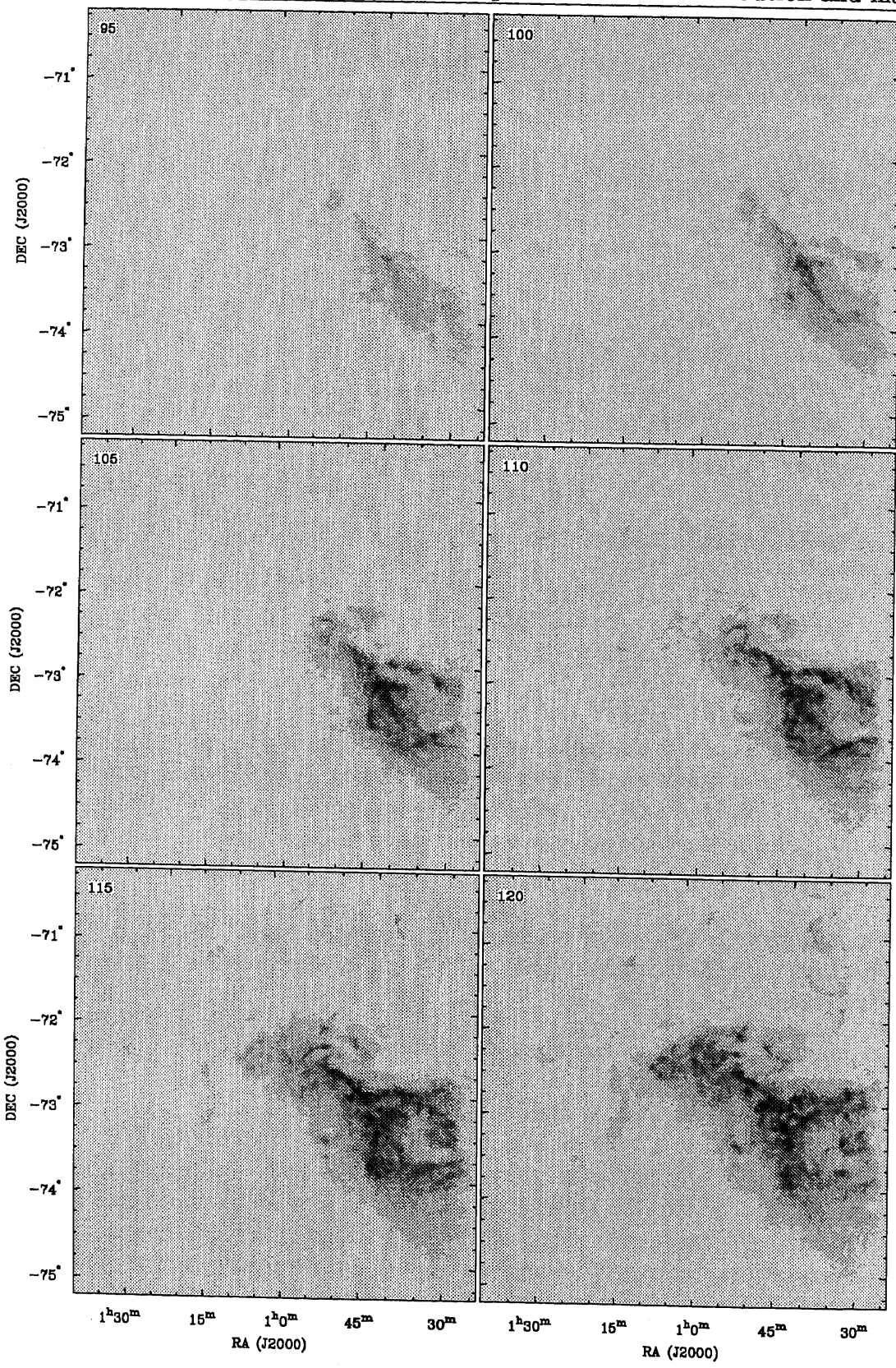

Figure 4.1 . The combined ATCA and Parkes HI mosaic of the SMC. Each panel is an RA-Dec image for the heliocentric velocity (in km s^{-1}) given in the top-left corner. The velocity spacing between panels is 4.95 km s^{-1}. The grey-scale intensity range is −11 to 126 K with a linear transfer function.

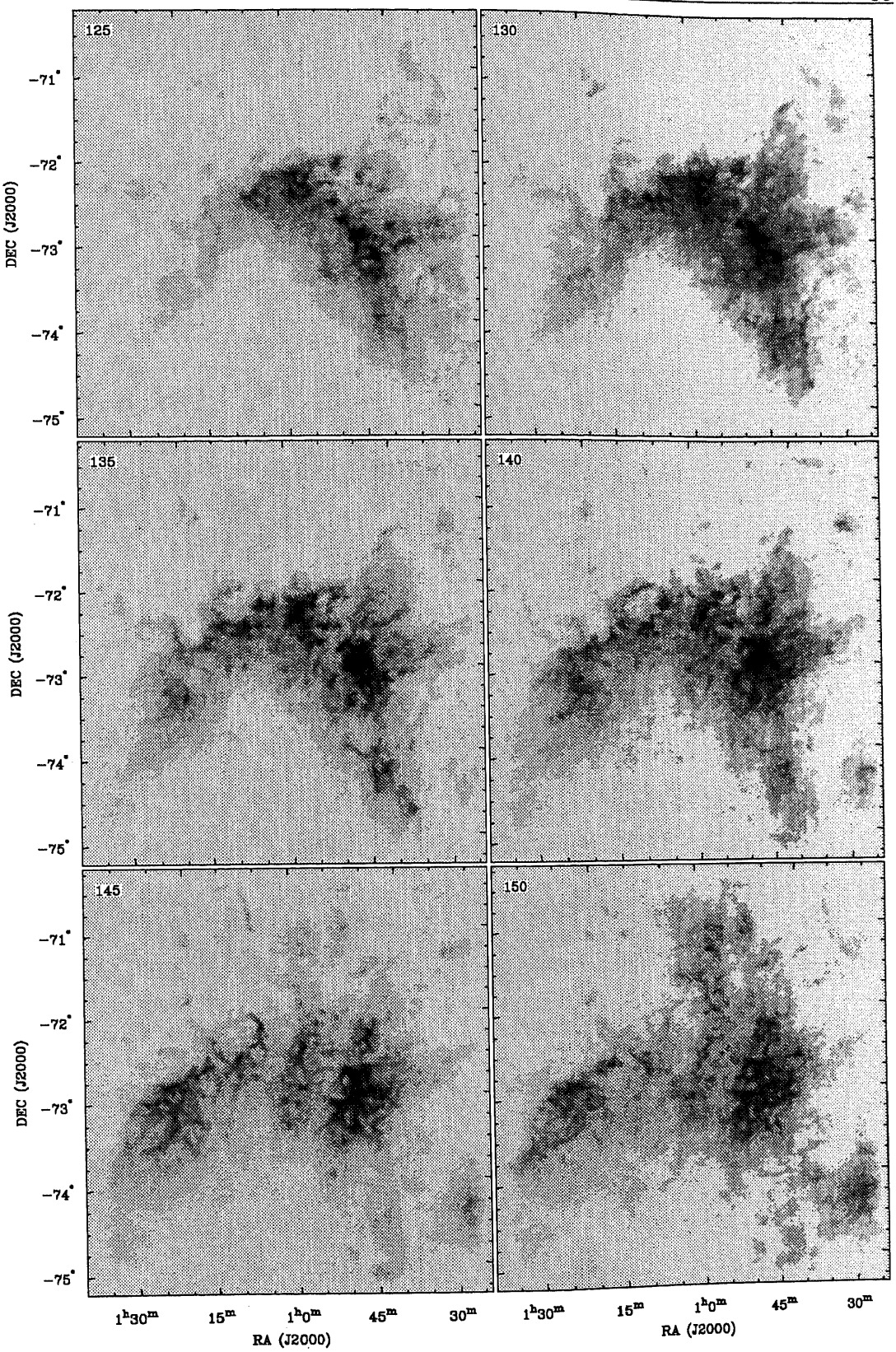

Figure 4.1 *continued*

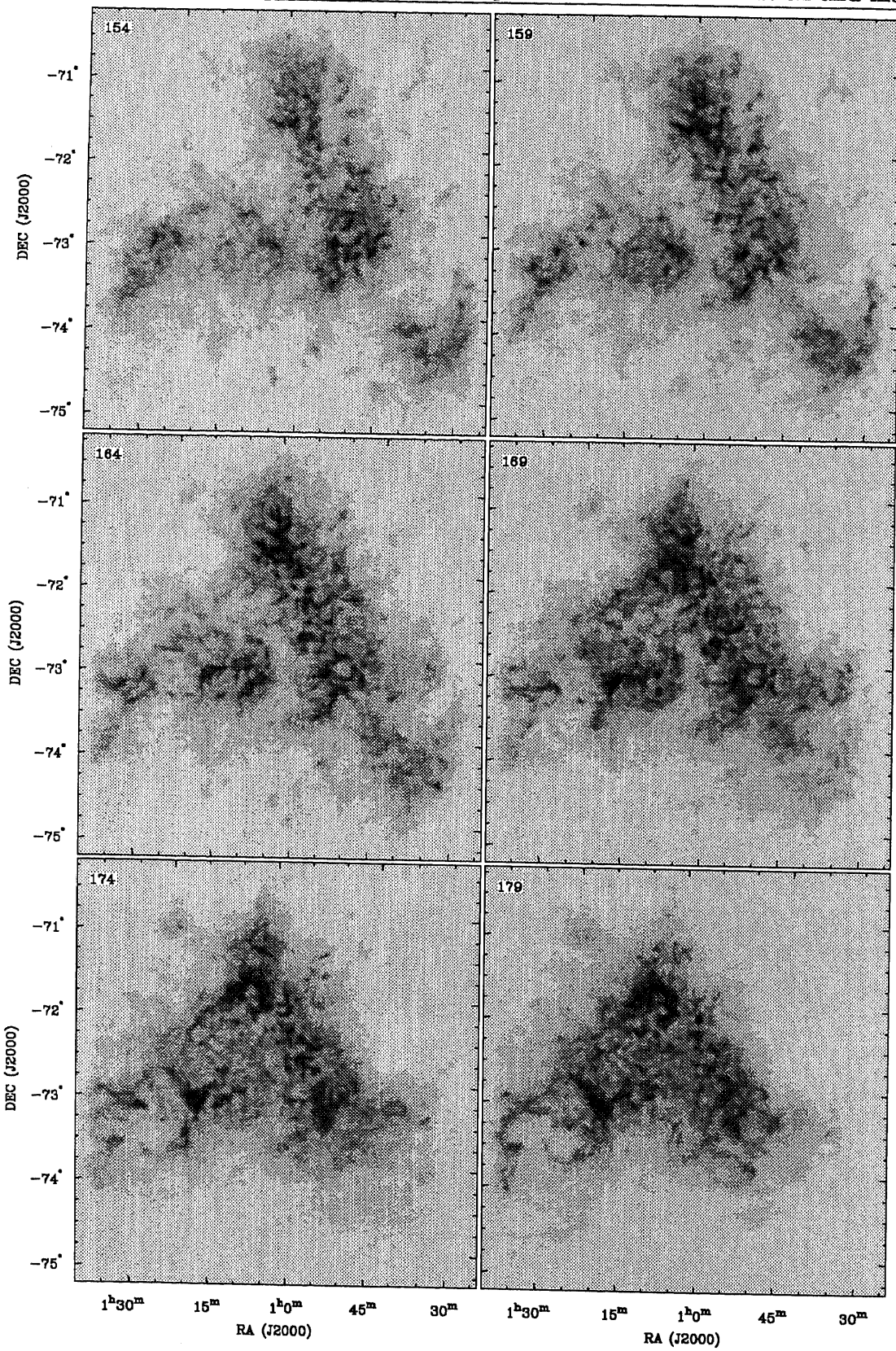

Figure 4.1 *continued*

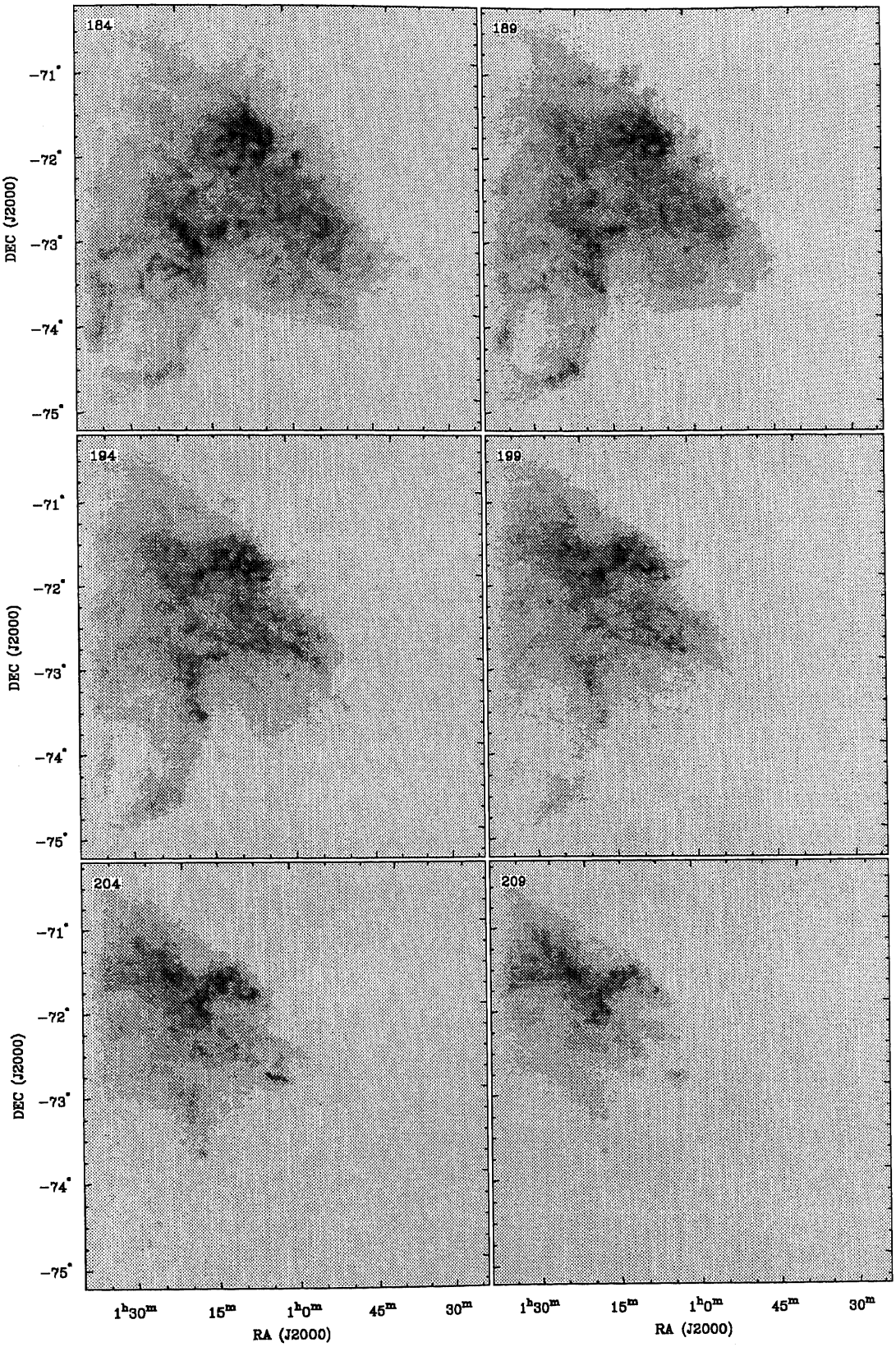

Figure 4.1 *continued*

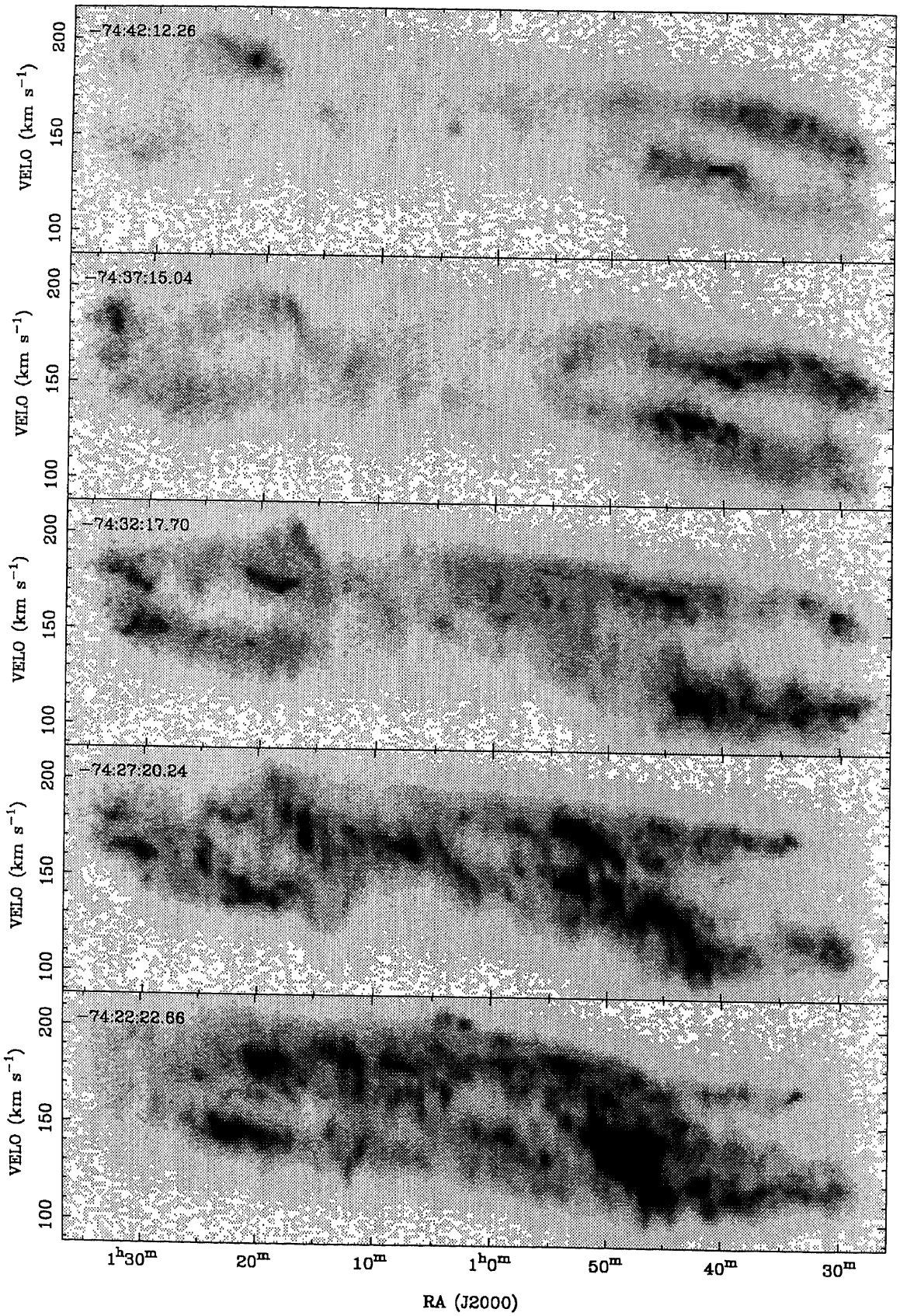

Figure 4.2 . Ten RA-velocity slices through the combined ATCA and Parkes HI data cube of the SMC, starting with Dec $-74°42'12''$ and ending with Dec $-72°17'42''$ (J2000). The thickness of each slice is 5 arcmin. The grey-scale range is: 0–45, 0–45, 0–55, 0–75, 0–75, 0–75, 0–75, 0–55, 0–45, 0–45 K, with a linear transfer function, respectively. Numerous

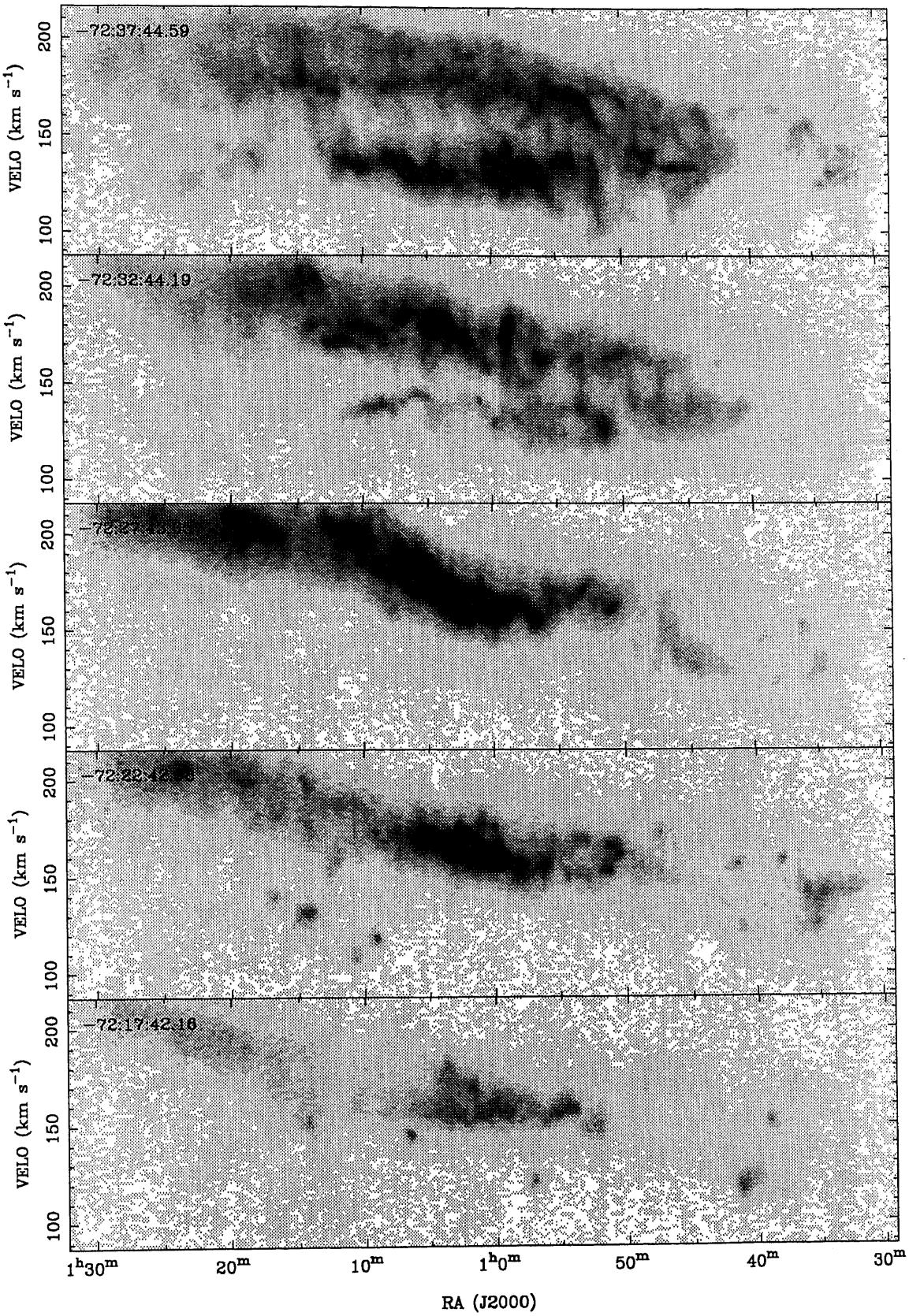

Figure 4.2 *continued*

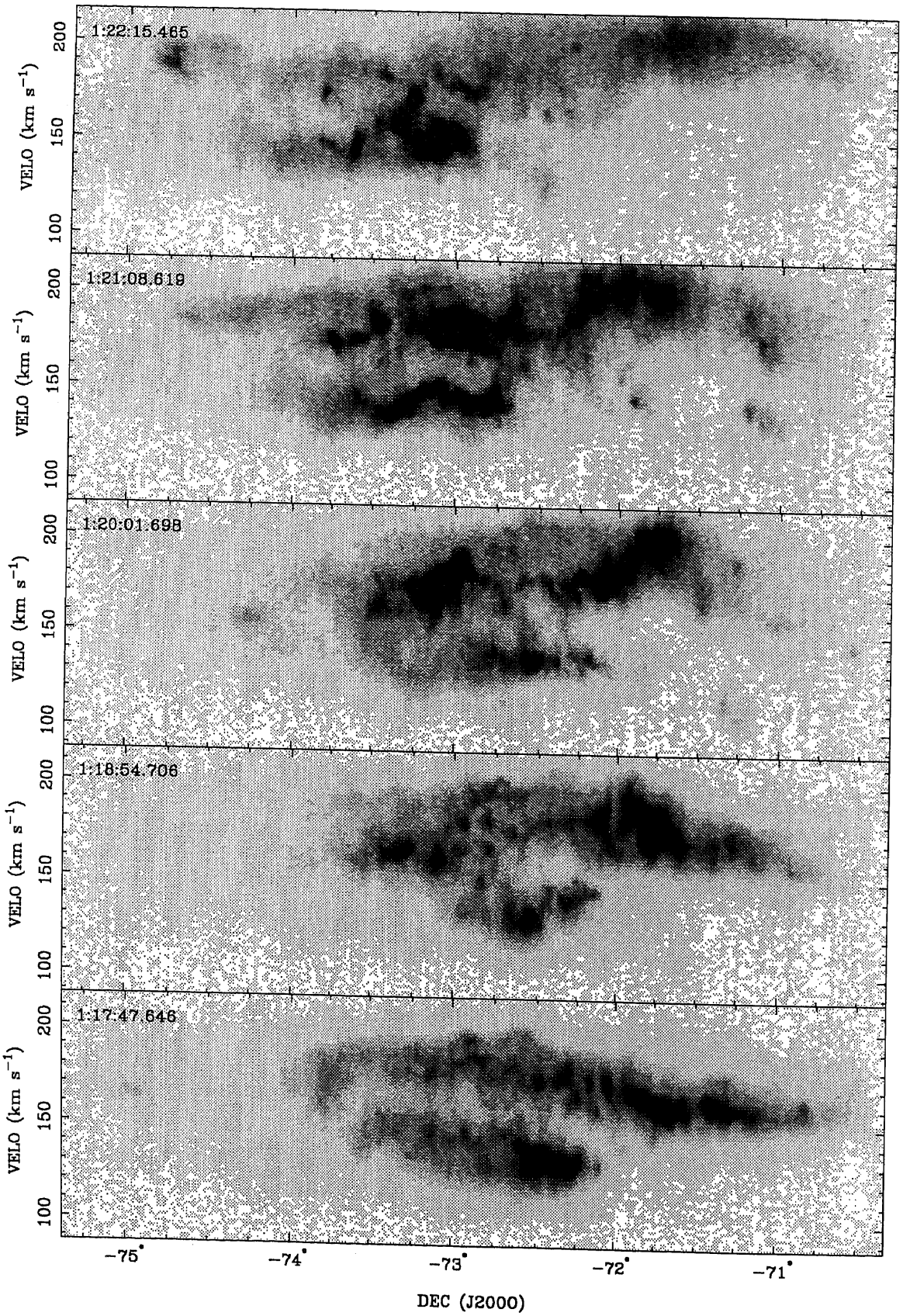

Figure 4.3 . Ten DEC-velocity slices through the combined ATCA and Parkes HI data cube of the SMC, starting with RA $01^h22^m15^s$ and ending with RA $00^h49^m38^s$ (J2000). The thickness of each slice is 5 arcmin. The grey-scale range is: 0–45, 0–45, 0–55, 0–75, 0–75, 0–100, 0–100, 0–75, 0–45, 0–45 K, with a linear transfer function, respectively.

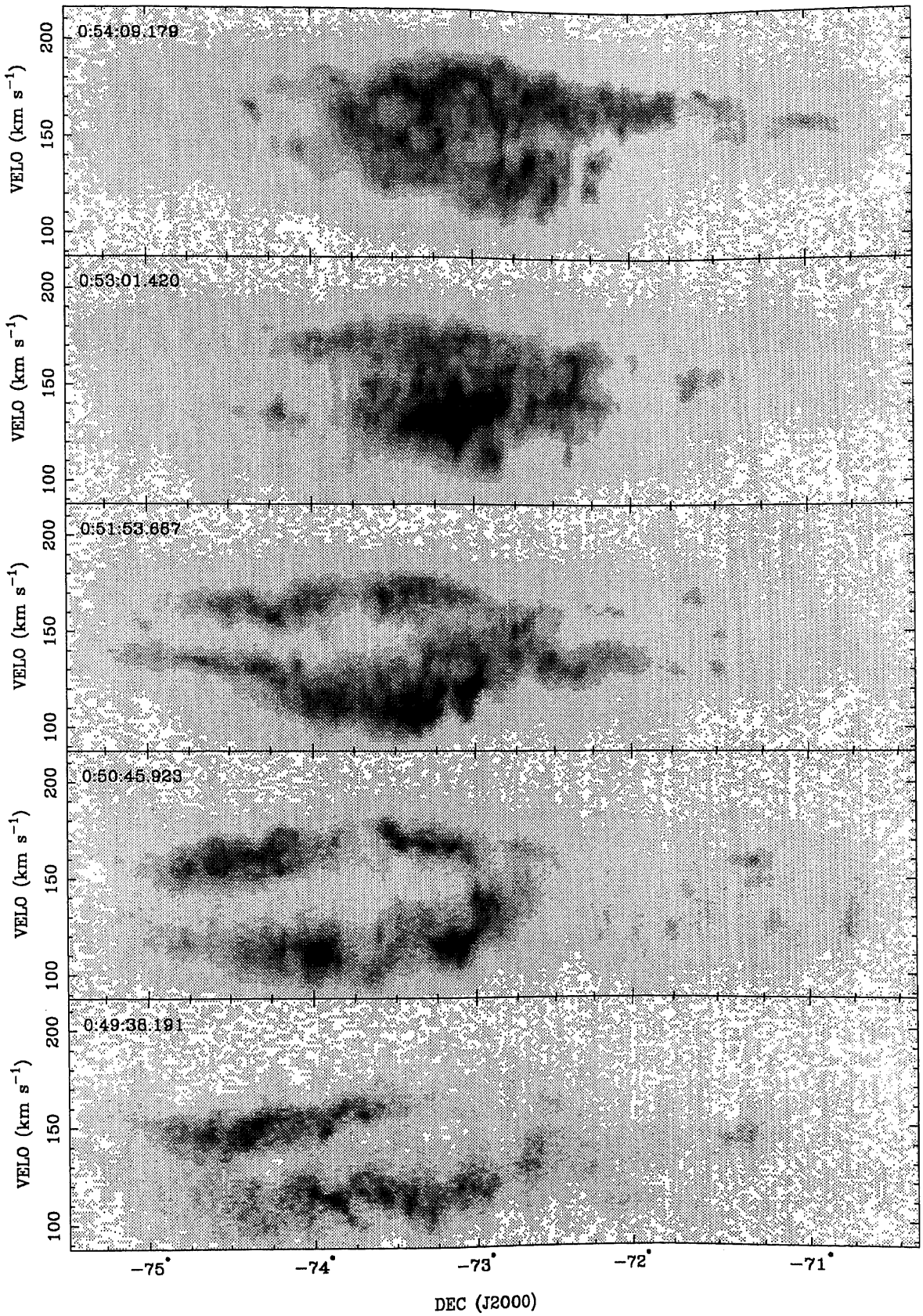

Figure 4.3 *continued*

on previous observations, is present and is partly caused by the parallax and the proper motion of the SMC. From the region of the bar, the SMC has three prominent extensions: (1) towards the north ($\sim$ 160 km s^{-1}); (2) towards the Wing region in the south-east ($\sim$ 160 km s^{-1}); and (3) towards the beginning of the Magellanic Stream in the north-east ($\sim$ 190 km s^{-1}). The latter two were also noted by Bajaja & Loiseau (1982).

The HI velocity profiles in the SMC are usually very complex, with multiple peaks, and have been a subject of a great controversy, variously interpreted as expanding shells of gas or spatially separate systems. The high resolution HI survey of the SMC (Staveley-Smith et al. 1997) suggests that most, if not all, of the line-splitting apparent in HI data, can be explained with a large number (501) of expanding shells present. As in Staveley-Smith et al. (1997), a significant number of expanding shells are apparent in the combined ATCA and Parkes data set. The largest of these shells (which can be seen in Fig. 4.2 and Fig. 4.3) will be discuss later in Chapter 6. Many of supershells have smaller shells on their perimeters, consistent with self-propagating star formation. In some cases (e.g. 145 km s^{-1}in Fig. 4.1), several shells or filamentary structures appear to align into 'chimney'-like structures. A quantitative discussion of the relationship of large-scale and small-scale HI structure is given in Chapter 8.

4.2 HI column density and mass

The HI column-density image of the SMC is shown in Fig. 4.4. While no large-scale symmetry is visible in the HI distribution, the concentrations of HI associated with the bar and the Eastern Wing, and northern extension are dominant. A 'bridge' appears to connect the bar with the Wing. The overall filamentary structure of the SMC remains surprisingly visible, which means that the line-of-sight depth has not washed out much structure.

Assuming a low optical depth, we calculate a lower limit to the total HI mass in the observed area of $(3.8 \pm 0.5) \times 10^8$ M$_\odot$. Hindman (1967) estimated the HI mass of a larger area, RA 00^h00^m to 01^h30^m and Dec $-70°$ to $-76°$ (B1975), to be slightly larger, 4.8×10^8 M$_\odot$. The total hydrogen mass of the area measured by Bajaja & Loiseau (1982) (RA 00^h00^m to 02^h00^m, Dec $-70°$ to $-76°$, B1950) is slightly higher still, $(5.5 \pm 0.4) \times 10^8$ M$_\odot$, after adjusting their assumed distance to 60 kpc. The main difference in our HI mass compared to that of previous authors appears to be the field of view. Calibration of the data sets appears to be consistent (c.f. Section 2.3).

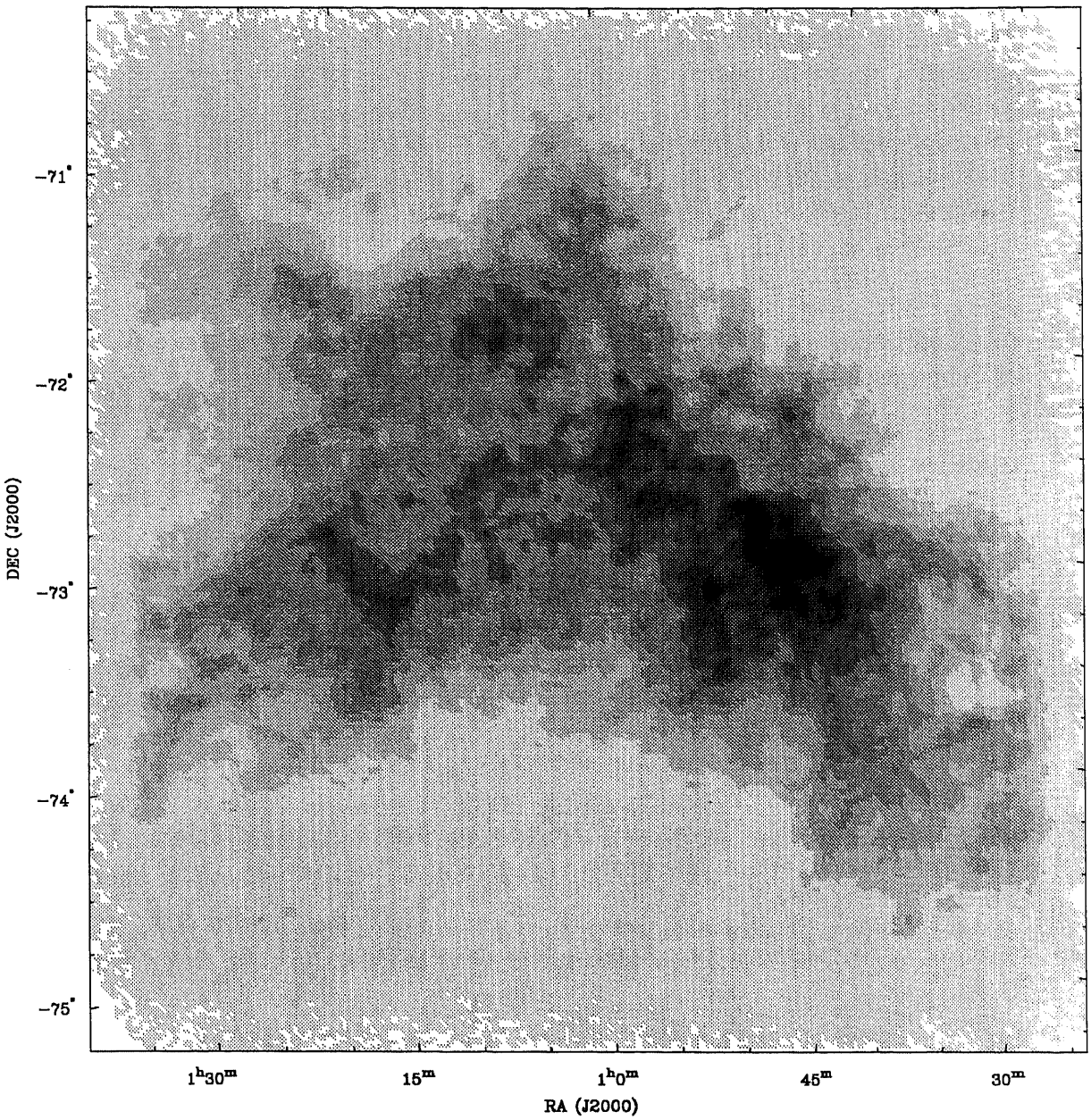

Figure 4.4 . An HI column-density image of the SMC. The grey-scale intensity range is 0 to 1.03×10^{22} atoms cm^{-2} with a linear transfer function. The maximum HI column density, 1.43×10^{22} atoms cm^{-2}, is at position RA $00^{h}47^{m}33^{s}$, Dec $-73°05'26''$ (J2000).

4.2.1 Correction for HI self absorption

The column densities of atomic hydrogen determined here may be under estimates of the true column density if the gas is optically thick in the 21-cm line. In order to estimate the importance of this self-absorption effect, we have compared our data with the results of an absorption survey of the SMC by J.M. Dickey et al. (1999, in preparation). That project has observed some 30 lines of sight toward compact continuum sources behind the SMC, to measure the 21-cm optical depth as a function of velocity. Comparing those results with the corresponding emission spectra measured here, we can compute correction factors for the column densities measured when assuming low optical depth.

If we assume that the absorption lines measured by Dickey et al. represent gas at a single temperature, the combined data can be used to derive an average correction factor,

$$f_c = \begin{cases} 1 + 0.667\,(\log N_{\rm HI} - 21.4) & \log N_{\rm HI} > 21.4 \\ 1 & \log N_{\rm HI} \leq 21.4 \end{cases} \qquad (4.1)$$

where $N_{\rm HI}$ is the column density in atoms cm^{-2} (Dickey et al. 1999, in preparation). Table 4.1 shows, for four different column-density ranges, the relevant area of the SMC, the uncorrected mass, the correction factor, and the corrected mass. Note that the lowest column density range ($< 25 \times 10^{20}$ cm^{-2}) is a lower limit, since there is a lot of emission beyond our field of observation. The final result is that the self-absorption correction increases the HI mass estimate from 3.8×10^8 M$_\odot$ to 4.2×10^8 M$_\odot$. This is a relatively small effect. In individual velocity channels, the self-absorption correction can be much larger, as much as a factor of two in some cases, but typically the absorption covers only a narrow range of velocities compared with the emission, and so the effect on the velocity integral is relatively small.

Table 4.1 . HI self-absorption corrections for different column density intervals in the SMC.

Column Density (10^{20} cm^{-2})	Area (deg^2)	Uncorrected HI Mass (10^8 M$_\odot$)	f_c	Corrected HI Mass (10^8 M$_\odot$)
< 25	18.3	1.35	1.0	1.35
25 to 65	0.62	1.89	1.1	2.08
65 to 100	0.85	0.50	1.3	0.65
> 100	0.11	0.10	1.5	0.15
Total	24.5	3.84		4.23

4.3 Comparison with Hα

Fig. 4.5 shows contours of HI column density superimposed on an Hα image of the SMC from Kennicutt et al. (1995). The Hα image shows the prominent HII regions including N19 and N66 in the bar and N84A in the eastern Wing. The image also reveals two loop-like structures in the Wing – one associated with the N84A HII region and the other being the supershell SMC1 (Meaburn 1980). Extended Hα emission is also very prominent in the SMC and contributes about 36 – 46 per cent of the total Hα emission (Kennicutt et al. 1995). It consists mainly of diffuse emission associated with the bar, but there are prominent filaments which appear to stream towards the Wing. The ionisation source of the diffuse medium in actively star forming galaxies, in general, is not well understood. Kennicutt et al. (1995) suggest as a possible reason photon leakages from the large HII regions, which could produce diffuse ionised regions quite far away from the sites of star formation if the porosity of the ISM is large.

As Fig. 4.5 shows, both HI and Hα are most prominent in the bar. However, there is an absence of HI around the brightest HII regions as a result of star formation and stellar winds. A prominent example of this is N66 at RA 00^h59^m, Dec $-72°11'$ (J2000). As noted previously, the HI extends beyond the diffuse Hα and the stellar bar, particularly towards the north and east. For the eastern wing, there is little general correlation between the Hα and the HI, although there is a tendency for HII regions to be near HI rims (see Chapter 6). For example, the V-shaped HI feature at RA 01^h14^m, Dec $-73°12'$ (J2000) appears to be associated in position and velocity with N84A. The bridge which connects the stellar bar with the wing contains filamentary structure in both Hα and HI. However, there is little detailed correlation between the two. A detail investigation of a possible correlation between Hα and HI is an imperative for understanding of the nature of the relationship between the local star formation rate (SFR) and gas density.

Kennicutt et al. (1995) find a power law relationship between HI and Hα only for high values of HI column densities (taken from Hindman 1967). However, they do not pay much physical attention to this correlation since the molecular gas, which contributes significantly to this correlation, is not included. Surprisingly, they do not see a typical cut-off in HI column density indicative of a star formation threshold.

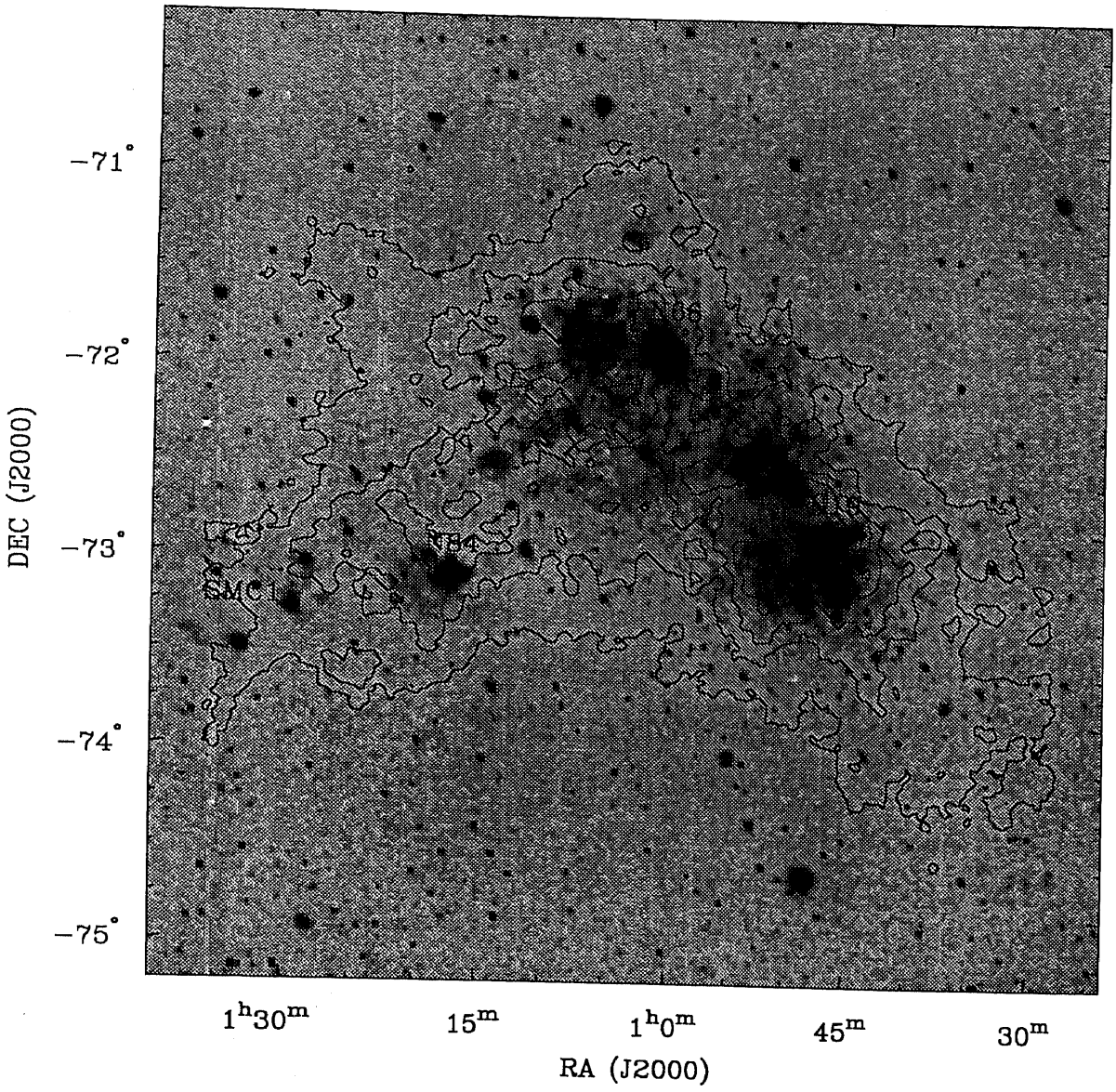

Figure 4.5 . Contours of the HI column density overlaid on the broad band Hα image of the SMC from Kennicutt et al. (1995). The contour interval is 5×10^{20} atoms cm^{-2} and contours are at 4, 6, 8 and 10 $\times$ contour interval.

Chapter 5

The SMC Velocity Field

5.1 Introduction

The velocity field of the SMC offers an unique opportunity to study the importance of the turbulent, random motions relative to gravitational motions, including gas motions due to tidal forces, in a member of an interacting system of galaxies. On smaller scales, the gas motions in the SMC may be influenced by the interstellar turbulence originating in numerous expanding shells. On larger scales, the gravitational interactions between the Galaxy, LMC and SMC appear to be responsible for some gas motions (Putman et al. 1998). But what is more responsible for the velocity field of the SMC: gravitational or turbulent motions? If the random motions are dominant on small-scales, on which scales do gravitational forces start to govern gas motions? Is the velocity field of the SMC consistent with the case of a rotating disk? If so, what can the rotation curve tell us about the mass-to-light ratio and the dark matter halo, since dwarf irregulars commonly have dynamically very important halos of dark matter (Walter et al. 1998)?

Many HI surveys of the SMC (Hindman 1967; Bajaja & Loiseau 1982; Stanimirovic et al. 1999) have noted a strong gradient in velocity from the south-west to the north-east. The velocity field of a flat disk in an uniform circular rotation, shows the characteristic 'spider' pattern with a gradient along the major kinematic axis. Hence, both Hindman (1967) and Bajaja & Loiseau (1982) modelled the SMC as a disk and explained the velocity gradient as a clear rotational effect, with some perturbations from circular motion. Hindman (1967) also suggested that a part of this gradient might be due to the binary motion of the SMC and LMC.

In this chapter, two different approaches for the analysis of the velocity profiles in the SMC are applied. The correction of the velocity field for the proper motion is also discussed and applied. Further on, a unimodal velocity field is used to derive the rotation curve of the SMC. The mass model, the mass-to-light ratio, the dark

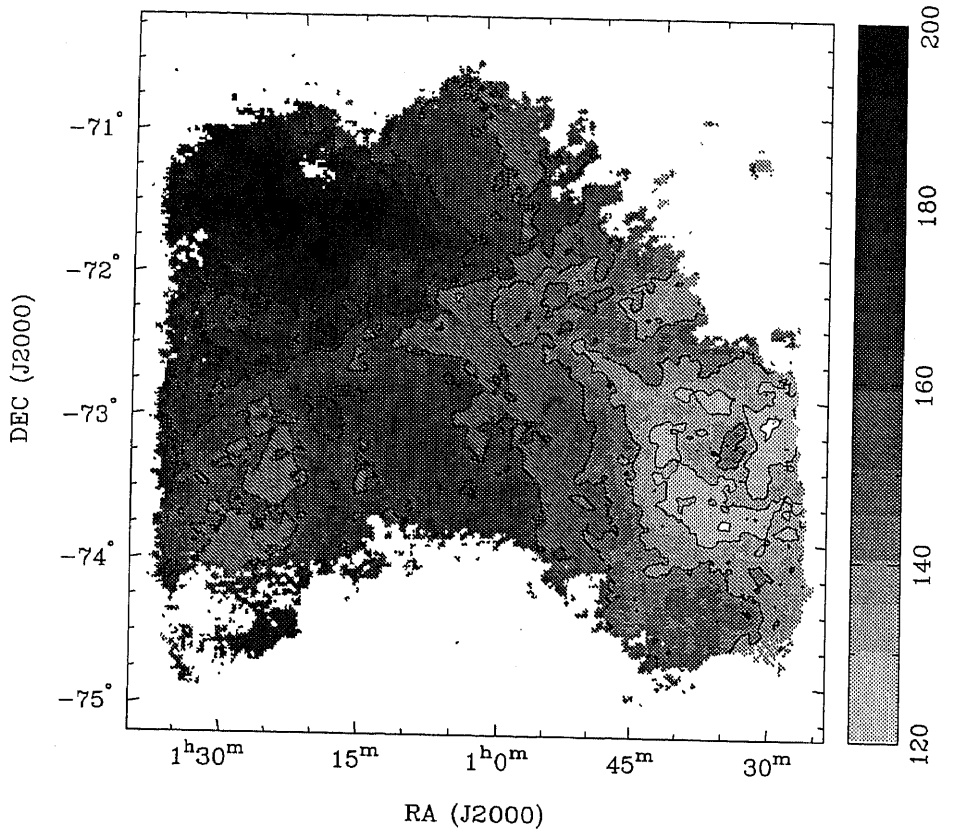

Figure 5.1 . The intensity-weighted mean velocity field of the SMC, derived from the combination of the ATCA and Parkes data. The grey scale range is 120 to 200 km s^{-1} with a linear transfer function. The contour levels range from 120 to 200 km s^{-1}, with the contour interval of 10 km s^{-1}.

matter halo, the vertical scale height and the disk stability are then investigated. The last part of the chapter addresses the issue of the depth of the SMC re-examining observations of Cepheids. The Cepheid and HI data are then compared with a few models of the 3-D structure in the SMC.

5.2 The profile analysis

We have used the full resolution data cube, after correction for short spacings, to determine the intensity-weighted mean velocity along each line-of-sight. This mean velocity field, Fig. 5.1, shows a strong velocity gradient from 91 km s^{-1} in the south-west to 200 km s^{-1} in the north-east. The isovelocity contours show some large-scale symmetry. However, clear distortions are visible in the north-west, corresponding most likely to several shells and filamentary features aligned into a chimney-like structure at velocity $\sim$ 123 km s^{-1} (Fig. 4.1), and in the south-east, towards the

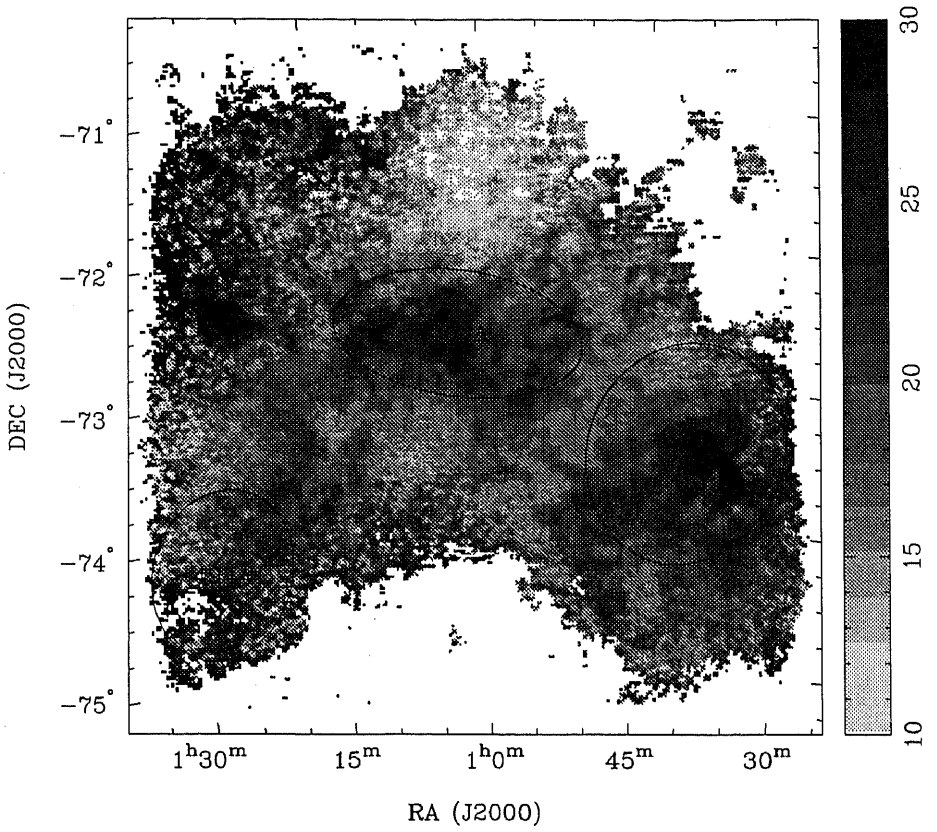

Figure 5.2 . The intensity-weighted velocity dispersion of the SMC from the second moment analysis. The grey-scale range is 10 to 30 km s^{-1}. Positions of the three largest shells in the SMC are overlaid (see Chapter 6).

Eastern Wing region, where again a supergiant shell 494A (see Chapter 6) was found. These perturbations seem to form a S-shaped feature, perpendicular to the direction of the main velocity gradient.

Also as a result of the moment analysis, Fig. 5.2 shows the second moment map or the intensity-weighted velocity dispersion. The velocity dispersion varies from 0 to 40 km s^{-1}across the SMC. The region around RA $01^h\ 00^m$, Dec $-71°30'$ (J2000) has the lowest dispersion. Interestingly, regions with higher dispersion, almost continuously cover the whole angular extent of the SMC for Dec $< -72°$ and resemble the HI distribution for $V_{\rm hel} < 150$ km s^{-1}. One possible interpretation is that higher velocity dispersion corresponds to regions with larger line-of-sight depth, which may be even due to the presence of separate gas entities. An alternative explanation could be a gas expansion, such as seen in HI shells. The latter case is supported with the highest velocity dispersion being associated with positions of the three largest supershells in the SMC, shown in Fig. 5.2.

5.2.1 The unimodal profile analysis

Velocity profiles in the SMC are usually very complex, having double or even multiple-peak components. Much of this complexity comes from the large population of expanding shells found (Staveley-Smith et al. 1997), which strongly influence the velocity field. Since the intensity-weighted mean velocity is biased towards the velocity component with higher intensity, it is not necessarily the best representation of complex velocity profiles. To avoid this bias, we find, for each line of sight, the minimum and maximum velocity for which the intensity is 5% of the peak value for that line of sight. The mean of the minimum and maximum velocity, determined in this way, is then taken to be our new velocity estimate. Since such an analysis requires high signal-to-noise ratio, we have used only the low resolution Parkes data cube. The resultant velocity field, smoothed to 20 arcmin, is shown in Fig. 5.3, together with the intensity-weighted mean Parkes velocity field.

The resultant velocity field shows a slightly more regular 'spider' pattern than the mean one, suggesting circular rotation for the main gaseous body of the SMC. The distortion from the large-scale symmetry at the north-west has disappeared, while some small irregularities at the north are still present. The Eastern Wing region also shows some deviations from the 'spider' pattern, proving its complexity, which may be caused by the interactions between the LMC and the SMC. The principal axes appear to be non-perpendicular. To show the difference between the intensity-mean and unimodal velocity fields and also justify the physical meaning of the unimodal velocity field, Fig. 5.4 shows the position-velocity slice at Dec $-72°40'33''$ (J2000) with cuts from the intensity–weighted mean (white colour) and unimodal (black colour) velocity fields superimposed. The slice was extracted using the KPVSLICE tool in the KARMA image processing package (Gooch 1995). The unimodal velocity field picks up better the central velocity along the line-of-sight, since it is less biased by the intensity.

5.2.2 The bimodal profile analysis

To investigate the possibility of having two spatially separate subsystems of gas along the line-of-sight, as suggested by some previous studies (Mathewson & Ford 1984; Mathewson, Ford, & Visvanathan 1986; Mathewson, Ford, & Visvanathan 1988; McGee & Newton 1981), we have modelled each velocity profile in the Parkes data cube with a superposition of two independent Gaussian functions. The task PROFIT in the GIPSY image package (van der Hulst et al. 1992) was used for this purpose. We limit our analysis only on two Gaussian functions, although some very complex profiles can be fit with a composite of more than two Gaussian components. The mean velocity of the first Gaussian component is 137 km s^{-1}, while the mean of the second component is 174 km s^{-1}. We label the components with 'L' and 'H', respectively.

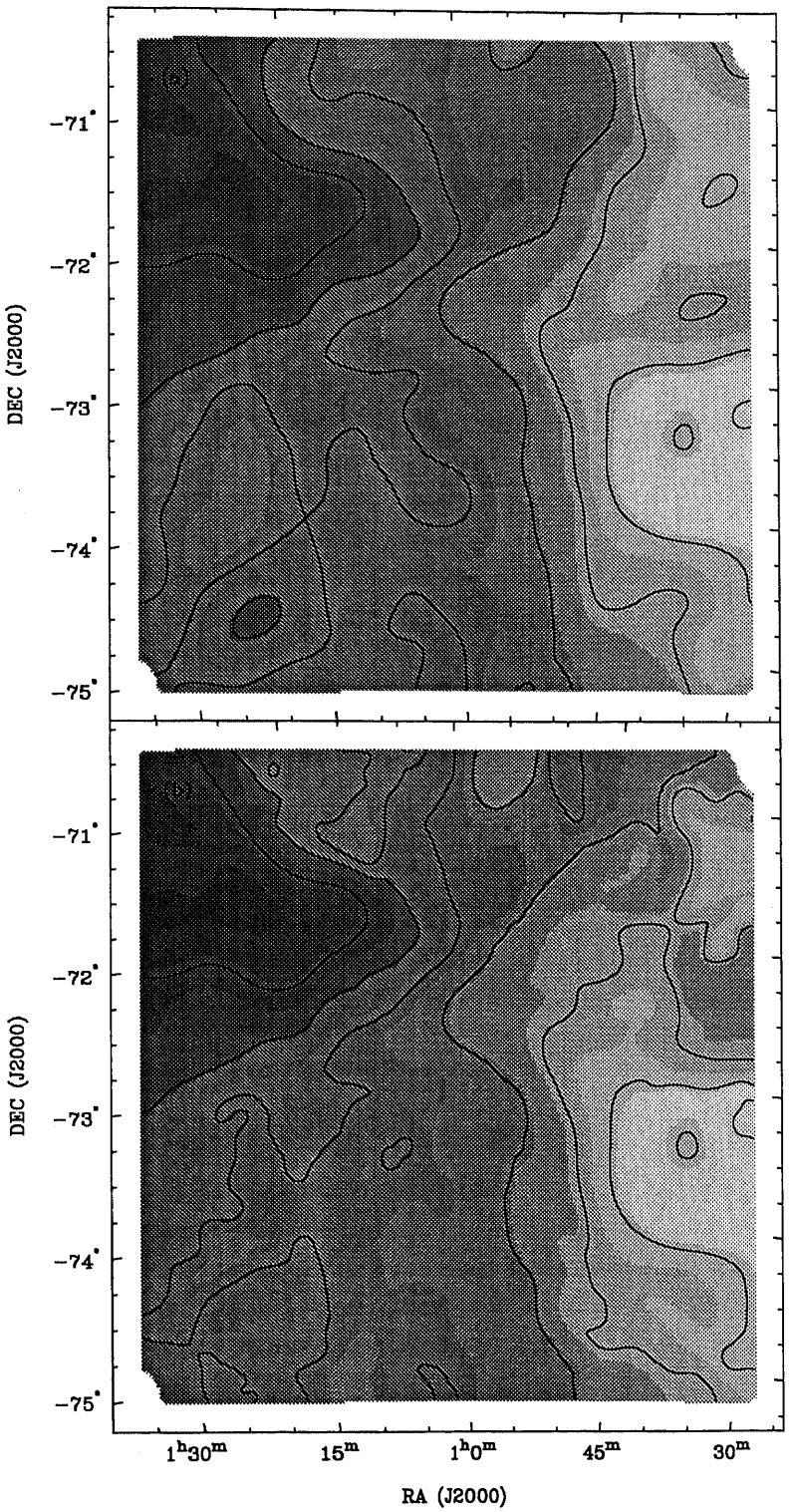

Figure 5.3 . The velocity field of the Parkes SMC data derived using: (a) the intensity-weighted mean along a line of sight; (b) the 5% cut-off along a line of sight. Both images have a resolution of 20 arcmin. The grey-scale range is 120 to 230 km s^{-1} with a linear transfer function. The contour levels range from 120 to 200 km s^{-1} with the contour interval being 12 km s^{-1}.

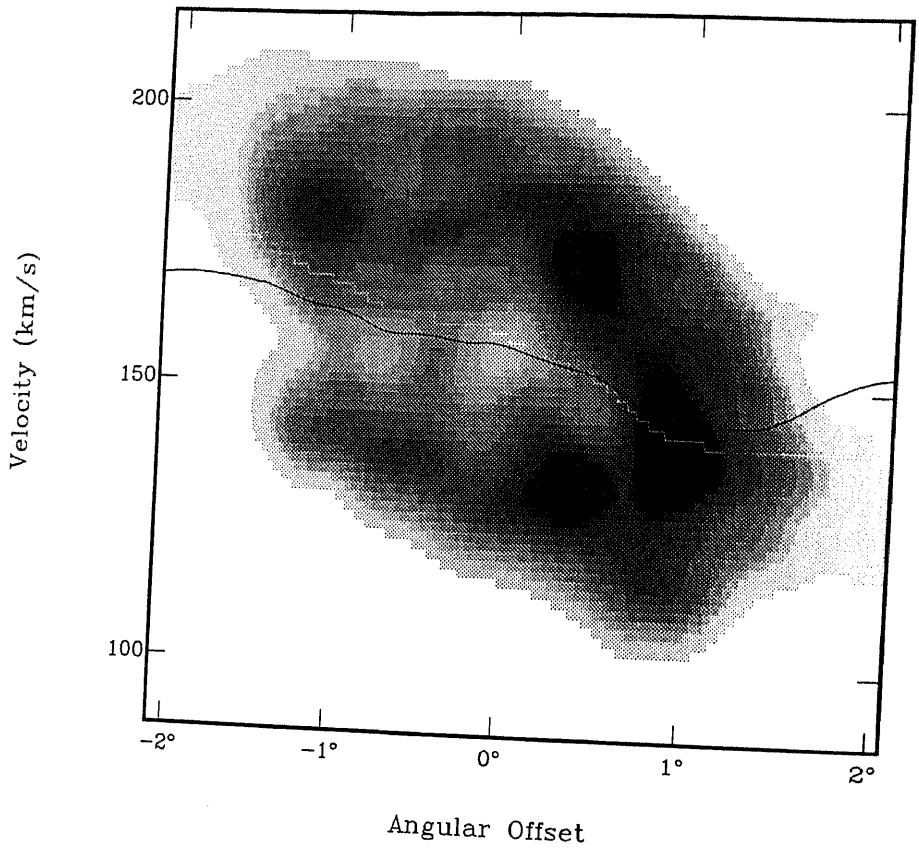

Figure 5.4 . The position-velocity slice through the Parkes data cube at Dec $-72°40'33''$ (J2000), extracted using the KPVSLICE in KARMA (Gooch 1995). The cuts from the intensity-mean (in white colour) and unimodal (in black colour) velocity fields at the same position are superimposed.

As a result of the bimodal profile analysis, various parameters of 'L' and 'H' components were mapped. Fig. 5.5 shows the peak intensity and the integrated intensity of both components, respectively. The integrated intensity images resemble very much the HI column densities obtained for velocities $V_{\rm hel} < 150$ km s^{-1} and $V_{\rm hel} > 150$ km s^{-1}, respectively. A hole is visible in the 'L' component (panel (c)), around RA $00^{\rm h}45^{\rm m}$, Dec $-73°01'$ (J2000), corresponding most likely to the region where HI was blown away. A large ring-like feature is visible in the 'H' component (panel (d)), centred at $\sim$ RA $01^{\rm h}07^{\rm m}$, Dec $-72°45'$ (J2000), which is only 5 arcmin east and 7 arcmin south from the centre of the largest supershell found in the SMC (see Chapter 6). The 'H' component also shows a tail-like feature towards the south-west around Dec $-74°30'$, and an interesting region of high brightness temperature, centred on the position of the peak brightness temperature in the whole SMC, RA $00^{\rm h}49^{\rm m}$, Dec $-73°06'$ (J2000) (Section 4.1).

In Fig. 5.6 several position-velocity plots of both velocity components are shown. In

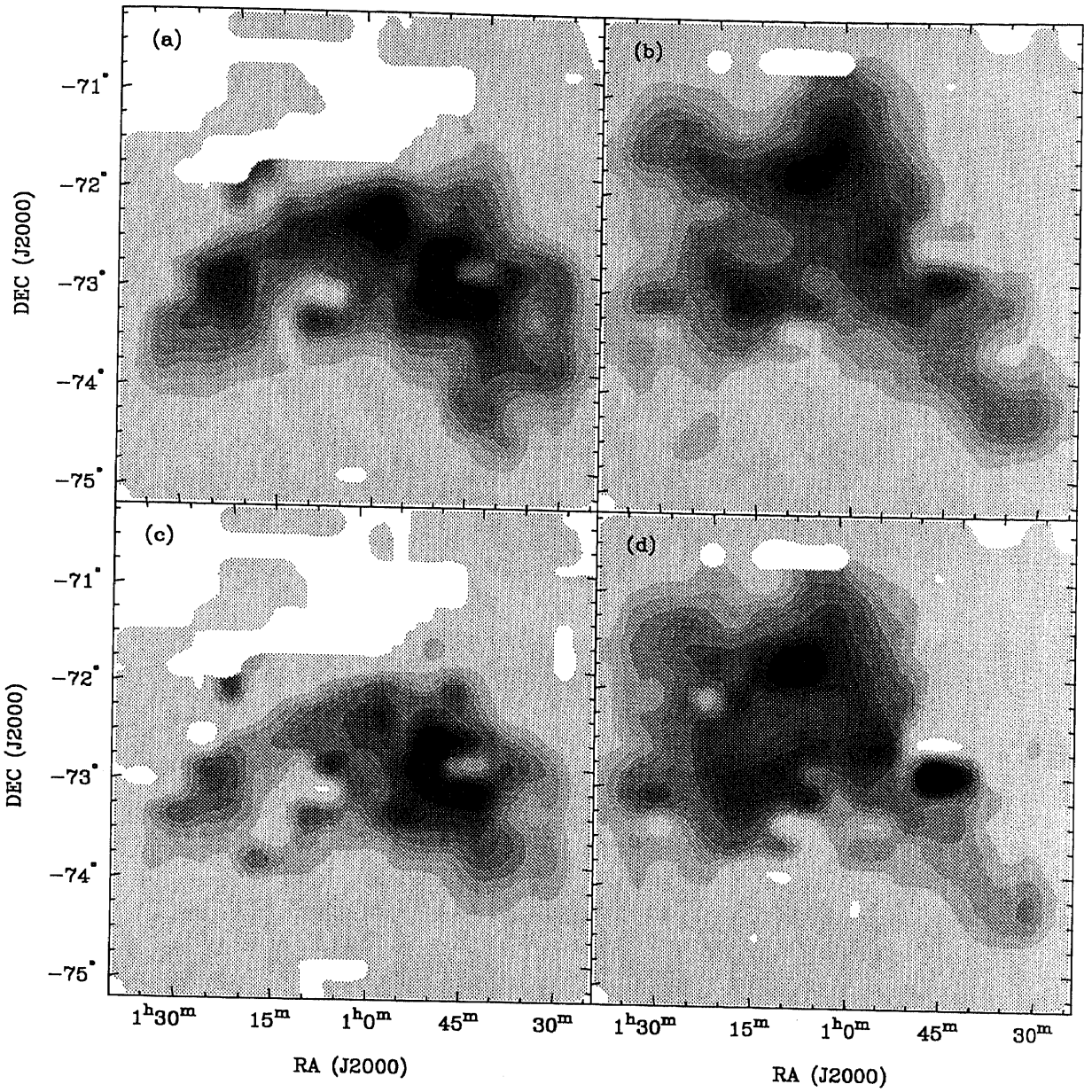

Figure 5.5 . (a) The peak intensity of the 'L' component. The grey-scale range is 0 to 37 K with a linear transfer function. (b) The peak intensity of the 'H' component. The grey-scale range is 0 to 48 K with a linear transfer function. (c) The integrated intensity of the 'L' component. The grey-scale range is 0 to 1680 K km s^{-1}. (d) The integrated intensity of the 'H' component. The grey-scale range is 0 to 1440 K km s^{-1}. All four images have resolution of 18.8 arcmin.

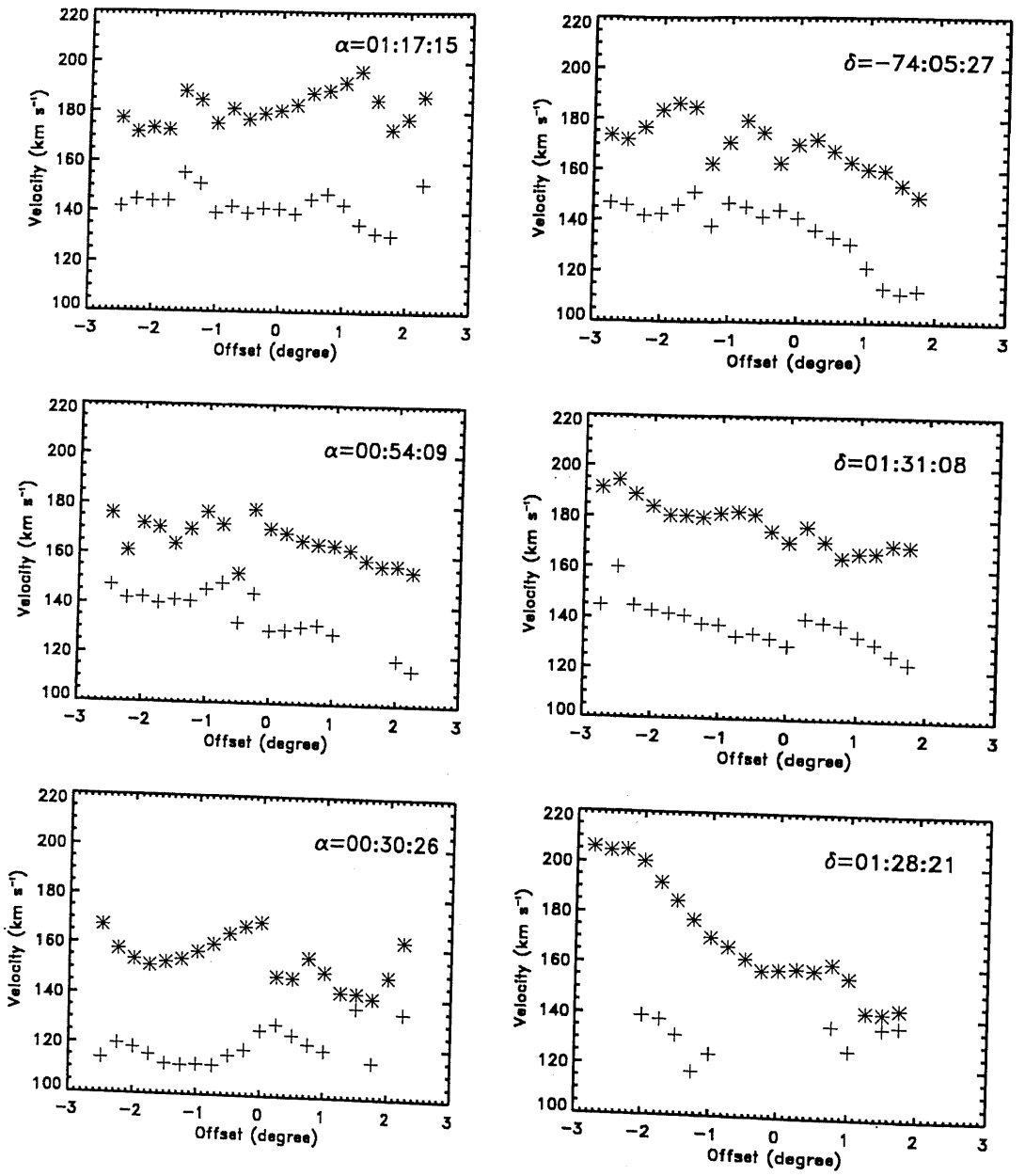

Figure 5.6 . Some examples of the position-velocity diagrams for the 'L' and 'H' components, taken for approximately constant RA (first column, with the RA value written in the top-right corner) and approximately constant Dec (second column, with the Dec value written in the top-right corner). Values for the 'L' component are shown with the cross sign (+), while 'H' component is represented with the asterisk sign (*).

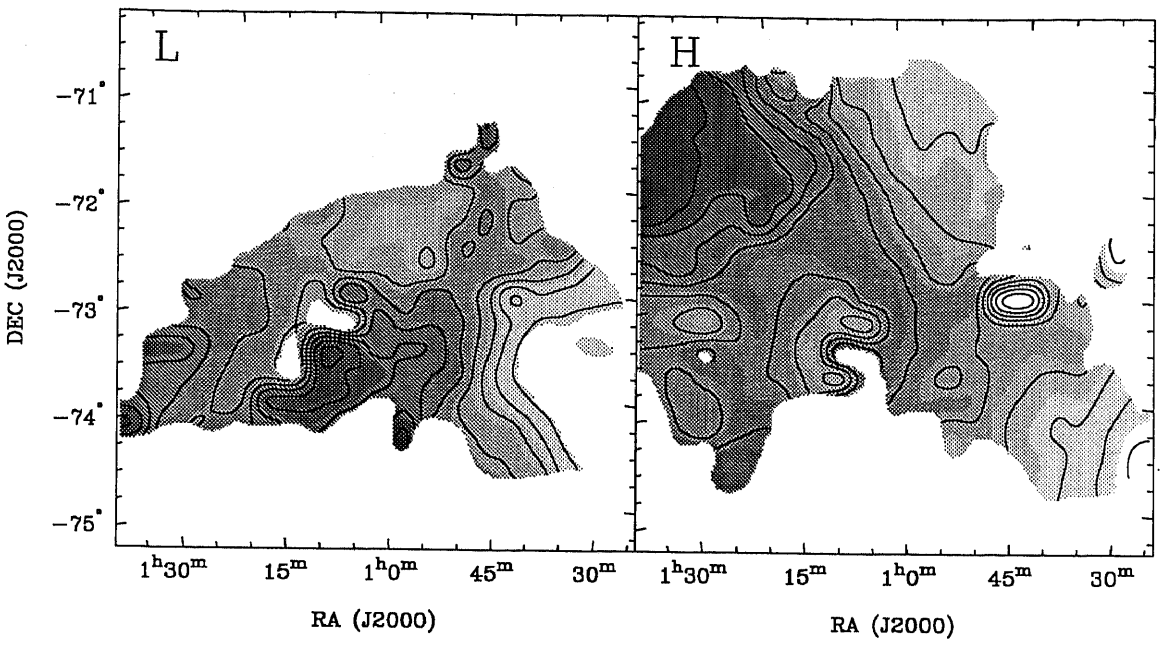

Figure 5.7 . The central heliocentric velocity of the 'L' and 'H' Gaussian components, respectively. The 'L' component ranges between 100 and 190 km s^{-1}, while 'H' component ranges between 130 and 210 km s^{-1}. The images have the grey-scale range 115–200 km s^{-1} and 150–250 km s^{-1}, respectively. The contour levels are from 100 to 190 km s^{-1} and from 130 to 210 km s^{-1}, respectively, having the contour interval of 6 km s^{-1}.

a similar study of the LMC (Luks & Rohlfs 1992), double peaks are found in $\sim$ 19 % of HI gas, and the position-velocity diagrams were necessary to classify different velocity components. In the case of the SMC, double peaks are present and clearly distinguishable over most of the angular extent of the SMC. Although the shape of both components changes significantly in the position-velocity diagrams with the position, both components show similar large-scale trends, being parallel in many cases with approximate separation of 40 km s^{-1}. Both 'L' and 'H' components also show a slight gradient in velocity from the south-west to the north-east.

This is shown in the images of the central heliocentric velocity of the two components, Fig. 5.7. Both velocity fields show a velocity gradient from the south-west to the north-east, and appear parallel to each other. Some large-scale symmetry of iso-velocity contours is visible at the south-west part of the 'L' component and at the north-east end of the 'H' component, while the rest of contours do not show much symmetry.

The velocity dispersion of both velocity components is shown in Fig. 5.8. The 'L' component has almost constant velocity dispersion of $\sim$ 22 km s^{-1}, with higher values in the Eastern Wing region and in the central region around a hole-like feature seen on the integrated intensity map, centred on RA 00^h45^m, Dec $-73°10'$

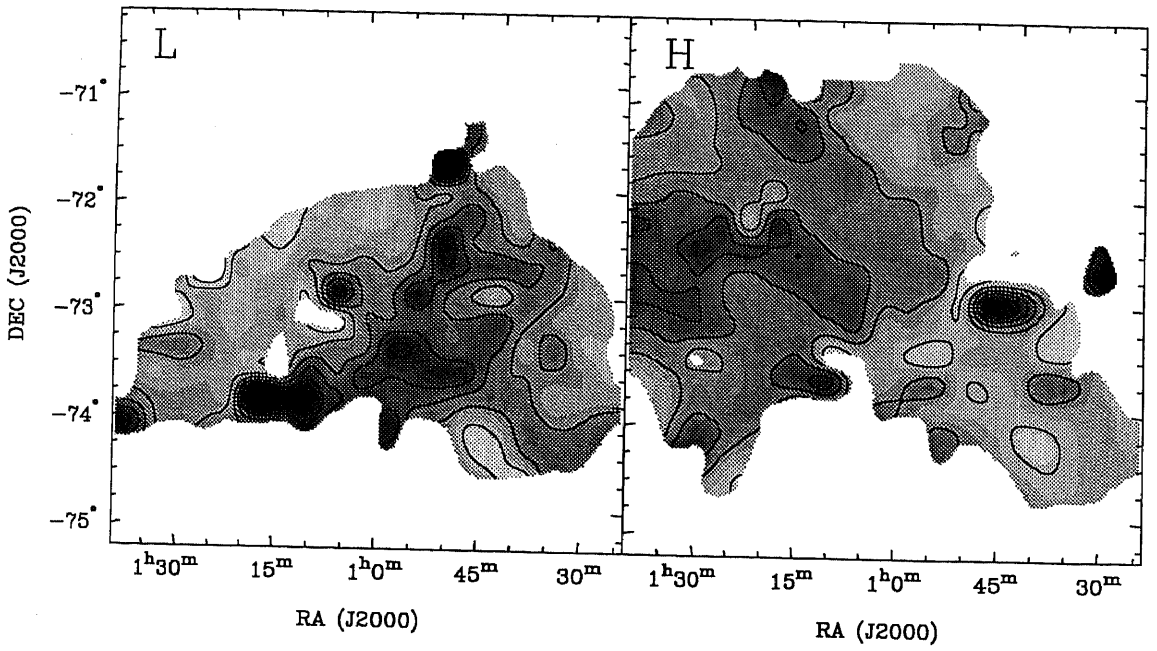

Figure 5.8 . The velocity dispersion of 'L' and 'H' components. It ranges from 0 to 80 km s^{-1} for the 'L' component and from 10 to 70 km s^{-1} for the 'H' component. Both images have the grey-scale range of 10–60 km s^{-1}.

(J2000). This later region was seen in the high resolution HI data (Section 4.1) as being broken up into numerous expanding shells. The 'H' component shows almost constant velocity dispersion of $\sim$ 18 km s^{-1} from the south-west to $\sim$ RA 01^h and then a gradient up to $\sim$ 50 km s^{-1} at the eastern edge of the image. The dispersion in velocity at the north-west might be related to the already mentioned shell-like feature in this component. The maximum dispersion in the 'H' component is associated with the region having the highest brightness temperature in the SMC.

As a result of the bimodal analysis of HI profiles, it seems that the HI profiles in the SMC can be decomposed into two separate velocity structures, having parallel velocity fields with an offset of $\sim$ 40 km s^{-1}. The velocity dispersion of the first component is almost constant, while it shows a gradient from the south-west to the north-east for the second component, suggesting possibly a larger line-of-sight depth for the 'L' component at the north-east. We compare these results with some observational and theoretical models later.

5.2.3 Correction for the proper motion of the SMC

It is widely believed that the Magellanic Clouds have always been satellites of the Galaxy (Murai & Fujimoto 1980). Hence, the binary motion of the SMC around the Galaxy combined with its large angular extent could have a significant contribution

to the observed velocity field. This contribution consists of the projection of the transverse velocity of the SMC's centre of gravity on the line of sight at each position. In the case of the large angular extent on the sky, this projection varies significantly across the field of observation and the velocity field could change significantly.

Table 5.1 . The proper motion of the SMC. References: (1) Kroupa et al. (1994), based on data for 8 stars from the Position and Proper Motion Catalogue; (2) Gardiner et al. (1994), from numerical simulations of HI in the Magellanic System; (3) Irwin et al. (1996), direct measurements uncorrected for reflex solar motion from 20 AAT 4m plates; (4) Kroupa & Bastian (1997), based on Hipparcos data for 11 stars; (1) & (4), derived from the combination of data in (1) and (4).

$\mu_\alpha \cos\delta$ (mas yr^{-1})	μ_δ (mas yr^{-1})	Reference
0.5 ± 1.0	-2.0 ± 1.4	(1)
0.8	-1.39	(2)
0.92 ± 0.20	-0.69 ± 0.20	(3)
1.23 ± 0.84	-1.21 ± 0.75	(4)
0.93 ± 0.64	-1.39 ± 0.66	(1) & (4)

The first measurement of the proper motion was the one by Kroupa, Röser, & Bastian (1994), followed by more accurate, but uncorrected for reflex solar motion, estimates by Irwin et al. (1996), using AAT 4m plates, and by Kroupa & Bastian (1997), using the Hipparcos data (see Table 5.1). The combination of data from Kroupa, Röser, & Bastian (1994) and Kroupa & Bastian (1997) resulted in the estimate of $\mu_\alpha \cos\delta = (0.93 \pm 0.64)$ mas yr^{-1} and $\mu_\delta = (-1.39 \pm 0.66)$ mas yr^{-1}, which is very similar to the predicted values from numerical simulations of the observed HI features in the Magellanic System by Gardiner, Sawa, & Fujimoto (1994). However, the uncertainties of measured values are still quite large. Therefore, we have decided to use values for the proper motion and the heliocentric transversal velocity of 424 km s^{-1}, based on the model of Gardiner, Sawa, & Fujimoto (1994).

At any position in the SMC, the real radial heliocentric velocity ($V_{\rm rad}$) can be obtained by subtracting the projection of the heliocentric transverse velocity of the centre of the SMC on the line-of-sight, from the observed radial heliocentric velocity ($V'_{\rm rad}$):

$$V_{\rm rad} = V'_{\rm rad} - \hat{\mathbf{d}} \cdot \mathbf{V}_{\rm t} \tag{5.1}$$

where $\mathbf{V}_{\rm t}$ is the vector of the heliocentric transverse velocity of the centre of the SMC and $\hat{\mathbf{d}}$ is the unit position vector of a particular point in the SMC in the standard heliocentric coordinate system. The values for the conversion between the observed

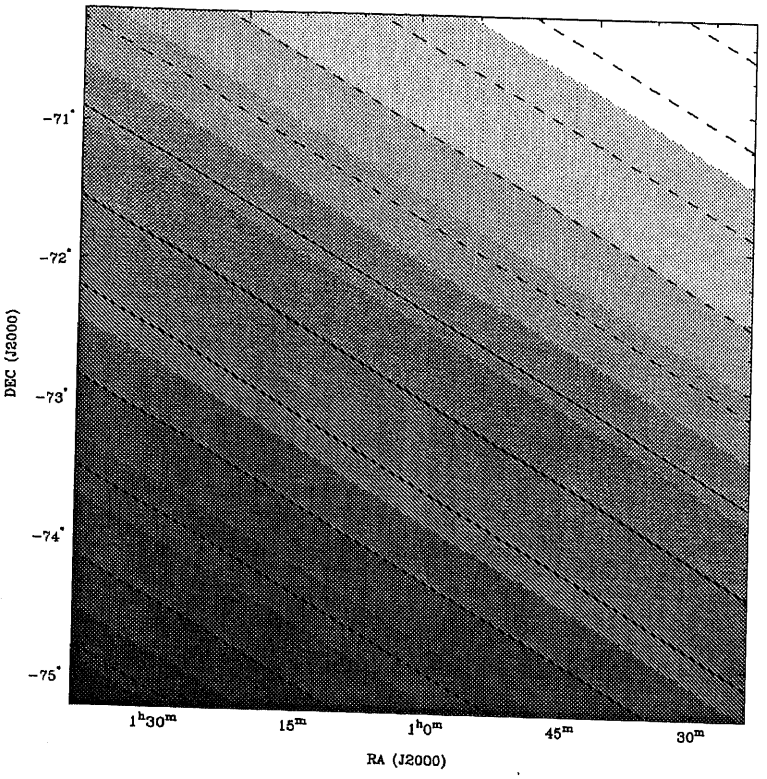

Figure 5.9 . The projection of the heliocentric transverse velocity of the centre of the SMC on the line-of-sight across the SMC. The grey-scale range is -15 to 35 km s^{-1}. Contours range from -25 to 25 km s^{-1} with a contour interval being 4 km s^{-1}.

and real heliocentric velocity, range between -23 km s^{-1}, at the north-west, and 28 km s^{-1}, at the south-east, and their distribution across the SMC is shown in Fig. 5.9. While along the line from the north-east to the south-west the corrections are minor, the north-west and the south-east corners of the image have significantly different values of $\sim \pm 20$ km s^{-1}. Further correction of the real heliocentric velocity field for the combined effect of solar motion and galactic rotation, provides conversion to the galactocentric reference frame ($v_{\rm rad}$):

$$v_{\rm rad} = V_{\rm rad} + \hat{\mathbf{d}} \cdot (\mathbf{V}_{\rm LSR} + \mathbf{v}_{\odot}) \tag{5.2}$$

with $\mathbf{V}_{\rm LSR}$ being the velocity vector of the Local Standard of Rest (LSR) relative to the Galactic centre and $\mathbf{v}_{\odot}$ being the Solar velocity vector relative to the LSR. All adopted values for all velocity vectors are given in Table 5.2. The velocity field from the unimodal profile analysis, corrected for the proper motion and converted to the galactic coordinate system, is shown in Fig. 5.10.

This final velocity field shows a clear velocity gradient from -15 km s^{-1}, at the south-west, to 53 km s^{-1}, at the north-east. It is more regular then previously seen.

Table 5.2 . The heliocentric transverse velocity vector of the centre of the SMC, the galactocentric velocity vector of the LSR relative to the Galactic centre and the galactocentric velocity vector of the Sun relative to the LSR, from Gardiner, Sawa & Fujimoto (1994). The centre of the SMC is assumed to be at RA $00^h52^m49^s$, Dec $-72°49'40''$ (J2000).

Space Velocity	Amplitude km s^{-1}	Direction l°	b°
$\mathbf{V}_t$	424	162	−15
$\mathbf{V}_{LSR}$	220	90	0
$\mathbf{v}_\odot$	16	53	25

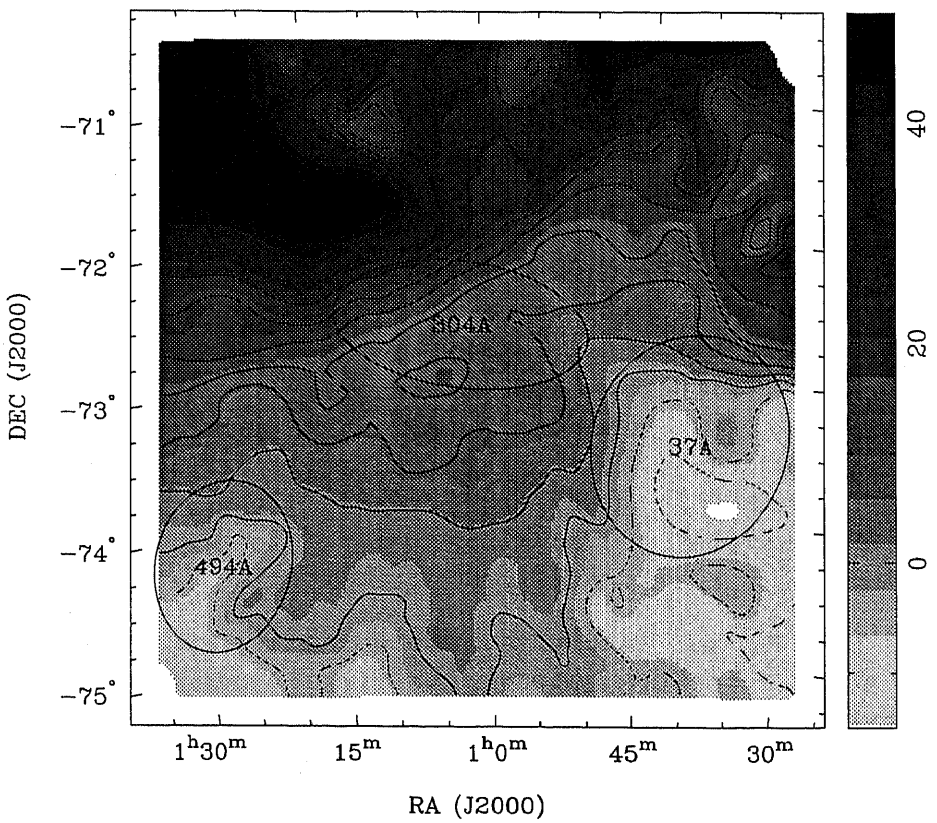

Figure 5.10 . The unimodal galactocentric velocity field of the SMC corrected for the proper motion. The grey-scale range is −15 to 50 km s^{-1} with a linear transfer function. The contour levels range from −20 to 50 km s^{-1}, with the interval of 5 km s^{-1}. Three largest supershells (Chapter 6) are superimposed.

This, together with a possible gradient of radial velocities of Cepheids (discussed in the next section), suggests that the SMC could be interpreted as some kind of a disk in the circular rotation. Positions of the three largest shells in the SMC are overlaid on the same figure, showing that supershells 304A and 494A might still be responsible for some of the perturbations in the velocity field. Being very large, these features must have had an important role in the dynamics and evolution of the whole SMC. We note that it is very hard to model the velocity field of each individual supershell, and subtract it from the main velocity field, because shells are usually asymmetric due to the inhomogeneous ISM surrounding them. Some perturbations are also visible on the north-west.

5.3 The rotation curve and the mass of the SMC

5.3.1 Tilted ring analysis

The unimodal velocity field corrected for the proper motion was used to obtain the major and minor kinematic axes, defined as directions of maximal and minimal velocity gradient, respectively. The principal kinematic axes are not exactly perpendicular. Their intersection, the apparent kinematic centre, is at $\sim$ RA $01^{h}05^{m}$, Dec $-72°25'$ (J2000) having systemic velocity of $\sim$ 20 km s^{-1}in the galactocentric reference frame. The position angle of the major kinematic axis is around 50°. The measured kinematic centre appears to be 4′ N from the position found by Hindman (1967), 0.6°E and 0.2°S from the position found by Loiseau & Bajaja (1981), and 0.9°E and 0.4°N from the nominal optical centre of the SMC (Westerlund 1997). The systemic velocity measured in previous radio studies is in extremely good agreement with the value found here, while we find a slightly smaller position angle of the major kinematic axis of 50°, relative to 55° found in Hindman (1967) and 57° found in Loiseau & Bajaja (1981). This is mainly due to our correction for the proper motion of the SMC.

The tilted ring algorithm ROCUR in the AIPS was then used to derive the HI rotation curve. The galaxy was divided into concentric rings, 7.5 arcmin wide, and the set of parameters: the rotation centre (x_0, y_0), the systemic velocity $V_{\rm sys}$, the inclination i, the rotational velocity $V_{\rm rot}$ and the position angle PA, was derived so that it represents well the observed velocity field at all radii. To achieve this ROCUR does the least-squares fitting to the function:

$$V(x, y) = V_{\rm sys} + V_{\rm rot} \cos(\theta) \sin(i) \tag{5.3}$$

with angle θ being the azimuthal angle and i being the inclination. In the first step, the position of the kinematic centre (x_0, y_0), the systemic velocity $V_{\rm sys}$ = 20 km

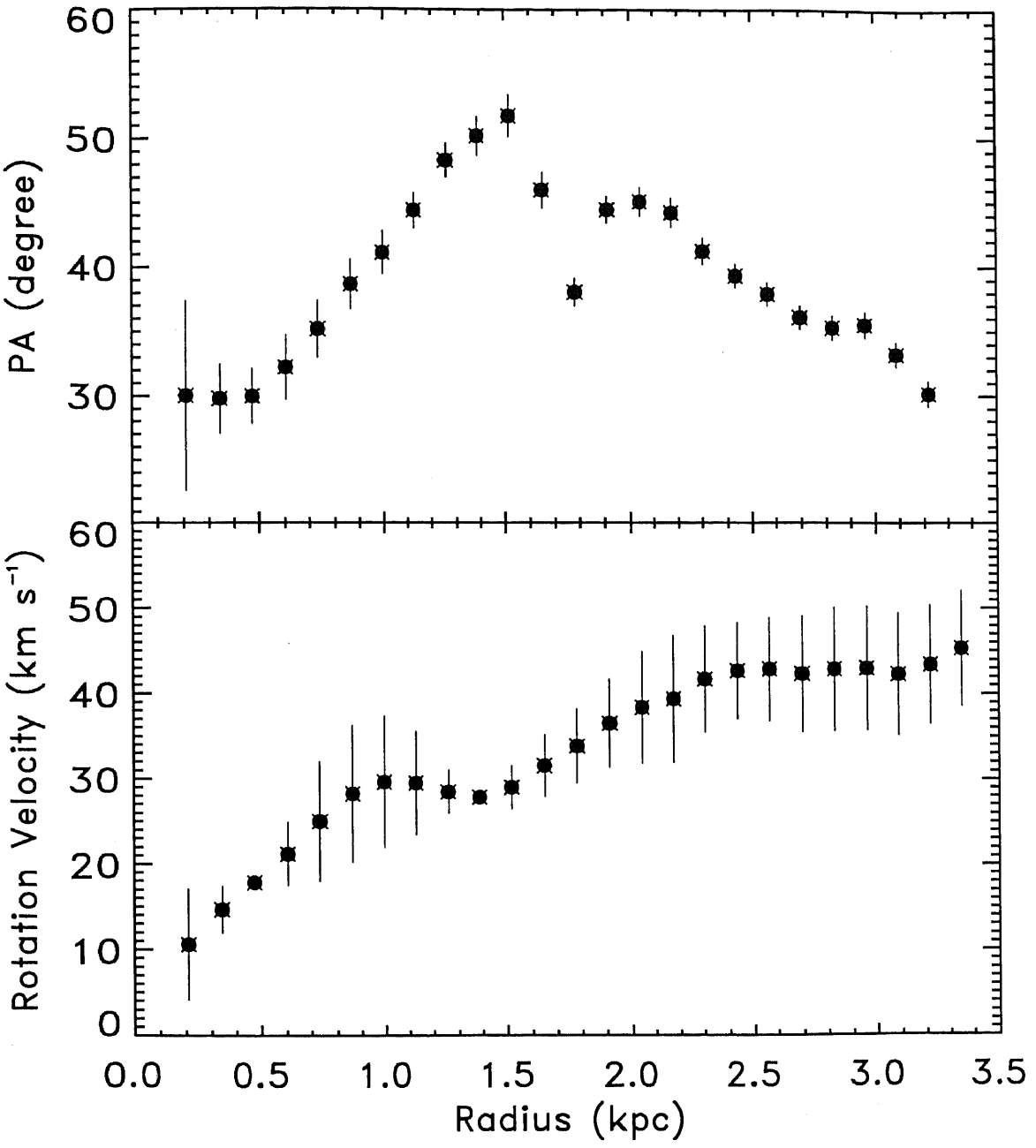

Figure 5.11 . The least-squares solution for the position angle (PA) of the kinematic line of nodes (top panel) and the rotational velocity ($V_{\rm rot}$) (bottom panel) as a function of radius. The mean position angle is 40°.

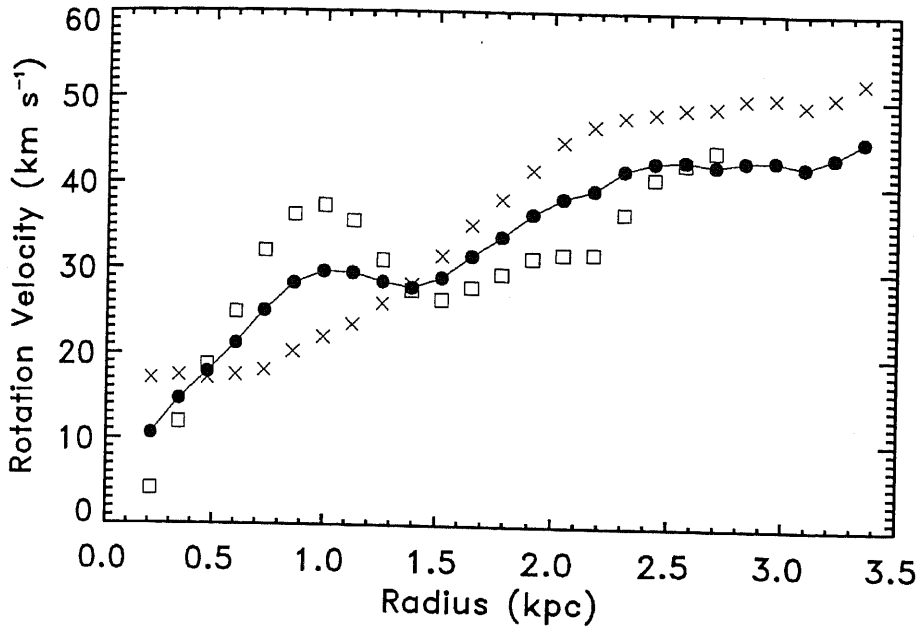

Figure 5.12 . The least-squares solution for the rotational velocity derived for the receding side (squares) and approaching side (crosses). The global solution is shown with filled circles.

s^{-1}and position angle of PA = 50° were kept fixed, in order to determine the least-square solution for the inclination. Due to non-circular motions, dominated mainly by shell kinematics, the inclination greatly varies, especially for the outer rings, but it is not plotted here. The value $i = 40° \pm 20°$ was adopted. In the next step, the position of the kinematic centre and the inclination were used to determine the least-squares solution for the systemic velocity of 24 km s^{-1}, being slightly higher than the initial estimate. During the fitting, the data in an open angle of 20° about the minor axis were excluded, since data points close to the minor axis have very uncertain $V_{\rm rot}$. Also, all data points in each of the rings were weighted by the $\cos^2(\theta)$ in order to down-weight data points with uncertain $V_{\rm rot}$. Finally, the solutions for the rotational velocity and position angle for each of the rings were determined (Fig. 5.11). The position angle varies systematically from 30° to 50°. The mean position angle of 40° is in good agreement with the photometric position angle of 45° in Westerlund (1997). Using the mean value, the global and the separate rotation curves for the receding and approaching sides of the velocity field, were derived, Fig. 5.11 and Fig. 5.12.

The receding and approaching curves appear to be significantly different, which is not surprising since the velocity field is quite asymmetric. In the inner part (up to $R = 1.5$ kpc), the receding curve has a more rapid rise than the approaching one, while both curves show a steady rise in the outer part. The approaching curve flattens around $R = 2.7$ kpc, but then shows a further rise. The uncertainty of

the global rotation curve (Fig. 5.11) was estimated from the level of asymmetry in the velocity field (Meurer et al. 1996). The error bars were taken to be the absolute difference between the values for the global curve and either the receding or approaching curve, whichever is larger.

The global rotation curve shows a rapid rise up to $R = 1.0$ kpc, where it reaches the first local maximum of ~ 30 km s^{-1}. For $R = 1.5 - 2.5$ kpc, rotation curve shows a steady rise, and then starts to flatten reaching the secondary maximum of $V_{\rm rot} = 43$ km s^{-1} at the turnover radius of ~ 2.5 kpc. For the last three rings, $R > 3.1$ kpc, the rotation curve starts to rise again, which is most likely an effect of a quite uncertain inclination for large radii. The maximum rotation velocity found in previous studies (Hindman 1967; Loiseau & Bajaja 1981) was ~ 36 km s^{-1}.

5.3.2 The asymmetric drift correction

The line-of-sight HI velocity dispersion ($\sigma_{\rm HI}$) was derived in Section 5.2 as the second moment map, see Fig. 5.2. This image was used to determine the elliptically averaged profile of the velocity dispersion in the deprojected rings (for $i = 40°$) centred at the kinematic centre and for PA=40°. The profile is shown in Fig. 5.13 in the top panel (solid line). Taking into account that the velocity resolution is ~ 2 km s^{-1}, the $\sigma_{\rm HI}$ profile was smoothed and approximated with the function shown on the same panel with a dashed line. This profile has a nice Gaussian shape with a small tail, which may be explained by the galactic fountain process (see Dickey 1996 and references therein). It peaks around the kinematic centre, where the gas is stirred up by stellar winds and supernovae explosions, and from $R = 0.7$ kpc has almost constant value of 21.5 km s^{-1}. A similar distribution of $\sigma_{\rm HI}$ has been found for face-on spiral galaxies (Dickey 1996), with $\sigma_{\rm HI}$ reaching a constant value of $6 - 9$ km s^{-1}at the outer radii, in many cases. The HI velocity dispersion appears to be significantly broader in the SMC than in spiral galaxies, or even in some other dwarf galaxies such is NGC 1705 (Meurer, Staveley-Smith, & Killeen 1998). The mean value, $\sigma_{\rm HI} = (22 \pm 2)$ km s^{-1}, is a significant fraction of the rotational velocity (Fig. 5.12). If interpreted as due to the random motions, rather then the bulk motions along the line-of-sight (Meurer, Staveley-Smith, & Killeen 1998), such high values for $\sigma_{\rm HI}$ suggest that the turbulence in the ISM of the SMC has an important influence on the system dynamics. To account for this dynamical support, we estimate the asymmetric drift correction (Meurer et al. 1996). However, it should be noted that other effects, such as: shocks, beam smearing, finite spectrometer channel widths (Dickey 1996), differing bulk motions along the line-of-sight (Meurer, Staveley-Smith, & Killeen 1998), magnetic fields (Ferrara 1996), could also contribute to the observed linewidths.

Under the assumption of a dynamical equilibrium in an axially symmetric system, Oort (1965) has derived the relationship between the mean circular and mean random velocities of stars. Assuming that the gas is in equilibrium and that the gas

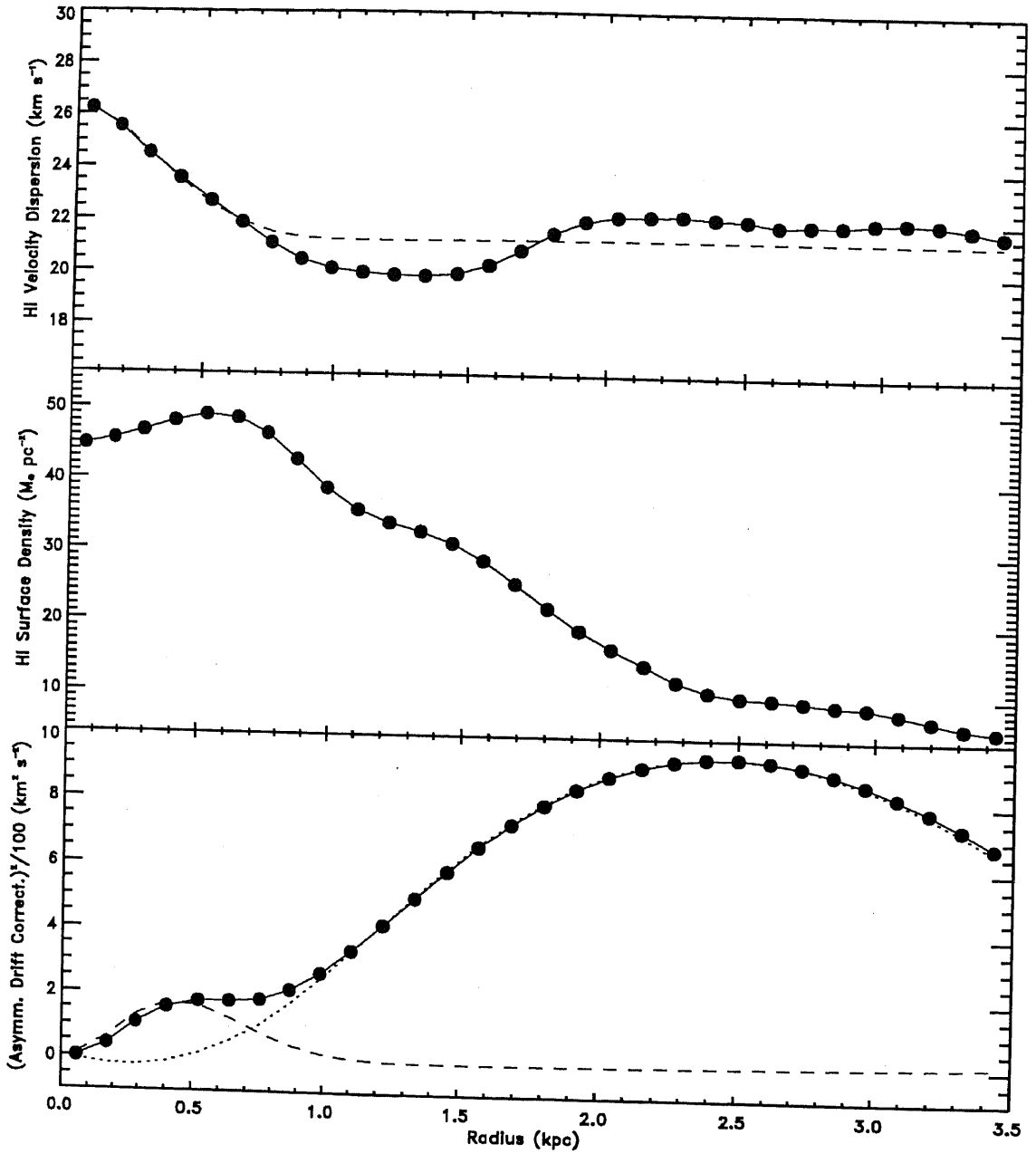

Figure 5.13 . (a) The radial distribution of the HI line-of-sight intensity-weighted velocity dispersion, derived by averaging $\sigma_{\rm HI}$ in elliptical annuli around the kinematic centre of the SMC and with PA=40° and $i = 40°$ (top panel, solid line). The approximation of the radial $\sigma_{\rm HI}$ profile used to derive the asymmetric drift correction (top panel, dashed line). (b) The radial distribution of the HI surface brightness, derived by averaging $\Sigma_{\rm HI}$ in elliptical annuli around the kinematic centre of the SMC and with PA=40° and $i =$ 40° (middle panel). The profile was derived assuming optically thin gas, and was corrected by 1.33 to account for neutral He. (c) The total asymmetric drift correction ($\sigma_{\rm D}^2/100$) shown with a solid line (bottom panel) and the contributions of $\sigma_{\rm HI}$ and $\Sigma_{\rm HI}$, shown with dashed and dotted lines, respectively.

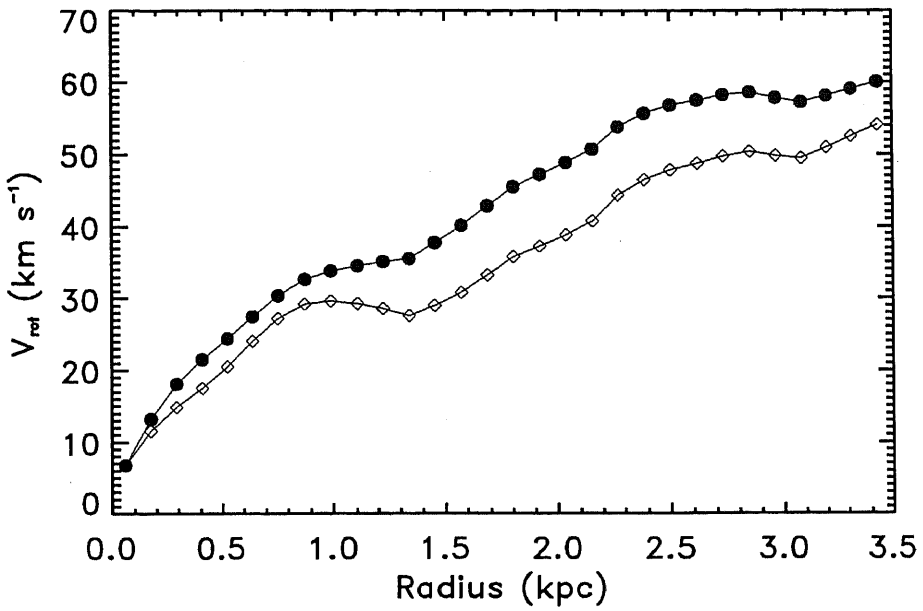

Figure 5.14 . The observed rotation curve (diamonds) may be corrected for the effect of pressure support due to the random motions. The resultant curve (filled circles) is what the rotation curve would look like in the absence of pressure support.

velocity ellipsoid is isotropic, Meurer et al. (1996) applies the same equations on the gas, and relates the circular velocity of gas with the observed rotational velocity by:

$$V_c^2 = V_{rot}^2 + \sigma_D^2 \tag{5.4}$$

where σ_D is the asymmetric drift correction given by:

$$\sigma_D^2 = -R\sigma_{HI}^2 \left[\frac{\partial \ln(\Sigma_{HI})}{\partial R} + 2\frac{\partial \ln(\sigma_{HI})}{\partial R} - \frac{\partial \ln(h_z)}{\partial R} \right] \tag{5.5}$$

with Σ_{HI} being the gas surface brightness (assuming HI plus neutral He) and h_z being the vertical scale height. Under the assumption of constant h_z, the last equation is simple to solve, since we can measure Σ_{HI} and σ_{HI}. The observed velocity dispersion σ_{HI} does not require any correction under the assumption of the isotropic gas velocity ellipsoid.

To determine Σ_{HI}, the HI surface brightness, multiplied by 1.33 to account for neutral He, was azimuthally averaged in deprojected circular annuli, for PA=40°and $i = 40°$. The profile is shown in the middle panel of Fig. 5.13. Interestingly, the central depression common for spiral galaxies (Giovanelli & Haynes 1988; Staveley-Smith

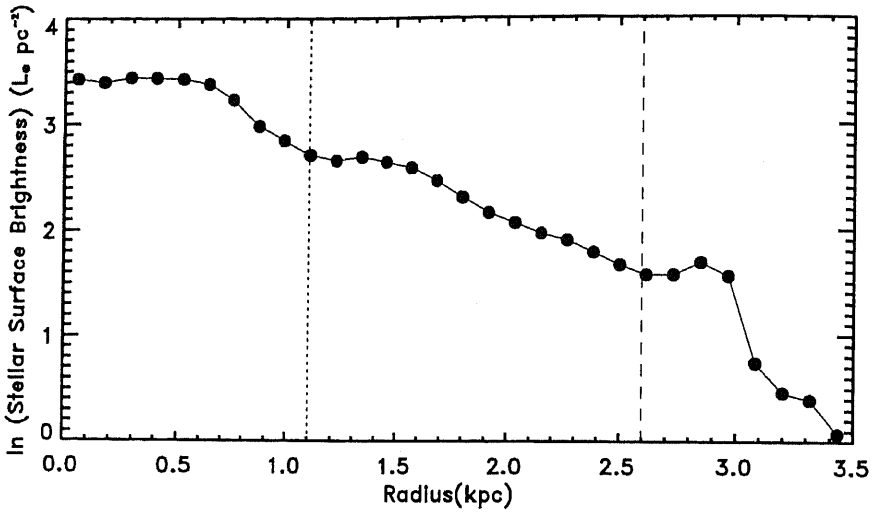

Figure 5.15 . The natural logarithm of the radial distribution of the stellar surface brightness (in $L_\odot$ pc^{-2}). The profile was derived by averaging broad band Hα image, scaled to match the total luminosity of the SMC in R-band, in elliptical annuli around the kinematic centre of the SMC and with PA=40° and $i = 40°$. The e-folding scale-length at 1.1 kpc is shown with the dotted line, and the departure from the Hα exponential distribution at 2.6 kpc is shown with dashed line.

et al. 1990) is seen, followed by approximately the Rice distribution, consisting of a broad Gaussian function with a long tail.

To estimate the asymmetric drift correction, functions $\ln(\Sigma_{\rm HI})$ and $\ln(\sigma_{\rm HI})$ were first fitted with a combination of a Gaussian and a polynomial function:

$$\ln(\Sigma_{\rm HI}) = -3.71 \exp \frac{1}{2}\left(\frac{R+1.03}{1.02}\right)^2 + 6.03 - 2.03R + 0.23R^2; \qquad (5.6)$$

$$\ln(\sigma_{\rm HI}) = 0.22 \exp \frac{1}{2}\left(\frac{R+0.01}{0.33}\right)^2 + 3.05 + 0.01R \qquad (5.7)$$

and then numerically differentiated with respect to R (in units of kpc). The standard deviation of fits is 0.04 for $\Sigma_{\rm HI}$ and 0.02 for $\sigma_{\rm HI}$. The final drift correction, as well as the contributions from $\Sigma_{\rm HI}$ and $\sigma_{\rm HI}$, are plotted in Fig. 5.13, in the bottom panel. In general, the corrections are quite significant with $0 < \sigma_{\rm D} < 40$ km s^{-1}. For the inner radii, the correction is dominated by the influence of $\sigma_{\rm HI}$, while for the outer radii, corrections are completely determined by $\Sigma_{\rm HI}$. The observed rotation curve corrected for the pressure support is presented in Fig. 5.14. The difference is significant. The prominent bump, observed around $R = 1$ kpc is now less significant, the corrected curve is steeper than the observed one for the inner radii, while both curves are almost parallel for the outer radii with an offset of ~ 10 km s^{-1}.

5.3.3 The mass model

A two-component mass model was fitted to the corrected rotation curve.

To derive the deprojected rotation curve due to the potential resulting from the neutral gas alone, the radial HI surface density profile (Fig. 5.13, middle panel) was used in the GIPSY's ROTMOD task (van der Hulst et al. 1992). The exponential density law was assumed for the vertical disk distribution, with the scale height of 1 kpc. The resultant rotation curve (V_g) is shown in Fig. 5.16 with dotted line.

To derive the deprojected rotation curve due to the optical surface density distribution, the broad band, Hα and continuum, image of the SMC (Kennicutt et al. 1995, see Fig. 4.5) was used. The image was smoothed to 20 arcmin resolution and scaled to match the total luminosity of the SMC in the R-band of 3.5×10^8 $L_\odot$ (de Vaucouleurs et al. 1991), in order to estimate the surface density of the old stellar population. The logarithm of the azimuthally averaged stellar surface brightness is presented in Fig. 5.15. The stellar density profile shows a possible central depression, similar to the HI density profile, but declines with the radius almost exponentially (excluding the central depression), much faster than HI. The profile was used to estimate the e-folding scale length of Hα at approximately 1.1 kpc (as the radius where the profile starts to depart from the exponential distribution), and the cut-off radius of Hα distribution, at $R(\mathrm{H}\alpha) = 2.6$ kpc.

The rotation curve arising from the stellar potential alone (V_*) was obtained using ROTMOD again and assuming, in the first approximation, that $M_*/L = 1$. The curve is shown in Fig. 5.16 with a dashed line, and interestingly it has a very similar shape to the gas rotation curve (V_g). The best fit of the total predicted rotational velocity, $\sqrt{V_g^2 + V_*^2}$ to the observed rotational velocity corrected for the pressure support, was obtained for $M_*/L = 0.83$ (solid line in Fig. 5.16). The two component mass model appears to fit the observed rotational velocities quite well, suggesting that no additional component, such as a dark halo, is needed to explain the rotation of the SMC.

The rotation velocity of the stellar component only, implies a total stellar mass of the SMC of 1.96×10^9 $M_\odot$, within the radius of 3 kpc. From Section 4.2 and after correction for neutral He, the mass of HI+He is 5.56×10^8 $M_\odot$, being almost a third of the stellar mass within the same radius. The total mass of the SMC, implied from the rotation curve, is thus 2.5×10^9 $M_\odot$. This is higher than the mass of 1.5×10^9 $M_\odot$, derived by Hindman (1967) within the slightly smaller radius of 2.6 kpc, but is in agreement with Gardiner, Sawa, & Fujimoto 1994 who assumed the total mass of at least 2×10^9 $M_\odot$.

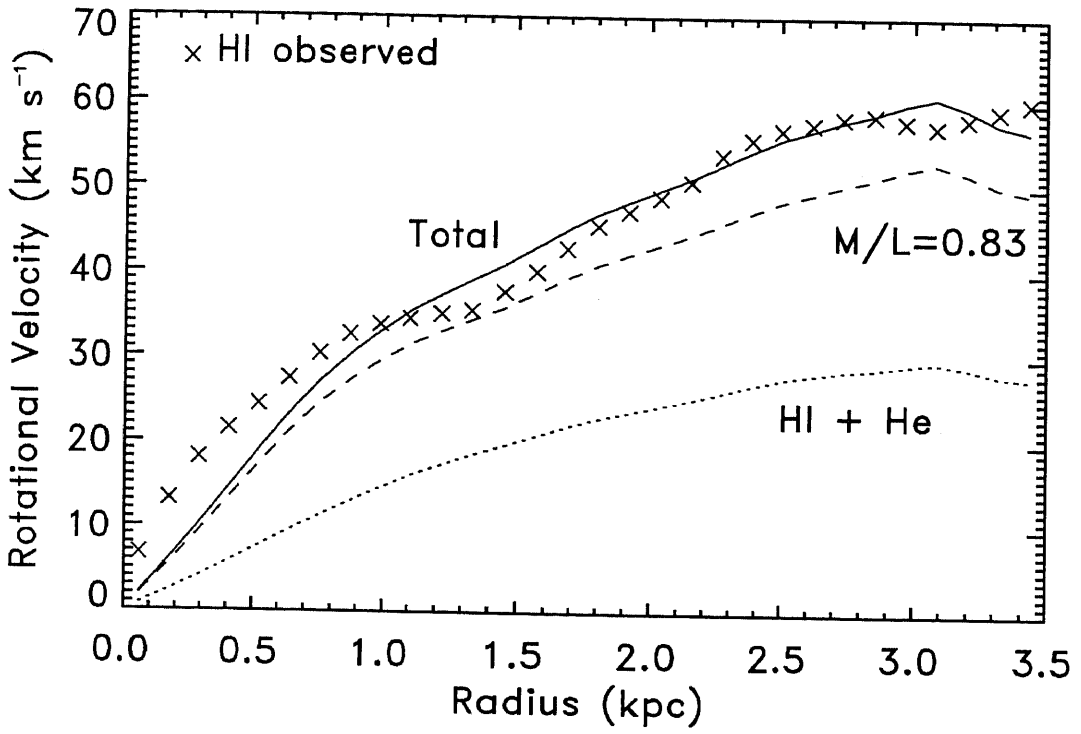

Figure 5.16 . The observed rotation curve, corrected for the pressure support (crosses), compared with the total predicted rotation curve (solid line), composed of: (a) the gaseous, HI+He, component (dotted line); (b) stellar component (dashed line) with the estimated mass-to-light ratio $M_*/L = 0.83$.

5.3.4 The vertical scale height (h_z)

To derive the mass model of the SMC, we have assumed a constant vertical scale height $h_z = 1$ kpc for both stars and gas. The same value was used by Hindman (1967). In the case of the Galaxy, various observations have shown that the thickness of the HI layer is, interestingly, approximately constant from 4 kpc to 8 – 10 kpc, but it decreases to < 100 pc near the nucleus, and increases enormously for $R > 10$ kpc (Dickey & Lockman 1990). Ferrara (1996) have shown that the vertical HI support in spiral galaxies, and particularly in the Milky Way, may be completely provided by turbulence and may result in the constancy of HI scale height.

For many other galaxies, due to the lack of direct measurements of the vertical scale height at different radii, it is common to assume in the first approximation that h_z does not change with the radius (Puche, Westpfahl, & Brinks 1992; Meurer et al. 1996; Kim 1998). However, once an approximate mass model of a galaxy is determined, it is possible to probe the variation of h_z with R.

In the model of a galactic disk by van der Kruit & Searle (1981) and van der Kruit

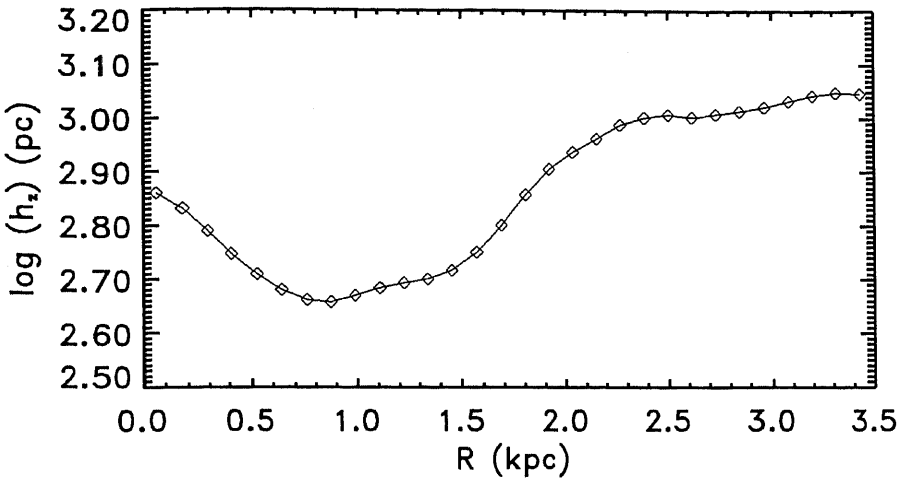

Figure 5.17 The logarithm of vertical scale height ($\log(h_z)$) as a function of radius.

& Searle (1982), the vertical density distribution follows $\rho(z) = \rho(0)\mathrm{sech}^2(z/z_0)$, a function which is close to exponential at higher z. In the case that both stars and gas have similar velocity dispersion, as in the SMC (Westerlund 1997), this model predicts the mid-plane scale height:

$$h_z = \frac{\sigma_{\mathrm{HI}}}{\pi \mathrm{G} \Sigma_{\mathrm{T}}} \tag{5.8}$$

where G is the gravitational constant and Σ_{T} is the total matter surface density. The vertical scale height of gas at different radii is shown in Fig. 5.17. The graph shows a significant variation of h_z. From $\sim$ 700 pc at the kinematic centre, h_z decreases reaching its minimum of 450 pc around $R = 0.7$ kpc, and then starts increasing, first slowly up to $R = 1.5$ kpc and then rapidly reaching almost 1.2 kpc at $R = 3.5$ kpc. The mean value of (800 ± 200) pc is quite close to what we have already assumed. This is similar to the trend of the vertical scale height found in M31 (Brinks & Burton 1984), where $h_z \approx 60$ pc at the inner parts but increases up to $\sim$ 185 pc at large radii. However, the scale height of the SMC disk is $\sim$ 8 times larger.

The newly estimated variation of h_z with R in Eq. 5.5 results in a change of σ_{D} and hence a slightly different rotation curve when corrected for the pressure support. The comparison of the newly corrected rotation curve with the rotation curves from separate gas and stellar potentials alone, derived under assumption of the constant h_z, requires a slight change to $M_*/L = 0.85$ for the mass-to-light ratio, and results in less than 5% higher total mass of the SMC. We will therefore assume $(2.6 \pm 0.1) \times 10^9$ $\mathrm{M}_\odot$ for the total mass of the SMC. It appears that the better estimate of $h_z(R)$ was not so critical for the pressure support correction. However, the variation of h_z with R, may be more critical in the determination of the rotation curve from the

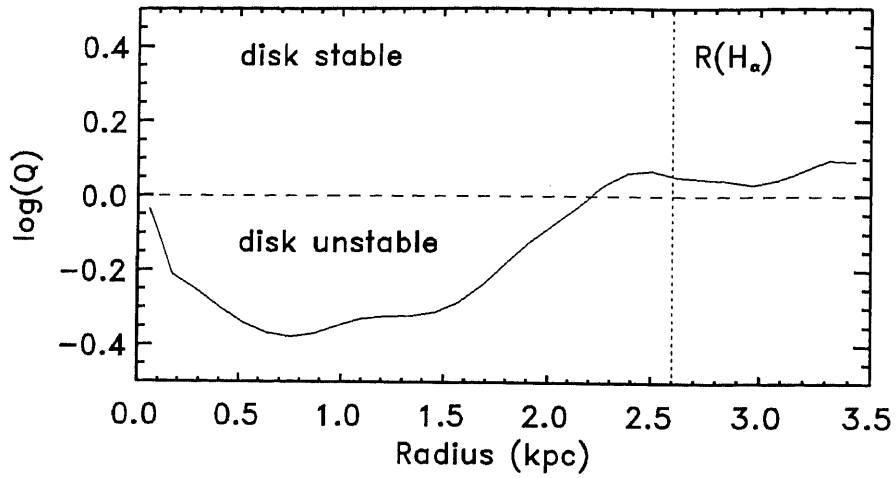

Figure 5.18 . Radial variation of Toomre's disc stability parameter Q. The dashed line shows $Q = 1$ which separates disc stable ($Q > 1$) from disc unstable phase ($Q < 1$). The edge of the Hα profile at approximately $R(\mathrm{H}\alpha) = 2.6$ kpc, is shown with a dotted line.

given density profile in the ROTMOD's algorithm. This algorithm can accept for now only a constant value for the vertical scale height. Future studies and algorithm improvements are hence necessary to investigate this relationship in more detail.

5.3.5 Disk stability

Going a step further, we can address the gravitational stability of the gaseous disk of the SMC and its possible consequences for star formation. If a disk is sufficiently cool and dense, its thermal pressure and centripetal acceleration can not support itself against self-gravity and the disk will fragment, which can lead to the new star formation (Meurer, Staveley-Smith, & Killeen 1998). The gravitational stability of a gaseous disk is determined by the Q parameter (Toomre 1964):

$$Q = \frac{\sigma_{\mathrm{HI}} k}{3.36 G \Sigma_{\mathrm{HI}}} \tag{5.9}$$

with k being given by:

$$k = \left(R \frac{d\Omega^2}{dR} + 4\Omega^2 \right)^{1/2} \tag{5.10}$$

where $\Omega = V_{\mathrm{rot}}/R$ is the angular velocity. According to the Toomre's stability criterion, the disk is stable for $Q > 1$, while regions with $Q \lesssim 1$ are unstable and

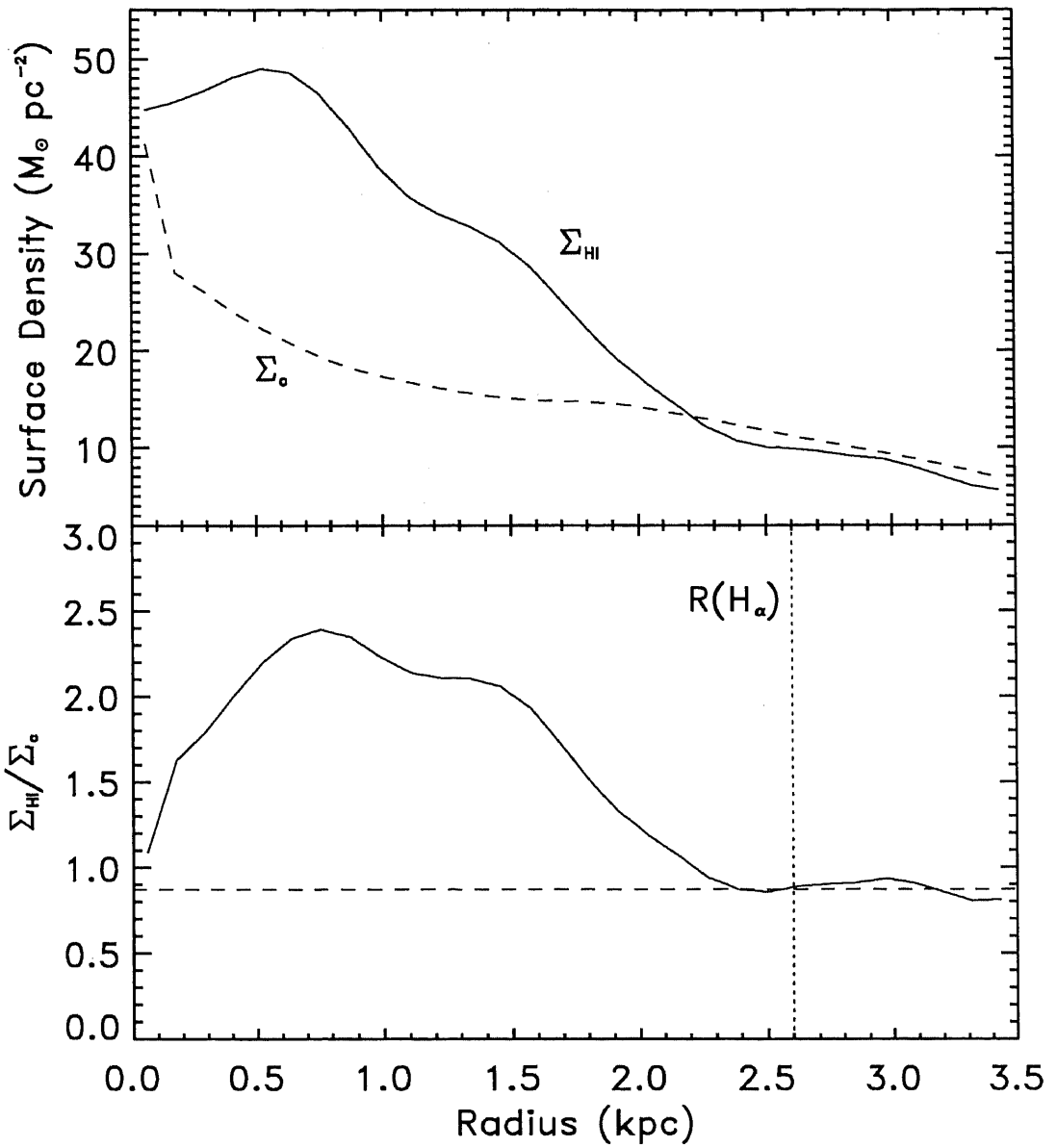

Figure 5.19 . Top panel: the radial distribution of the observed ($\Sigma_{\rm HI}$) and critical ($\Sigma_{\rm c}$) surface density of the gas in the SMC. Bottom panel: the radial distribution of the ratio of the observed to critical surface density ($\alpha = \Sigma_{\rm HI}/\Sigma_{\rm c}$). The dashed line shows $\alpha = 0.87$ and the dotted line represents the edge of the Hα profile at approximately $R({\rm H}\alpha) = 2.6$ kpc.

under possible fragmentation (Binney & Tremaine 1987). The estimated values of Q, as a function of radius, are shown in Fig. 5.18. For this purpose, the derived angular velocity was fitted with the second order polynomial function before taking its derivative. The plot shows that the most of the gaseous disk, for $R < 2.2$ kpc, is unstable and, most likely, under vigorous star formation. The unstable region appears to be quite extended, reaching almost the edge of the Hα profile, $R(\mathrm{H}_\alpha) \approx 2.6$ kpc, which delineates the parts of the gaseous disk under most recent star formation.

From Eq. 5.9, much higher velocity dispersions of 30 – 50 km s^{-1} are required, within $R < 2.2$ kpc, in order to stabilise the disk. An equivalent explanation is the surface density of the gas. From Eq. 5.9 we can determine the so called critical surface density, defined as the surface density for $Q = 1$. Both observed (Σ_{HI}) and critical (Σ_{c}) surface densities are shown in Fig. 5.19 (top panel). The curves are very different for the inner radii. It appears that a much slower and almost an exponential decrease of the gas surface density with the radius is required to obtain a stable gaseous disk in the SMC. The ratio of the observed to critical surface density ($\alpha = \Sigma_{\mathrm{HI}}/\Sigma_{\mathrm{c}}$) is shown in the same figure (bottom panel). For the unstable part of the disk, α varies between 1.0 and 2.5, while it has the constant value of $\alpha = 0.87 \pm 0.04$ for the stable part of the disk. An interesting relationship between the star formation threshold and the large-scale gravitational disk stability has been found by Kennicutt (1989). Their sample of normal galaxies have shown the constant value $\alpha = 0.67 \pm 0.17$ at the outer edge of the active star forming regions. This means that the most of the star formation, in these galaxies, is taking place for $\alpha > 0.67$, and hence for $Q < 1.5$, suggesting the empirical stability threshold for the star formation of $Q = 1.5$. The same effect appears to be present in the SMC. The stable part of the gaseous disk starts near the Hα cut-off radius at 2.6 kpc, having a constant value of α, which is in agreement with the empirical stability threshold found by Kennicutt (1989).

5.4 The 3-D structure of the SMC

The 3-D structure of the SMC has been a matter of great controversy in the past. Since early mapping of HI, complex HI profiles pointed out the existence of unusual motions of the gas (Hindman 1967). Hindman (1967) has also suggested a first model of the SMC, as a flattened disk with three supergiant shells in the main body.

From the analysis of the radial velocity distributions of HI, stars, HII regions and planetary nebulae, Mathewson & Ford (1984) and Mathewson, Ford & Visvanathan (1986, 1988) suggested the 'two separate entities' model for the SMC, whereby the SMC is, along most of its angular extent, broken into two velocity subsystems (the Small Magellanic Cloud Remnant, SMCR, and the Mini Magellanic Cloud, MMC). The SMCR and MMC are separated in velocity by ~ 40 km s^{-1}and have their own

nebular and stellar populations. The reason they gave for this great disruption of the SMC was its close encounter with the LMC some 2×10^8 yr ago. To constrain spatially the two velocity subsystems, Mathewson, Ford, & Visvanathan (1988) measured distances and radial velocities of 61 Cepheids. They found a distance scatter of $\sim$ 20 kpc suggesting a large depth for the SMC, and the distance gradient from the north-east to the south-west. Also, the 'clustering effect for Cepheids' was pointed out, whereby the Cepheids tend to cluster in groups of similar radial velocity and distance. The Population I Cepheids in Mathewson, Ford, & Visvanathan (1988) suggested that the heliocentric velocity increases with distance, which is in agreement with the theoretical tidal models of the interactions between the LMC and the SMC (Murai & Fujimoto 1980). The estimated depth of the SMC was supported by Hatzidimitriou & Hawkins (1989) from a study of the intermediate-age (halo) population.

A slight modification of the 'two separate entities' model was given by Torres & Carranza (1987), who found four, instead of two, different velocity components from the radial velocities of HI, supergiants, emission and planetary nebulae, and IS calcium. A similar result has been found by Martin, Maurice, & Lequeux (1989), who have identified the low and high velocity component with the SMCR and MMC, respectively. However, Martin, Maurice, & Lequeux (1989) concluded that most of the young stars lie within a depth of < 10 kpc, which suggests a much smaller depth for the SMC than $\sim$ 20 kpc seen by Mathewson, Ford, & Visvanathan (1988).

Caldwell & Coulson (1986) discussed the geometry of the SMC, also using Cepheids, and came up with the 'bar and three arms' model. Their general distribution of Cepheid distances suggested that the SMC consists of a 5-to-1 central bar seen edge-on, and an arm of material pulled from the centre of the SMC. Two sides of the bar are also labelled as the near arm, located at the north-east, and the far arm, located at the south-west, while the pulled material is seen in front of the far arm. A comparison with the HI data from Mathewson & Ford (1984) showed that the bifurcation in Cepheid distances at the south-west matches the bifurcation seen in HI. They also found that the distance increases from the north-east towards the south-west, but that velocity decreases with the distance, opposite to the previous model.

The new high resolution HI data provides an opportunity to address the complex question of the 3-D structure in the SMC again. Since HI spectral line data contain information about the radial velocity but not distance, to relate radial velocities of individual features with their physical distances, we use observations of Cepheids for which both the radial velocity and the distance have been determined. The only such sample of Cepheids, available in the literature, is the one from Mathewson, Ford, & Visvanathan (1988) of Cepheids along the major optical axis of the SMC. The Cepheid positions (accurate to 1.5 arcsec), the infrared magnitude corrected for reddening ($\langle I_v \rangle_0$), the distance (accurate to $\pm$ 3 kpc at the distance of the SMC) and the systematic heliocentric radial velocity (accurate to 15 km s^{-1}), were taken from

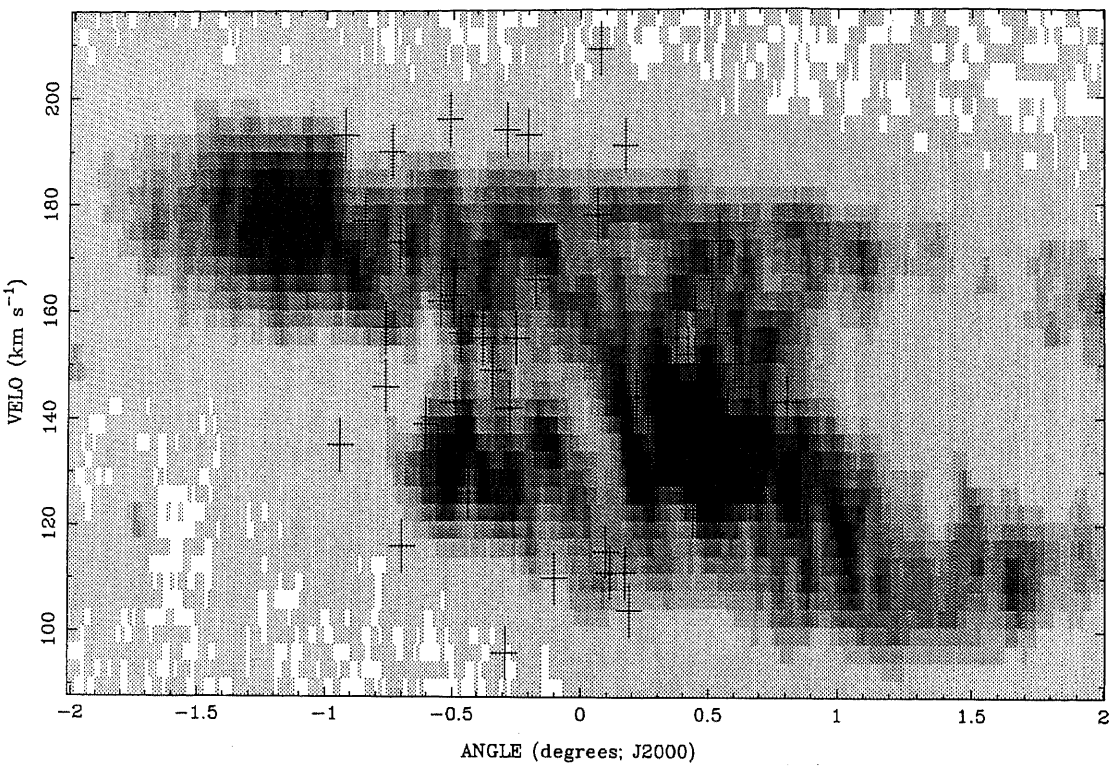

Figure 5.20 . A position-velocity cut through the HI data cube along the major optical axis of the SMC, centred at RA $00^h53^m5^s$, Dec $-72°45'58''$ (J2000) and having the position angle of $\sim 40°$. The grey-scale range is 0 to 100 K, with a linear transfer function. The positions and velocities of Cepheids, from Mathewson, Ford & Visvanathan (1988) are projected on the HI slice.

Mathewson, Ford, & Visvanathan (1988). We have measured the total HI column density towards each of the stars from the combined ATCA and Parkes data set.

5.4.1 Cepheids and HI

In Fig. 5.20, the positions of 61 Cepheids are projected on the position-velocity slice taken through the (combined ATCA and Parkes) high resolution HI data cube along the major optical axis (centred at RA $00^h53^m5^s$, Dec $-72°45'58''$ (J2000) and having the position angle of $\sim 40°$). The HI slice shows numerous small-scale shell-like features and two very large ones corresponding to the two largest supergiant shells found in the SMC, 304A and 37A (see Chapter 6). A comparison of the distribution of Cepheids with the distribution of HI shows that there is no obvious correlation of Cepheids with particular HI features, within the given accuracy. The Cepheids do not prefer the HI emission regions from HI holes. For example, there is a large concentration of stars in the region of strong HI around the angular offset of 0°–1°.

The region around angular offset of $-0.5°$, having an appearance of a honeycomb of HI shells, seems to be full of Cepheids. This region is also very close to the centre of the supergiant shell 304A. The minimal dynamical age of 304A is 1.4×10^7 yr, while ages of Cepheids are between 10^7 yr and $1\text{–}2\times10^8$ yr (Tsvetkov 1980; Mathewson, Ford, & Visvanathan 1986). It is hence possible that some of the Cepheids are associated with the shell, being either responsible for the shell explosion or being formed in the secondary star formation induced by shell expansion.

5.4.2 The depth of the SMC

In Fig. 5.21 the distance and the heliocentric velocity of Cepheids are plotted along the major optical axis (panels (a) and (b)), as well as against each other (panels (c) and (d)). The radial-velocity distribution on panel (b) shows a void of Cepheids around angular offset of $\pm0.2°$ at intermediate velocities. Although Mathewson, Ford, & Visvanathan (1988) claim that the sample is here almost complete for Cepheids having period longer than 4 days, there are fewer Cepheids detected in this region than in the surrounding ones. It is hard to photometrically detect Cepheids in the regions with a very high stellar density, such as in this region which is close to the optical centre of the SMC. Therefore, it is more likely that the sample is not complete here. The radial velocities of Cepheids in the north-east seem to be on average larger than for Cepehids in the south-west, weakly confirming the HI velocity gradient which would support the idea of the the circular rotation of the SMC.

Panel (a) (Fig. 5.21) shows that the distance distribution of Cepheids along the major optical axis extends over almost 30 kpc, if the distance errors are accurate. Mathewson, Ford, & Visvanathan (1988) interpreted this as a large line-of-sight depth through the SMC. However, the distance gradient from the north-east to the south-west (fitted line on panel (a)) is only 9 kpc, which is somewhat smaller. The north-east part of the SMC is closer to us than the south-west part. The average scatter in distance appears larger for the south-west than for the north-east, suggesting that the south-west part of the SMC has a larger line-of-sight depth. While the radial velocities of all Cepheids do not show any correlation with distance (panel (c)), the Cepheids only in the south-west part show a possible velocity gradient with the distance (fitted line on the panel (d)).

Welch et al. (1987) have pointed out that the determination of the Cepheid distances in Mathewson, Ford, & Visvanathan (1986) suffers from a few possible problems: an inconsistent correction to mean magnitude; the assumption of zero intrinsic width for the period-luminosity (P-L) relation ($\langle I_v\rangle_0 \propto -2.90\log P$); and sample inhomogeneity. This could result in much larger distances than found by Welch et al. (1987), who conclude that the SMC does not extend in depth beyond its tidal radius (4 – 9 kpc). Another source of error in the distance determination is from the

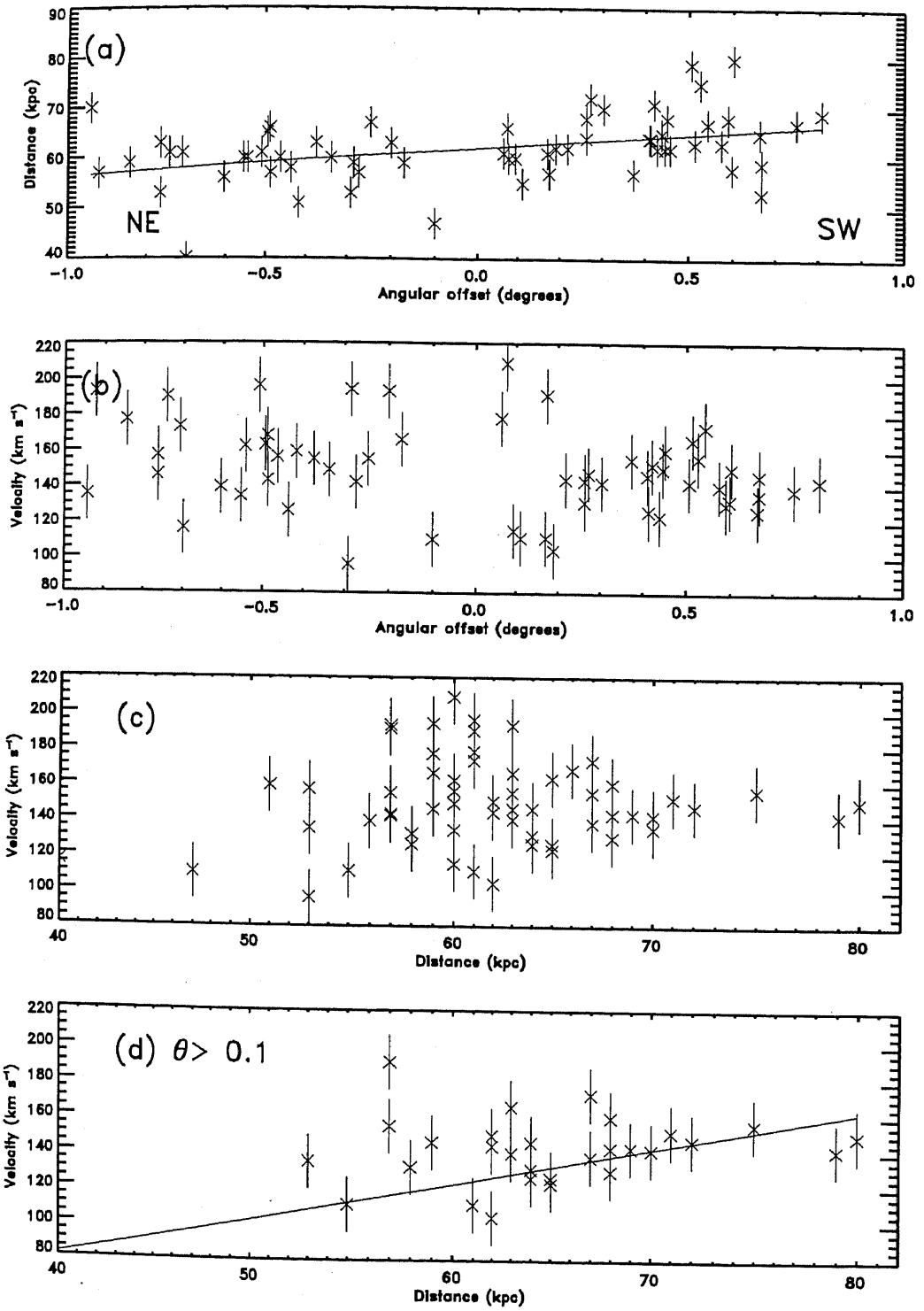

Figure 5.21 . The data from Mathewson, Ford & Visvanathan (1988) of 61 Cepheids in the SMC. (a) The Cepheid distances, having uncertainty of $\sim$ 3 kpc, along the major optical axis of the SMC, centred at RA $00^h53^m5^s$, Dec $-72°45'58''$ (J2000) and having position angle of $\sim$ 40°. The least-squares fit is overlaid. (b) The heliocentric radial velocity, having an uncertainty of 15 km s^{-1}, along the major optical axis. The least-square fit is overlaid. (c) The heliocentric velocity versus distance. (d) The heliocentric velocity versus distance for Cepheids in the south-west part of the SMC, with an angular offset larger than 0.1°.

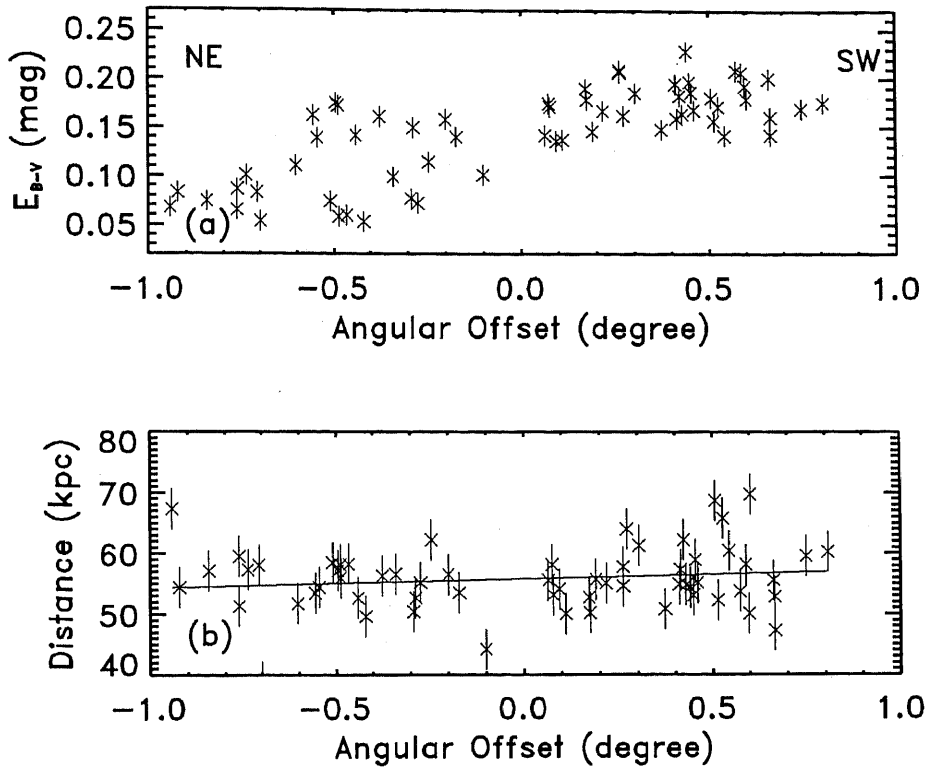

Figure 5.22 . (a) The extinction estimate towards each of the stars (uncertainty $\sim$ 0.01 mag) shows significant variation along the optical major axis. (b) Newly corrected Cepheids distances (uncertainty of $\sim$ 3.3 kpc, estimated assuming 0.06 mag for the intrinsic dispersion of the P-L relation). The least-squares fit is overlaid. The mean distance of the SMC appears to be (56 ± 5) kpc.

fact that Mathewson, Ford, & Visvanathan (1986) have assumed the same value for reddening, and hence for the interstellar absorption, for all Cepheids. Assuming a constant value of 8.2×10^{-5} for the dust-to-gas ratio in the SMC (see Chapter 8 for discussion), we derive the extinction (E_{B-V}) for each of the stars. The relationship $A_{I_V} = 1.94E_{B-V}$ (Schlegel, Finkbeiner, & Davis 1998) was then used to determine the interstellar absorption (A_{I_V}) and the period-magnitude relation ($M_{\langle I_V\rangle_0} = -2.06 - 2.90 \log P$, from Mathewson, Ford, & Visvanathan 1986) to determine Cepheid distances. Fig. 5.22 shows the Cepheid extinction and the newly determined distance distribution.

The internal extinction increases significantly along the major optical axis, from 0.05 mag at the north-east to 0.2 mag at the south-west. This results in the interstellar absorption ranging from 0.1 to 0.4 mag, which is much larger than the value of 0.06 mag assumed previously (Caldwell & Coulson 1986; Mathewson, Ford, & Visvanathan 1988). The mean value of the Cepheid extinction measured by Caldwell & Coulson (1985), $E_{B-V} = (0.054 \pm 0.021)$ mag, although quite uncertain, appears

to be ~ 2.6 times smaller than the mean value estimated here of (0.14 ± 0.05) mag. Our vales for extinction are most likely overestimated in some cases, since they are based on the measurements of the total amount of dust and gas in the direction of the star. However, our mean extinction agrees well with the mean value of $E_{B-V} = (0.125 \pm 0.009)$ mag estimated by Sasselov et al. (1997) from the EROS photometry of a large sample of Cepheids in the SMC. Sasselov et al. (1997) also confirmed observationally that the intrinsic width of the P-L relation is larger, for 0.14 mag, in the SMC than in the LMC due to the metallicity effect.

The important thing to notice, is that our measurements show a definite differential extinction across the SMC, being much higher at the south-west relative to the north-east. This results in the Cepheid distances ranging over a narrower range with no significant distance gradient (~ 3 kpc), but still slightly larger depth at the south-west. The lower mean distance of (56 ± 5) kpc is in agreement with previous values (Westerlund 1997). No correlation of the newly determined distances with velocity is seen. Hence, the correction for the interstellar absorption can significantly influence the distance determination and easily bring the depth of the SMC within its tidal radius ($4 - 9$ kpc).

5.4.3 Comparison with other models

The HI data and new Cepheid distances are compared here with two other models for the geometry of the SMC.

5.4.3.1 The 'SMCR & MMC' model (Mathewson et al.)

As a result of the bimodal analysis (Section 5.2.2), the SMC's velocity field could be interpreted as a composition of two different velocity entities, having parallel velocity fields with an offset of ~ 40 km s^{-1}. The mean velocities of our 'L' and 'H' components, as well as their mean velocity separation, agree surprisingly well with the 'SMCR & MMC' model. We also found that the 'L' component has almost constant velocity dispersion, while the 'H' component shows a gradient in velocity dispersion from the south-west to the north-east, suggesting a possible gradient in the depth of the 'H' component. However, this does not agree with the distance distribution found in Mathewson, Ford, & Visvanathan (1986) (their Fig. 7), according to which the SMCR should also show almost constant dispersion, but the velocity dispersion of the MMC should increase in the opposite direction, from the north-east to the south-west.

The Cepheid distance determination by Mathewson, Ford, & Visvanathan (1986) and Mathewson, Ford, & Visvanathan (1988) has already been discussed and appears to be insufficient. The two velocity-entities model seems to be inconsistent with the new distance determination of Cepheids. Two separate velocity components could

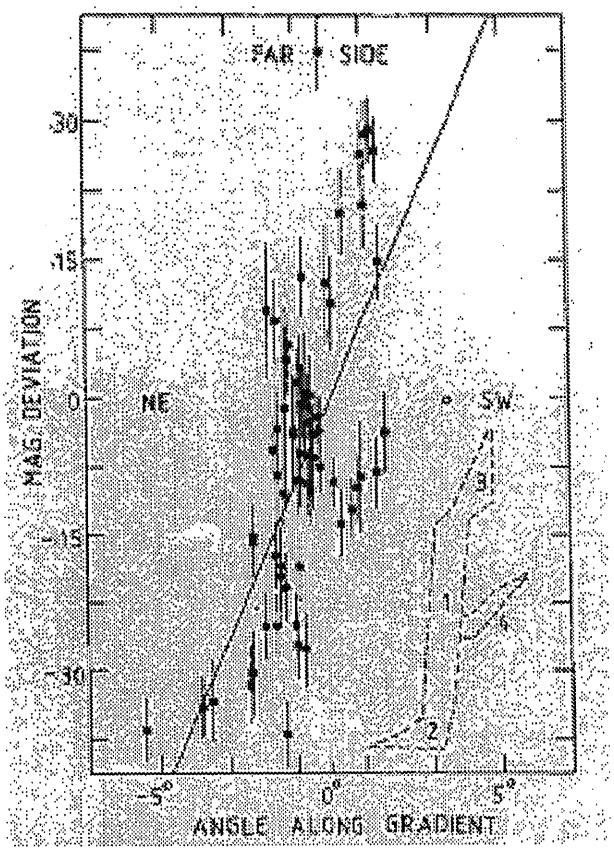

Figure 5.23 . Fig. 7 from Caldwell & Coulson (1986). To show the effect of the line-of-sight structure, the period-luminosity-colour (PLC) magnitude residuals are plotted versus angle along the direction with position angle of 58°. The dashed outline sketches the 'bar and three arms' model: (1) the main bar; (2) the near arm; (3) the far arm; and (4) the material extending from the centre.

be a consequence of the statistical data handling of complex HI profiles, with no substantial physical basis.

5.4.3.2 The 'bar and three arms' model (Caldwell & Coulson 1986)

Care must be taken when comparing Fig. 7 from Caldwell & Coulson (1986) (see Fig. 5.23) with Fig. 5.22 since different areas are considered and also Cepheid positions were projected along different directions. Caldwell & Coulson (1986) analysed an area twice as large and are therefore more sensitive to tidal effects in the Magellanic Bridge and Stream. Only the region corresponding to angles between $-1°$ and $1°$ (Fig. 5.23) is of relevance here. This region shows a clear bifurcation in the magnitude deviation, and hence in distances, at the south-west (Caldwell & Coulson 1986), matching the bifurcation seen in HI too.

The south-west bifurcation in HI is interpreted in this thesis as due to the presence of the expanding supergiant shell 37A. See Fig. 5.20 at around offset angle 1.5° (also Section 6.2.1). Hence, some of the Cepheids seen by Caldwell & Coulson (1986) could be explained as being formed in the secondary star formation (the minimal dynamical age of 37A is 1.7×10^7 yr). The Cepheid distances determined by Caldwell & Coulson (1986) and spanning over $\sim$ 20 kpc, appear to be inconsistent with the results by Welch et al. (1987), who found the same dispersion in the period-luminosity-colour (PLC) relation, but a depth of less than 10 kpc. The difference between these two analyses is in the assumption of the intrinsic dispersion of the PLC relation. While Caldwell & Coulson (1986) assumed that all dispersion comes from the geometry of the SMC, Welch et al. (1987) argued that some intrinsic uncertainty has to be allowed in the PLC relation. Also, it was shown (Section 5.4.2) that the use of a constant value for the interstellar absorption in the SMC, as in Caldwell & Coulson (1986), is not appropriate and could significantly change the distance gradient. This could then significantly change both the arm of the material pulled from the centre and the sausage-like 5-to-1 bar.

5.4.3.3 The theoretical models by Gardiner et al. (1994) and Gardiner & Noguchi (1996)

Gardiner, Sawa, & Fujimoto (1994) and Gardiner & Noguchi (1996) have performed N-body simulations of the gravitational interactions in the Galaxy-LMC-SMC system in order to reproduce the observed features in the Magellanic System. While the LMC and the Galaxy have been represented with fixed potentials, the SMC has been represented by a two-component particle system (Gardiner & Noguchi 1996) consisting of a nearly spherical halo and a rotationally supported disk. The numerical simulations have been further used to evolve the SMC model under the influence of external forces. The best model resulted in the disk being quickly transformed into the highly inclined but not much elongated bar (with the inclination of 45° and a length of 5 kpc) and having the position angle of 50°. The global features reproduced in the Magellanic System are in good agreement with HI observations of Mathewson & Ford (1984) and Putman et al. (1998). Looking at the 3-D structure of the SMC only, the best model of the evolved disk and halo component (Fig. 10 and Fig. 11 in Gardiner & Noguchi 1996, shown together here as Fig. 5.24) shows: (i) a strong vertical and slightly tilted feature in position-velocity space, at $\sim$ RA $00^h\ 50^m$ (B1950), with a heliocentric velocity gradient from 70 to 220 km s^{-1}; (ii) a tidal bridge towards the Eastern Wing region, starting at $V_{\rm hel} \approx 170$ km s^{-1} eastward from the main feature; and (iii) a tidal tail, starting at $V_{\rm hel} \approx 120$ km s^{-1} and going first westwards from the main feature and then turning to the east, passing the main feature at $V_{\rm hel} > 200$ km s^{-1} and reaching heliocentric velocities up to 300 km s^{-1}. The model also predicts that distances of the tidal bridge and tail increase with heliocentric velocity (see Fig. 5.24).

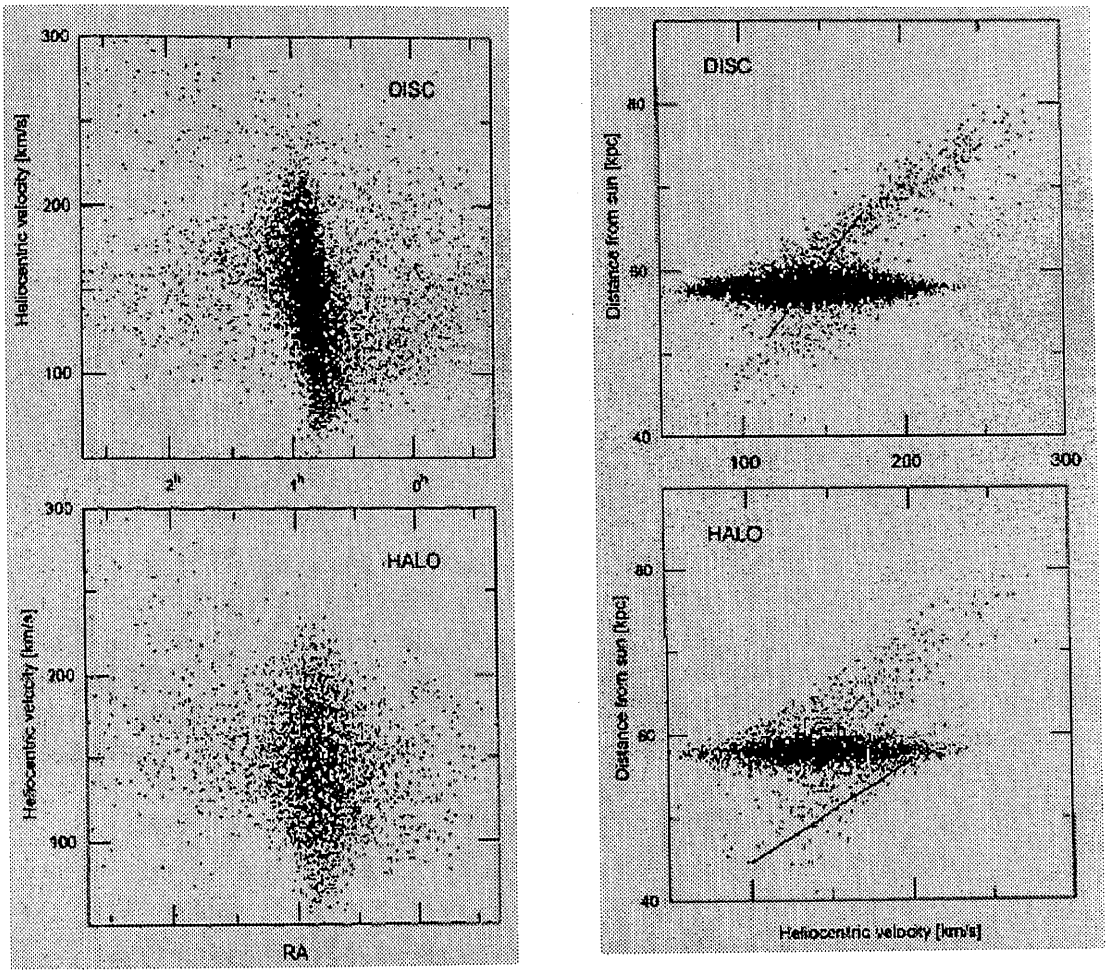

Figure 5.24 . Fig. 10 and Fig. 11 of Gardiner & Noguchi (1996). Particles within the range $-78° <$ Dec $< -68°$ (B1950) are plotted. The region corresponding to HI data studied here is $00^h\ 30^m <$ RA $< 01^h\ 30^m$. This figure is compared with Fig. 5.25 which is in the J2000 reference frame. However, the difference in the reference frames is not significant, being approximately equal to the Parkes FWHM.

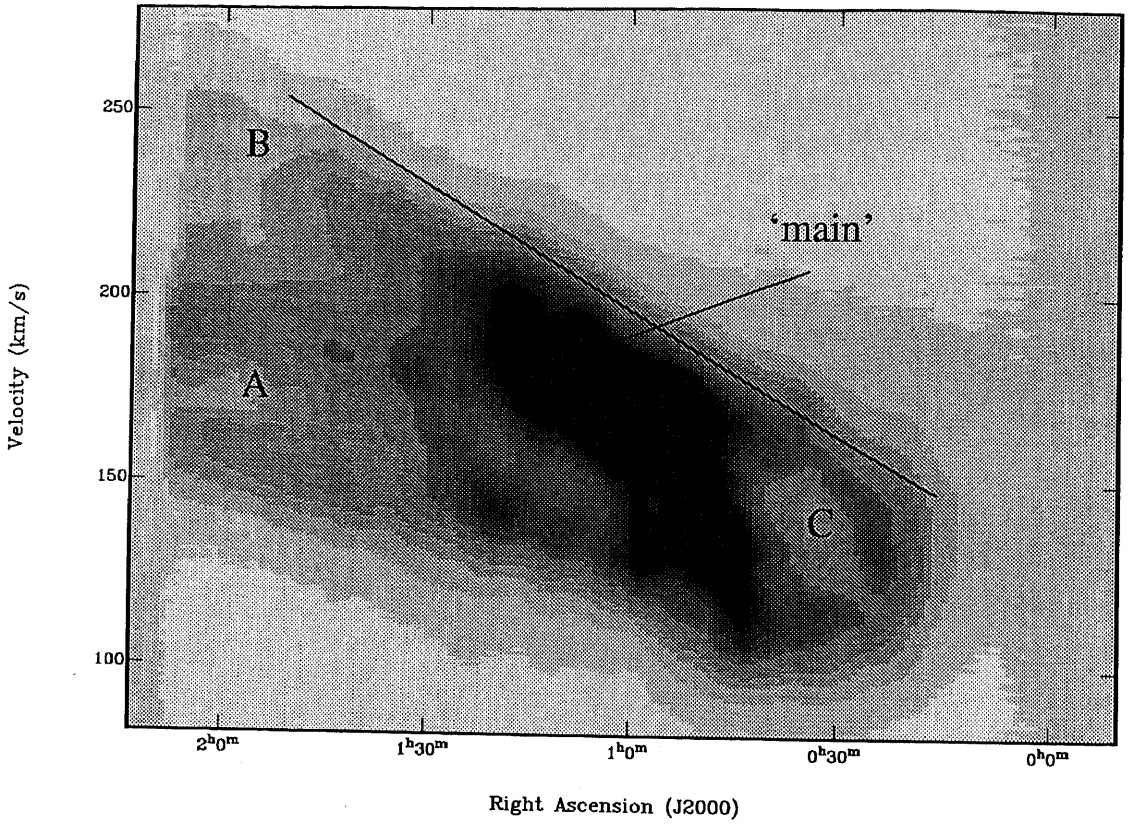

Figure 5.25 . The RA-velocity slice averaged over $-74°<$ Dec $< -68°$ (J2000) to be consistent with Fig. 10 from Gardiner & Noguchi (1996) (see Fig. 5.24). This extended data was obtained with the Parkes narrow-band Multibeam system during a commissioning run. The main emission feature is labelled as 'main', two tail-like features are labelled with 'A' and 'B', while the loop-like feature at the south-west is labelled with 'C' (see text).

The inclination and the position angle of the SMC bar derived for the best model ($i = 45°$, PA $= 50°$) are similar to the observational results obtained in Section 5.3 from the SMC velocity field ($i = 40°$, PA $= 40°$). The predicted depth of the SMC bar ($\sim$ 5 kpc) is in agreement with Cepheid distances in Welch et al. (1987) and Cepheid distances estimated in Section 5.4.2. The area enclosed in our observations contains only the central region of the SMC. To compare the internal HI kinematics with the model predictions, we have used the recent (Aug 1998) Parkes narrow-band Multibeam commissioning observations of the SMC, which enclose a slightly larger area. The RA-velocity slice of the data cube centred at the centre of the SMC and averaged over $-74°<$ Dec $< -68°$ (J2000), is shown in Fig. 5.25. The slice in Fig. 5.25 is hence comparable with Fig. 5.24, taken from Gardiner & Noguchi (1996), for $00^h\ 30^m <$ RA $< 02^h\ 00^m$. Within the region enclosed by these observations, the model predicts the central feature to be seen, and also parts of the tidal bridge and

tail.

The strong emission feature (labelled as 'main') is seen in Fig. 5.25, stretching over the same RA range as suggested for model's central feature, but having slightly less steep velocity gradient, from $\sim$ 100 to 200 km s^{-1}. Comparing with the model, the whole extension of this feature could be identified hence with (i). At the north-east, centred at RA 01^h 55^m (J2000) and $V_{hel} \approx 170$ km s^{-1}, a tail like feature 'A' is seen, stretching in velocity between 150 and 200 km s^{-1}. This coincides with the beginning of Gardiner's tidal bridge, streaming further into the Magellanic Bridge. For higher velocities, 200 – 250 km s^{-1}, a tail-like feature 'B' can be recognised, going eastwards from the 'main' feature, and resembling very much the Gardiner's tidal tail at these velocities. The 'B' and the 'main' features form a very sharp edge from the north-east to the south-west (shown with the solid line in Fig. 5.25). The south-west region is still a puzzle. We do not have a large enough image here to distinguish the origin of the loop-like feature 'C'. It is not clear whether this feature is connected with the feature 'B', similar to Gardiner's tidal tail, or it is an expanding shell in the outskirts of the 'main' feature.

Hence, a comparison of: (1) the observed rotational parameters (determined in Section 5.3); (2) the newly determined Cepheid distances (determined in Section 5.4.2); and (3) the internal HI kinematics (this Section), with the predictions by different models for the 3-D structure in the SMC, was presented here. Both HI and Cepheid data appear to support mostly the theoretical model by Gardiner, Sawa, & Fujimoto (1994) and Gardiner & Noguchi (1996). The central region of the SMC could be identified as a rotationally supported bar, with the line-of-sight depth which does not exceed the tidal radius (4 – 9 kpc), and having a significant support from random motions. These motions mainly originate in the interplay between the star formation and the surrounding ISM (see Chapter 6). They are also predominantly responsible for the observed HI line splitting within the central region of the SMC, while the outskirts of the SMC's bar show some evidence for particular tidal features predicted by Gardiner, Sawa, & Fujimoto (1994) and Gardiner & Noguchi (1996). However, further studies, including a larger area around the SMC and the distance determination of more objects within the SMC, are necessary for better understanding of the 3-D structure.

5.5 Summary

- The first part of the chapter investigates the velocity profiles in the SMC. The unimodal velocity field suggests circular rotation of the main gaseous body. The bimodal analysis shows that HI profiles could be decomposed into two different velocity structures, having parallel velocity fields with an offset of $\sim$ 40 km s^{-1}. The correction for the proper motion appears to be significant for the velocity field, resulting in a more regular 'spider' pattern.

- This has led to the determination of the rotation curve and the total mass of the SMC. The best rotation curve has been obtained for $i = 40°$, PA $= 40°$and $V_{sys} = 24$ km s^{-1}. It has a rapid rise up to $R = 1.0$ kpc, and less steep but steady rise further on up to the turnover radius of ≈ 2.5 kpc. The asymmetric drift correction of the observed rotation curve due to the pressure support seems to be significant. The corrected rotation curve is more regular and has rotation velocity of ~ 60 km s^{-1} at the turnover radius of 2.5 kpc. It can be modelled with a composition of rotation curves arising from gaseous and stellar potentials, for $M_*/L = 0.83$. No additional component, such as a dark matter halo, is needed. The vertical scale height varies significantly with radius. The gaseous disk of the SMC is unstable up to $R(\mathrm{H}\alpha) = 2.6$ kpc and stable further on, having a stability threshold $\alpha = 0.87 \pm 0.04$. This supports the relationship between the star formation threshold and the gravitational disk stability found by Kennicutt (1989).
- The 3-D structure of the SMC has been re-examined in the last part of this chapter, using the combined ATCA and Parkes data and the Cepheid data from Mathewson, Ford, & Visvanathan (1988). No obvious coincidence between HI and Cepheids has been found. The Cepheid distances were re-examined and it was shown that the correction for the interstellar absorption can significantly influence the distance gradient. The newly determined distances imply much smaller depth of the SMC. The HI and Cepheid data could be interpreted as a rotationally supported bar within the central part of the SMC, theoretically predicted by Gardiner & Noguchi (1996). Some possible tidal features, suggested by Gardiner & Noguchi (1996), are also seen at the outskirts of the bar when a slightly larger area is used. Within the central part of the SMC, the observed HI line splitting may originate in the interplay between the star formation and the surrounding gas, rather than in spatially separate components or in different arm-like features sticking out of a very elongated bar.

Chapter 6

The largest HI shells in the SMC

6.1 Introduction

HI surveys of the Galaxy (Heiles 1979; Heiles 1984), M31 (Brinks & Bajaja 1986), M33 (Deul & den Hartog 1990), Holmberg II (Puche, Westpfahl, & Brinks 1992), the LMC (Kim et al. 1997) and other galaxies, show the presence of many giant and supergiant shells ($r \gtrsim 300$ pc), as well as associated features such as filaments, incomplete shells, 'worms' and chimneys. This suggests that such features are probably a general phenomenon in gas-rich galaxies and fill appreciable fractions of the ISM. In the SMC, 495 giant shells and 6 supergiant shells have already been catalogued (Staveley-Smith et al. 1997).

Such features are explained by Bruhweiler et al. (1980) and Tomisaka, Habe, & Ikeuchi (1981) as the evolution of an OB association in which an HI cavity is created by the strong stellar winds of massive stars. Elmegreen & Chiang (1982) show that, after a short time ($\gtrsim 3$ Myr), the most massive stars become supernovae (SN) and the corresponding energy input can lead to runaway expansion and the formation of a supergiant shell. As the dynamic age of the largest observed supergiant shells is much greater than the time it takes for massive stars to evolve, big associations with $\sim 10^2$–10^3 massive stars (McCray & Kafatos 1987) or regions of continuous formation and/or multiple formation of massive stars (Bomans et al. 1995) are needed to provide the shell with sufficient energy. One possibility for the latter is that star formation at one place can initiate star formation at another place, either by a stochastic process where the propagation is given with a certain probability (Gerola & Seiden 1978), or by a deterministic process where the propagation results from a chain of events (Palous 1996). If the expanding shell is located in a plane-stratified medium, it can expand upward forming a quasi-cylindrical or cone-like structure perpendicular to the disk (Tomisaka & Ikeuchi 1987; MacLow & McCray 1988). These 'HI chimneys' may be the source of the 'worm-like' features noted in our own Galaxy by Heiles (1984).

The hot gas retained inside the interstellar shells of young stars and supernovae is believed to be the sole source of the 'third-phase' of the ISM in galaxies (McKee & Ostriker 1977). Measuring the filling factor of the HI shells (the porosity parameter) therefore sets an important lower limit on the volume fraction of hot gas and gives an insight into ISM physics.

Another possible origin of supergiant shells in our Galaxy is the collision of the infalling gas with gas in the Galactic Plane (Tenorio-Tagle 1981; Kulkarni & Heiles 1988). Recent studies of the gamma-ray bursts (GRBs) suggest that the GRBs could also leave kiloparsec-scale remnants in the ISM, being another alternative creator of supergiant shells (Efremov, Elmegreen, & Hodge 1998; Loeb & Perna 1998). One of the possible origins of the GRBs is the 'hypernovae' collapse of spinning massive stars (Paczyński 1998), which could release a huge amount of kinetic energy ($> 10^{52}$ ergs) into the surrounding medium. At the beginning, the GRB blast wave expands like a multiple supernovae remnant, until it reaches the pressure-driven snowplow phase (Efremov, Elmegreen, & Hodge 1998). Later on, GRB and supernovae shell are governed by different mechanisms: a SN shell by the continuous energy input, a GRB shell by the momentum conservation after shell cooling. Some statistical studies of shell properties may permit one to recognise and distinguish these different processes involved in shaping the ISM.

Three supergiant shells in the SMC were noted by Hindman (1967). Meaburn (1980) later added another supergiant shell found on an Hα plate. Staveley-Smith et al. (1997) lists a further six supergiant shells found using the ATCA data alone (together with 495 giant shells). However, because of missing low spatial-frequency information, the sensitivity to the largest shells was very low. In this chapter, the evidence for the very largest shells in the SMC is re-examined and some of their observed and derived properties are discussed. Another seven new shell candidates are listed with some of their properties. The volume fraction occupied by all shells in the SMC is discussed in relation to different models of the ISM. Finally, the shell radius and expansion velocity differential distribution functions for the SMC, Holmberg II, M31, M33 and the LMC are considered and compared with predictions by the standard model of the OB superbubble evolution (Weaver et al. 1977; McCray & Kafatos 1987; Oey & Clarke 1997).

6.2 Properties of new supershells

6.2.1 The three largest supergiant shells

Inspection of the complete SMC data cube revealed three very large (radii $\gtrsim$ 600 pc) HI structures, each with the properties of an expanding supergiant shell (SGS). Each feature was visible in several successive position-velocity images as a partly complete

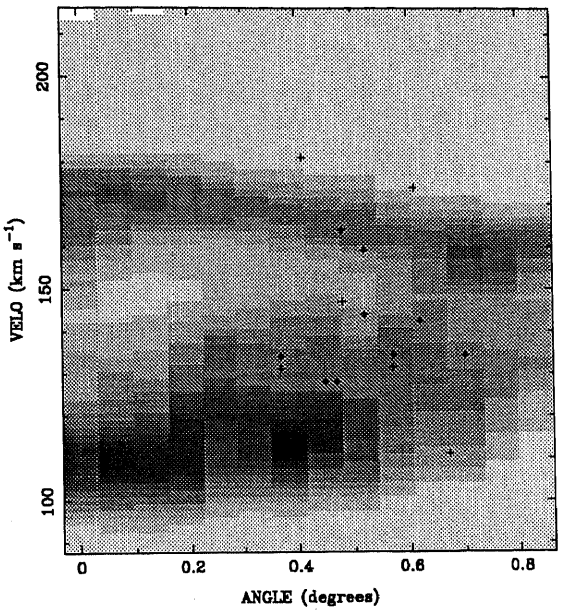

Figure 6.1 . Radius–velocity plot for SGS 37A. For each velocity, the average radius of the emission from the centre of the shell is computed and plotted versus heliocentric velocity. The grey-scale intensity range is −3 to 69 K. Positions of some HII regions are overlaid (from Torres & Carranza 1987 and Smith & Weedman 1973).

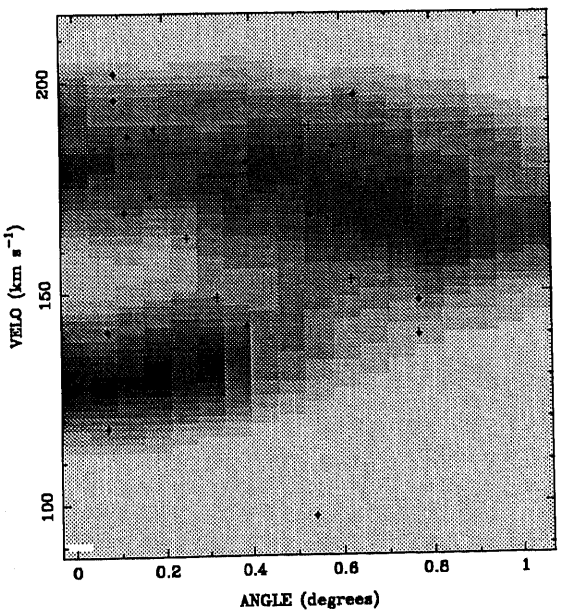

Figure 6.2 . Radius–velocity diagram for SGS 304A. The grey-scale intensity range is −2 to 76 K. Positions of some HII regions are overlaid (from Torres & Carranza 1987 and Smith & Weedman 1973).

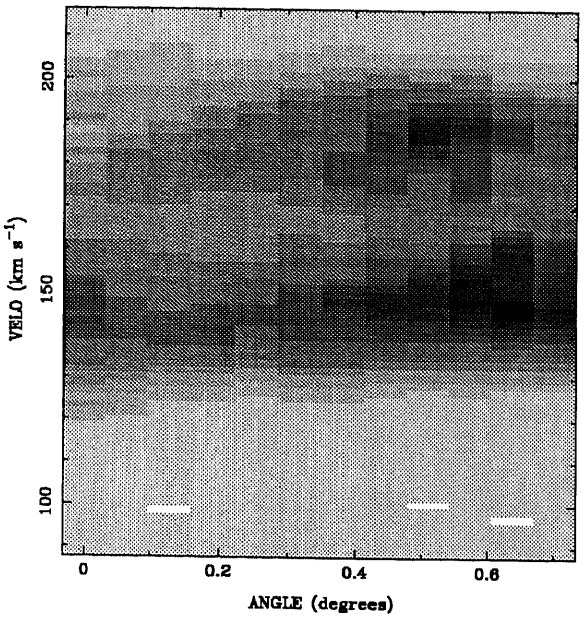

Figure 6.3 . Radius–velocity diagram for SGS 494A. The grey-scale intensity range is −2 to 50 K.

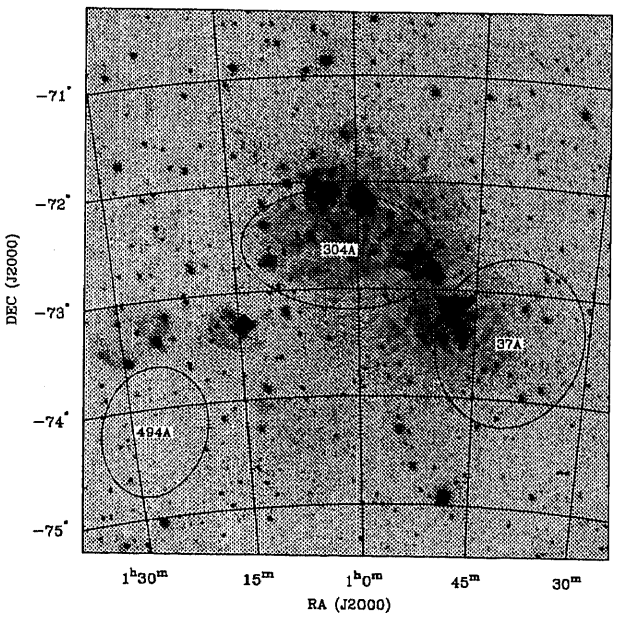

Figure 6.4 . Positions of supergiant shells in the SMC superimposed on the Hα image from Kennicutt et al. (1995). A J2000 coordinate grid is overlaid. The position of each shell is given with an ellipse having shell's major and minor semi-axis and position angle.

ellipse with a common centre (see Fig. 4.2 and Fig. 4.3). All three supergiant shells may consist of smaller interlocked or superimposed shells. Their rims often contain smaller shells, implying propagating star formation or breakouts from the low density regions.

The expansion of the SGSs is shown in the radius-velocity plots, Fig. 6.1 – 6.3. The azimuthally averaged spectra are plotted as a function of radius from the centre of the shell. At small radii, the line of sight passes near the shell centre, and the highest blueshifts and redshifts are seen. At larger radii, the radial velocities gradually approach the system velocity until the radius equals the maximum shell radius. For a thin spherical shell seen in projection, the observed velocity is given by:

$$V = V_{\rm hel} \pm v_{\rm s}\sqrt{1-\left(\frac{\theta}{\theta_o}\right)^2} \qquad (6.1)$$

where V is the observed velocity, θ is the projected radius, $V_{\rm hel}$ is the central shell velocity, θ_o is the shell radius, and $v_{\rm s}$ is the expansion velocity.

The positions of some known HII regions (from Torres & Carranza 1987 and Smith & Weedman 1973) are overlaid on the first two plots. The HII regions are more scattered in velocity than the HI, but nevertheless appear to avoid the shell interior. This suggests secondary star–formation.

Table 6.1 . Observed properties of the three supergiant shells with $r > 600$ pc in the SMC.

Supergiant Shell	RA (J2000)	Dec (J2000)	Heliocentric Velocity $V_{\rm hel}$ (km s^{-1})	Expansion Velocity $v_{\rm s}$ (km s^{-1})	Semi Axis Major (pc)	Semi Axis Minor (pc)	Position Angle ψ (°)	Surface Density σ ($M_\odot$ pc^{-2})
37A	00:40:26	-73:28:06	141	28	840	750	160	8.5
304A	01:02:16	-72:38:12	154	27	910	470	80	21.1
494A	01:27:18	-74:12:24	159	28	650	540	150	2.6

In Table 6.1 the observed properties of these SGSs: identification, position (RA and Dec), central heliocentric velocity ($V_{\rm hel}$), expansion velocity (half the velocity separation of the peaks – $v_{\rm s}$), semi-major and semi-minor axes, position angle (ψ), and surface density (σ), are presented. All three SGSs were identified in both RA-velocity and Dec-velocity maps and the given position is an average of both measured positions. The major axis was measured in the plane containing the largest shell dimension. The surface density is the sum of the mean surface densities of both hemispheres measured using position–velocity maps. The final value is corrected for foreground and background gas, using the surface density measured near the central heliocentric velocity of each SGS.

The expansion velocities for all shells are similar, ~ 28 km s^{-1}. The semi-major axes

range from 650 to 910 pc, and the surface densities (through both hemispheres) range from 2.6 $M_\odot$ pc^{-2} for 494A to 21.1 $M_\odot$ pc^{-2} for 304A. SGS 304A appears to have the most non-circular shape in projection (see Fig. 5.15).

Table 6.2 . Derived properties of the three supergiant shells with $r > 600$ pc in the SMC.

Supergiant Shell	Dynamical Age T (10^7 yr)	HI Mass m_{HI} ($M_\odot$)	Ambient Density n_0 (atoms cm^{-3})	Energy Required Φ (10^{53} erg)	SNs Required	Volume Factor f_v	Mass Fraction f_m
37A	1.7	3.3 $\times 10^7$	0.6	13.0	1$\times$ 10^3	0.06	0.09
304A	1.4	5.7 $\times 10^7$	1.9	21.5	2$\times$ 10^3	0.04	0.15
494A	1.2	5.6 $\times 10^6$	0.3	2.27	2$\times$ 10^2	0.03	0.02

The derived physical properties for each shell are given in Table 6.2: dynamical age (T), mass of the swept-up HI (m_{HI}), average ambient density (n_0), energy input required (Φ), number of input supernovae required, volume fraction (f_v) and HI mass fraction (f_m). The total mass of the swept-up hydrogen was calculated from $m_{HI} = 2\pi r^2 \sigma$, where r is the geometric average of semi-major and semi-minor axes and σ is the surface density. Following the discussion by McCray & Kafatos (1987) on the evolution of a supergiant shell caused by an OB association, the main growth of a supergiant shell comes from combined effects of supernovae explosions. In the case of a large OB association, the rate of supernova explosion remains constant and the luminosity of a supergiant shell can be calculated from

$$\Phi = 1.5 \times 10^5 \left(\frac{r}{100\mathrm{pc}}\right)^5 \left(\frac{T}{10^6\mathrm{yr}}\right)^{-3} \left(\frac{n_0}{1\mathrm{cm}^{-3}}\right) L_\odot \qquad (6.2)$$

(this equation is derived in Staveley-Smith et al. 1997 from equation 21 in Weaver et al. 1977). The dynamical age is obtained from $T = (3/5)(r/v_s)$. Assuming an average kinetic energy input per supernova of $\sim 10^{51}$ erg (McCray & Kafatos 1987), we calculate the number of supernovae required to produce these SGSs. The volume factor as the fraction of the SMC volume occupied by the shells is determined assuming 2 kpc for the radius of the SMC. The last column in Table 6.2 shows the fraction of the total SMC mass corresponding to each SGS.

All SGSs have significant expansion velocities compared to the SMC escape velocity of ≈ 50 km s^{-1}. This implies that a breakout from the main gaseous body of the SMC is possible.

6.2.1.1 Comparison with previous work

Two of the SGSs listed in Table 6.1 (37A and 494A) correspond to objects already catalogued in Staveley-Smith et al. (1997) (SMC HI-10 and 491, respectively).

Because of the large size of these shells, the current data supersede the previous data. The change in measured position resulted in the change of the shell numbers. Thus SMC HI-10 and 491 no longer exist. The other SGS (304A) was not noted in Staveley-Smith et al. (1997) because of its large size.

The spatial distribution of 495 giant shells in the SMC catalogued in Staveley-Smith et al. (1997) shows that the two oldest shells are located in the south-west of the SMC. It is interesting to note that the oldest SGS, 37A, is also located in the south-west.

All three SGSs appear to be related to Hindman's (1967) shells. The centre of SGS 37A is displaced from the centre of Hindman's second shell, almost 43 arcmin north, but the average radius is almost the same: 45.4 arcmin compared with Hindman's 45 arcmin. The central velocities and expansion velocities are slightly different: 141 km s^{-1} versus 129 km s^{-1} and 27.8 km s^{-1} versus 21 km s^{-1}, respectively. We measure the mass of swept-up HI to be 3.3 $\times 10^7$ $M_\odot$, while Hindman measured 1.0 $\times 10^7$ $M_\odot$.

The largest supergiant shell, 304A, appears also to correspond with Hindman's largest shell. The positions match remarkably well (within 7 arcmin). Central heliocentric velocities and expansion velocities are also very close: 154.5 km s^{-1} versus 160 km s^{-1} and 27.0 km s^{-1} versus 23 km s^{-1}, respectively. The HI mass is $\sim 6 \times 10^7$ $M_\odot$, while Hindman measured 2×10^7 $M_\odot$.

SGS 494A is $\sim$ 26 arcmin south from Hindman's third shell but with about the same average radius: 34 arcmin versus Hindman's 30 arcmin. Its central heliocentric velocity is 159.4 km s^{-1} versus Hindman's 160 km s^{-1} and expansion velocity is 28.2 km s^{-1} versus Hindman's 19 km s^{-1}. It is interlocked with SMC HI-491 and that could have caused some confusion in identifying it in previous observations. We measure 6×10^6 $M_\odot$ for the HI mass, while Hindman measures 3×10^6 $M_\odot$.

6.2.2 Other new shell candidates

Table 6.3 . List of positions, radii, heliocentric velocities, expansion velocities, ages and required wind luminosities for seven new supegiant shells with $r > 200$ pc.

Supergiant Shell	RA (J2000)	Dec (J2000)	Shell Radius		Heliocentric Velocity	Expansion Velocity	Age	Wind Luminosity
			r		V_{hel}	v_s	T	$\log(L_s/n_0)$
			(')	(pc)	(km s^{-1})	(km s^{-1})	(10^6 yr)	($L_\odot$ cm^3)
34A	00:40:06	-71:28:16	20	342	141	21	9.5	4.9
84A	00:44:23	-72:26:18	18	313	148	20	9.2	4.8
182A	00:52:34	-72:26:55	19	337	151	18	11.0	4.7
198A	00:53:58	-73:00:59	12	205	150	34	3.5	5.1
389A	01:10:50	-73:35:30	18	315	186	24	7.7	5.0
394A	01:11:59	-72:22:28	18	321	191	16	11.8	4.5
411A	01:14:32	-72:54:40	16	281	163	24	6.9	4.9

The new data cube also reveals seven new supergiant shell candidates, with radii > 200 pc. These features have been identified in the previous manner, by inspecting position-velocity images. Some of observed and derived properties of the new shell candidates are shown in Table 6.3.

6.3 Supershells and the ISM

SGSs 37A and 494A appear to be reasonably uniform ellipses in position-velocity space, showing both hemispheres and with no apparent breakouts. Applying the theory of the supershell evolution (McCray & Kafatos 1987), they are most likely driven by $\sim 10^3$ and 10^2 supernovae (Table 2), respectively. However, SGS 304A is more complex, and much of the shell structure in the north is missing. This suggests that, if interpreted as an expanding SGS, the interior hot gas has vented out. The required energy (2.1×10^{54} erg), and therefore number of SNe ($\sim 2 \times 10^3$), is very large.

Positions of all three SGSs in the SMC are superimposed on an Hα image from Kennicutt et al. (1995) in Fig. 6.4. Two SGSs, 37A and 494A, have Hα emission on their rims, suggesting that their expansion stimulates new star formation. The other, SGS 304A, seems to be associated with the extended Hα emission in the north-east of the bar and has the bright HII regions, N66 and N36 on the northern perimeter, where the HI shell has a gap. All three SGSs appear to have reached an age ($> 10^7$ yr) when they do not produce enough ionising radiation to make visible any inner HII rims (McCray & Kafatos 1987). The HI and Hα filaments (see Chapter 4 and Fig. 5.15) seen near 304A may be associated with chimneys and outflow from the supershell. X–ray observations can give important constraints for the interpretation of these SGSs.

The derived properties, dynamical age, the HI mass and required energy, show that the largest SGSs in the SMC fit quite well into the population of SGSs discovered in other galaxies. For the Galaxy, M31, M33, IC10, M101 and NGC6946, the dynamical age varies from $\sim 10^7$ to 10^8 yr, mass from $\sim 10^7$ to 10^8 $M_\odot$ and energy from $\sim 10^{52}$ to 10^{54} erg (see review by van der Hulst & Kamphuis 1991). Compared with M31 and M33, the dynamic ages and sizes of the SGSs in the SMC are similar, but the HI masses and required energies are much higher. This is probably because of the SMC's very high ambient density. Compared with the Galaxy, SGSs in the SMC are all younger but have comparable masses and energies.

The volume fraction occupied by these three SGSs is 0.13 which, together with the volume fraction occupied by shells catalogued in Staveley-Smith et al. (1997) (excluding SMC HI-10 and 491 which correspond to 37A and 494A, respectively), and the volume fraction occupied by 7 new shell candidates, gives a total fraction of 0.4. In three-dimensional space, a volume factor of 0.4 implies a very 'bubbly'

morphology. In the standard expanding shell model (Weaver et al. 1977), the interior is filled with hot gas. This therefore gives a lower limit of 0.4 for the volume factor of the hot gas in the SMC. This is somewhat lower than $\sim$ 0.7–0.8 predicted by the 'three–phase' ISM model of McKee & Ostriker (1977). In this model, the ISM consists of the cold clouds (with temperature $T_c \sim 100$ K, and the density $n_c \sim 10$ cm^{-3}) surrounded by the warm ionised gas ($T_w \sim 6 - 8\times10^3$ K and $n_w \sim 0.3$ cm^{-3}) within the pervasive hot gas ($T_h \sim 10^6$ K and $n_h \lesssim 3 \times 10^{-2}$ cm^{-3}). A similar discrepancy between the observations and the 'three–phase' ISM model has been already noticed in other galaxies (Brinks 1990). An alternative 'chimney' model of the ISM by Norman & Ikeuchi (1989) allows a two–phase model, consisting of the cold clouds surrounded by the warm ionised gas, to change to a three–phase model with an increase in the SN rate and/or decrease of the total gas density. This model suggests that the galactic disk and halo are connected by chimneys which are consequences of superbubble breakouts from the disk. Chimneys bring hot gas into the halo and provide global mass and energy exchange between disk and halo. This model finds 0.1 for the filling factor of the hot gas in the Galaxy, suggesting the chimney model for the ISM in the Galaxy. A similar value for the filling factor was inferred from observations for M31 by Brinks & Bajaja (1986). Using the estimate for the volume filling factor of the hot gas in the SMC of 0.4, the model by Norman & Ikeuchi (1989) could imply that the ISM of the SMC is in the chimney mode.

The total volume factor $\Sigma f_v \approx 0.4$ of all shells in the SMC agrees very well with the prediction of Oey & Clarke (1997). Assuming standard adiabatic shell evolution and continuous star formation, Oey & Clarke derive the differential size distribution of OB superbubbles in a uniform ISM. They then derive the three–dimensional porosity parameter of 0.3 for the SMC. Such good agreement would imply, as stressed by Oey & Clarke, that the large–scale structuring of the ISM in the SMC is mostly determined by OB superbubbles and that no additional fundamental process is needed to explain the creation of the observed HI shells. However, their model assumes that most of the shells have stalled, contrary to the observations.

The mass fraction of the HI swept up by the largest SGSs, $\Sigma f_m \approx 0.26$ is somewhat greater than their filling factor, $\Sigma f_v \approx 0.13$, and implies that a substantial fraction of the total SMC mass is involved. This high mass fraction suggests that these large–scale features must have had an important role in the evolution of the SMC.

6.4 Comparison with other galaxies

The distribution functions of various shell parameters contain valuable information about the structure, kinematics and energetics of the multi-phase ISM. Comparison of these distribution functions for galaxies belonging to different morphological types, as well as with the predictions by various models of the superbubble evolution, could help to probe the nature of the ISM and the dominant processes at

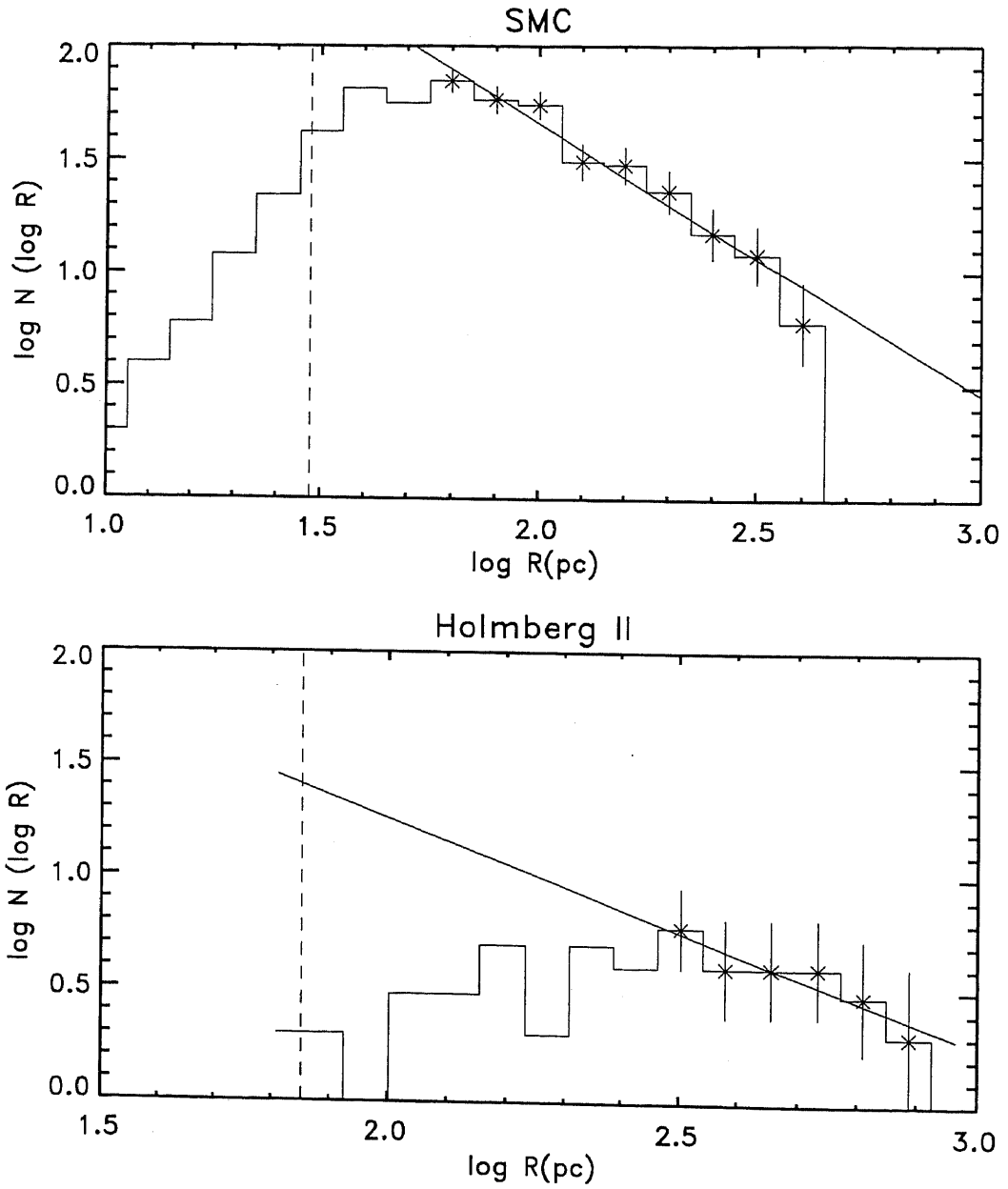

Figure 6.5 . The histogram of shell radii, on a logarithmic scale, from HI surveys of the SMC, Holmberg II, M31 and M33. The survey resolution limit is shown by the vertical dashed lines. The power-law fits to the data in bins with error bars are shown with solid lines. The determined slope γ_r in the logarithmic space, $\log N(\log R) = \gamma_r \log R + \delta_r$, is related to the slope α_r in the linear space, $N(R) \propto R^{-\alpha_r}$, by $\alpha_r = 1 - \gamma_r$.

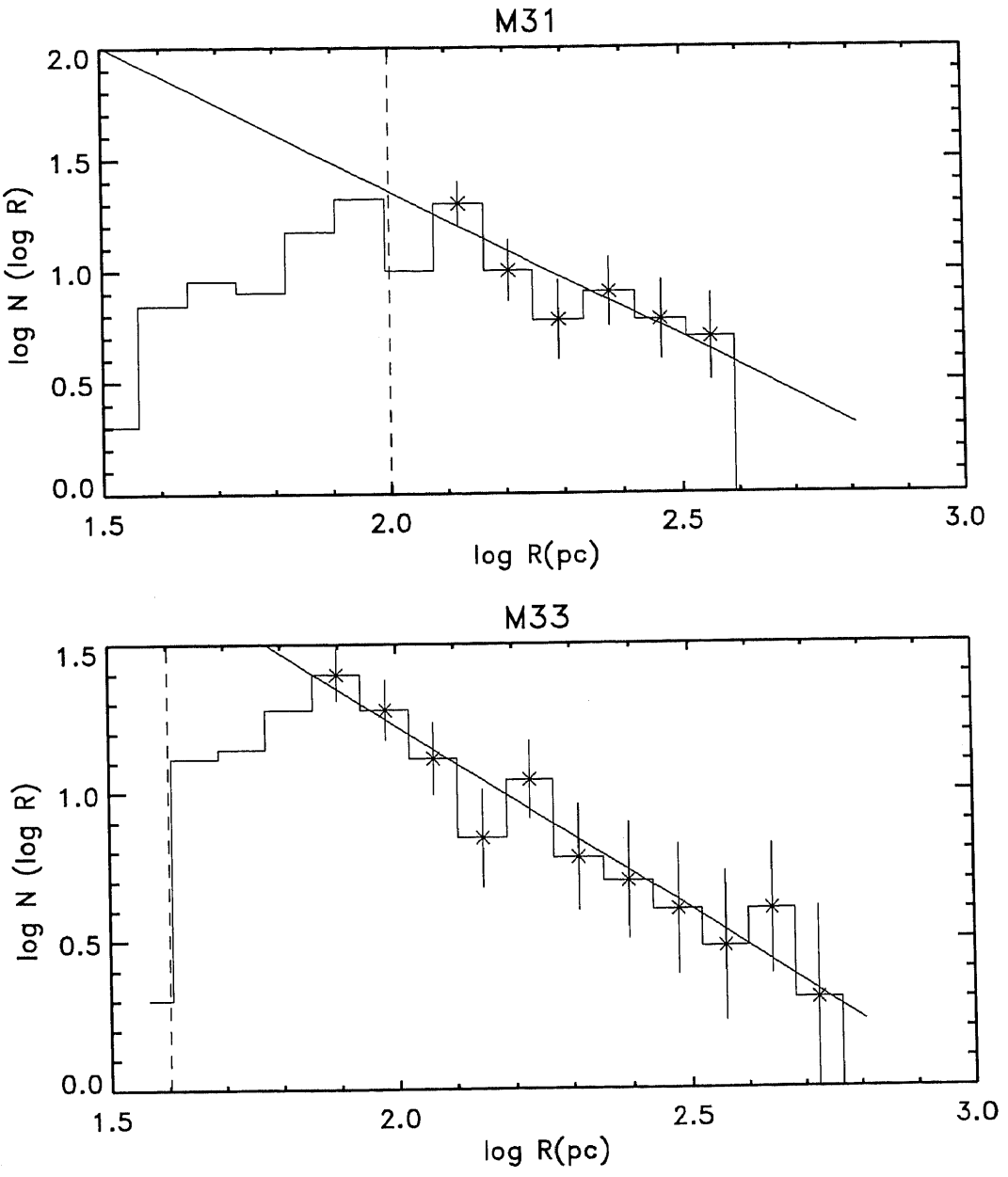

Figure 6.5 *continued*

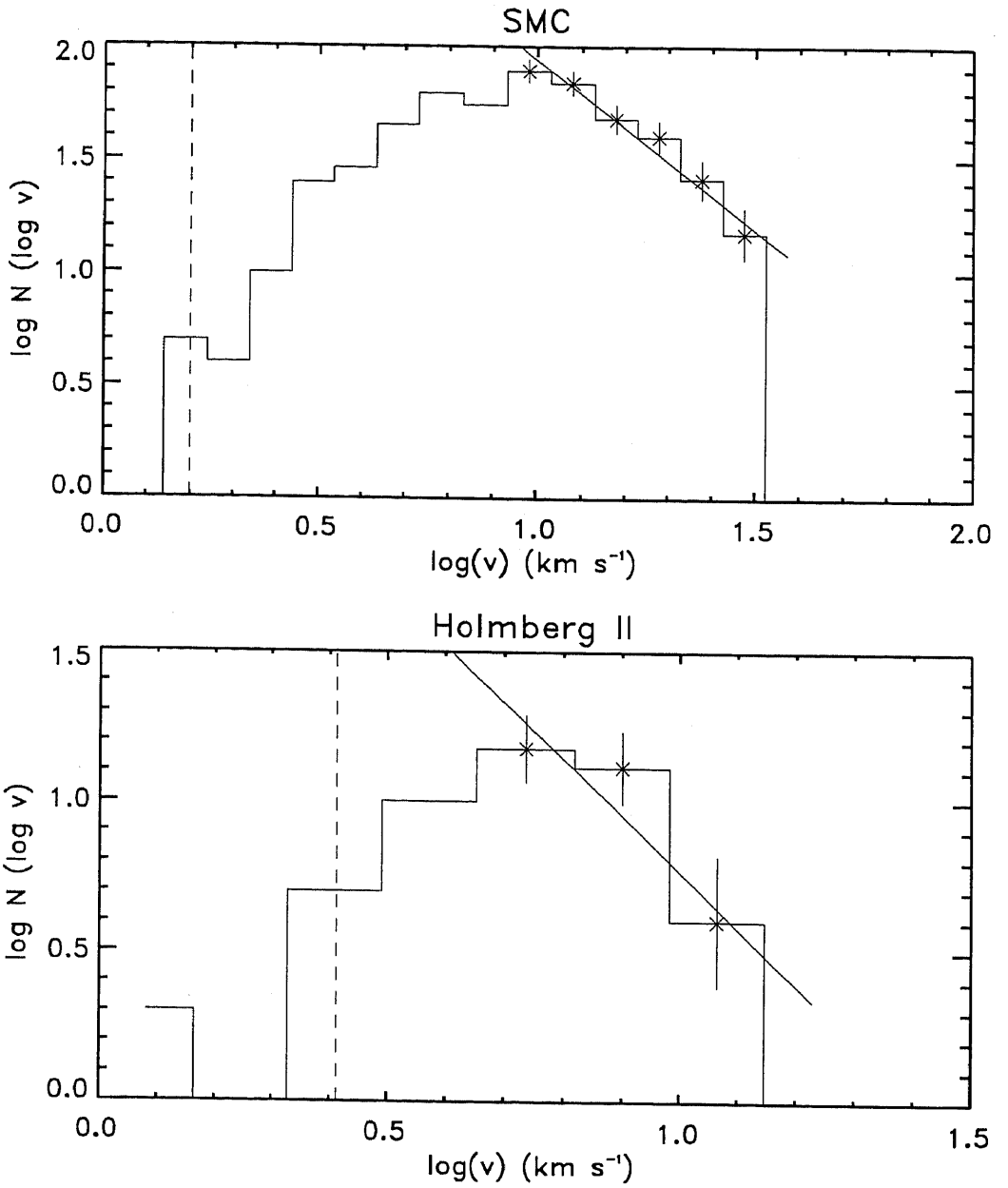

Figure 6.6 . The histogram of shell expansion velocities, on a logarithmic scale, from HI surveys of the SMC, Holmberg II, M31 and M33. The survey resolution limit is shown by the vertical dashed lines. The power-law fits to the data in bins with error bars are shown with solid lines. The determined slope γ_v in the logarithmic space, $\log N(\log v) = \gamma_v \log v + \delta_v$, is related to the slope α_v in the linear space, $N(v) \propto v^{-\alpha_v}$, by $\alpha_v = 1 - \gamma_v$.

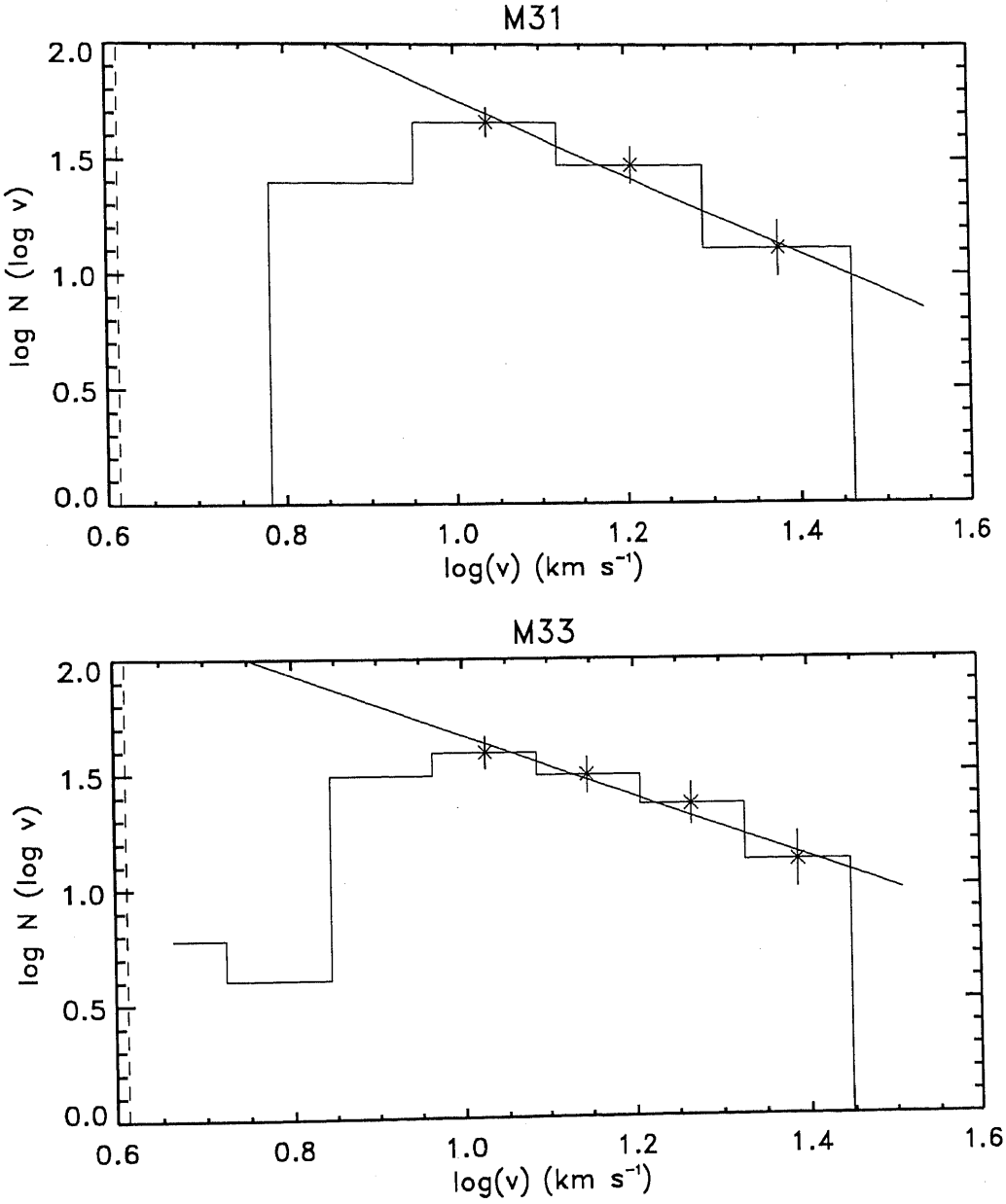

Figure 6.6 *continued*

work.

All shells and shell candidates found in the SMC were used to derive the shell radius and expansion velocity distribution functions, Fig. 6.5 and Fig. 6.6. For comparison, the same distribution functions were derived for another Magellanic irregular galaxy Holmberg II (Puche, Westpfahl, & Brinks 1992) and for two disk galaxies, M31 (Brinks & Bajaja 1986) and M33 (Deul & den Hartog 1990). The least-square power-law fits to the data are overlaid on each figure. Table 6.4 summarises the total number of shells, the peak, cut-off and fitted slope of the size and velocity expansion distribution, and the HI scale height for each galaxy, including data for the LMC (Kim 1998). As was noted by Oey & Clarke (1997), the catalogue of HI holes for the SMC appears to be mainly complete for $R > 100$ pc.

Table 6.4 . The total number of shells ($N_{\rm shells}$), the peak, cut-off radius and slope of the shell radii distribution, the peak, cut-off velocity and slope of the shell expansion velocity distribution, and the HI scale height for five different galaxies.

Galaxy	$N_{\rm shells}$	Radius			Expansion velocity			Scale height
		Peak (pc)	Cut-off (pc)	Slope $\alpha_{\rm r}$	Peak (km s^{-1})	Cut-off (km s^{-1})	Slope $\alpha_{\rm v}$	(pc)
SMC	509	50	400	2.2±0.3	10	30	2.5±0.4	$\sim 800^a$
Holm II^b	51	250	800	2.0±0.2	6	15	2.9±0.6	625
M31^c	140	75	350	2.3±0.4	10 – 12	22	2.7±0.5	120
M33^d	148	80	~ 400	2.2±0.2	8	22	2.3±0.5	100
LMC^e	102	125	-	2.5±0.4	14	-	-	170

[a] see Section 5.3.4

[b] from Puche, Westpfahl, & Brinks (1992)

[c] from Brinks & Bajaja (1986)

[d] from Deul & den Hartog (1990)

[e] from Kim (1998)

All four shell size distribution functions derived here show a peak radius and a sharp cut-off at high radii. The shell size distribution function for the SMC, M31, M33 and LMC peaks at similar values, while for Holmberg II it appears to peak at much larger radius, $\sim$ 250 pc. Holmberg II also has the largest cut-off radius. As the cut-off radius and HI scale height in Holmberg II are larger than in M31 or M33, a possible correlation between the morphological type of galaxies and the shell sizes was suggested by Puche, Westpfahl, & Brinks (1992) and Walter (1999). In dwarf galaxies, the gravitational potential is lower and the HI layer is thicker than in spirals, allowing shells to grow larger before breaking out. Surprisingly, shells in the SMC do not support this idea. Although a dwarf irregular galaxy, the SMC has a cut-off radius comparable to that in M31 and M33, but much larger HI scale height.

All derived expansion velocity distribution functions also show a peak velocity and a high-velocity cut-off. Shells in Holmberg II have the smallest range of expansion velocities and these velocities are systematically lower than in other listed galaxies. As most of the supergiant shells in Holmberg II have $R > 300$ pc, they are most likely old, hence their smaller expansion velocity. The shell expansion velocities in M31 and M33 have the same range, $4 - 29$ km s^{-1}, but the observations have the same low velocity resolution of 4 km s^{-1}. The expansion velocity histograms are very similar and peak between 8 and 12 km s^{-1}. The data for the SMC and the LMC have the best dynamic range with the best velocity resolution of ~ 1.6 km s^{-1}. The LMC expansions peak at a slightly higher value than for the SMC.

The shell-size distribution functions for these five galaxies can be well-fitted by a power-law, $N(R) \propto R^{-\alpha_r}$ (Table 6.4), for shell radii between the peak and the cut-off radius. The inclusion of 10 new SGSs in the SMC have slightly changed the largest bins in the shell radii histogram, and hence the fitted slope, strengthening the power-law fit derived in Oey (1998). At first glance, the power-law slopes for the SMC, M31 and M33 look very similar, while the shell-size distribution function of Holmberg II appears significantly different. However, within the given uncertainties, all five galaxies seem to have the same slope, $\langle \alpha_r \rangle = 2.2 \pm 0.4$, although it would be reasonable to expect the slopes to differ for galaxies of different morphological types (Oey & Clarke 1997). Hence, very similar power-law slopes probably mean that similar processes are responsible for shell creation and evolution in all five galaxies.

The shell expansion velocity distribution for the SMC can be well-fitted by a power-law, $N(v) \propto v^{-\alpha_v}$, between the peak and the cut-off velocity, with $\alpha_v = 2.5 \pm 0.4$. The inclusion of a few new SGSs in the SMC, with large expansion velocities, have again slightly changed the largest bins in the expansion velocity histogram, and hence the fitted slope, relative to the power-law fit derived in Oey & Clarke (1998). The other three galaxies also show power-law behaviour of $N(v)$, although the dynamic range and velocity resolutions are lower, resulting in larger uncertainties. The power-law slopes are also similar with the mean slope being $\langle \alpha_v \rangle = 2.6 \pm 0.5$. Another interesting result is that the slopes α_r and α_v appear to be equal within the given uncertainties for the SMC, M31 and M33.

In Fig. 6.7 the expansion velocity of giant shells in the SMC is plotted as a function of shell radius, showing a definite correlation. Assuming that the mechanical energy, which provides the shell expansion, comes from the continuous action of stellar winds (Eq. 6.2), the curves of constant wind luminosity were superimposed on the same figure, showing that shell luminosities range between $\sim 10^{35}$ and 10^{38} erg s^{-1}. For this purpose a constant density for the ambient ISM of 1 cm^{-3}, was used. Lines of the constant dynamical age are also overlaid, showing that the giant shell ages span from 10^6 to 10^7 yr, with most of the giant shells being $3 - 5$ Myr old. The correlation between R and v is also shown in Fig. 6.8, where $\log(v)$ is plotted as a function of $\log(R)$. While for giant shells with $R < 300$ pc, $v \propto R^{\gamma}$, with $\gamma \approx 1.0 \pm 0.3$, the expansion velocity of supergiant shells appears to limit to $v \approx 30$ km s^{-1}.

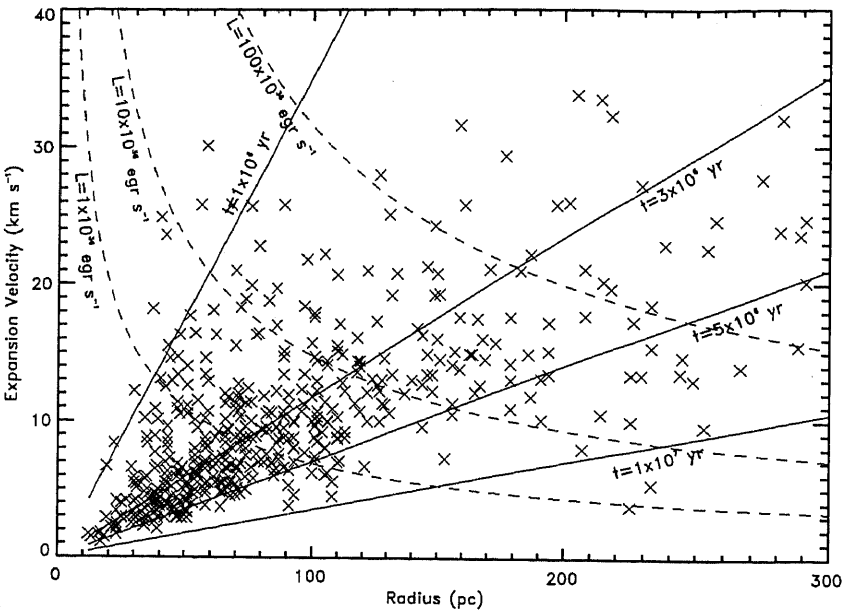

Figure 6.7 . Expansion velocity of giant shells in the SMC versus their radius. Dashed curves represent values of constant wind luminosity of 1×10^{36}, 10×10^{36}, 100×10^{36} erg s^{-1}. The solid lines represent dynamical ages of 1×10^6, 3×10^6, 5×10^6 and 1×10^7 yr.

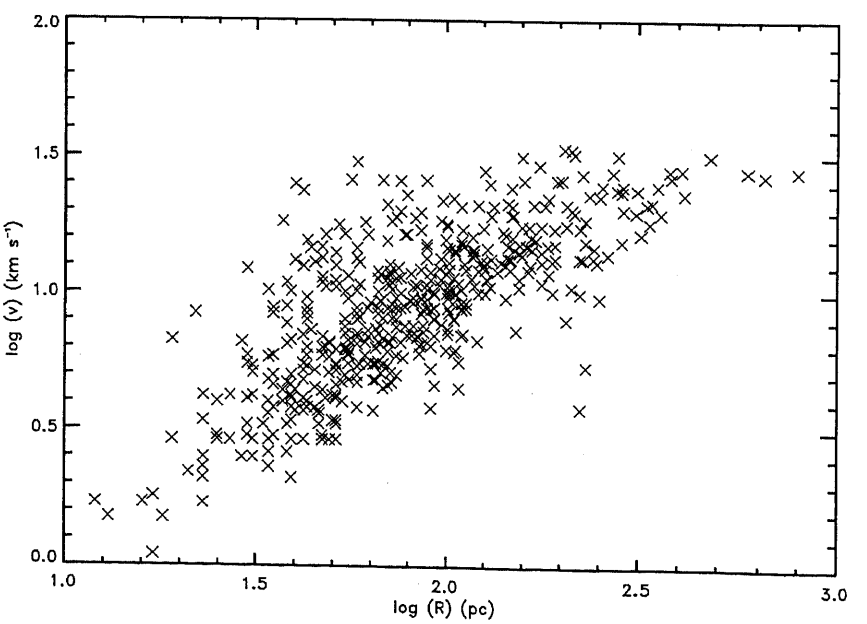

Figure 6.8 The shell expansion velocity as a function of shell radius in the log space.

6.5 Comparison with the standard model

The standard model for the evolution of SGSs (Weaver et al. 1977; McCray & Kafatos 1987) assumes that shell expansion is powered by the stellar winds and, especially, SNs from the parent OB association. It is also assumed that the mechanical luminosity (L), dominated by SNs, remains constant with time. The spectrum of this mechanical luminosity in any galaxy, is a very important parameter for a prediction of the differential shell-size or expansion velocity distribution function within the standard model, as shown by Oey & Clarke (1997). Oey & Clarke (1997) have considered both a constant mechanical luminosity and a power-law mechanical luminosity function (MLF), $N(L) \propto L^{-\beta}$. The slope β of the MLF is related to the slope a of the HII luminosity function (HII LF), by $\beta \leq a$. Hence, as a can be obtained from observations, it usually serves as an upper limit of β. However, empirical measurements imply that one can easily assume $\beta = a$ in most cases (Oey & Clarke 1997).

Another important parameter in modelling the SGS evolution is the nature of the SGS creation, which may be considered to be either continuous (the case when SGSs are generated continuously at the constant rate), or a single burst (the case when all SGSs were created in an instantaneous burst). For each case, the shell-size and expansion velocity distribution functions can be derived, as well as the relationship between the shell radius (R) and the mean expansion velocity ($\overline{v}$) for an ensemble of shells being at different stages of their evolution. These predictions can then be compared with the same functions inferred from observations (discussed and derived in the previous section).

We follow the discussion in Oey & Clarke (1997) to derive $N(R)$, as well as $N(v)$ and $\overline{v}(R)$, in three different cases within the standard adiabatic model. In all three cases power-law behaviour for all three function can be expected.

1. **Continuous creation, single luminosity**
   Assuming that SGSs are continuously created and that the input mechanical luminosity is equal for all shells, results in: $N(R) \propto R^{2/3}$, $N(v) \propto v^{-7/2}$, and $\overline{v} \propto R^{-2/3}$. Hence, neither $N(R)$, $N(v)$ or $\overline{v}(R)$ depend on β.

2. **Single burst, luminosity spectrum**
   If all shells were created at the same instant and the input mechanical luminosity has a power-law distribution of $N(L) \propto L^{-\beta}$, then the standard model predicts that both $N(R)$ and $N(v)$ have the same slope equal to $4 - 5\beta$, while $\overline{v}(R) \propto R$.

3. **Continuous creation, luminosity spectrum**
   The last case considers continuous shell creation together with the power-law distribution of $N(L)$, and results in: $N(R) \propto R^{2(1-\beta)}$, $N(v) \propto v^{-7/2}$, and $\overline{v}(R) \propto R^{-2/3}$, for expanding shells only.

It was shown in the previous section that the shell-size and expansion velocity distribution functions for the SMC, Holmberg II, M31 and M33, can be well-fitted by power-laws $N(R) \propto R^{-\alpha_r}$ and $N(v) \propto v^{-\alpha_v}$. The values for slopes α_r and α_v are listed in Table 6.4. Since all slopes are positive, it appears that the shell evolution in none of these four galaxies can be explained by the first case (continuous creation, single luminosity), which predicts negative α_r.

In the case of the SMC, M31 and M33, the slopes α_r and α_v appear to be equal within the estimated uncertainties, suggesting that the second case for the SGS evolution, with a single burst and a luminosity spectrum, could explain the shell creation and evolution. The most complete data set for the SMC provides even further evidence, with a significant coherency in the dynamical age for the giant shells (Staveley-Smith et al. 1997 and previous section) and $\overline{v}(R) \propto R^{\gamma}$, where $\gamma = 1.0 \pm 0.3$. Now, we can use a mean slope of functions $N(R)$ and $N(v)$, $\alpha = (\alpha_r + \alpha_v)/2$, to estimate the slope of the MLF for these three galaxies. These estimated values for β are shown in Table 6.5, together with the slopes of the HII LF estimated from observations (a_{obs}). Note that in general $\beta \leq a$, but empirical measurements suggest $\beta = a$ for many galaxies (Oey & Clarke 1997). However, we find that all newly estimated slopes β are significantly lower than their upper values found from observations, but are still within the expected ranges.

Table 6.5 . Observed and derived parameters for the case of a single burst and a continuous luminosity function. The mean slope, $\alpha = (\alpha_r + \alpha_v)/2$, the estimated slope of the MLF (β) derived from $\beta = (4 + \alpha)/5$, and the slope of the HII LF estimated from observations (a_{obs}) in listed references. Note that in general $\beta \leq a$.

Galaxy	α	β	a_{obs}	HII Reference
SMC	2.3 ± 0.5	1.3 ± 0.1	1.9	(1)
Holm II		-	1.4	(2)
M31	2.5 ± 0.6	1.3 ± 0.1	2.1	(1)
M33	2.2 ± 0.4	1.2 ± 0.1	2.0	(1)

(1) Kennicutt, Edgar, & Hodge (1989)
(2) Hodge, Strobel, & Kennicutt (1994)

Oey & Clarke (1997) have used the third case for the standard shell evolution, a continuous creation and a luminosity spectrum, with the slopes for the MLF being equal to the slopes of the HII LF (taken from the fourth column in Table 6.5). This resulted in their predictions for the slope of the shell-size distribution function, α_r^p, for all four galaxies. We list their estimates, as well as slopes fitted here from observations in Table 6.6.

The model predictions for slopes of $N(R)$ and $N(v)$ appear to agree very well with observations for Holmberg II, while the predicted values of α_r^p and α_v^p for the SMC, M31 and M33 are significantly steeper than found by observations. In the case of the

Table 6.6 . Predicted slopes of $N(R)$ and $N(v)$, α_r^p and α_v^p, in the case of a continuous shell creation and a luminosity spectrum by Oey & Clarke (1997). Slopes α_r and α_v were fitted here from the shell-size and expansion-velocity histograms (also shown in Table 6.4).

Galaxy	α_r	α_v	α_r^p	α_v^p
SMC	2.2 ± 0.3	2.5 ± 0.4	2.8 ± 0.4	3.5
Holm II	2.0 ± 0.2	2.9 ± 0.6	1.8 ± 0.4	3.5
M31	2.3 ± 0.4	2.7 ± 0.5	3.2 ± 0.4	3.5
M33	2.2 ± 0.2	2.3 ± 0.5	3.0 ± 0.4	3.5

SMC, α_r^p agrees with α_r within the estimated uncertainties, but α_v^p is significantly different from α_v. The continuous shell creation and a luminosity spectrum also predict negative slopes for $\overline{v}(R)$. This is in contradiction with the correlation found for the SMC (Fig. 6.8), where $\overline{v}(R) \propto R$.

Using only the SMC shell radii histogram, Oey & Clarke (1997) concluded that the SMC shells support the case of continuous creation and a luminosity spectrum. However, in this case, the most dominant shells in the $N(R)$ distribution should be already stalled, which is not observed. Staveley-Smith et al. (1997) have measured significant velocity expansions for all shells. To overcome this discrepancy, Oey & Clarke (1997) suggest that some shells could have spurious expansion velocities, e.g. resulting from the blowout from a high-density to a low-density region, as suggested by Oey (1998).

The creation and evolution of SGSs in the SMC, Holmberg II, M31 and M33 appear to be consistent with the predictions by the standard model. The SGSs in Holmberg II suggest a continuous shell creation and a power-law luminosity spectrum in this galaxy, while the shell creation and evolution in the SMC, M31 and M33 is better explained by a single shell burst and a power-law luminosity spectrum. Therefore, the OB SGSs seem to contribute significantly to the large-scale structuring of the ISM in these four galaxies. However, is this the only fundamental process responsible for the shell-size and expansion velocity distribution functions? To answer this question, high spatial and velocity resolution observations of other galaxies of different morphological types are required, in order to produce complete shell samples for statistical investigation. At the same time, revised and more detailed models for the creation and evolution of SGSs, with a special emphases on statistical properties, are needed.

6.6 Summary

- The combined ATCA and Parkes data set reveals the existence of ten SGSs which were previously undetectable in the ATCA data alone. The three largest

ones have diameters ranging up to 1.8 kpc and require energies (in the standard supernova-driven model) up to 2×10^{54} erg. They also appear to be related to the SGSs originally noted by Hindman (1967). The volume fraction occupied by these three features is only 0.13 and the mass fraction of the swept up HI is 0.26, suggesting that they have had a very important role in the evolution of the SMC.

- The total filling factor of all known SMC shells of 0.4 gives a lower limit for the volume factor of the hot gas in the SMC. This is lower than predicted by the 'three-phase' model of the ISM (McKee & Ostriker 1977), but in agreement with the prediction by Oey & Clarke (1997) for the ISM governed by the creation and evolution of OB superbubbles.
- The shell radius and expansion velocity distribution functions for the SMC, as well as for Holmberg II, M31 and M33, can be well fitted by the power-laws: $N(R) \propto R^{-\alpha_r}$ and $N(v) \propto v^{-\alpha_v}$, with slopes α_r and α_v being surprisingly similar for the SMC, M31 and M33. Comparison of these functions with predictions by the standard adiabatic model for the shell evolution, shows a good agreement and suggests continuous shell creation in Holmberg II, and a single burst of shells in the SMC, M31 and M33. In all cases a power-law mechanical luminosity function is required.

Chapter 7

IR data presentation and results

7.1 Introduction

As well as HI (at 21cm) and ionised carbon (at 158 μm), dust (at infrared wavelengths) is another important tracer of the cool ISM. It is a source of coupling between neutral gas, ionised gas and radiative pressure, and it provides a mechanism, in denser regions, for extinction and molecule formation (Dyson & Williams 1980). As different types of dust grains exist in the ISM, what are their compositions, distributions and abundances in the SMC?

Early studies of the dust properties in the SMC, undertaken with ground based instruments (Koornneef 1982; Koornneef 1984; Koornneef & Israel 1985; Bouchet et al. 1985; Israel & Koornneef 1988; Martin, Maurice, & Lequeux 1989; Lequeux 1989), were limited to the brightest objects and covered a negligible fraction of the area of the SMC (Schwering & Israel 1989). The advent of the infrared all-sky survey by the Infrared Astronomical Satellite (IRAS) resulted in the first complete IR survey of the SMC, which produced a list of point sources, presented as the IRAS Point Source Catalog (JIWG 1988, henceforth IRAS-PSC), and a series of maps produced from Pointed Observations (POs) (Schwering 1988), having a resolution of $\sim$ 8 arcmin. However, the intrinsic IRAS telescope optics is 1 arcmin at 60 μm and 1.7 arcmin at 100 μm. By combining several scans at different position angles, it is possible to reconstruct reliable images with a resolution close to the original diffraction limit. This has been done for many individual fields using the IPAC HiRes program, and has been done for the Galactic Plane (Cao et al. 1999). Methods are discussed by Rice (1993) and Bontekoe, Koper, & Kester (1994).

This chapter concentrates mainly on the dust properties of the SMC. The first part of the chapter, Section 7.2, describes selection and processing of the IRAS survey and non-survey (POs) data using the HIRAS program. The high resolution IR images are presented and the IR morphology of the SMC is considered. The new data are

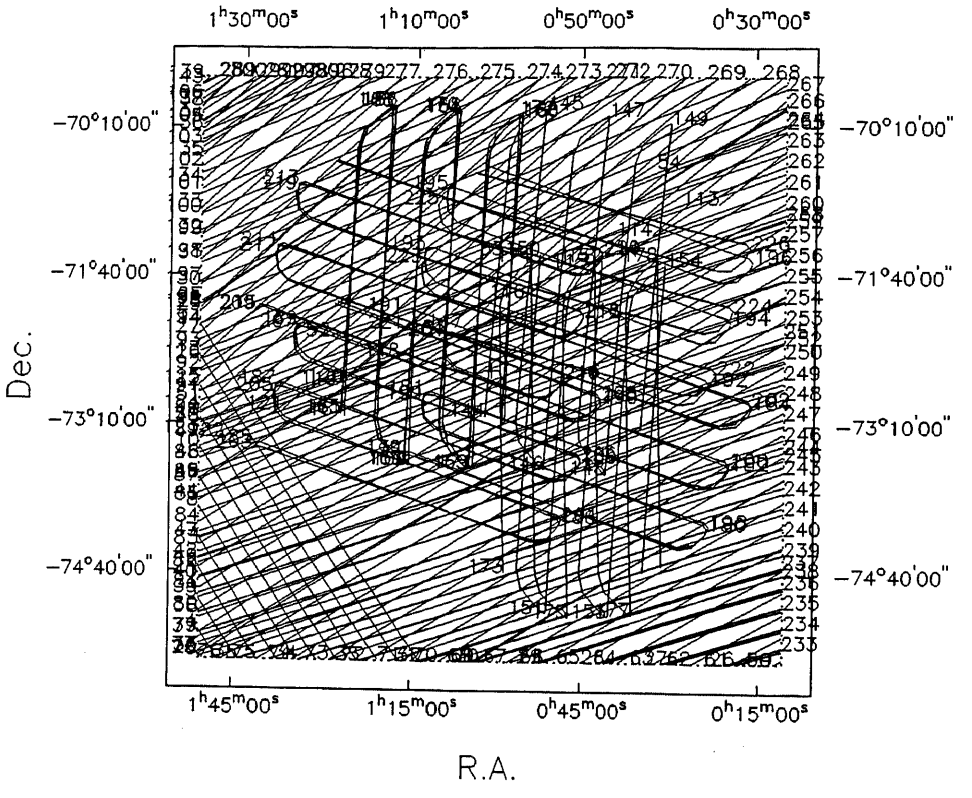

Figure 7.1 . The IRAS scan pattern of the SMC (J2000). Three sets of scans of survey data are present: HCON-1 and HCON-2 (see IRAS Catalogs and Atlases Explanatory Supplement, Beichman et al. 1985), which are almost parallel and run from south-east to north-west, and HCON-3, perpendicular to both but covering just a small area at south-east. 14 DMP Pointed Observations (Young et al. 1985) covering central region of the SMC in various directions are also shown.

compared with other IRAS and COBE/DIRBE data, the integrated IR spectrum of the SMC is discussed and details of the assumed dust model are outlined. In the second part, Section 7.3, dust properties such as the dust temperature and dust column density distributions are derived and presented. The total dust mass and its uncertainty are estimated and discussed in detail.

7.2 HIRAS data and results

7.2.1 Data origin and processing

The HIRAS program (Bontekoe, Koper, & Kester 1994) was used to produce the high resolution IR maps of the SMC from the IRAS all–sky survey data in three

sets of scans in conjunction with 14 DMP Pointed Observations (POs). For different types of pointed observations see Young et al. (1985). Note that HIRAS should not be confused with HiRes, which uses a maximum correlation technique (Aumann, Fowler, & Melnyk 1990). The scan pattern of the data used in this paper is shown in Fig. 7.1. The addition of the PO's nearly doubled the amount of data, but the main reason for their inclusion is the fact that the SMC survey data are taken predominantly in one direction over the map (i.e. from southeast to northwest), while the POs add scans with various other angles.

In the calibration procedure, data samples from detectors known to be noisy were discarded and glitches in the data (due to cosmic-ray hits) were identified and removed. The zodiacal emission model was then subtracted from all data scans individually. To provide the calibration consistency between different scans, an iterative 'de-striping' algorithm was applied to account for the baseline differences between the scans. For more details on IRAS data calibration and pre-processing see Assendorp et al. (1995) and Bontekoe, Koper, & Kester (1994). After subtraction of the zodiacal emission model and subsequent 'de-striping', the zero-point of the data is arbitrary. Since there is no clear selection criterion, a (personal) judgement must be made based on the distribution of all data values. One possibility is to take the fiducial zero point such that typically three to five percent of all the data becomes negative. An alternative, used here, is to determine the half-width at half maximum of the distribution of data values, and subtract this half-width from the value of the mode of the distribution (i.e. where the maximum occurs). Both methods yield the best possible IRAS images, which, however, still require some careful post-processing flat-fielding.

Bayesian data analysis (based on Bayesian probability theory), employed in the HIRAS program, requires an uncertainty for every measured quantity (see Sivia 1996 for an excellent tutorial). This property is used extensively to incorporate known instrumental effects as an extra contribution to the uncertainty of the input data. These instrumental effects include: the lossy data compression scheme on board the satellite, detector memory effects and glitches due to cosmic ray hits. The data correction for truncation effects in the data digitisation is also made. Note that a number of the above calibration steps are performed by comparing the data against fiducial data sampled from a low-resolution map. As a single pre-processing pass of the calibration steps was found to be not sufficient enough, after every convergence of the HIRAS program some further refinements in the calibration was made. Typically three to four iterations are needed until no further improvements seem possible.

The HIRAS program uses the Pyramid Maximum Entropy (PME) method, an application of the maximum entropy package MemSys5 (Gull & Skilling 1991), to reconstruct reliable images at a resolution approaching the diffraction limit of the IRAS telescope. In the PME algorithm the image is reconstructed in a number of parallel images, containing respectively 1 by 1 pixels, 2 by 2 pixels, 4 by 4 pixels, 8

by 8 pixels, etc. up to the final pixel number (here 1024 by 1024 pixels). Each image covers the entire map area and represents a certain correlation length or resolution size. The images are combined into a single image and the entropy of the image is calculated as the sum of the entropies of the individual images. Maximising the entropy ensures that large scale structure is preferentially reconstructed in a channel image with large pixels.

The resulting images of the SMC have a resolution of $\sim$ 1 arcmin for the 12, 25 and 60 μm data and $\sim$ 1.7 arcmin for 100 μm data. As the actual resolution and the dynamic range depend on the local sampling pattern (and source brightness), they vary slightly across the maps. To obtain true intensities from the in-band ones, we have applied colour-corrections from the IRAS Catalogs and Atlases Explanatory Supplement (Beichman et al. 1985). After fitting the observed integrated spectrum with a power law, the correction factors are derived to be 0.93, 0.92, 0.99, 1.00 for 12, 25, 60 and 100 μm, respectively. All images were flat-fielded to remove the residual background.

7.2.2 IR morphology

The resulting high resolution IRAS images of the SMC in all four bands are shown in Fig. 7.2. The HIRAS data resembles the IR distribution across the SMC found in previous studies, but for the first time contain information on scales as small as $\sim$ 1 arcmin (for 12, 25 and 60 μm) and $\sim$ 1.7 arcmin (for 100 μm). While the 12 and 25 μm images trace mainly hot HII regions and foreground stars with little diffuse IR emission, the 60 and 100 μm data show a lot of diffuse emission with a wealth of filamentary structure. Some residual, low-level stripes (below the 3 - σ noise level) are still visible in the 12 and 25 μm images, due to the scan pattern. The astrometric and photometric agreement of point sources with the IRAS-PSC are on average good, although PME fluxes are 10–20 % higher (for more detail on image quality estimate and comparison see Bontekoe, Koper, & Kester 1994). As the SMC has a high ecliptic latitude, the contribution of the zodiacal emission is not significant, unlike in the Galaxy where 12, 25 and 60 μm bands are severely contaminated (Schlegel, Finkbeiner, & Davis 1998). This, together with the mainly flat and featureless Galactic background around the SMC, enables good reconstruction of the diffuse IR emission.

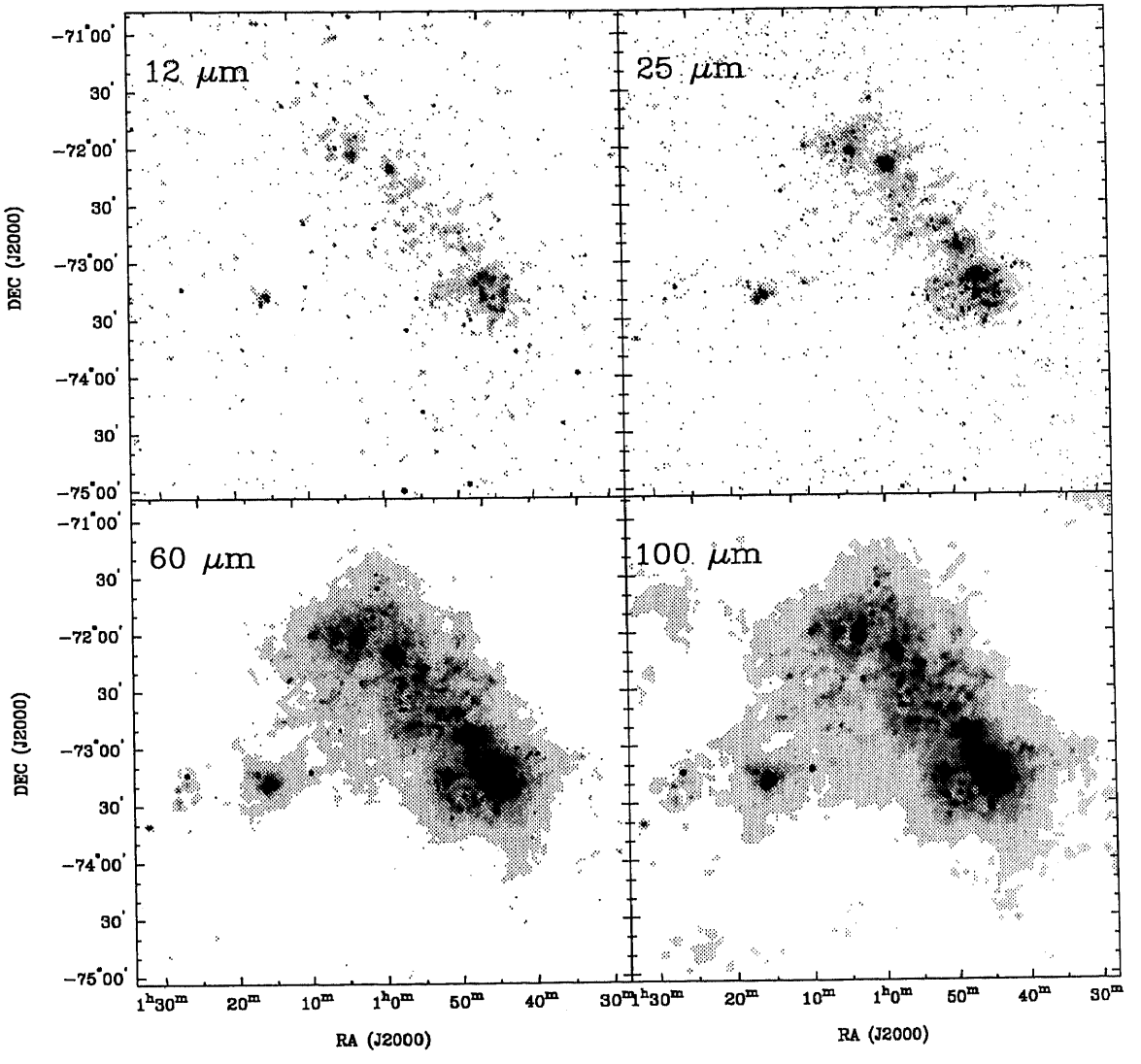

Figure 7.2 . The high resolution PME IRAS images of the SMC at 12, 25, 60 and 100 μm. The grey-scale intensity range is: 0.2 to 1.2, 0.2 to 1.9, 0.6 to 13 and 0.6 to 27 MJy sr^{-1}, respectively, with a linear transfer function. 12, 25 and 60 μm images have resolution of $\sim$ 1 arcmin, while 100 μm image has resolution of $\sim$ 1.7 arcmin.

7.2.3 Comparison with other IR observations

Table 7.1 . Comparison of integrated IR flux densities of the SMC from different surveys. The area covered is ~ 6.25 deg^2.

Band (μm)	DIRBE[a] (Jy)	DIRBE + ISSA[b] (Jy)	HIRAS[c] (Jy)	IRAS (POs)[d] (Jy)
1.25	510 ± 25	-		-
2.2	400 ± 37	-		-
3.5	220 ± 31	-		-
4.9	110 ± 43	-		-
12	80 ± 30	-	105 ± 30	147 ± 26
25	460 ± 180	-	310 ± 170	385 ± 56
60	8450 ± 370	-	6700 ± 1060	7170 ± 957
100	15800 ± 2720	15000 ± 2610	13600 ± 1930	13900 ± 1810
140	14000 ± 5600	-		-
240	9600 ± 4400	-		-

[a] COBE/DIRBE data in public domain

[b] from Schlegel, Finkbeiner, & Davis 1998

[c] this paper

[d] Schwering 1988

In Table 7.1 we show a comparison of the integrated flux densities from our data with IR data from three other sources:

1. COBE/DIRBE maps*for 1.25–240 μm, with a resolution is 0.7 deg. We have applied colour corrections from Hauser et al. (1998) and applied a foreground correction, but have not applied any specific zodiacal emission corrections.
2. A composite of COBE/DIRBE and IRAS/ISSA maps at 100 μm, corrected for the zodiacal background and colour, with 6 arcmin resolution (from Schlegel, Finkbeiner, & Davis 1998). We further applied a correction to remove extended foreground Galactic emission.
3. IRAS non-survey 'Pointed Observation' images, corrected for both zodiacal emission and colour, with 8 arcmin resolution (from Schwering 1988).

Flux densities in Table 7.1 were obtained by summing the maps over an area of 6.25 deg^2 which contains the optical bar and the Eastern Wing. Error estimates are dominated by the background corrections and uncertainties in the absolute flux density scale.

*The COBE datasets were developed by the NASA Goddard Space Flight Center under the guidance of the COBE Science Working Group and were provided by the NSSDC.

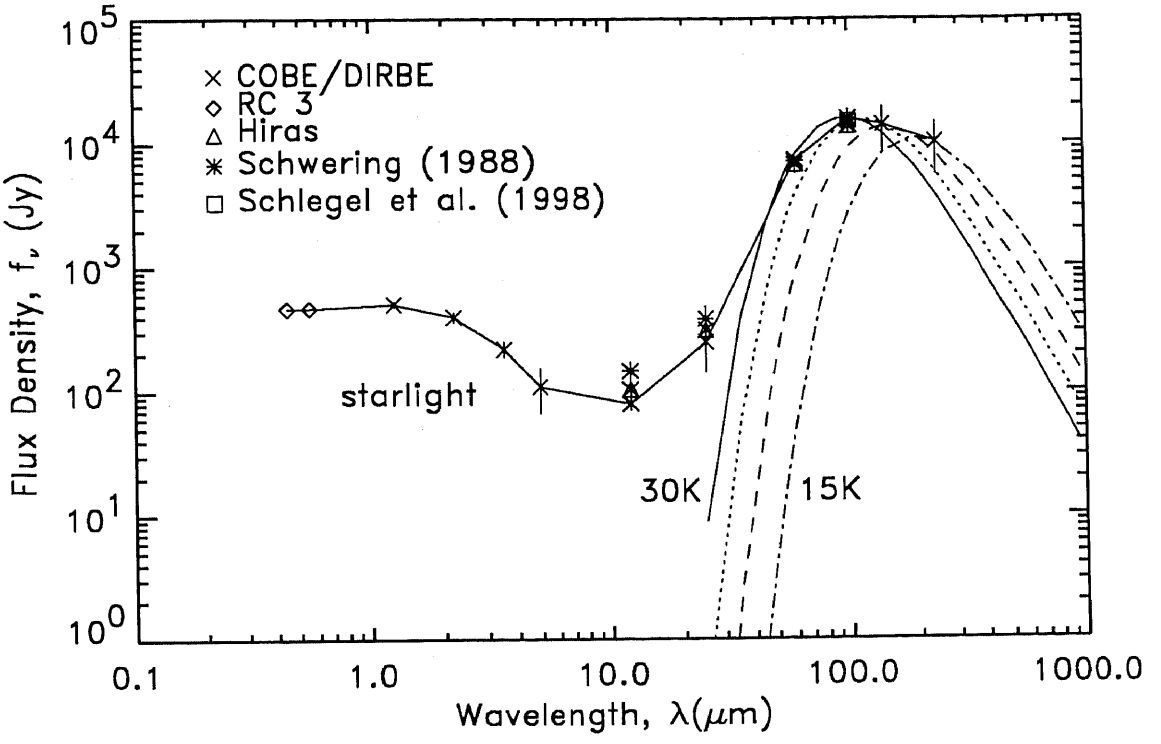

Figure 7.3 . The integrated IR spectrum of the SMC from five different data sources: COBE/DIRBE data (cross), the Third Reference Catalogue of Bright Galaxies (de Vaucouleurs et al. 1991) (diamond), HIRAS data (triangle), Schwering (1988) (asterisk) and Schlegel, Finkbeiner & Davis (1998) (square). The quasi-blackbody spectra for temperature $T_d = 30$ K (solid line), 25 K (dotted line), 20 K (dashed line) and 15 K (dash-dotted line), and assumed dust mass absorption coefficient $\kappa_\nu = 41(\nu/c)^{2.0}$ cm^2 g^{-1}, are overlaid.

Except for the 4.9, 12 and 25 μm COBE/DIRBE data, where the zodiacal emission peaks and the SMC emission is at a minimum, flux densities from all data sources seem to be comparable within 10–20 % uncertainty. We find very good agreement between HIRAS and IRAS fluxes. Surprisingly, integrated flux densities measured by COBE/DIRBE for 60 and 100 μm (from both (i) and (ii)) are higher than HIRAS or IRAS fluxes by about 10–20 %, whereas the COBE/DIRBE Explanatory Supplement (Wheelock et al. 1994) gives a linear transformation between IRAS and DIRBE data, in which the IRAS brightnesses are 13% and 28% higher than DIRBE brightnesses at 60 μm and 100 μm, respectively. A possible reason why we measure higher COBE/DIRBE integrated flux densities for the SMC could be a position or resolution dependent brightness transformation between IRAS and DIRBE data.

The integrated HIRAS spectrum of the SMC is shown in Fig. 7.3 and compared with data from the above three data sources. Flux densities for 0.4 and 0.5 μm were estimated from the blue and visual apparent magnitudes of the SMC, obtained from the Third Reference Catalogue of Bright Galaxies (de Vaucouleurs et al. 1991,

henceforth RC 3), and they seem to be consistent (though do not overlap) with COBE/DIRBE data. The stellar radiation is responsible for the $\lambda \lesssim 4$ μm part of the spectrum. The overall spectrum peaks at ~ 100 μm, although in νf_ν units the spectrum peaks at ~ 1 μm. Unlike Galactic IR emission which shows a secondary peak around $\lambda \sim 10$ μm (Cox & Mezger 1989), the SMC IR spectrum has a local minimum at $\lambda \sim 12$ μm. Therefore, the excess near–IR and mid–IR emission is not prominent, indicating that PAH molecules, responsible for IR emission at these wavelengths, play a less important role in the SMC than in the Galaxy.

Quasi-blackbody spectra, $\kappa_\nu B_\nu(T_\mathrm{d})$, for dust mass absorption coefficient $\kappa_\nu \propto \nu^{2.0}$ and a range of dust temperatures $T_\mathrm{d} = 30$, 25, 20, 15 K, are overlaid in Fig. 7.3. The far–IR part of the spectrum ($\lambda \gtrsim 45$ μm) seems to be reasonably well–modelled with a composition of the quasi-blackbody curves for temperature range 15–30 K. This means that large dust grains are predominantly responsible for IR emission at $\lambda \gtrsim 45$ μm. The discrepancy for ~ 30 μm $< \lambda < 45$ μm corresponds probably to the presence of some very small grains (VSGs).

7.2.4 SMC dust model and assumptions

The dust model we assume is based on studies by Mathis, Rumpl, & Nordsieck (1977), Draine & Anderson (1985), Dwek et al. (1997), Li & Greenberg (1997), Rodrigues et al. (1997), and consists of:

1. large silicate and carbonaceous (graphite or amorphous carbon) grains, with sizes $a \gtrsim 0.05$ μm (so–called normal grains)
2. very small carbonaceous grains (VSGs), with sizes $a \lesssim 0.005$ μm
3. PAH molecules.

While the early dust models in general considered bare silicate and carbonaceous grains, the most recent models are more complex and consider silicate cores coated by the carbonaceous mantle or composite dust grains (collections of very small dust particles loosely attached to one another) (see Li & Greenberg 1997 for a review). The very recent work by Zubko (1999) suggests a dust model for the SMC which consists of a mixture of the silicate core–organic refractory mantle and composite grains, and also includes silicon nanoparticles. However, this model has been fit only to the observational data for the star AzV 398, situated in the SMC bar.

The main constraint for the abundances of dust grains comes from the SMC extinction curve. Compared to the Galaxy, the SMC has a much straighter extinction curve with: (a) a weaker ~ 0.2 μm bump; and (b) a stronger FUV rise (Lequeux 1989; Sauvage & Vigroux 1991). Although the carrier of the 0.2 μm bump is still uncertain, it is generally ascribed to the VSGs (Li & Greenberg 1997; Rodrigues et al. 1997). Hence, (a) implies an absence of VSGs particularly responsible for the

0.2 μm bump. However, a significant abundance of VSGs, in general, may still be present in the SMC, as suggested by the integrated IR spectrum for $\lambda < 45$ μm. As the FUV extinction originates from PAH molecules, (b) suggests that the SMC is over-abundant in PAHs, which is in contradiction to the low integrated 12 μm emission (see Table 7.1), produced mainly by PAHs. Rodrigues et al. (1997) find evidence that the increase of FUV extinction is associated with regions in the SMC protected from the Interstellar Radiation Field (ISRF) (such as molecular clouds). In general, it seems that PAH molecules are not very abundant in the SMC.

The most of the IR emission of the SMC, for $\lambda > 45$ μm, seems to arise from large grains (component (i)). These grains are in a thermal equilibrium with the ISRF and radiate as quasi-blackbody emitters within a narrow temperature range (Dwek et al. 1997). We assume that the FIR emission is optically thin and that the radiation is isotropic. Along each line-of-sight, therefore, the IR intensity I_ν is an integral over all dust temperatures:

$$I_\nu = \int_T \rho_T \kappa_\nu B_\nu(T) dT, \tag{7.1}$$

where ρ_T is the mass density of a dust component at temperature T and κ_ν is the mass absorption coefficient (opacity). The mass absorption coefficient is given by:

$$\kappa_\nu = \kappa_{100\mu\mathrm{m}} (\lambda/100\mu\mathrm{m})^{-n}, \tag{7.2}$$

with n varying between 2.0 for graphite, 1.5 for silicate and 1.0 for amorphous carbon. We assume $\kappa_{100\mu\mathrm{m}} = 41$ cm^2 g^{-1} and adopt $n = 2.0$ (Reach et al. 1995; Schlegel, Finkbeiner & Davis 1998).

7.3 Dust temperature distribution

The integrated IR spectrum in Fig. 7.3 and the discussion in Section 7.2.4 indicate that normal grains are the most abundant type of dust grains in the SMC. They emit as quasi-blackbodies at $\lambda \gtrsim 60$ μm within a narrow temperature range. Therefore, under the simplification that along each line-of-sight only one temperature component is present, the ratio of two spectral points of a quasi-blackbody (I_ν) is recursively related to dust temperature T_d by:

$$T_\mathrm{d} = \frac{h(\nu_1 - \nu_2)}{k \ln\left(\left(\frac{\nu_1}{\nu_2}\right)^{3+n}\left(\frac{I_{\nu_2}}{I_{\nu_1}}\right) + C_\mathrm{T}\right)} \tag{7.3}$$

with h and k being Planck's and Boltzmann's constants respectively, n being exponent of the absorption coefficient ($n = 2.0$) and C_T being a temperature-dependent

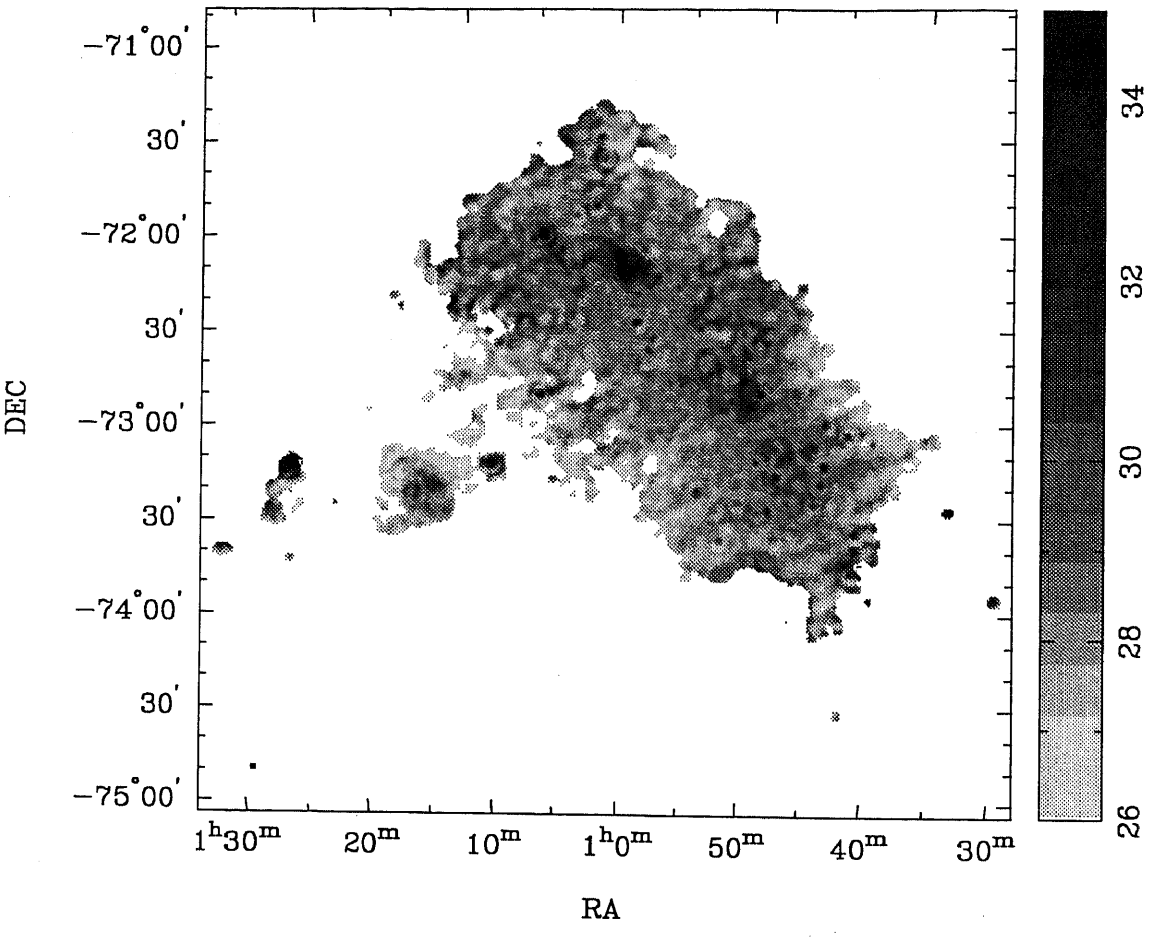

Figure 7.4 . The dust temperature image of the SMC derived from the 60 and 100 μm ratio map. The grey-scale intensity range is 26 to 35 K, with a linear transfer function. The maximum temperature, 45 K, is at position RA $01^h24^m42^s$, Dec $-73°11'45''$ (J2000), which corresponds to N88 (Davies, Elliot, Meaburn 1976).

correction factor:

$$C_T = \left(1 - (\frac{\nu_1}{\nu_2})^{3+n}(\frac{I_{\nu_2}}{I_{\nu_1}})\right) \exp\left(\frac{-h\nu_2}{kT_d}\right) \tag{7.4}$$

(Schwering 1988). However, Schwering (1988) shows that using $C_T = 0$ at the 60 and 100 μm bands introduces an error of only 1 K in dust temperature determinations, if $T_d < 45$ K.

To match the point-spread functions of 60 and 100 μm images, both images were smoothed to 2.3 arcmin resolution and the 60-to-100 μm ratio image was derived. Further, applying equation (3), with the assumption that $C_T = 0$, and with a 4-σ flux cut-off (to stop noise from increasing), we derive the dust temperature image.

The resultant dust temperature image is shown in Fig. 7.4. The temperatures vary from 45 K close to HII regions in the optical bar and the Eastern Wing (e.g. N88),

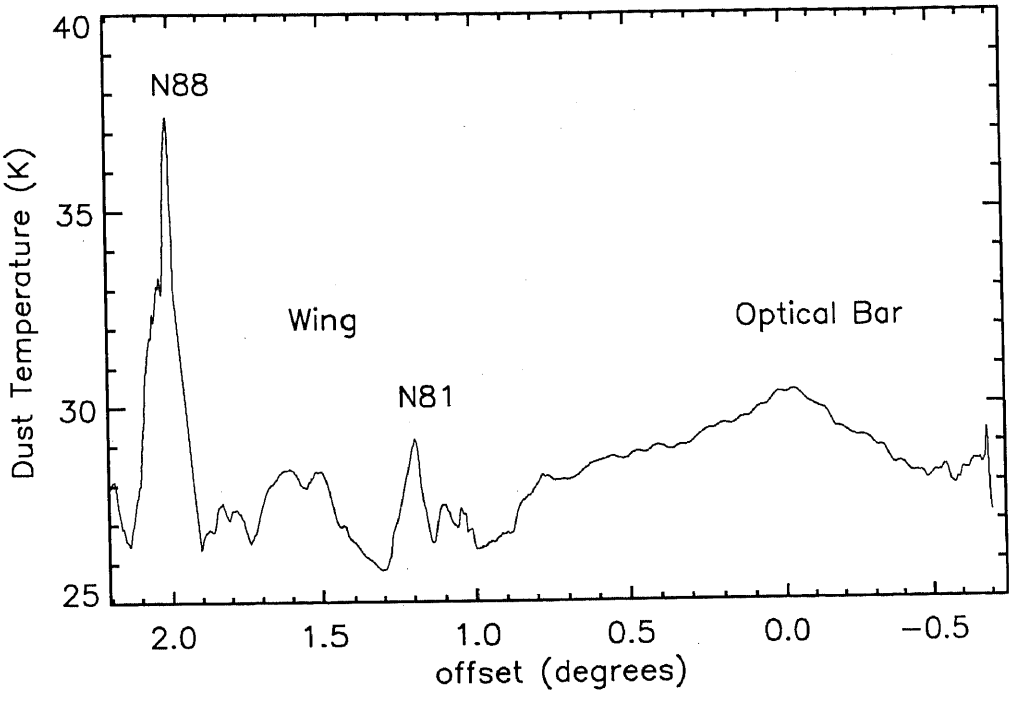

Figure 7.5 . The dust temperature integrated along the optical major axis (at position angle of 40°) and plotted as a function of distance (in degrees) from RA $00^{h}52^{m}$, Dec $-73°00'$ (J2000) along the minor optical axis, starting from south-east.

dropping to 23 K off at the outskirts of the SMC. To compare with the previous results of Schwering (1988), we identify three different temperature regimes in Fig. 7.4:

1. $23 < T_{\rm d} < 29$ K – corresponds to diffuse emission originating from dust heated by the ISRF and covering $\sim$ 54 % of the area.
2. $29 < T_{\rm d} < 31$ K – corresponds to the hot diffuse emission in the environment of prominent HII regions and covering $\sim$ 39 % of the area.
3. $31 < T_{\rm d} < 45$ K – corresponds to discrete hot HII regions and covers $\sim$ 7 % of the area shown in Fig. 7.4.

Because of our greater resolution, the overall temperature range we find is greater than that measured by Schwering (1988). Surprisingly, though, we find that the diffuse dust component (1) is much more extensive than the negligible figure suggested by Schwering.

Fig. 7.5 shows the dust temperature, integrated along the optical major axis (position angle 40°), as a function of distance along the minor optical axis. The optical

bar of the SMC, the Eastern Wing and HII regions N88 and N81 are very prominent. The decrease of the dust temperature towards the edges of the optical bar and Eastern Wing (noted above) is now very prominent. This is unlike the case for the Galaxy (Sodroski et al. 1994) and probably reflects the expected decrease of the ISRF away from regions of high stellar density in the SMC. In the Galaxy, emission at 60 μm appears to have a component due to very small dust grains which are not in thermal equilibrium. In the SMC, this component appears to be less significant.

For the Galaxy, Sodroski et al. (1994) find that 60–75 % of the far-IR luminosity (at 140 and 240 μm) arises from cold ($\sim$ 17–22 K) dust associated with diffuse HI clouds, 15–30 % from cold ($\sim$ 19 K) dust associated with molecular clouds and less than 10 % from warm ($\sim$ 29 K) dust in extended HII regions. These temperature ranges are somewhat lower than we find in the SMC, suggesting that the SMC has a stronger ISRF, possibly due to lower metallicity and higher star-formation rates. Schlegel, Finkbeiner & Davis (1998) also find, from 100 and 240 μm all-sky data, that the Galactic dust temperature is lower than that in the SMC, varying between 17 and 21 K.

7.3.1 Dust mass column density

For a homogeneous object, in an optically thin case ($\tau_\nu << 1$) the dust mass column densities (per unit solid angle) can be calculated from:

$$N_{\rm d} = \frac{I_\nu}{\kappa_\nu B_\nu(T_{\rm d})} \frac{1}{\Delta\Omega} \tag{7.5}$$

where $\Delta\Omega$ is a solid angle corresponding to an area of 1 cm^2 at the distance of the SMC (Schwering 1988). The slow local variation of the dust temperature enables us to use the dust temperature image, with 2.3 arcmin resolution, in conjunction with 100 μm intensity image having 1.7 arcmin resolution. Therefore, the resolution of the derived dust mass column density image is 1.7 arcmin. The distribution of the dust column density across the SMC is shown in Fig. 7.6. This map shows a wealth of small scale structure, with a variety of filamentary and shell-like features in the optical bar and towards its edges. We will discuss some of these later in more detail. The column densities range from 0 to 2.1×10^8 M$_\odot$ sr^{-1}, or 0 to 9.4 $\times 10^8$ dust particles cm^{-2} (where a conversion factor from M$_\odot$ sr^{-1} to dust particles cm^{-2} is equal to 4.45 for the mass of an average grain of 1.3×10^{-17} kg (Schwering 1988)). The highest values correspond to HII regions in the optical bar and Eastern Wing.

Equation 7.5 shows that the derived value for $N_{\rm d}$ strongly depends on $T_{\rm d}$. For the same value of I_ν, a decrease of $T_{\rm d}$ from 31 K to 23 K would increase $N_{\rm d}$ by a factor of 5. The same equation shows that a strong correlation between I_ν and $N_{\rm d}$ should be expected, as can be seen in Fig. 7.7. The slope of this correlation decreases for higher values of I_{100} showing that, for higher temperature, IR intensity increases

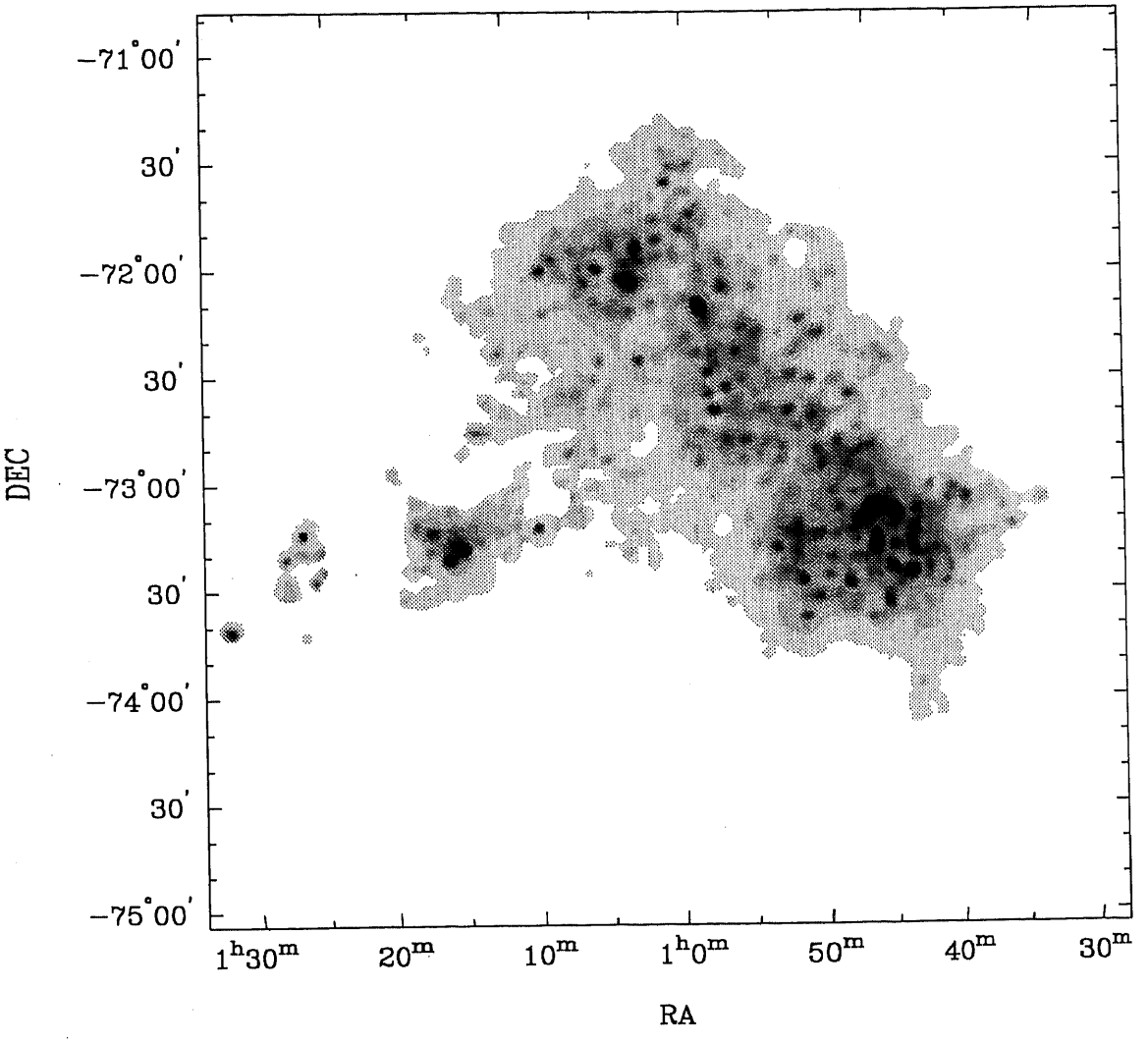

Figure 7.6 . The dust mass column density image of the SMC. The grey-scale range is 0 to 7 $\times 10^7$ $M_\odot$ sr^{-1} with a linear transfer function. The maximum column density is 2.1 $\times 10^8$ $M_\odot$ sr^{-1}. The conversion factor from $M_\odot$ sr^{-1} to dust particles cm^{-1} is equal 4.45. The image has resolution of 1.7 arcmin.

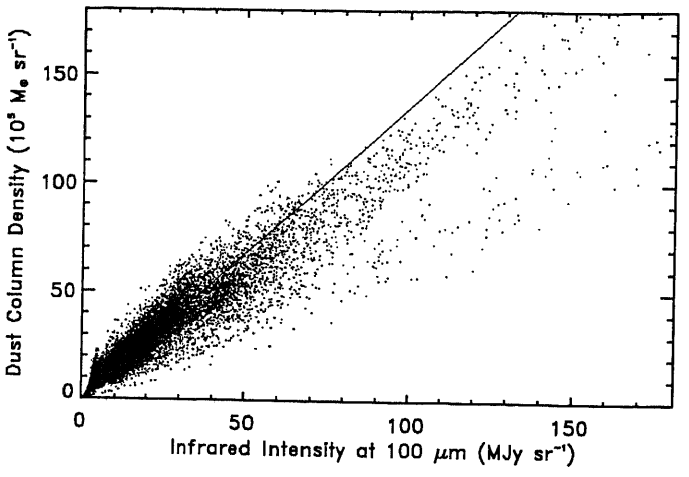

Figure 7.7 . A pixel-to-pixel comparison of the IR intensity at 100 μm (I_{100}) and the dust column density ($M_{\rm d}$), showing a strong correlation. The slope decreases for higher values of I_{100} due to the temperature effect. The linear data fit is overlaid.

much faster than the dust column density.

7.3.2 Dust mass ($M_{\rm d}$) and its uncertainty

An initial estimate of the dust mass of $M_{\rm d} = (1.8 \pm 0.2) \times 10^4$ M$_\odot$ was obtained by spatially integrating the dust mass column densities. This is slightly higher than derived by Schwering (1988), $M_{\rm d} = (1.4 \pm 0.2) \times 10^4$ M$_\odot$, with most of the difference being due to the wider temperature range present in the higher-resolution data. The slightly different area used for the integration of dust column density may also contribute.

Although dust grains emit within a narrow temperature range, a line-of-sight can pass through regions with a different ISRF and therefore with different dust temperature components. Hence, for an object with a large line-of-sight depth, the assumption of a single dust temperature along each line-of-sight might be a crude approximation. This contributes mainly to the uncertainty of the derived dust mass ($M_{\rm d}$) (Draine 1990). To estimate how big the effect can be, the data were compared with a simple dust model from Schlegel, Finkbeiner & Davis (1998).

If a region in the SMC contains an amount (M_{23}) of dust at temperature 23 K, plus a mass fraction $f_{\rm T}$ of dust at temperature T, IR intensities corresponding to these two temperature components are given by:

$$I_\nu^{23} = \frac{M_{23}}{\alpha_\nu e^{h\nu/23k}} \tag{7.6}$$

$$I_\nu^{\mathrm{T}} = \frac{M_{\mathrm{T}}}{\alpha_\nu e^{h\nu/k\mathrm{T}}}, \tag{7.7}$$

where $\alpha_\nu = c^2/\kappa_\nu 2h\nu^3$. The measured IR intensity is then equal to a sum of both intensity components: $I_{\mathrm{tot}}(\nu) = I_\nu^{23K} + I_\nu^{\mathrm{T}}$.

Under the assumption of a single dust temperature along a line-of-sight, $I_{\mathrm{tot}}(\nu)$ for both 60 and 100 μm is used in equation 7.3 to estimate the dust temperature T', which will have a value between 23 K and T. This provides a further estimate of the dust column density and dust mass M_{d}' in the region, which is always less than the true dust mass.

However, if we consider both temperature components present, the dust mass is simply:

$$M_{\mathrm{d}} = M_{23} + \frac{f_{\mathrm{T}}}{(1-f_{\mathrm{T}})} M_{23}. \tag{7.8}$$

The ratio of recovered (M_{d}') and true dust mass (M_{d}) is then given by:

$$R(f,T) = \frac{M_{\mathrm{d}}'(f_{\mathrm{T}},T)}{M_{\mathrm{d}}(f_{\mathrm{T}})} \tag{7.9}$$

and is a two-dimensional function of f_{T} and T, bounded by 1. For a range of mass fractions of the second component, f_{T}, and a range of temperatures of the second component, T, Fig. 7.8 shows contours of the ratio of recovered dust mass and true dust mass.

Assuming a single dust temperature model, we have calculated (Section 7.3) temperatures in the SMC to be in the range 23–45 K, with the temperature of the diffuse dust component in the range 23–31 K. From Fig. 7.8, for $19 < T < 30$ K, the true dust mass is underestimated by < 30 %. Temperatures higher than 31 K (e.g. near HII regions) only occur in a small area of the SMC ($\sim$ 7 %) and probably do not contribute significantly to an underestimate of the dust mass.

Another important source of uncertainty in the derived dust mass is cold dust. Because of the quasi-blackbody cooling nature of dust grains, $I_\nu \propto T^{4+n}$, cold dust (< 20 K) does not contribute significantly to the IR intensity. Therefore, a large amount of cold dust can be masked by the presence of a small amount of cool ($\sim$ 25 K) or warm ($\sim$ 50 K) dust.

The lower limit for dust temperature, contributing to IR emission at 100 μm, in the Galaxy is 17 K (Schlegel, Finkbeiner & Davis 1998). Since the SMC has a stronger ISRF than the Galaxy, we would not expect dust in the SMC to be cooler than dust in the Galaxy. Taking 17 K, therefore, as a lower limit for the temperature of cold dust in the SMC, we find from Fig. 7.8 that the total dust mass would be at most underestimated by 60 %. A similar estimate was found in Schwering (1988) using different methods. This provides an estimate of the total dust mass in the SMC, $M_{\mathrm{d}} = 1.8^{+1.3}_{-0.2} \times 10^4$ M$_\odot$.

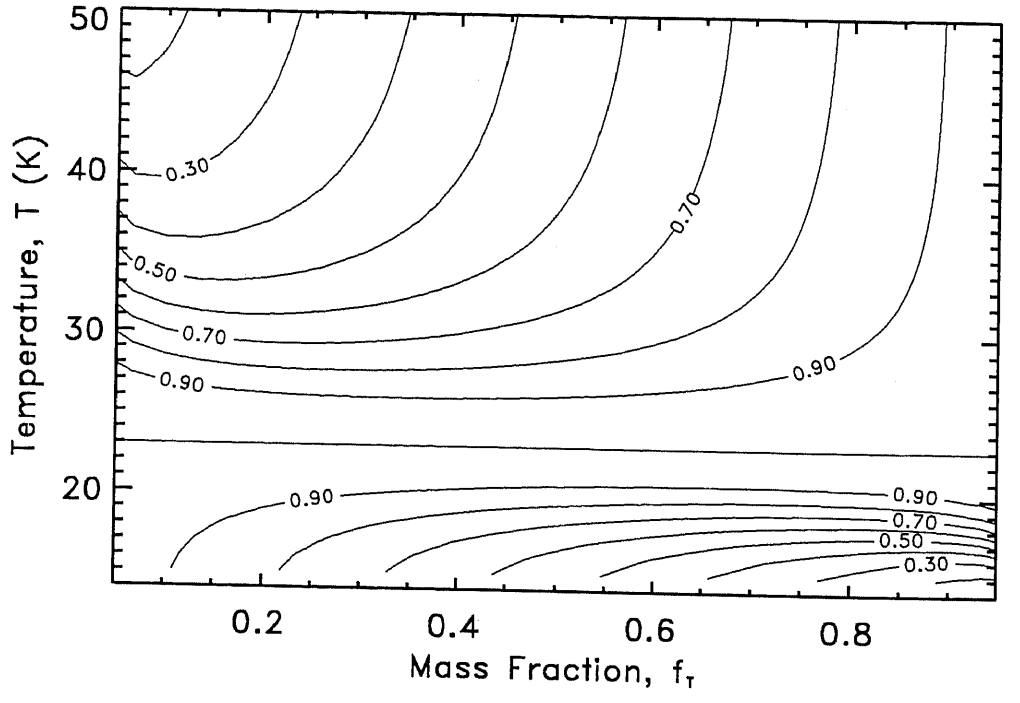

Figure 7.8 . Contours of the ratio of the recovered and true dust mass plotted as a function of temperature and the mass fraction f_T of dust at temperature T. Following Schlegel, Finkbeiner & Davis (1998), this plot illustrates how much the true dust mass can be underestimated if a single temperature is assumed where two temperatures are present (23 K and T).

7.4 Summary

- The high angular resolution far-infrared images of the Small Magellanic Cloud (SMC), at 12, 25, 60 and 100 μm, were presented here for the first time. These images were reconstructed from survey and non-survey (PO) data, obtained with the IRAS, using the Pyramid Maximum Entropy algorithm. The angular resolutions of the images are 1 arcmin at 12, 25 and 60 μm and 1.7 arcmin at 100 μm.

- The integrated HIRAS spectrum of the SMC compares well with previous observations. The spectrum peaks around 100 μm and has a local minimum around 12 μm, suggesting that PAH molecules do not play an important role in the SMC. The far-IR part of the spectrum can be reasonably well modelled with a composition of the quasi-blackbody curves for temperature range 15 – 30 K. This points out that large dust grains, which are in thermal equilibrium, are predominantly responsible for IR emission at $\lambda \gtrsim 45$ μm.

- The standard dust model, outlined here, was used to derive a temperature map and a dust column density distribution. Dust temperatures range from 23 to 45 K which is, on average, warmer than for the Galaxy, though there is a deficit of warm, very small dust grains in the SMC. While estimating the total mass of cool dust, it was found that the dust mass may be underestimated by $< 30\%$ due to the presence of different temperature components along the line-of-sight, and altogether by $< 60\%$ if the dust cooler than 20 K exists in the SMC. The total amount of cool dust in the SMC is thus $1.8^{+1.3}_{-0.2} \times 10^4$ $M_\odot$.

Chapter 8

Dust and gas in the SMC

8.1 Introduction

In this chapter, the relationship between the neutral gas and the dust in the SMC is investigated on various spatial scales using a few different approaches. The HI data were presented in Chapter 4. The IR data, presented in Chapter 7, match perfectly the resolution of HI, enabling a detail comparison of the two, all the way down to 30 pc.

In the first part of this chapter, Section 8.2, a possible spatial variation of the dust-to-gas mass ratio is probed. On the assumption that gas and dust are well-mixed, a presence of a large amount of molecular hydrogen and/or cold dust ($T < 15$ K) is investigated. Alternatively, an intrinsic variation of the dust-to-gas mass ratio and its relationship with the metallicity are suggested. The average value of the dust-to-gas mass ratio is also compared with previous studies.

The second part of this chapter, Section 8.3, addresses the statistical investigation of both dust and HI content in the ISM, as well as their mutual correlation. The spatial power spectrum is used, as a statistical descriptor, to examine HI brightness distribution for velocity channels ~ 5 km s^{-1} wide. As the result, an alternative fractal model is suggested for the ISM in the SMC. The IR intensity fluctuations are further discussed, followed by the dust and HI column density fluctuations. Finally, the coherency spectrum is employed to investigate statistically the correlation between gas and dust over a wide range of spatial scales.

8.2 Dust-to-gas mass ratio ($D_{\rm g}$)

The comparison of the IR intensity, at all wavelengths from 100 μm to 1 mm, and HI column density in the case of our own Galaxy have shown a good linear correlation

for low flux levels (Schlegel, Finkbeiner & Davis 1998; Boulanger et al. 1996), with $I_{100} \approx 0.5W_{\rm HI} + 0.3$ ($W_{\rm HI}$ is velocity-integrated HI brightness temperature in units of K km s^{-1}and I_{100} is in units of MJy sr^{-1}). Substantial scatter has been found for higher flux levels and has been usually attributed to the presence of molecular hydrogen. In the case of the SMC, Schwering (1988) has noted a good qualitative correlation between the IRAS 100 μm intensity and HI column density (using radio data from McGee & Newton 1981), with remarkable differences in some cases (such as N66), where he suggests gas is either completely blown away or in molecular form. It was also found that $I_{100} \propto N_{\rm HI}^{\beta}$, with $\beta = 2.2$, showing that IR intensity increases with the HI column density much faster in the SMC than in the Galaxy. The HIRAS data at 100 μm and the HI column density, used here, show similar results: a tight correlation between I_{100} and $N_{\rm HI}$ is seen within the optical bar and the central part of the Eastern Wing, while in the Eastern Wing in general and especially in the region between the optical bar and the Wing, the correlation is much weaker.

To compare HI column density (Section 4.2) with the dust mass column density (Section 7.3.1), we first apply corrections for self-absorption to the HI data (see Section 4.2.1) and obtain the total HI column density. The dimensionless dust-to-gas mass ratio, shown in Fig. 8.1, is then derived. The image has a range between 0 and 6×10^{-4}, showing that the gas content (by mass) in the SMC is much higher than the dust content. A significant variation of $D_{\rm g}$ is visible across the SMC, with a variety of small scale features. The main impression the dust-to-gas ratio image leaves is a 'granulated' appearance revealing various HII regions with a significantly higher dust-to-gas mass ratio relative to the spatially averaged value across the whole SMC of 2.5×10^{-5}. It is believed that the gas and dust are well mixed together in the ISM (Cox & Mezger 1989). The local variation of the dust-to-gas ratio therefore reflects more local phenomena, such as:

1. an atomic gas deficiency due to H_2 formation;
2. excess dust created in regions of massive star formation; and
3. the presence of cold dust not emitting at 100 μm.

Similar variation of $D_{\rm g}$ in the SMC has been noted in Schwering (1988) (with a peak of 1.5 $\times10^{-4}$), who has attributed most of it to the presence of a significant amount of molecular gas. We address this question further in more detail. In Fig. 8.2 we show the dust-to-gas mass ratio integrated along the optical major axis and plotted as a function of distance from the optical bar. This profile, together with Fig. 8.1, distinguishes a few regions with a significantly different values of $D_{\rm g}$.

8.2.1 $D_{\rm g}$ in discrete HII regions

The highest values of the dust-to-gas ratio are found in discrete bright HII regions (e.g. N81 and N88). HII regions as, in general, sites of the most recent star forma-

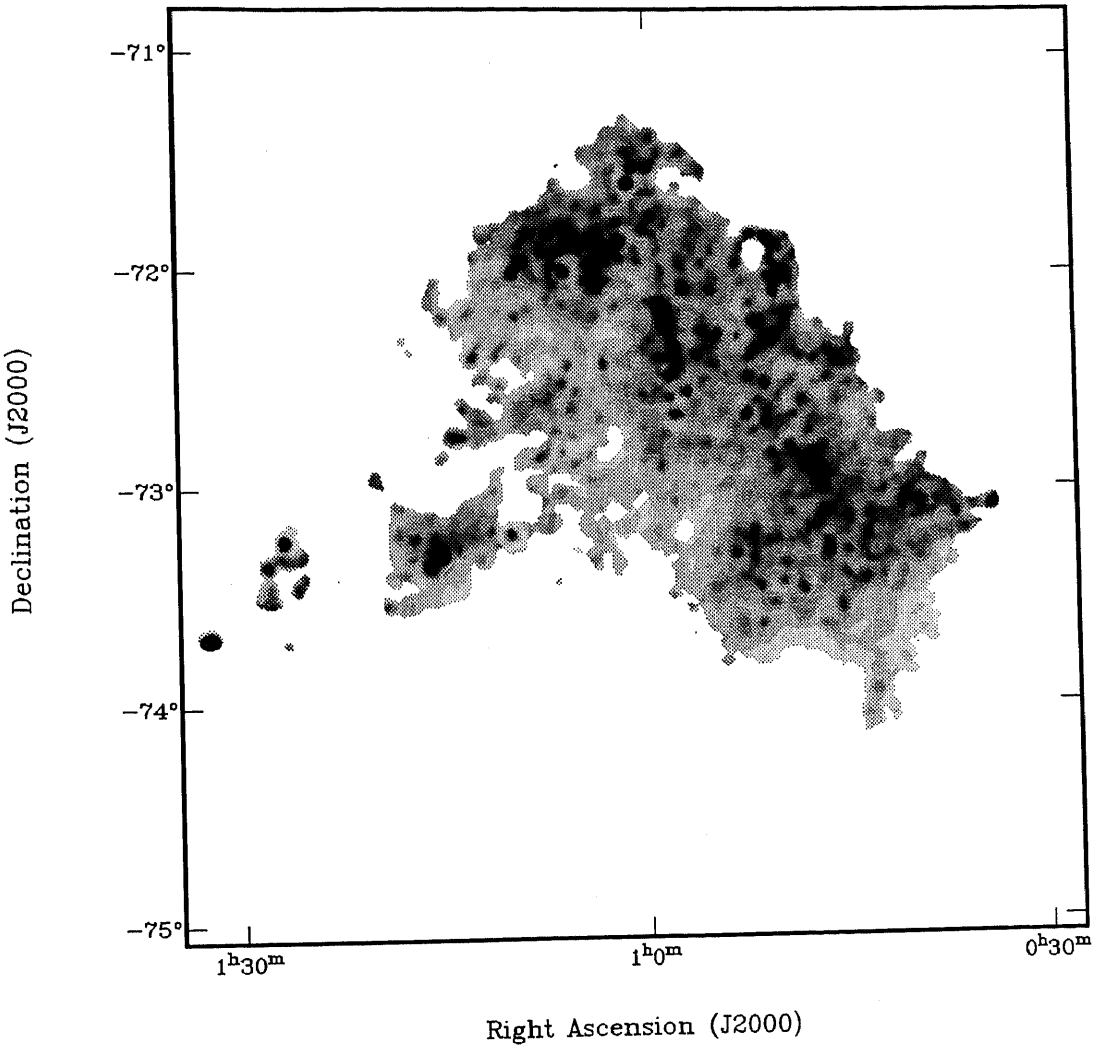

Figure 8.1 . The dust-to-gas mass ratio map of the SMC. The grey-scale range is (0 – 1) $\times 10^{-4}$, with a linear transfer function. The maximum dust-to-gas mass ratio of 6 $\times$ 10^{-4} corresponds to N88 and is at position RA $01^h24^m3^s$, Dec $-73°13'45''$ (J2000).

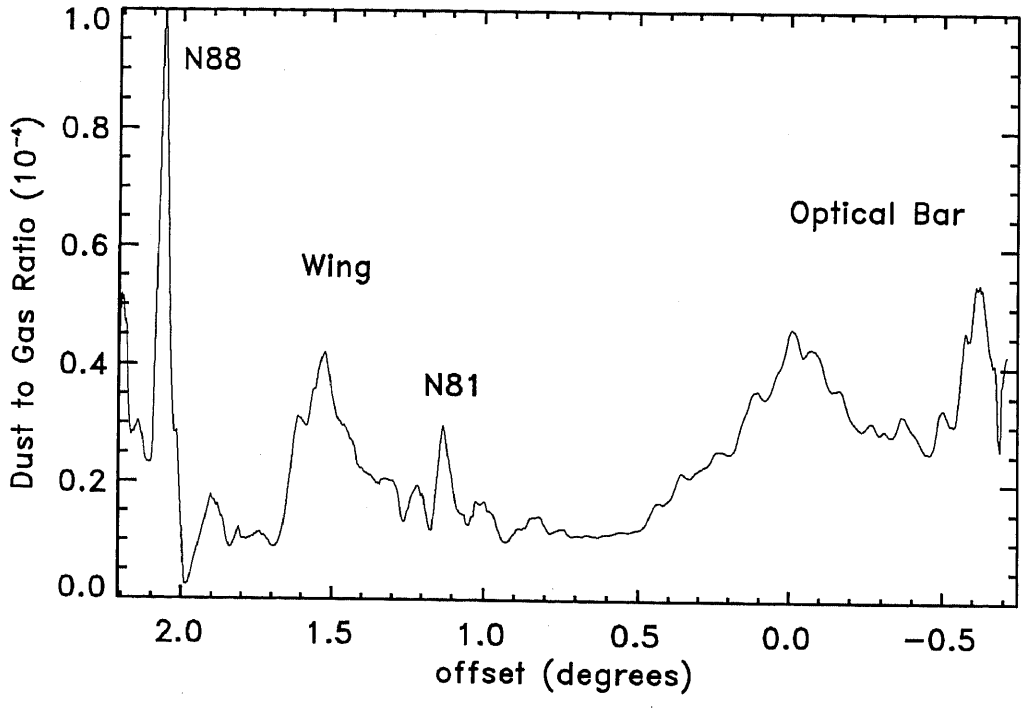

Figure 8.2 . The dust-to-gas mass ratio (D_g) integrated along the optical major axis (at position angle of 40°) and plotted as a function of distance (in degrees) from RA 00^h52^m, Dec −73°00′ (J2000) along the minor optical axis, starting from south-east. This slice has the same resolution as the one in Fig. 7.5.

tion are usually located on the edges or embedded in the clouds of dense and cold gas (Gordon 1988). The brightest HII regions in the SMC are usually found to be larger and more diffuse than the ones in the Galaxy (Copetti 1990), and their morphology can be explained by the metallicity effect. Being in such a low-metallicity environment, the size of the CO-emitting core within a molecular cloud, associated with an HII region, shrinks while the photon-dominated region (PDR) simultaneously increases its volume (Israel et al. 1996).

The 100 μm IR emission and also HI emission, associated with an HII region, come from a dense layer surrounding the HII region (Gordon 1988). These layers are usually dust and gas rich with dust temperatures (in the SMC) of 31 – 45 K. Kurt et al. (1995) and Kurt & Dufour (1998) examined abundances of C, N and O in a few HII regions in the SMC. They find that, for N88 in particular, the O/H ratio is not indicative of O enrichment arising from mass loss. This is supportive of case (1) (Section 8.2) for the apparent excess dust associated with N88. The O/H ratio found for N88 is very similar to values found in a few other HII regions in the SMC. A similar effect has been found in the Galaxy where Reach, Wall, & Odegard (1998)

find that most of their excess IR emission from high latitude clouds comes from dust associated with molecular gas.

8.2.2 Hidden gas, hidden dust or a real dust-to-gas gradient?

Both the optical bar and the Eastern Wing show in general a similar trend in D_g, peaking in the middle of the region, where most of the recent star formation is concentrated, and having a steep decrease towards the edges (Fig. 8.2). Diffuse regions in the immediate environment of HII regions, have a dust-to-gas ratio very close to the estimated spatial average value (2.5×10^{-5}). Being less exposed to the strong radiation field, their gas content is mostly atomic. Since the IR intensity at 30 K peaks around 100 μm, the measured dust mass is reasonably well-estimated. Therefore, the estimated values for the dust-to-gas ratio for these regions are probably accurate.

An interesting feature stands out in Fig. 8.2. The dust-to-gas ratio drops significantly in the region between the bar and the Eastern Wing. The measured dust temperature here reaches almost the minimum value (23 K). If a significant amount of dust cooler than 23 K is present, an underestimate of the total dust mass could explain the decrease in D_g (case (3) in Section 8.2). In the study of a sample of nearby, spiral galaxies, Alton et al. (1998) indeed found that cold dust ($T_d \leq$ 18–21 K) is more prevalent at larger galactic radii.

On the other side, further towards the west from the middle of the bar, the profile in Fig. 8.2 shows, interestingly, a secondary maximum almost at the edge of the bar. This increase mainly comes from the loop-like feature shown in Fig. 8.1. This is associated with the HI shells: SMC HI-199, SMC HI-202 and SMC HI-170 (Staveley-Smith et al. 1997) and with the several neighbouring HII regions. Most likely, molecular gas formation (case (1), Section 8.2) is again responsible for the high value of D_g.

Let us try now to explain the observed variation of D_g as a result of local phenomena (i) and (iii) only. We assume first that the real value of the dust-to-gas ratio is around 1.25×10^{-5} in the region between the optical bar and the Eastern Wing, and that all values for $D_g > 1.25 \times 10^{-5}$ come from the atomic gas deficiency due to the presence of significant amount of molecular hydrogen. Measuring the dust and HI mass in the regions of the SMC where $D_g > 1.25 \times 10^{-5}$, we can estimate the mass of the molecular hydrogen which needs to be added so that the dust-to-total gas ratio in the SMC can everywhere have a constant value of 1.25×10^{-5}. The result is that the required mass of molecular hydrogen is about 8.4×10^8 $M_\odot$, i.e. ~ 2 times that of atomic hydrogen, and almost 30 above the estimated mass of H_2 of 3×10^7 $M_\odot$ from CO observations (Rubio, Lequeux, & Boulanger 1993). The total H_2 mass of the SMC of $(0.75 \pm 0.25) \times 10^8$ $M_\odot$, estimated by Israel (1997), after a

re-examination of the CO to H_2 conversion factor, is still more than 10 times lower than here suggested value. We therefore conclude that the assumption, in which all dust excess comes from the molecular gas, appears to be untenable.

Another alternative for the variation in D_g (of almost a factor of 3) is the presence of cold dust, not seen at 60 or 100 μm. The low-resolution COBE/DIRBE data at 140 and 240 μm give the best available constraint on dust content on temperatures < 20 K. The 240/140 μm ratio map is noisy and has low resolution (0.7 deg) but provides evidence for temperatures as low as 15 K, somewhat lower then the HIRAS lower limit of 23 K. If we assume all of the 240 μm luminosity, Fig. 7.3, arises from dust at 15 K, then the 'hidden' cold dust mass is $\sim 2.4\times10^4$ $M_\odot$. This is still insufficient to explain variation in D_g. However, at lower temperatures there can be an even larger amount of dust present, as shown on Table 8.1. It is questionable whether dust so cold can exist in the SMC, and especially in such an amount. Future observations at longer IR wavelengths are necessary in order to understand the role such cold dust may play in the ISM. However, the interesting point to note is that cold dust is capable of hiding a huge amount of matter.

Table 8.1 . An estimate of the mass of cold dust having temperature of 15, 12, 10 or 8 K. Values are derived under assumption that a particular dust temperature (at 15, 12, 10 or 8 K) is entirely responsible for the total luminosity at 240 μm, obtained from the low-resolution COBE/DIRBE data.

Temperature (K)	15	12	10	8
Mass ($M_\odot$)	2.4×10^4	9.5×10^4	3.7×10^5	2.9×10^6

However, for the time being, it appears that neither the atomic gas deficiency due to hidden H_2, nor the presence of hidden cold dust can explain the derived variation of D_g. Although a combination of these effects most likely plays an important role, the existence of the third scenario, the intrinsic spatial variation of D_g, seems to be very likely. Intrinsic radial gradients in D_g have been seen in several nearby spiral galaxies (Viallefond, Goss, & Allen 1982; Viallefond & Goss 1986; Walterbos & Schwering 1987; van der Hulst et al. 195; Issa, MacLaren, & Wolfendale 1990) and in our own Galaxy (Sodroski et al. 1997). Sodroski et al. (1997) explain a decreases of D_g with increasing Galactocentric distance as being due to a decrease of the stellar efficiency in recycling of the disk material. As dwarf galaxies, in general, have stochastic star formation and chemical evolution, it is usually hard to notice any radial dependence in their D_g (Issa, McLaren & Wolfendale 1990). The significant large-scale trend in D_g in the SMC, from the optical bar to the Eastern Wing (Fig. 8.2), may suggest a radial gradient of D_g, seen for the first time in a dwarf galaxy.

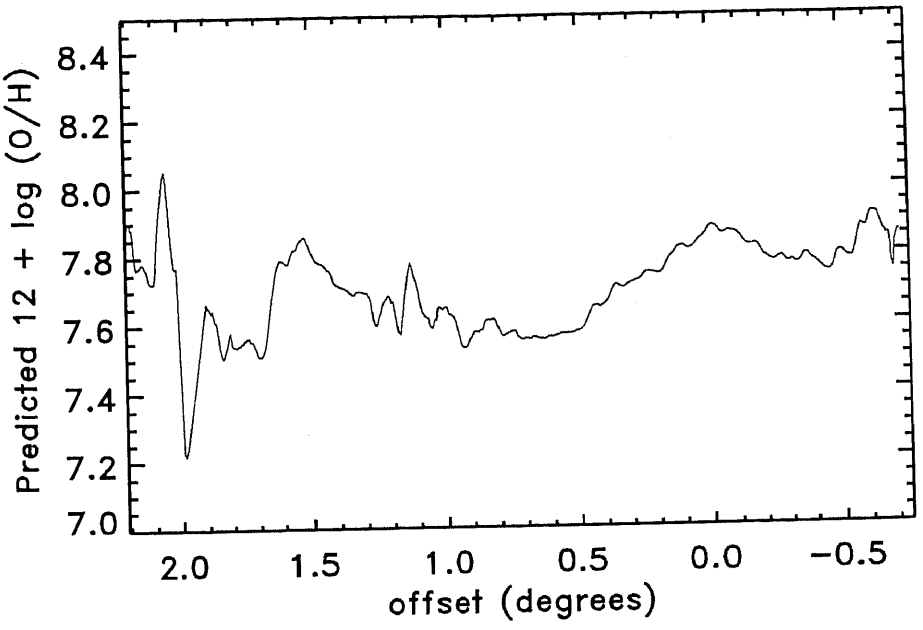

Figure 8.3 . The predicted variation of the oxygen abundance in the SMC for the profile of the dust-to-gas mass ratio shown in Fig. 8.2 using the correlation found by Lisenfeld & Ferrara (1998). The profile was scaled using the metallicity of HII region N88 from Kurt et al. (1995).

8.2.3 The relationship between D_g and metallicity

Dwek (1998) has presented a model for the dynamical and chemical evolution of dust abundances and composition in the ISM of the Galaxy. In this model, the grain life-cycle starts with the grain formation in quiescent stellar outflows and/or explosive eruptions of novae and type II supernovae. Once formed, dust grains get ejected into the ISM where they are further processed under exposure to various processes which influence their abundance and physical properties. While various processes in the ISM are very destructive for dust grains, the grain growth by the accretion process plays a very important role in establishing the dust mass.

The Dwek (1998) model predicts that D_g decreases with the galactocentric radius and that its decrease tightly follows the ISM metallicity, regardless of the star formation history of the ISM. The correlation between D_g and metallicity appears to be a consequence of the fact that the relative efficiency of the grain destruction and grain accretion processes is constant with time. Both the D_g radial dependence and the correlation with metallicity agree well with the observational results for the Galaxy by Sodroski et al. (1997). The variation of D_g in the SMC may also probe metallicity variations and the evolutionary history of the SMC.

Further support to the dust evolutionary model by Dwek (1998) is given by Lisenfeld

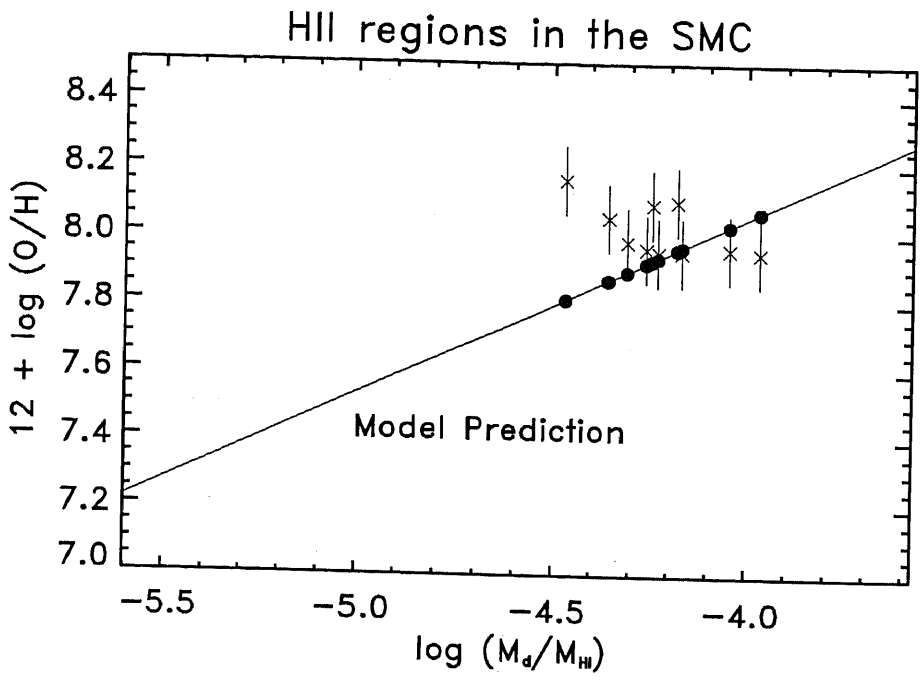

Figure 8.4 . The correlation between the dust-to-gas mass ratio and the oxygen metallicity suggested by Lisenfeld & Ferrara (1998), scaled by the metallicity of HII region N88 from Kurt et al. (1995). Several HII regions in the SMC, from Dufour & Harlow (1977), Pagel, Edmunds & Fosbury (1978) and Kurt & Dufour (1998), are shown with crosses. Their oxygen metallicities predicted by the correlation were shown with filled circles.

& Ferrara (1998) who examined the variation of D_g with metallicity in a sample of dwarf galaxies (including the SMC). They found a correlation between oxygen abundance and dust-to-gas mass ratio given by:

$$12 + \log \mathrm{O/H} \propto (0.52 \pm 0.25) \log(M_d/M_{HI}). \tag{8.1}$$

Their trend of metallicity as a function of D_g is similar to the trend found by Dwek (1998) in a few different Galactic regions, though with a significant offset. This may be due to the stochastic nature of star formation and chemical evolution in dwarf galaxies and their underestimated dust content (Dwek 1998).

We have applied the correlation from Lisenfeld & Ferrara (1998) to the distribution of D_g along the minor optical axis in the SMC, the spatial variation of the oxygen abundances can be predicted. The profile is plotted in Fig. 8.3 showing a variation by a factor of two along the minor optical axis, which is quite reasonable. Hence, if the suggested relation between the metallicity and D_g holds in the SMC, a variation in metallicity across the SMC by factor of ~ 2 could completely explain the observed variation in D_g.

To test whether the suggested correlation by Lisenfeld & Ferrara (1998) can be applied for the SMC, D_g was measured for a few HII regions with known metallicity (from Dufour & Harlow 1977; Pagel, Edmunds, & Fosbury 1978; Kurt & Dufour 1998). The metallicities estimated using the correlation (filled circles) and the values obtained from observations (crosses) are plotted in Fig. 8.4. The model is disappointing in that the current HII metallicity data do not fit the predicted correlation, and may even suggest a negative gradient of the oxygen metallicity as a function of D_g whose physical meaning would be hard to explain. It should be noted, though, that most of these HII regions are situated in the optical bar and have very homogeneous properties. Therefore, they may not well represent regions with significantly different value of D_g. Future metallicity measurements of a wider range of objects spread over the SMC are necessary to test the suggested correlation between dust-to-gas ratio and metallicity.

Another important conclusion from the model by Dwek (1998) is that the dust composition (relative abundance of carbon-to-silicate grains) varies with time. As a consequence, several classes of galaxies, with different dust compositions, should be observed. The first class represents young, low-evolved galaxies, where carbon grains are much less abundant than silicate grains. These galaxies have a weak extinction bump at ~ 0.2 μm. According to its extinction curve and the dust grain abundances (see Section 7.2.3), the SMC could belong to this category. The second class of galaxies has the extinction curve represented with the Galactic extinction curve, while the model also predicts the existence of the intermediate-age systems, with an excess extinction peak around 0.2 μm, relative to the Galactic one.

8.2.4 Comparison with previous work

Two methods for determination of the average dust-to-gas ratio are available in the literature:

1. where the dust mass is determined from measured IR intensities, and the HI mass is determined from 21 cm spectral line observations ($M_{\rm HI}/M_{\rm d}$), as used in this paper;
2. where the extinction is determined from photometric observations of stars in the SMC ($E_{\rm B-V}$), and the HI mass ($M^*_{\rm HI}$) is measured in front of these stars from the profile of the Lyman α interstellar absorption line ($M^*_{\rm HI}/E_{\rm B-V}$).

The relationship between quantities $M_{\rm HI}/M_{\rm d}$ and $M^*_{\rm HI}/E_{\rm B-V}$, obtained in these two methods, is given by:

$$\frac{M_{\rm HI}}{M_{\rm d}} = R\left[\frac{M^*_{\rm HI}}{E_{\rm B-V}}\frac{m_{\rm d}}{m_{\rm HI}}(1.086\pi a^2 Q_{\rm V}^{\rm ext})\right]^{-1}, \qquad (8.2)$$

Table 8.2 Comparison of the dust-to-gas ratio in the SMC with previous work.

Reference	$N^*_{\rm HI}/E_{\rm B-V}$ (10^{22} atoms cm^{-2} mag^{-1})	$M_{\rm d}/M^a_{\rm HI}$ (10^{-5})	Method	$\frac{M_{\rm d}^{\rm SMC}}{M_{\rm HI}^{\rm SMC}}/\frac{M_{\rm d}^{\rm MW}}{M_{\rm HI}^{\rm MW}}$ [b]
Bouchet et al. (1985)	3.7	6.1	(2)	0.125
Martin et al. (1989)	4.6	7.5	(2)	0.100
Lequeux (1989)	5.0	8.1	(2)	0.100
Schwering (1988)	-	5.0	(1)	0.018
this paper	-	8.2	(1)	0.031

[a] Obtained using equation 8.2 for method (2).

[b] Bouchet et al. (1985) and Lequeux (1989) assume Galactic value for $N^*_{\rm HI}/E_{\rm B-V}$ of 4.8×10^{21} atoms cm^{-2} mag^{-1}. We have applied the same value on data from Martin, Maurice & Lequeux (1989). For the dust-to-gas value estimated in this paper we use an estimate for an average Galactic dust-to-gas ratio ($M_{\rm d}^{\rm MW}/M_{\rm HI}^{\rm MW}$) of 1/375 from Schwering (1988).

where $R = A_{\rm V}/E_{\rm B-V}$ is the ratio between the visual extinction and the colour excess, a is an average size (radius) of dust grains, $Q_{\rm V}^{\rm ext}$ is the visual extinction efficiency factor, and $m_{\rm d}$ and $m_{\rm HI}$ are masses of an average dust grain and an HI atom, respectively. The conversion strongly depends on parameters R, a and $Q_{\rm V}^{\rm ext}$, whose values are poorly known and also vary from galaxy to galaxy. To compare our results for $M_{\rm HI}/M_{\rm d}$ with values previously found for $M^*_{\rm HI}/E_{\rm B-V}$, we have assumed values: $R = 2.72 \pm 0.18$ (Bouchet et al. 1985), $a = 1 \times 10^{-7}$ m (Schwering 1988) and $m_{\rm d} = 1.3 \times 10^{-17}$ kg (Schwering 1988). The estimate of $Q_{\rm V}^{\rm ext}$ is complex and its value depends on grain nature (size and the refractive index of grain material), geometry and a wavelength. We have assumed here value $Q_{\rm V}^{\rm ext} = 1$, estimated for $\lambda = 0.5$ μm and spherical silicate dust grains having radius of 1×10^{-7} m (from Fig. 3.9 in Evans 1994).

In Table 8.2 we give a comparison of our derived average dust-to-gas ratio with previous estimates, as well as a comparison of the dust-to-gas ratio of the SMC with that of the Milky Way. Note that this value was derived as a ratio of total dust mass (1.8×10^4 M$_\odot$) and total mass of HI (2.2×10^8 M$_\odot$), within around $2° \times 2°$ area of the SMC and shown in Fig 8.1. All estimates of the average dust-to-gas ratio ($M_{\rm d}/M_{\rm HI}$) in the SMC are quite close, although the conversion parameters between independent methods (1) and (2) (R, a and $Q_{\rm V}^{\rm ext}$) are quite uncertain. The value derived from method (1) in Schwering (1988) is slightly lower than the other ones. The average dust-to-gas ratio derived here is very similar to values obtained by Lequeux (1989) and Martin et al. (1989), although two very different methods were used. The estimated average dust-to-gas ratio in the SMC is almost 30 times lower than in the Galaxy, using an average Galactic dust-to-gas ratio of 1/375 from Schwering (1988).

8.3 Statistical investigation of HI and dust spatial distribution

Instead of describing individual ISM features qualitatively, an alternative way is to view them as they were produced with some random process (Lazarian 1995) and attempt to characterise them with a statistical descriptor. Many statistical descriptors have been used for such a purpose and some of their advantages and/or disadvantages can be found in Lazarian (1994) and Lazarian & Pogosyan (1997). We use here the 2-D spatial power spectra, for both HI and IR data, and the cross spectrum between the two. Although these statistical functions do not provide the complete description of the ISM, they give the hierarchy of scales on which structure is present in the ISM, allowing us, for example, to probe the topology of the ISM and the processes involved in its creation.

8.3.1 HI spatial power spectrum

Following previous work in our own Galaxy by Crovisier & Dickey (1983) and Green (1993), the power spectrum of the HI emission fluctuations in the SMC is examined here. With the ATCA and Parkes data combined, we are sensitive to fluctuations with angular sizes ranging from 1.6 arcmin to $\sim 4^\circ$, or over 2 orders of magnitude. Moreover, as the distance to the SMC is well-established (we assume 60 kpc, ignoring any depth), angular size is directly related to physical size, unlike in our own Galaxy where distance determination is relatively uncertain. The corresponding range in linear size is 30 pc to 4 kpc.

The images, uncorrected for self-absorption, for a given velocity range were Fourier transformed. The average value of the square of the modulus of the transform, $\langle \Re^2 + \Im^2 \rangle$, was then measured in 18 annuli of equal width in $\log \sqrt{u^2 + v^2}$ (u and v are the coordinates in the Fourier plane, being measured in wavelengths, λ). As some parts of the Fourier plane corresponding to the ATCA data were not fully sampled (see Fig. 2.6 in Section 2.2), we applied a mask. This mask excluded points outside the ellipse defining the longest baseline (semi-major axis $u = 2230\lambda$), and in three elliptical annuli of semi-major axes $u = 730$, 1440, and 1880λ, respectively. Note that averaging over annuli in the $u - v$ plane was performed assuming the azimuthal isotropy of the spatial power spectra. We address this question again in Section 8.3.3.

Fig. 8.5 shows the two-dimensional spatial power spectra for six heliocentric velocity intervals 21.5 km s^{-1} wide. The spectra are remarkably well fitted by a power law, $P(k) \propto k^\gamma$ (k is in units of λ), over the whole linear size range. This implies that there is no preferred cloud size in the SMC. Because of the quality of the data set, the effects of noise and noise-bias (see Green 1993) are negligible. Unlike Green,

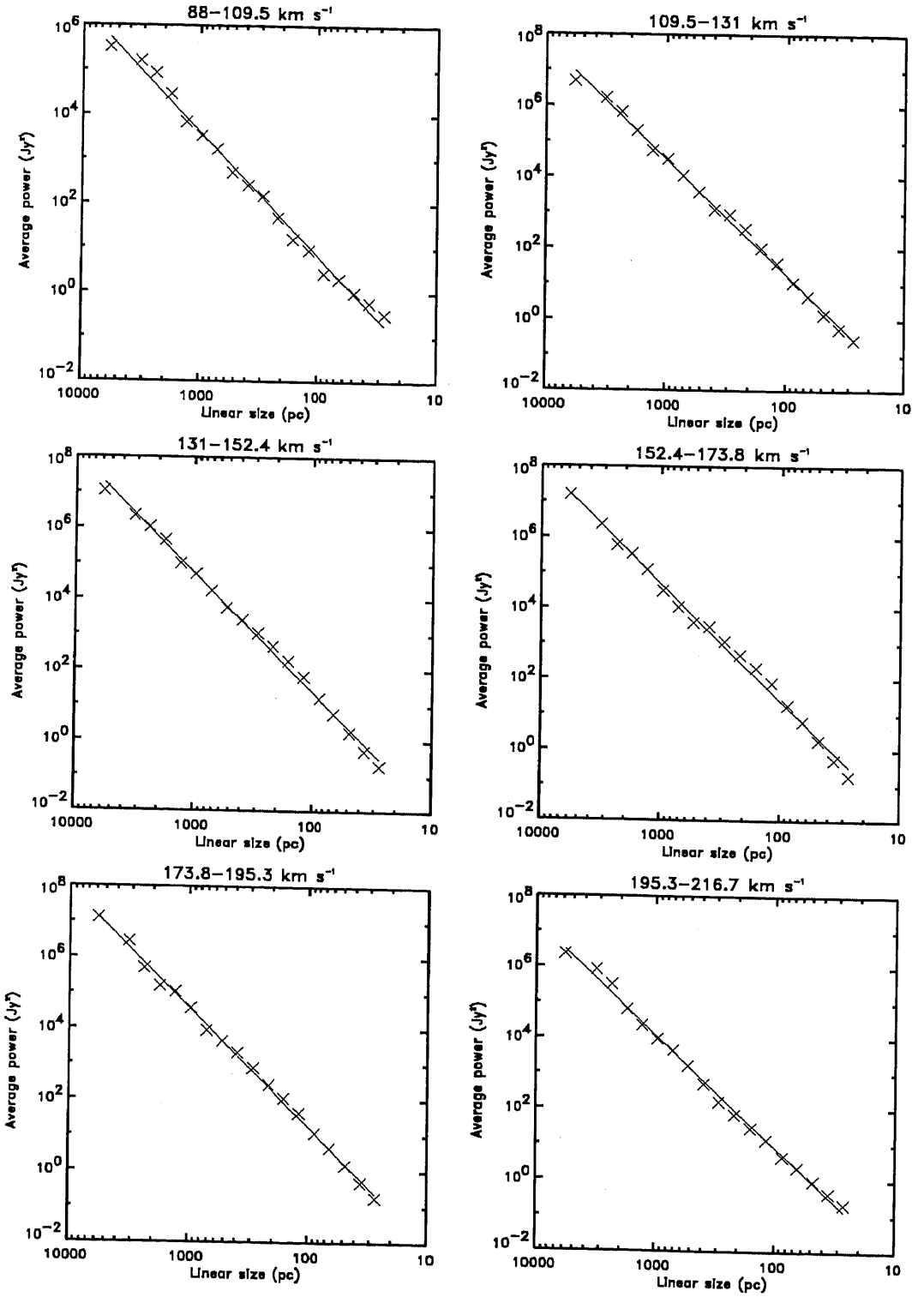

Figure 8.5 . The two-dimensional spatial power spectrum for six heliocentric velocity intervals in the SMC. The linear size L, is related to the radius k in the $u-v$ plane by $L(\mathrm{pc}) = d(\mathrm{pc})/k(\lambda)$, where $d = 60 \times 10^3$ pc is the distance to the SMC. Least-squares fits are overlaid.

and Crovisier & Dickey, we did not work directly in the observed $u-v$ plane as our data were a combination of 320 ATCA fields and corresponding Parkes data for the whole region. Fig. 8.6 shows that the index of the power law, estimated for velocity intervals ~ 5 km s^{-1} wide, is approximately constant over the full velocity range, with an average value being $\langle\gamma\rangle = -3.04 \pm 0.02$. The average power at 1 kpc shows similar velocity structure to the integrated flux density profile (Fig. 8.6), although the lower velocity peak shows a higher level of emission fluctuations, despite its lower mass. Possibly, this is because of higher optical depth in the high-velocity component. After allowing for distance differences between the SMC and that part of the Galaxy studied by Green ($\sim$ 10 kpc) the power at 100 pc is higher in the SMC, as expected due to gas-richness. The velocity profile of the 100-pc power also follows the integrated flux-density profile. No discontinuity is seen at the transition ($\sim$ 420 pc) between the single-dish and interferometer data.

In order to test the two-dimensional spatial power spectrum in a smaller region of the SMC, we have applied the same method to the eastern Wing (area about 4 deg^2). Spectra are again very well fitted by a power law for the whole range of linear scale. In Fig. 8.7 we show the index of the power-law fit, together with the integrated flux density and the average power at 1 kpc. The average power at 1 kpc follows the total flux profile better, suggesting that this part of the SMC has lower optical depth. This provides more power on smaller scales and therefore a slightly lower average index, $\langle\gamma\rangle = -2.85 \pm 0.02$.

For our own Galaxy, the interferometer data of Crovisier & Dickey (1983) and Green (1993) show power-law indices of -3.0 and -2.8, respectively. This implies that similar mechanisms are responsible for the HI emission fluctuations both in the Galaxy and in the SMC although the SMC is more gas rich and has a much younger environment.

At much smaller physical scales (below 0.2 pc), it was believed that emission fluctuations disappear in the Galaxy (Crovisier, Dickey, & Kazes 1985). Extrapolation of the SMC power spectrum would also appear to suggest negligible emission fluctuations. At small scales, however, recent observations of absorption profiles against background continuum sources imply the presence of small dense HI clouds with a size of $\sim$ 75 AU in the Galaxy (Davis, Diamond & Goss 1996). Frail et al. (1994) also suggest that small-scale HI structure with a size range of 5 – 100 AU may constitute a significant fraction (10 to 15 per cent) of the cold neutral medium (CNM) in the ISM. If interpreted as density (rather than temperature) fluctuations, it therefore seems unlikely that this small-scale structure is related to the physical processes responsible for the hierarchy found here and may, for example, be related to a more local phenomenon such as shocks around individual low-mass stars.

Heiles (1997) also points out a 'pressure dilemma' whereby such small clouds appear to have very high thermal pressures compared with the equilibrium hydrostatic pressure of the ISM. He suggests an alternative geometric solution for the CNM in which

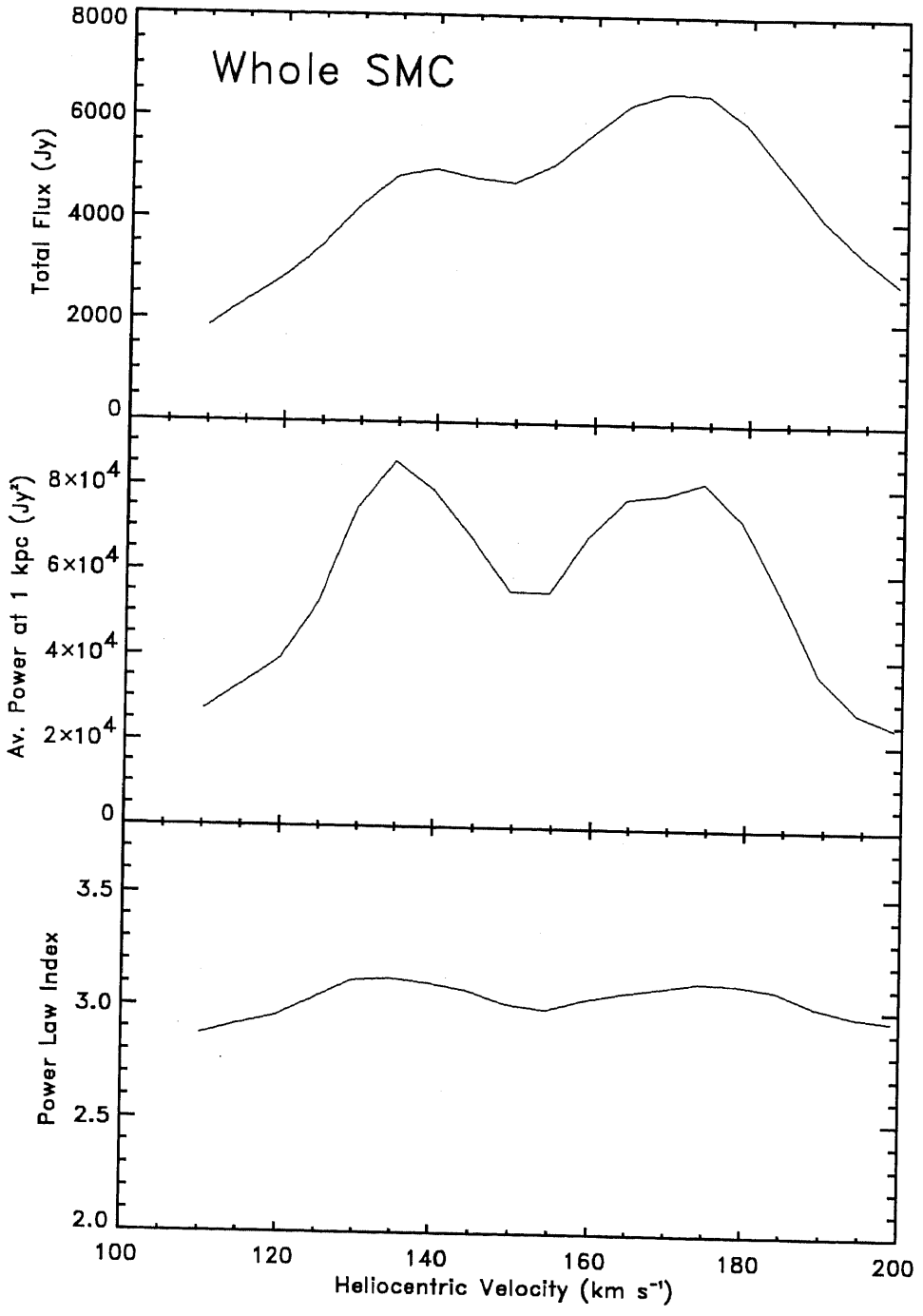

Figure 8.6 . The total flux density in Jy (top), the average power at 1 kpc in Jy^2 (middle), and the slope of the 2-dimensional spatial power spectrum $(-\gamma)$ of the whole SMC (bottom) plotted as a function of heliocentric velocity. The average slope is -3.04 ± 0.02.

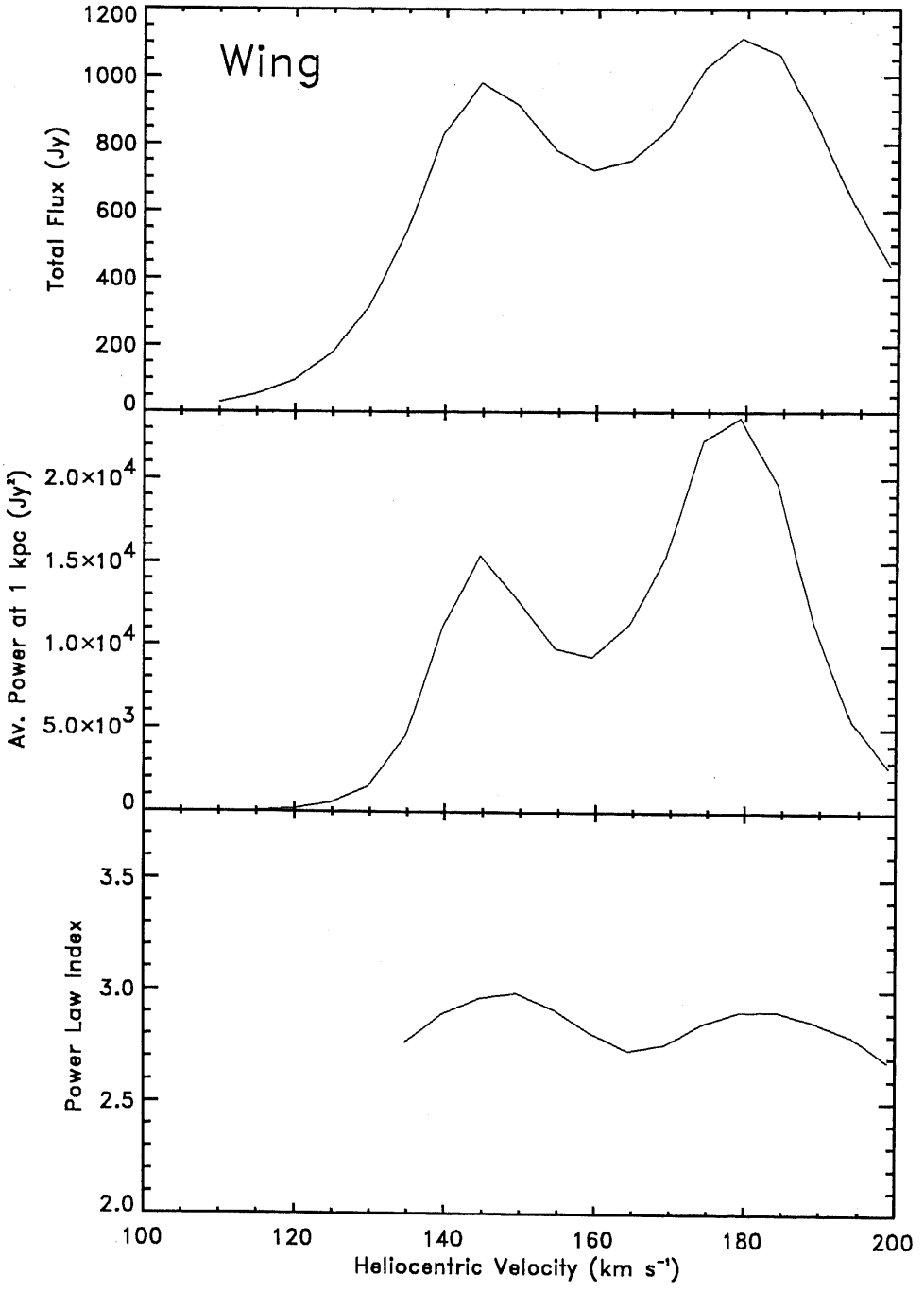

Figure 8.7 . The total flux density in Jy (top), the average power at 1 kpc in Jy^2 (middle), and the slope of the 2-dimensional spatial power spectrum $(-\gamma)$ of the eastern Wing (bottom) plotted as a function of heliocentric velocity. The average slope is -2.85 ± 0.02.

very open filaments and sheets contribute about 30 and 10 per cent, respectively to the total column density of the CNM.

We note that there is a problem in studying the HI density fluctuations through emission–line observations in that we are not able to distinguish the warm and cold phases of the neutral hydrogen. The cold phase occupies a small fraction of the ISM whereas the warm phase filling factor is as much as $\sim$ 30 per cent in the Galaxy (Kulkarni & Heiles 1988). The warm-to-cold mass fraction in the Galaxy is $\sim$ 3.2 (Dickey 1995), compared with 1.6, 2.0 and 4.6 for the galaxies M31, LMC and M33, respectively (Dickey 1995). The latest results by Dickey et al. (1999) suggest that the cold phase is very sparse in the SMC and that the warm-to-cold mass fraction is as high as 5 – 7. Therefore, the spatial power spectrum in the SMC will also be biased towards the warm neutral medium (WNM), whereas absorption studies are biased toward the CNM.

8.3.2 A fractal model of the ISM?

Observations of interstellar clouds have shown that hierarchical structuring is present on a wide range of spatial scales. Some cloud properties, such as size distribution, mass distribution, density and velocity dispersion show distributions consistent with fractal structure (Elmegreen & Falgaróne 1996). A similar inference can be made from the power-law nature of the HI spatial power spectrum.

Throughout, we assume the mathematical foundations of fractal geometry given by Falconer (1997). He refers to a set F as a fractal if:

1. F has details over a large range of scale;
2. F is too irregular to be described in traditional geometrical language.

A fractal often has the following properties, in addition:

3. some form of self-similarity, approximate or statistical;
4. a 'fractal dimension' (defined in some way) which is greater than its topological dimension.

We use the fractal dimension $D_{\rm H}$, given by Hausdorff (see Falconer 1997), which is smaller than or equal (for many sets) to the more popular box-counting or capacity dimension. For more information see Falconer (1997). The projection theorem says that the plane projection of a Borel set F (which Falconer uses as any subset of 3-dimensional Euclidean space, R^3) has a dimension equal to $D_{\rm p} = \min\{2, D_{\rm H}(F)\}$.

One of the usual manifestations of fractal structure (which is a fractal graph of the intensity distribution $I(\alpha, \delta)$ in this case) is that the power spectrum and correlation

function of I show power-law behaviour (Falconer 1997). This leads to the possible interpretation of the power spectrum of the SMC as caused by fractal structure of the ISM in the SMC. The connection between the nature of the power spectrum and possible fractal structure was not made by Crovisier & Dickey (1983) nor Green (1993).

Following Falconer's discussion (Falconer 1997, p.158), the autocorrelation function, $C(L)$ (where L is the distance between two points or, here, a diameter of an HI cloud) of the fractal function is approximately a power-law:

$$C(L) \propto L^{4-2s}, \tag{8.3}$$

where s is the box-counting dimension of the graph of I. As the power spectrum, $P(k) \propto k^{\gamma}$ (k is in units of λ), is the Fourier transform of the autocorrelation function, we find $C(L)$ from:

$$C(\mathbf{L}) = \int\int P(\mathbf{k}) e^{i\mathbf{L}.\mathbf{k}} d\mathbf{k}. \tag{8.4}$$

As $k \propto L^{-1}$:

$$C(L) \propto \int k^{1+\gamma} dk \propto L^{-\gamma-2}, \tag{8.5}$$

where $\langle\gamma\rangle = -3.04 \pm 0.02$. Hence, equating Eq. 8.3 and Eq. 8.5, we find that the box-counting dimension of the graph of I is 1.5 which is an upper limit for the projected Hausdorff dimension. Direct application of the projection theorem, assuming the whole ISM of the SMC to be a Borel set, gives an upper limit for the volume fractal dimension of 1.5. However, contrary to simple fractal models, the ISM presents a distribution of optical depths which will modify the relationship between the projected and volume dimension (Pfenniger & Combes 1994). From experience with a number of fractals, Beech (1992) thus suggested the following simple relationship between the projected (D_{p}) and volume fractal dimension (D): $D = D_{\mathrm{p}} + 1$. This relationship has been widely used by many authors (e.g. Elmegreen & Falgarone 1996; Elmegreen 1997), but it has not been rigorously proven, as pointed out by Westpfahl et al. (1999). If used here, the volume fractal dimension $D = 2.5$ can be estimated for the HI content in the SMC.

Similar results for the projected fractal dimension of interstellar clouds were obtained using the area-perimeter relationship (Falgarone, Phillips, & Walker 1991; Vogelaar & Wakker 1994). The results are remarkably similar for atomic, molecular and dust components of interstellar clouds and range between 1.3 and 1.5 (for references see Falgarone et al. 1991). Also, recent study by Westpfahl et al. (1999) finds the projected fractal dimension for HI in seven galaxies in the M81 group to range between 1.2 and 1.5. Assuming the size distribution for substructures inside a fractal given with $N(\lambda > L) \propto L^{-D}$ (from Mandelbrot 1983), Elmegreen & Falgarone

(1996) measure the volume fractal dimension of molecular clouds to be 2.3 ± 0.3 using data from published surveys.

The projected fractal dimension derived for HI in the SMC, $D_p = 1.5$, for structures present on scales from 30 pc to 4 kpc, is therefore very similar to the projected dimension derived for interstellar clouds, using different tracers, with much smaller spatial scales ($\sim 0.05 - 100$ pc). This may imply that the same mechanism causes the fractal structuring of all ISM components over a large range of spatial scales. A very similar projected fractal dimension found for the SMC and several galaxies in the M81 group, most likely points to the same interstellar processes at work in various galaxies.

The volume fractal dimension of 2.5 implies that the size distribution of substructures (on scales l) greater than L will behave as $N(l > L) \propto L^{-2.5}$, while the distribution of cloud size per linear size interval is given by $n(L)dL \propto L^{-3.5}dL$. Similarly, the mass–size relation obeys $M(L) \propto L^{2.5}$. These relations can be combined to give the cloud mass distribution function which is, interestingly, independent of fractal dimension: $n(M)dM \propto M^{-2}dM$ (Elmegreen & Falgarone 1996). Similar distributions have been derived for molecular clouds from CO observations (slope of -1.79) and for diffuse and IRAS clouds in the Galaxy (slope ranging between -1.5 and -2) (see Elmegreen & Falgarone 1996).

The fractal model of the ISM suggests highly inhomogeneous structure organisation, different from any of the 'traditional' ISM models which have 1 or 2 levels of hierarchy. The dense regions of the ISM seem to be made of small and dense clouds ('atoms') and therefore are highly clustered, while the bulk of the ISM matter seems to have very low density (Elmegreen 1989).

Different processes such as turbulence, chaos, self-gravity, percolation or some chemical processes can produce fractal structuring of an interstellar environment, even with similar fractal dimensions (Pfenniger & Combes 1994; Scalo 1987). However, analogies with laboratory fluids suggest that turbulence may have the most significant role in the ISM (Elmegreen & Falgarone 1996). A simple relationship between the 2-D spatial power spectrum, $P(k)$, and the 3-D turbulence energy spectrum, $\varepsilon(k)$: $\varepsilon(k) \propto P(k)k^2$, was suggested by Lazarian (1995). In the case of the SMC, this results in $\varepsilon(k) \propto k^{-1.04}$. The resultant spectrum is somewhat flatter than the predicted spectrum for the 3-D Kolmogorov (incompressible) turbulence: $\varepsilon(k) \propto k^{-1.67}$. Lazarian (1994) argues that this is not surprising, since the Kolmogorov picture of turbulence is not adequate for the compressible ISM.

8.3.3 The spatial power spectrum of the IR intensities

The 2-D spatial power spectra of the IR intensity fluctuations at 60 and 100 μm (I_{60} and I_{100}) are derived here. Both images, I_{60} and I_{100}, were first Fourier transformed.

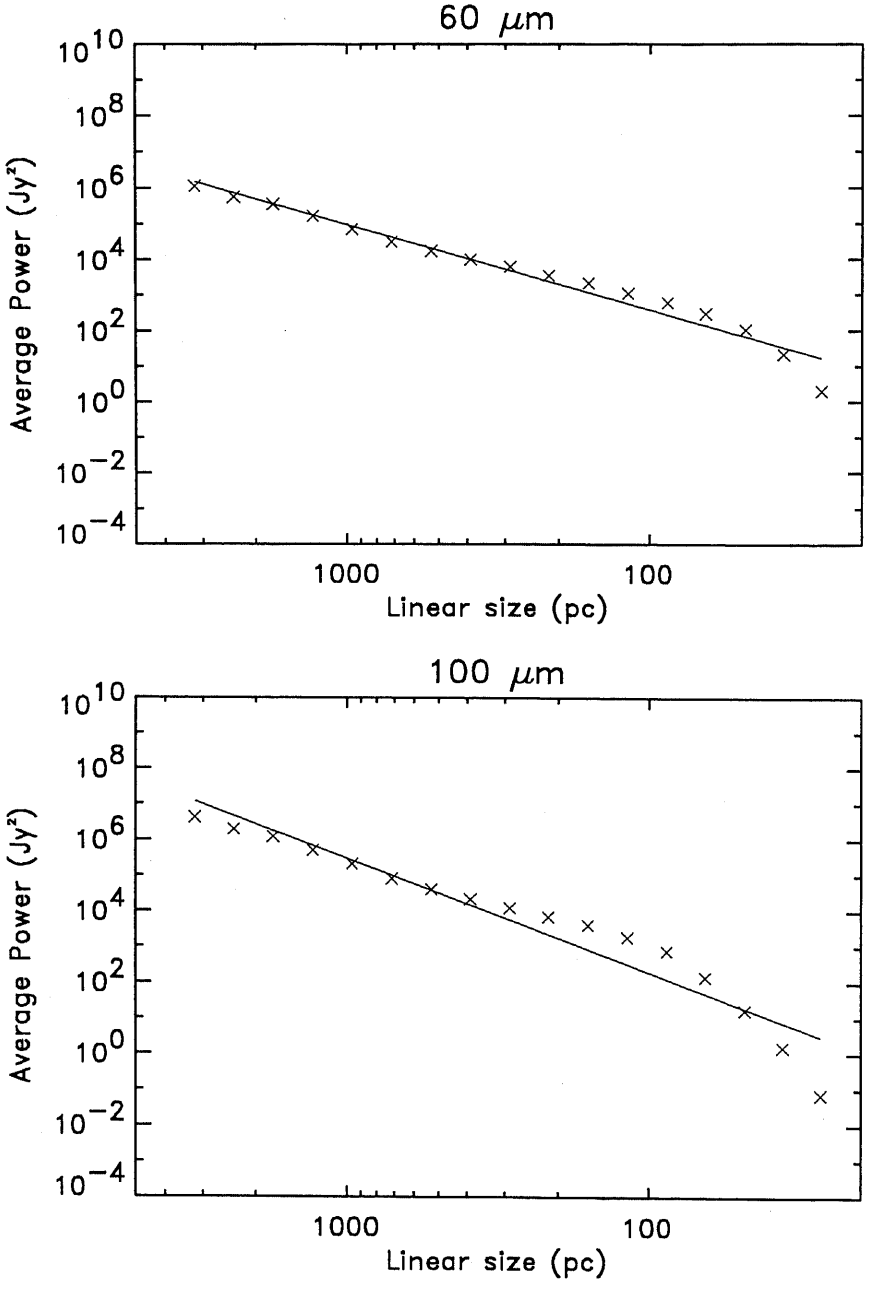

Figure 8.8 . The 2-D spatial power spectrum of the 60 and 100 μm intensity maps. Linear size L, is related to the radius k in the $u-v$ plane by $L(\mathrm{pc}) = d/k(\lambda)$, where $d = 60 \times 10^3$ pc is the distance to the SMC. The overlaid least-square fits, $P(k) \propto k^{-2.4}$ (top) and $P(k) \propto k^{-3.2}$ (bottom), were derived excluding the last three data points.

We call their Fourier transforms X_{60} and X_{100}, respectively. The average value of the square of the modulus of the transforms, $\langle X_{60}X_{60}^*\rangle$ and $\langle X_{100}X_{100}^*\rangle$, were then measured in 17 annuli of equal width in $\log\sqrt{u^2+v^2}$ (u and v are the coordinates in the Fourier plane measured in units of λ and $*$ denotes a complex conjugate of a given function), in the same way as for HI.

The resultant spectra are shown in Fig. 8.8. Both spectra can be reasonably well fitted by a power law, $P(k) \propto k^{\gamma}$ (where k represents spatial frequencies), over the linear size range $\sim$ 50 pc to $\sim$ 4 kpc, with $\gamma_{60} = -2.4 \pm 0.2$ for 60 μm band and $\gamma_{100} = -3.2 \pm 0.3$ for 100 μm band. However, the slopes steepen significantly around 50 pc, resulting in much steeper power spectra for smaller spatial scales. This might suggest that there is not enough IR small-scale structure to contribute to the power spectrum at these spatial scales. However, a significant power may be also missing on larger spatial scales ($>$ 50 pc) because of the quasi-blackbody cooling nature of dust grains, whereby the IR intensity fluctuations will be dominated by warm dust ($T \sim 50$ K), masking the real power of the cool dust ($T \sim 25$ K). From the discussion in Section 8.2.2, it appears that is not likely that so large amount of cool dust is missing to be able to influence sufficiently the spectrum over a wide range of larger spatial scales ($>$ 50 pc). It is likely though, that the cool dust may concentrate in small clumps, causing hence a significant underestimate of power on very small spatial scales, and therefore a change of the power-law slope.

The derived power-law index for 100 μm band is, nevertheless, similar to the indices found previously for the Galaxy. Gautier et al. (1992) have measured the spatial power spectrum for a few Galactic cirrus clouds at 100 μm, over the angular scale 2 arcmin to 8 deg, and found a good power law fit with an average slope of $\gamma = -3$. Recently, Schlegel, Finkbeiner & Davis (1998) have found a more shallow slope of $\gamma = -2.5$ from the full sky 100 μm maps for angular scales of 1.1 deg and over.

We now address the question of radial symmetry of the derived spatial power spectra. In the case when a significant preferred alignment of structure is present, caused by, for example, the tidal stretching or shear, the power spectra will significantly vary for different position angles (azimuth) in the Fourier plane. The azimuthal isotropy of the spatial power spectra has been tested for the Galaxy by Gautier et al. (1992), in case of dust, and by Green (1994), in case of HI, and no significant variation has been found. We perform here a similar test for the dust power spectra of the SMC. The same method for measuring a spatial power spectrum was applied on four different segments in the Fourier plane (with position angles 0°– 45°, 45°– 90°, 90°– 135°and 135°– 180°, respectively), performing data averaging in 17 annuli within each segment. The resultant spectra for 60 μm image are shown in Fig. 8.9. A possible systematic trend is visible for larger spatial scales. Values for third and fourth segments seem to be consistently lower that values for first and second segment. This shows that power spectra for third and fourth segments have more power on larger spatial scales, which corresponds to a possible alignment of structure in direction northeast–southwest. This result is not surprising since the

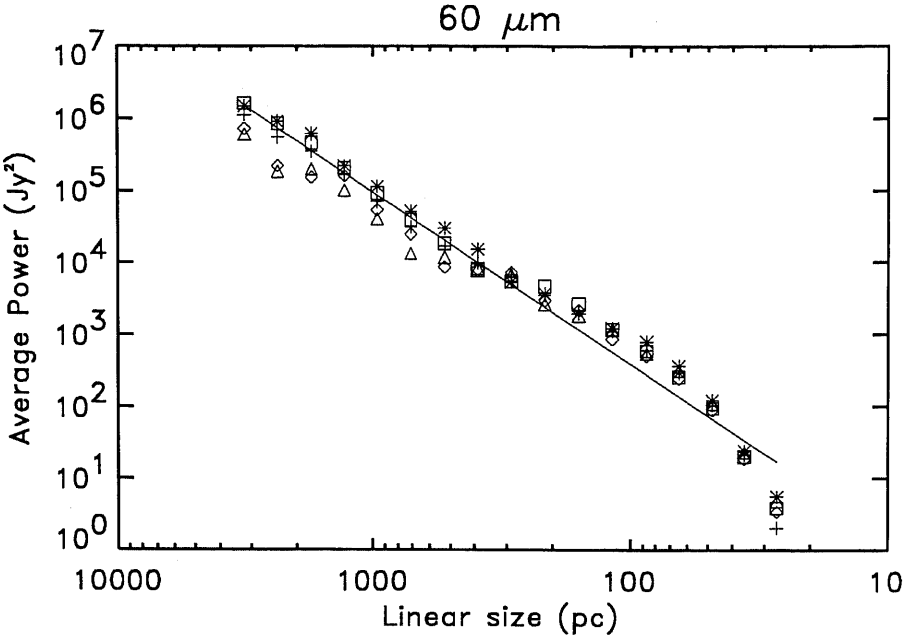

Figure 8.9 . The 2-D spatial power spectra of the 60 μm intensity map over the linear size range $\sim$ 30 pc to $\sim$ 3 kpc. To test the azimuthal symmetry of the spatial power spectrum, radial averaging have been performed within four different segments in the Fourier plane: 0°– 45°(asterisk), 45°– 90°(square), 90°– 135°(diamond) and 135°– 180°(triangle). The radially averaged data points within the whole Fourier plane are shown with a plus sign (+) and overlaid with the least-square fit.

optical bar, the most prominent large scale feature on IR images, is exactly in this direction. However, all variations with azimuth seem to be small and within the estimated uncertainties, suggesting that derived spectra can be assumed to be radially symmetric.

8.3.4 Spatial power spectrum of HI and dust column densities

To investigate the statistical correlation between the dust and gas (Section 8.3.5), the 2-D spatial power spectra of the dust and gas column densities are first required. Hence, both dust ($N_{\rm d}$) and gas ($N_{\rm HI}$) mass column density images were Fourier transformed ($X_{\rm d}$ and $X_{\rm HI}$ are used to denote Fourier transforms of dust and HI, respectively). Assuming the azimuthal isotropy, tested in the previous section, the average value of the square of the modulus of the transforms, $\langle X_{\rm d} X_{\rm d}^{*} \rangle$ and $\langle X_{\rm HI} X_{\rm HI}^{*} \rangle$, was then measured in the usual way. Before Fourier transforming, blank pixels in the dust mass column density image were substituted with a constant value to avoid the edge effects problem. Some masking was also applied on $X_{\rm HI}$ to exclude four elliptical annuli where the ATCA data were not fully sampled (see Section 8.3.1).

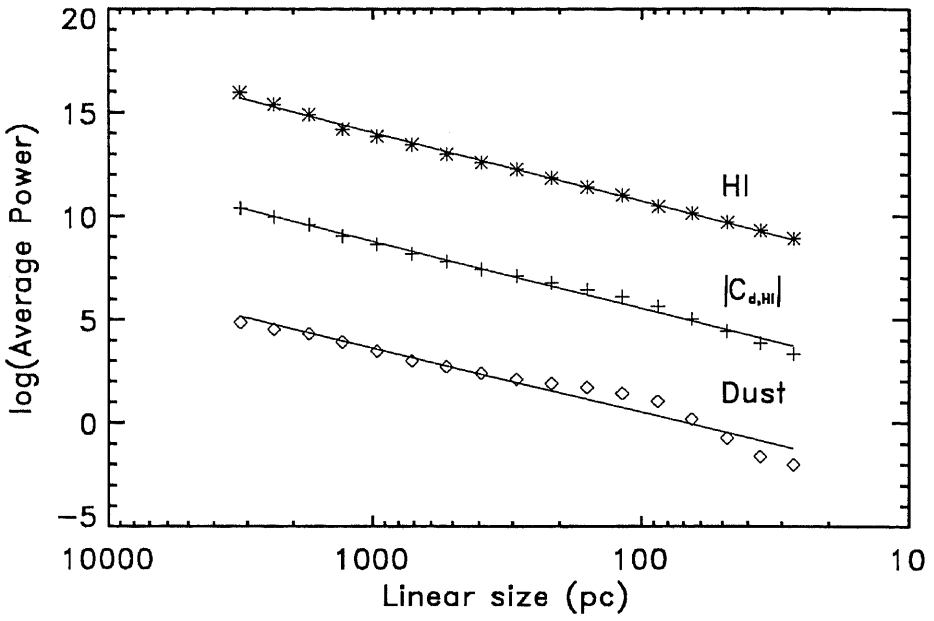

Figure 8.10 . The 2-D spatial power spectra of dust and HI mass column densities, labelled as 'Dust' and 'HI' (in units of $M_\odot^2$), together with the spatial amplitude cross spectrum of dust and HI, labelled with $|C_{d,HI}|$ (in units of $M_\odot$), which will be used in the next section.

Both dust (P_d) and HI (P_{HI}) spatial power spectra are shown in Fig. 8.10 labelled as 'Dust' and 'HI'.

Both P_d and P_{HI} are well fitted by a power law over the whole range of spatial scales (30 pc to 3.2 kpc). The power spectrum of the HI column density shows a remarkably tight power-law fit, $P_{HI}(k) \propto k^{-3.31\pm0.01}$. The power spectrum of the dust column density can be fitted with $P_d(k) \propto k^{-3.1\pm0.2}$. This spectrum also shows a slight change of slope on very small spatial scales (< 50 pc). Some deficiency of power on very large spatial scales may also be present, most likely due to the opacity effect and/or a lack of complete sampling on these spatial scales. Nevertheless, slopes for P_d and P_{HI} appear to be quite similar.

The power-law behaviour of the HI spatial power spectrum with result $P_{HI}(k) \propto k^{-3.05}$ was discussed previously in Section 8.3.1 for the same HI data but using much thinner velocity slices ($\sim$ 5 km s^{-1}). The spatial power spectrum of the HI mass column density (integrated data cube along the whole velocity range, therefore being a 'thick' velocity slice) is presented here for the first time. There is a significant change in the power-law index from $\gamma = -3.04 \pm 0.02$ for 'thin' velocity slices to $\gamma = -3.31$ for a 'thick' velocity slice. The simple explanation is that integration along the velocity axis has washed out some small scale structure, leaving more power on the larger spatial scales. However, Lazarian & Pogosyan (1999) argue that the slope variation for different velocity slices contains important information about

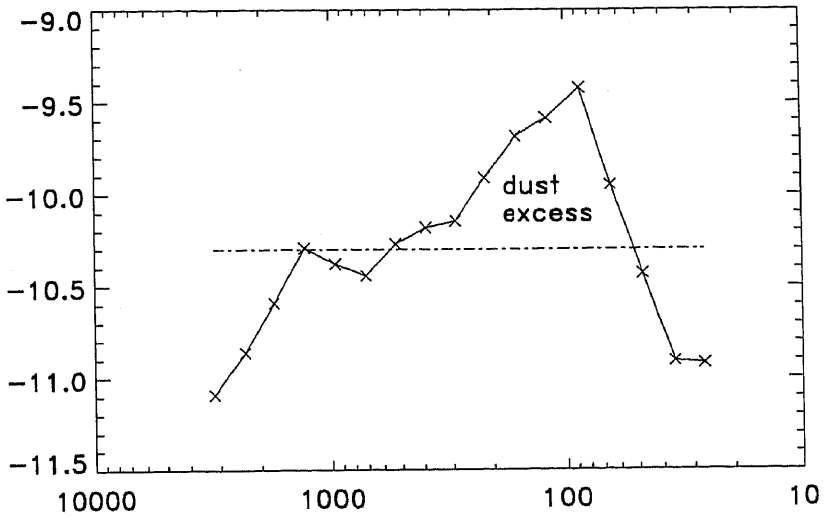

Figure 8.11 . The logarithm of the ratio of dust and HI column density spatial power spectra, $\log(P_{\rm d}(k)/P_{\rm HI}(k))$.

the origin of the spatial power spectrum. They show that 'thick' velocity slices represent HI density fluctuations, while 'thin' slices show the turbulent velocity fluctuations. The power spectra in Section 8.3.1 therefore seem to have a significant velocity contribution.

The slope of $P_{\rm d}$ agrees well with the predictions by Padoan, Jones, & Nordlund (1997), although very different approaches have been performed. In the investigation of the distribution of dust in dark molecular clouds by Lada et al. (1994), the simultaneous determination of colours for hundreds of stars was performed. A plot of the mean visual extinction (A_V) versus its dispersion (σ), $\sigma - A_V$, showed an interesting correlation which appears to have an important role in the study of structure of dark clouds. Padoan, Jones, & Nordlund (1997) have shown that the $\sigma - A_V$ correlation originates in the strong fluctuations of the 3-D density distribution in dark clouds, produced by random supersonic motions. Their numerical simulations of the 3-D random density distribution shaped by supersonic flows show a power-law behaviour of the spatial power spectra, $P(k) \propto k^{-2.6\pm0.5}$, which is consistent with observations of the cloud IC5146 by Lada et al. (1994). Projected in two dimensions, this results in the 2-D density fluctuation spectrum, with the slope between -3.0 and -3.1 (P. Padoan, private communication).

The power-law fit of both dust and HI column density power spectra shows that the hierarchical structure organisation is present within dust and HI content of the ISM in the SMC, with no preferred spatial scales for dust and HI clouds. The power-law

indices for dust and HI are similar, showing that similar processes are most likely involved in the shaping of both dust and HI content of the ISM. If interpreted as due to the fractal nature, the power-law fits suggest the projected fractal dimension of $D_p = 1.4 \pm 0.1$, or the volume fractal dimension of $D = 2.4 \pm 0.1$ (see Section 8.3.2), which is very similar to the estimated volume fractal dimension of molecular clouds by Elmegreen & Falgarone (1996). The newly determined slopes also imply the 3-D turbulence energy spectrum $\varepsilon(k) \propto k^{-1.2\pm0.1}$, which is slightly closer to the slope of the 3-D Kolmogorov turbulence, $\varepsilon(k) \propto k^{-1.67}$.

However, an interesting excess in the power coming from all dust clouds in the SMC, of about 10^2, relative to the power of HI clouds may be present for spatial scales 50 – 500 pc, as indicated in Fig. 8.10. The ratio of dust and HI column density power spectra, plotted with a logarithmic scale, shows this more clearly in Fig. 8.11. For very large spatial scales, > 1 kpc, there appears to be a deficiency of dust power relative to HI power, resulting most likely from the missing very cold dust. Surprisingly, the total power of dust clouds on very small spatial scales, with sizes < 50 pc, also shows a deficiency.

8.3.5 The spatial coherency spectrum

Finally, the correlation between HI and dust column density is investigated using the cross spectrum, $C_{d,HI} = \langle X_d X_{HI}^* \rangle$. $C_{d,HI}$ is a complex function and its amplitude, $|C_{d,HI}|$ (shown on Fig. 8.10), was used to derive the spatial coherency spectrum (Yuen & Fraser 1979) presented on Fig. 8.12:

$$K_{d,HI}(k) = \frac{|C_{d,HI}(k)|^2}{P_d(k)\ P_{HI}(k)}. \tag{8.6}$$

Some characteristics of the derived spatial and cross spectra in this chapter are summarised in Table 8.3.

Table 8.3 A summary of all $P(k) \propto k^\gamma$ slopes derived in this chapter.

	γ
60 μm intensity	-2.4 ± 0.2
100 μm intensity	-3.2 ± 0.3
HI 'thin' slices ($\sim$ 5 km s^{-1})	-3.04± 0.02
N_d, dust column density	-3.1 ± 0.2
HI 'thick' slice, HI column density	-3.31± 0.01
$\|C_{d,HI}\|$, cross spectrum	-3.23± 0.03

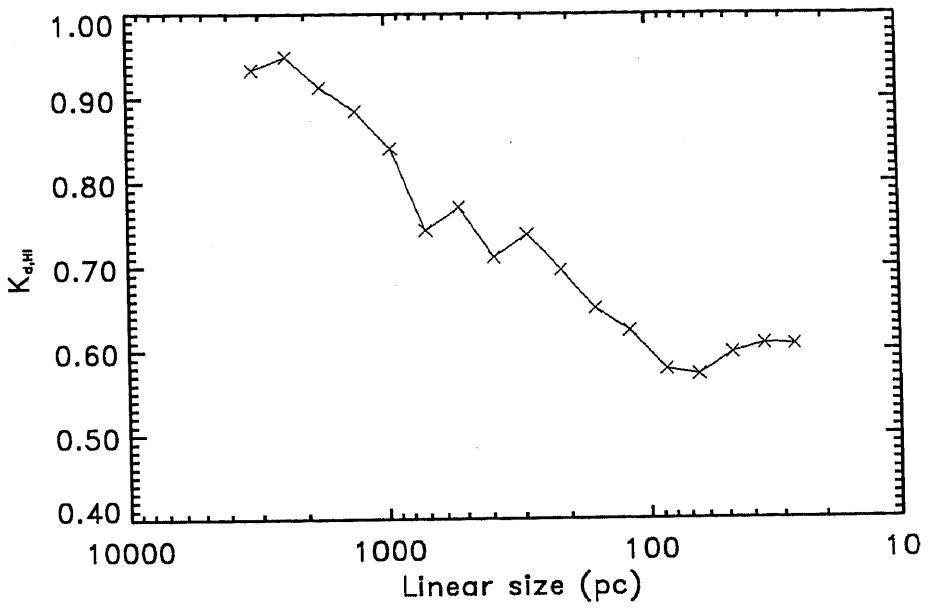

Figure 8.12 The spatial coherency spectrum of dust and HI mass column densities.

The spatial coherency spectrum is a measure of correlation between two functions on different spatial scales. Its values range between 0 and 1. In the case of two independent processes $K_{\rm d,HI}(k) = 0$ for all k, while $K_{\rm d,HI}(k) = 1$ (for all k) if one process is a linear function of the other one, or both processes are linear functions of some third random process. Fig. 8.12 shows that in general, dust and HI are spatially well correlated over a wide range of spatial scales. $K_{\rm d,HI}$ increases from $\sim$ 0.6 to $\sim$ 1, for spatial scales from $\sim$ 50 pc to the largest one used here to measure the power spectrum, $\sim$ 3.2 kpc. For very small spatial scales (30 – 50 pc), which mainly correspond to HII regions, no good correlation is expected because hydrogen here leaks, being either ionised or in molecular form. However, Fig. 8.12 shows on these scales a small bump in $K_{\rm d,HI}$. We note that this may be caused by an underestimate of cold dust on these spatial scales, as already discussed.

8.4 Summary

- The dust-to-gas mass ratio shows a significant spatial variation between the optical bar and Eastern Wing. If interpreted as a deficiency of atomic gas, the mass of molecular hydrogen of $\sim 8 \times 10^8$ $M_\odot$ is required. This is about double the HI mass and about 30 times the mass accounted from CO studies. If interpreted as a deficiency of cold dust, a huge amount ($\sim 10^6$ $M_\odot$) of very cold dust may not be seen by IRAS or COBE/DIRBE. Although a combination of both deficiencies most likely plays an important role, it is hard to believe that cold gas and dust may exist in such amounts. Hence, an explanation for

an intrinsic variation of the dust-to-gas mass ratio is required.

- The intrinsic spatial variation of the dust-to-gas mass ratio may be explained with the metallicity variations, as suggested by Dwek (1998) and Lisenfeld & Ferrara (1998). However, current observational data for HII regions in the SMC do not support the proposed correlation between the metallicity and the dust-to-gas ratio.
- The average dust-to-gas ratio is, by mass, 8.2×10^{-5} which is a factor of ~ 30 below the Galactic value.
- The spatial power spectra of HI brightness distribution, the IR intensity at 60 and 100 μm, HI column density and dust column density, obey the relation, $P(k) \propto k^{\gamma}$. This suggests a hierarchical structure organisation with no preferred sizes for dust and HI clouds. The power-law indices are very similar for HI and dust column densities, with $\langle\gamma\rangle = -3.2$. One interpretation of the $P(k)$ power-law is that the dust and HI content of the ISM in the SMC has fractal nature, consisting of a hierarchy of HI and dust cloud structures created, for example, by homogeneous turbulence. The inferred projected fractal dimension $D_{\rm p} = 1.4$ and the volume fractal dimension of $D = 2.4$. This is similar to values obtained by other authors for molecular clouds in the Galaxy and may imply similar mechanisms for structure formation. The fractal model of the ISM is also consistent with a low space-filling factor for the neutral gas.
- The spatial coherency spectrum shows that dust and gas are spatially well correlated for spatial scales larger than 50 pc, with the correlation coefficient ranging between 0.6 and 1.

Chapter 9

Conclusions

9.1 Summary of results

This section gives an overview of main results throughout this thesis.

This thesis uses HI observations over a large area ($\sim$ 20 deg^2), containing the SMC, obtained with the ATCA and Parkes telescopes using a large number of pointing centres. The mosaicing technique for obtaining interferometric observations proved to be especially suitable for this purpose, since it recovered information on some missing spatial frequencies. However, in the presence of a significant extended structure, information on the shortest spatial frequencies must be provided. It was shown in Chapter 3 that the shortest spatial frequencies can be successfully obtained with a single-dish and that the interferometer and single-dish data can be then combined using several different methods, which all result in a great improvement in the final images. This chapter discussed how to calibrate one data set relative to another one, and examined the theory and applications for two linear and two non-linear methods of data combination. All four methods showed satisfactory result when the same, *a-priori*-determined, calibration scaling factor was used. The first method, data combination in the Fourier domain, is the fastest one but requires careful *a priori* cleaning of the interferometer data. The second method, data combination before deconvolution, slightly overweights the single-dish data. The performance of the third method, data combination during deconvolution using single-dish data as the 'default' information, depends heavily on the size of the spatial frequency overlap. Theoretically the best fit to both interferometer and single-dish data is provided by the fourth method, the 'joint' deconvolution of both data sets. However, this is the least robust method.

The high resolution HI observations, after adding information on the shortest spacings, revealed a great complexity and variety of the HI structures in the SMC, as presented and discussed in Chapter 4. The most prominent features are numerous

expanding shells (509 in total) with various sizes and expansion velocities, investigated later in more detail in Chapter 6. The three largest supergiant shells were found especially due to addition of the Parkes data. Their diameters range up to 1.8 kpc and required energies (in the standard supernovae-driven model) up to 2×10^{54} erg. The most common reason for the creation of such huge objects in the ISM appears to be the fascinating interplay between star formation and the surrounding medium. The statistical view of some shell properties, showed that the shell radius and expansion velocity distribution functions can be well fitted by the power-laws: $N(R) \propto R^{-\alpha_r}$ and $N(v) \propto v^{-\alpha_v}$. The slopes α_r and α_v were found to be surprisingly similar for the SMC, M31 and M33. The distribution functions $N(R)$, $N(v)$ and $\overline{v}(R)$ support the standard adiabatic model for the shell evolution and suggest a single burst of shells in the SMC, together with a power-law mechanical luminosity spectrum.

The velocity field, the distances of Cepheids from previous studies, and the controversial 3-D structure of the SMC, were re-examined in Chapter 5. The velocity field, after correction for the proper motion, as well as Cepheid radial velocities and newly determined distances, suggest that the central part of the SMC can be interpreted as a rotationally supported bar, with a line-of-sight depth which does not exceed the tidal radius. The observed rotation curve, corrected for the pressure support, has a rotation velocity of $\sim$ 60 km s^{-1} at the turnover radius of 2.5 kpc. It can be modelled with a composition of rotation curves arising from gaseous and stellar potentials, with $M_*/L = 0.83$. No additional component, such as a dark matter halo, is needed. The same chapter demonstrates a definite differential extinction across the SMC, being almost twice as high in the south-west direction than in the north-east direction. This results in a much smaller gradient of Cepheid distances, bringing the depth of the SMC to within its tidal radius (4 – 9 kpc). It is argued that the random motions, originating in the interplay between the star formation and the surrounding ISM, are responsible for the observed HI line splitting within the central region of the SMC, rather than from spatially separate components or different arm-like features proposed previously. Also, some evidence for particular tidal features at the outskirts of the SMC's bar were presented. However, it is clear that further studies, including a larger area around the SMC and the distance determination of more objects within the SMC, are necessary for a better understanding of the 3-D structure.

It was demonstrated in Chapter 7 that the old IRAS data at 12, 25, 60 and 100 μm can be successfully reconstructed with much higher resolution, of $\sim$ 1 arcmin for 12, 25 and 60 μm and $\sim$ 1.7 arcmin for 100 μm, using the HIRAS program. The new HIRAS data revealed for the first time a lot of diffuse and filamentary IR structure of the SMC. The integrated IR spectrum proved to be a precious tool for establishing the composition and abundances of different dust grains. There appears to be a deficiency of warm, small dust grains in the SMC, although the dust temperature (23 – 45 K) is on average warmer in the SMC than in the Galaxy (17 – 30 K). It was

pointed out that the role of cold dust grains ($T < 20$ K) is still not well understood and that these grains can contribute significantly to the total dust mass.

The high resolution HI and IR data enabled this thesis to challenge the assumption of the dust and gas being well-mixed in the ISM. A significant variation of the dust-to-gas mass ratio, of almost a factor of 3, was demonstrated in Chapter 8. Reasons, such as an excess of molecular gas (of about double that of the HI mass) and/or a deficiency of cold dust (of up to $\sim 10^6$ $M_\odot$), discussed here, were shown to be not adequate enough to explain the observed variation. An alternative, intrinsic variation of the dust-to-gas mass ratio was therefore proposed, and its possible correlation with the metallicity variations was investigated. Most likely, all three effects are partially responsible for the variation of the dust-to-gas mass ratio. However, it was stressed that the current observational constraints do not allow the distinction to be made between which effects are the most dominant.

The statistical view of the high resolution HI data, in Chapter 8, proved to be very valuable for probing the intrinsic topology of the gaseous content in the ISM. The spatial power spectrum of HI column density distribution showed an impressively tight power-law fit, $P_{\rm HI}(k) \propto k^{-3.31\pm0.01}$, consistent with a hierarchical organisation of HI clouds, with no preferred sizes. This reinforced the fact that the topology of the ISM is far more complex than assumed in the current models of the ISM, suggesting that more realistic density functions should be considered in physical processes, starting with the theory of radiative excitation and transfer. In the same manner, the statistical view of the dust column density distribution, using the spatial power spectrum, showed again a power-law behaviour, $P_{\rm d}(k) \propto k^{-3.1\pm0.2}$, with no preferred sizes for dust clouds.

Through the spatial coherency spectrum in Chapter 8, it was shown that dust and gas are spatially well correlated on intermediate and large scales. The remarkable similarity of the spatial power spectra for the HI and dust column density distributions suggests a unique and ubiquitous hierarchical structure organisation, most likely governed by the Kolmogorov type turbulence. It was argued that one interpretation of the power-law spatial power spectra can be in an alternative model of the ISM, having a fractal nature with the volume fractal dimension of 2.4.

9.2 Future directions

As was shown in this thesis, the central part of the SMC can be interpreted as a rotationally supported bar. However, some evidence for the particular tidal features, predicted theoretically by Gardiner, Sawa, & Fujimoto (1994) and Gardiner & Noguchi (1996), is present at the outskirts of the bar. The new Parkes narrow-band Multibeam survey of the whole Magellanic System is well underway. This survey will provide observations of a larger area around the SMC, thus shedding more light on

the 3-D structure of the SMC. At the same time, the distance determination of more and widely distributed objects within the SMC is essential to better constrain the depth of the SMC. This can be done using accurate Cepheid distances, which may come from the microlensing experiments now being performed by several groups.

A comparison of the shell size and expansion velocity distribution functions for the SMC, M31, M33 and Holmberg II with the predictions by the standard adiabatic model for the shell creation and evolution, shows some consistency. However, the model suggests a single burst of shells for the SMC, M31 and M33. As the well-evolved galaxies, such are M31 and M33, exhibit continuous star formation rather than a single burst, some discrepancy between the observations and current models appears to be present. A wealth of observational data exist for galaxies of different morphological types. The ball seems to be passed on to the theory in which revised and more detailed models for the creation and evolution of SGSs, including more realistic density functions, should allow better comparison with observations, resulting in an improvement of our understanding of shell phenomenon in the ISM.

Section 8.2 demonstrated, using very simple tools, an important role that very cold dust may have in the ISM. The obvious questions that emerge are: how cold can dust be in the SMC and in what amounts is it present? Observations at sub-mm wavelengths, using the SEST telescope or the forthcoming Atacama Millimetre Array, could significantly improve our knowledge on this matter.

In the investigation of the dust-to-gas mass ratio in the SMC, a significant spatial variation was found. Section 8.2.3 discusses an intrinsic nature of this variation originating in the metallicity variation across the SMC. However, a sparse number of HII regions with measured oxygen abundance does not support the correlation proposed by Lisenfeld & Ferrara (1998). A further study of the origin of the dust-to-gas ratio variation will tremendously benefit from the metallicity measurements of wider range of objects spread over the SMC.

The recent observations of the tiny (AU-scale) structure in the ISM, mentioned in Chapter 1, open a few interesting questions in relation to the studied 2-D spatial power spectra. How does the tiny-scale structure fit into the continuous hierarchy of structures observed on larger spatial scales? Is there only one population of the tiny-scale structure? What is the fraction of the ISM occupied by these tiny features? Are the AU-size clumps the smallest 'atomic' clumps of the fractal ISM? The SMC is very useful for probing the role that the tiny-scale structure plays in the ISM. In order to establish the form of the HI power spectra on much smaller spatial scales than studied here, I am already involved in the VLBI observations of the opacity fluctuations towards several extragalactic sources behind the SMC.

Bibliography

Alton P. B. et al., 1998, A&A, 335, 807

Assendorp R., Bontekoe T. R., de Jonge A. R. W., Kester D. J. M., Roelfsema P. R., Wesselius P. R., 1995, A&AS, 110, 395

Aumann H. H., Fowler J. W., Melnyk M., 1990, AJ, 99, 1674

Baars J. W. M., Genzel R., Pauliny-Toth I. I. K., Witzel A., 1977, A&A, 61, 99B

Bajaja E., Loiseau N., 1982, A&AS, 75, 251

Bajaja E., van Albada G. D., 1979, A&A, 75, 251

Beech M., 1992, Ap&SS, 192, 103B

Beichman C. A., Neugebauer G., Habing H. J., Clegg P. E., Chester T. J., 1985, Infrared astronomical satellite (IRAS) catalogs and atlases, Explanatory supplement, Jet Propulsion Lab., California Inst. of Tech., Pasadena, California

Binney J., Tremaine S., 1987, Galactic dynamics. Princeton University Press, Princeton, New Jersey, p. 362

Bomans D. J., Points S., Weis K., Chu Y.-H., 1995, RevMexAASC, 3, 77B

Bontekoe T. R., Koper E., Kester D. J. M., 1994, A&A, 284, 1037

Bouchet P., Lequeux J., Maurice E., Prevot L., Prevot-Burnichon M. L., 1985, A&A, 149, 330

Boulanger F., Abergel A., Bernard J.-P., Burton W. B., Desert F.-X., Hartmann D., Lagache G., Puget J.-L., 1996, A&A, 312, 256

Bracewell R. N., 1978, The Fourier Transform and its Applications. McGraw-Hill Book Company, USA, p. 209

Braun R., 1997, ApJ, 484, 637

Briggs D. S., 1995, Ph.D thesis. New Mexico Institute of Mining and Technology, Socorro, NM

Brinks E., 1990, in Thronson H. A., Shull J. M., ed, The Interstellar Medium in Galaxies. Kluwer Academic Publishers, p. 39

Brinks E., Bajaja E., 1986, A&A, 169, 14

Brinks E., Burton W. B., 1984, A&A, 141, 195

Bruhweiler F. C., Gull T. R., Kafatos M., Sofia S., 1980, ApJ, 238, 27L

Caldwell J. A. R., Coulson I. M., 1985, MNRAS, 212, 879

Caldwell J. A. R., Coulson I. M., 1986, MNRAS, 218, 223

Cao Y., Prince T. A., Terebey S., Beichman C., 1999, AJ, submitted

Copetti M. V. F., 1990, A&A, 229, 533

Cornwell T., Braun R., 1989, in ASP Conference Series, Vol. 6, Perley R., Schwab F., Bridle A., ed, Synthesis imaging in radio astronomy. Astronomical Society of the Pacific, San Francisco, Ch. 8, p. 167

Cornwell T. J., 1988, A&A, 202, 316

Cornwell T. J., Holdaway M. A., Uson J. M., 1993, A&A, 271, 697

Cox D. P., Smith B. W., 1974, ApJ, 189, L105

Cox P., Mezger P. G., 1989, A&AR, 1, 49C

Crane P. C., Napier P. J., 1989, in ASP Conference Series, Vol. 6, Perley R., Schwab F., Bridle A., ed, Synthesis imaging in radio astronomy. Astronomical Society of the Pacific, San Francisco, Ch. 7, p. 139

Crovisier J., Dickey J. M., 1983, A&A, 122, 282

Crovisier J., Dickey J. M., Kazes A., 1985, A&A, 146, 223

Davies R. D., Elliot K. H., Meaburn J., 1976, MNRAS, 81, 89D

Davis R. J., Diamond P. J., Goss W. M., 1996, MNRAS, 283, 1105

de Vaucouleurs G., de Vaucouleurs A., Corwin H. G., Buta R. J., Paturel G., Fouque P., 1991, Third reference catalogue of bright galaxies. Springer-Verlag, New York

Deul E. R., den Hartog R. H., 1990, A&A, 229, 362

Diamond P. J., Goss W. M., Romney J. D., Booth R. S., Karbela P. N. M., Mebold U., 1989, ApJ, 347, 302

Dickey J. M., 1995, in ASP Conference Series, Vol. 80, Ferrara A., McKee C. F., Heiles C., Schapiroeds P. R., ed, The Physics of the Interstellar Medium and Intergalactic Medium. Astronomical Society of the Pacific, San Francisco

Dickey J. M., 1996, in Blitz L., Teuben P., ed, Unsolved problems of the Milky Way, I.A.U. Symposium No. 169. Kluwer, Dordrecht, p. 489

Dickey J. M., Garwood R. W., 1989, ApJ, 341, 201

Dickey J. M., Lockman F. J., 1990, A&AR, 28, 215

Dickey J. M., Mebold U., Stanimirovic S., Staveley-Smith L., 1999, ApJ, submitted

Dieter N. H., Welch W. J., Romney J. D., 1976, ApJ, 206, L113

Draine B. T., 1989, in ASP Conference Series, Vol. 12, Blitz L., ed, The evolution of the interstellar medium. Astronomical Society of the Pacific, San Francisco, p. 193

Draine B. T., 1990, in Thronson H. A. J., Shull J. M., ed, The Interstellar Medium in Galaxies. Kluwer, Dordrecht, p. 483

Draine B. T., Anderson N., 1985, ApJ, 292, 494

Dufour R. J., Harlow W. V., 1977, ApJ, 216, 706

Dwek E., 1998, ApJ, 501, 643

Dwek E. et al., 1997, ApJ, 475, 565

Dyson J. E., Williams D. A., 1980, Physics of the interstellar medium. Manchester University Press, Manchester, England, p. 29

Dyson J. E., Williams D. A., 1997, Physics of the interstellar medium. Institute of Physics Publishing, Bristol, England, p. 25

Efremov Y. N., Elmegreen B. G., Hodge P. W., 1998, ApJ, 501, 163L

Ekers R. D., Rots A., 1979, in Image Formation from Coherence Functions in Astronomy, I.A.U. Colloquim No. 49. Reidel, p. 61

Elmegreen B. G., 1989, ApJ, 344, 306

Elmegreen B. G., 1997, ApJ, 477, 196

Elmegreen B. G., 1998, Proc. Astron. Soc. Aust., 15, 74E

Elmegreen B. G., Chiang W.-H., 1982, ApJ, 253, 666E

Elmegreen B. G., Falgarone E., 1996, ApJ, 471, 816

Evans A., 1994, The Dusty Universe. John Wiley & Sons, Praxis Publishing, Chichester, England, p. 54

Faison M. D., Goss W. M., Diamond P. J., Taylor G. B., 1998, AJ, 116, 2916F

Falconer K., 1997, Fractal Geometry. Wiley J. & Sons Ltd, Baffine Lane, England, p. 25

Falgarone E., Phillips T. G., Walker C. K., 1991, ApJ, 378, 186

Ferrara A., 1996, in Blitz L., Teuben P., ed, Unsolved problems of the Milky Way, I.A.U. Symposium No. 169. Kluwer, Dordrecht, p. 489

Fiedler R., Dennison B., Johnston K. J., Waltman E. B., Simon R. S., 1994, ApJ, 430, 581

Field G. B., Goldsmith D. W., Habing H. J., 1969, ApJ, 155, L149

Frail D. A., Weisberg J. M., Cordes J. M., Mathers C., 1994, ApJ, 436, 144

Gardiner L. T., Noguchi M., 1996, MNRAS, 278, 191

Gardiner L. T., Sawa T., Fujimoto M., 1994, MNRAS, 266, 567

Gautier T. N., Boulanger F., Perault M., Puget J. L., 1992, AJ, 103, 1313

Gerola H., Seiden P. E., 1978, ApJ, 223, 129

Giovanelli R., Haynes M. P., 1988, in Kellermann K., Verschur G. L., ed, Galactic and Extragalactic Radio Astronomy. Springer-Verlag, New York, Ch. 12, p. 528

Gooch R. E., 1995, in ASP Conference Series, Vol. 101, Jacoby G. H., Barnes J., ed, Astronomical Data Analysis Software and Systems V. Astronomical Society of the Pacific, San Francisco, p. 80

Gordon M. A., 1988, in Kellermann K., Verschur G. L., ed, Galactic and Extragalactic Radio Astronomy. Springer-Verlag, New York, p. 37

Green D. A., 1993, MNRAS, 262, 327

Gull S. F., Skilling J., 1991, MEMSYS5 Users Manual, Maximum Entropy Data Consultants Ltd.

Hatzidimitriou D., Hawkins M. R. S., 1989, MNRAS, 241, 667

Hauser M. G., Kelsall T., Leisawitz D., Weiland J., 1998, COBE Diffuse Infrared Background Experiment (DIRBE) Explanatory Supplement, NASA/GSFC, Greenbelt, MD, version 2.3, COBE Ref. Pub. No. 98-A

Heiles C., 1979, ApJ, 229, 533

Heiles C., 1984, ApJS, 55, 585

Heiles C., 1997, ApJ, 481, 193

Herbig G. H., 1977, in de Jong T., Maeder A., ed, Star formation, I.A.U. Symposium No. 75. Reidel, Dordrecht, p. 283

Hindman J. V., 1967, Aust. J. Phys., 20, 147

Hindman J. V., Kerr F. J., McGee R. X., 1963, Aust. J. Phys., 16, 570

Hindman J. V., McGee R. X., Carter A. W. L., Holmes E. C. J., Beard M., 1963, Aust. J. Phys., 16, 552

Hodge P. W., Strobel N. V., Kennicutt R. C., 1994, PASP, 106, 309

Holdaway M. A., 1998, in Taylor G. B., Carilli C. L., Perley R. A., ed, Synthesis imaging in radio astronomy II, ASP Conference Series. Astronomical Society of the Pacific, San Francisco, Ch. 8

Irwin M. J., Demers S. D., Kunkel W. E., Malin D., 1996, BAAS, 188.6510

Israel F. P., 1997, A&A, 328, 471

Israel F. P., Koornneef J., 1988, A&A, 190, 21

Israel F. P., Maloney P. R., Geis N., Herrmann F., Madden S. C., Poglitsch A., Stacey G. J., 1996, ApJ, 465, 738

Issa F. P., MacLaren I., Wolfendale A. W., 1990, A&A, 236, 237

JIWG , 1988, IRAS Point Source Catalog, Version 2, Jet Propulsion Lab., California Inst. of Tech., Pasadena, California

Kennicutt R. C., Bresolin F., Bomans D. J., Bothun G. D., Thompson I. B., 1995, AJ, 109, 594

Kennicutt R. C., Edgar B. K., Hodge P. W., 1989, ApJ, 337, 761

Kennicutt R. C. J., 1989, ApJ, 344, 685

Kerr F. J., Hindman J. V., Robinson B. J., 1954, ApJ, 7, 297

Kim S., 1998, Ph.D. thesis, The Australian National University

Kim S., Staveley-Smith L., Sault R. J., Kesteven M. J., McConnell D., Freeman K. C., 1997, Publ. Astr. Soc. Australia, 14, 119

Knapp G. R., 1990, in Thronson H. A., Shull J. M., ed, The Interstellar Medium in Galaxies. Kluwer Academic Publishers, p. 3

Koornneef J., 1982, A&A, 107, 247

Koornneef J., 1984, in van der Bergh S., de Boer K., ed, Structure and Evolution of the Magellanic Clouds, I.A.U. Symposium No. 108. Reidel, Dordrecht, p. 333

Koornneef J., Israel F. P., 1985, ApJ, 291, 156

Kraus J. D., 1966, Radio Astronomy. McGraw-Hill Book Company, USA, p. 73

Kroupa P., Bastian U., 1997, New Astronomy, 2, 77

Kroupa P., Röser S., Bastian U., 1994, MNRAS, 266, 412

Kulkarni S. R., Heiles C., 1988, in Kellermann K., Verschur G. L., ed, Galactic and Extragalactic Radio Astronomy. Springer-Verlag, New York, p. 95

Kurt C. M., Dufour R. J., 1998, Rev. Mex. Astron. Astrof., 7, 202K

Kurt C. M., Dufour R. J., Garnett D. R., Skillman E. D., Mathis J. S., Peimbert M., Torres-Peimbert S., Walter D. K., 1995, Rev. Mex. Astron. Astrof., 3, 223K

Lada C. J., Lada E. A., Clemens D. P., Bally J., 1994, ApJ, 429, 694

Lazarian A., 1994, Ap&SS, 216, 207

Lazarian A., 1995, A&A, 293, 507L

Lazarian A., Pogosyan D., 1997, ApJ, 491, 200L

Lazarian A., Pogosyan D., 1999, ApJ, submitted

Lequeux J., 1989, in de Boer K. S., Spite F., Stasinska G., ed, Recent Developments of MC Research. Observatoire de Paris, Meudon, France, p. 119

Li A., Greenberg J. M., 1997, A&A, 323, 566

Lisenfeld U., Ferrara A., 1998, ApJ, 496, 145

Loeb A., Perna R., 1998, ApJ, 503, 35L

Loiseau N., Bajaja E., 1981, RevMexAA (Serie de Conferencias), 6, 55

Luks T., Rohlfs K., 1992, A&A, 263, 41

MacLow M., McCray R., 1988, ApJ, 324, 776

Mandelbrot B. B., 1983, The Fractal Geometry of Nature, Rev. ed. of: Fractals. c1977. W.H. Freeman and Company, New York

Marscher A. P., Moore E. M., Bania T. M., 1993, ApJ, 419, L101

Martin N., Maurice E., Lequeux J., 1989, A&A, 215, 219

Mathewson D. S., Cleary M. N., Murray J. D., 1974, ApJ, 190, 291

Mathewson D. S., Ford V. L., 1984, in van der Bergh S., de Boer K., ed, Structure and Evolution of the Magellanic Clouds, I.A.U. Symposium No. 108. Reidel, Dordrecht, p. 125

Mathewson D. S., Ford V. L., Visvanathan N., 1986, ApJ, 301, 664M

Mathewson D. S., Ford V. L., Visvanathan N., 1988, ApJ, 333, 617

Mathis J. S., Rumpl W., Nordsieck K. H., 1977, ApJ, 217, 425M

McCray R., Kafatos M., 1987, ApJ, 317, 190

McGee R. X., Newton L. M., 1981, Publ. Astr. Soc. Australia, 4, 189

McGee R. X., Newton L. M., 1982, Publ. Astr. Soc. Australia, 4, 308

McKee C. F., 1995, in ASP Conference Series, Vol. 80, Ferrara A., McKee C. F., Heiles C., Shapiro P. R., ed, The physics of the interstellar medium and intergalactic medium. Astronomical Society of the Pacific, San Francisco, p. 292

McKee C. F., Ostriker J. P., 1977, ApJ, 218, 148

Meaburn J., 1980, MNRAS, 192, 365

Meurer G. R., Carignan C., Beaulieu S. F., Freeman K. C., 1996, ApJ, 111, 1551

Meurer G. R., Staveley-Smith L., Killeen N. E. B., 1998, MNRAS, 300, 705

Moore E. M., Marscher A. P., 1995, ApJ, 452, 671

Murai T., Fujimoto M., 1980, PASJ, 32, 581

Norman C. A., Ikeuchi S., 1989, ApJ, 345, 372

Oey M. S., 1998, in Chu Y.-H., Suntzeff N., Hesser J., Bohlender D., ed, New Views of the Magellanic Clouds, I.A.U. Symposium No. 190. Reidel, Dordrecht, in press

Oey M. S., Clarke C. J., 1997, MNRAS, 289, 570

Oey M. S., Clarke C. J., 1998, in Franco J., Carraminana A., ed, Interstellar Turbulence. Cambridge U. Press, in press

Oort J. H., 1965, in Blaauw A., Schmidt M., ed, Stars and stellar systems V: Galactic structure. University of Chicago Press, Chicago, p. 455

Paczyński B., 1998, ApJ, 494, 45L

Padoan P., Jones B. J. T., Nordlund A. P., 1997, ApJ, 474, 730

Pagel B. E. J., Edmunds M. G., Fosbury R. A. E., 1978, MNRAS, 184, 569

Palous J., 1996, in Blitz L., Teuben P., ed, Unsolved problems of the Milky Way, I.A.U. Symposium No. 169. Kluwer, Dordrecht, p. 583

Pfenniger D., Combes F., 1994, A&A, 285, 94

Puche D., Westpfahl D., Brinks E., 1992, AJ, 103, 1841

Putman M. E. et al., 1998, Nat, 394, 752

Reach W. T. et al., 1995, ApJ, 451, 188

Reach W. T., Wall W. F., Odegard N., 1998, ApJ, 507, 507

Reynolds R. J., 1988, ApJ, 333, 341

Rice W., 1993, AJ, 105, 67R

Rodrigues C. V., S.J. A. M. M., Coyne G. V., Piirola V., 1997, ApJ, 485, 618

Roger R. S., Milne D. K., Wellinton K. J., Haynes R. F., Kesteven M. J., 1984, Publ. Astr. Soc. Australia, 5(4), 560

Rubio M., Lequeux J., Boulanger F., 1993, A&A, 271, 9

Sasselov D. D. et al., 1997, A&A, 324, 471

Sault R. J., 1984, VLA Scientific Memo 154, NRAO, Socorro

Sault R. J., Killeen N., 1998, Miriad Users Guide, Australia Telescope National Facility

Sault R. J., Staveley-Smith L., Brouw W. N., 1996, A&AS, 120, 375

Sault R. J., Teuben P. J., Wright M. C. H., 1995, in ASP Conference Series, Vol. 77, Shaw R. A., Payne H. E., Haynes J. J. E., ed, Astronomical Data Analysis and Software Systems IV. Astronomical Society of the Pacific, p. 433

Sauvage M., Vigroux L., 1991, in Haynes R. F., Milne D. K., ed, The Magellanic Clouds, I.A.U. Symposium No. 148. Kluwer, Dordrecht, p. 407

Scalo J. M., 1987, in Hollenbach D. J., Thonson H. A., ed, Interstellar Processes. D. Reidel Publishing Company, p. 347

Schlegel D. J., Finkbeiner D. P., Davis M., 1998, AJ, 500, 525

Schwarz U. J., Wakker B. P., 1991, in Cornwell T. J., Perley R. A., ed, Radio Interferometry: Theory, Techniques and Applicationd, I.A.U. Colloquim No. 131, p. 188

Schwering P., 1988, Ph.D. thesis, Sterrewacht Leiden

Schwering P. B. W., Israel F. P., 1989, A&AS, 79, 79

Sivia D. S., 1996, Data analysis, a Bayesian tutorial. Clarendon Press, Oxford

Slavin J. D., Cox D. P., 1993, ApJ, 417, 187

Smith M. G., Weedman D. W., 1973, ApJ, 179, 461

Sodroski T. J. et al., 1994, ApJ, 428, 638

Sodroski T. J., Odegard N., Arendt R. G., Dwek E., Weiland J. L., Hauser M. G., Kelsall T., 1997, ApJ, 480, 173

Spitzer L. J., 1954, ApJ, 120, 1S

Spitzer L. J., 1956, ApJ, 124, 20

Spitzer L. J., 1978, Physical processes in the interstellar medium. J. Wiley & Sons, Inc, New York, USA, p. 1

Sramek R. A., Schwab F. R., 1989, in ASP Conference Series, Vol. 6, Perley R., Schwab F., Bridle A., ed, Synthesis imaging in radio astronomy. Astronomical Society of the Pacific, San Francisco, Ch. 7, p. 117

Stanimirovic S., Staveley-Smith L., Dickey J. M., Sault R. J., Snowden S. L., 1999, MNRAS, 302, 417

Staveley-Smith L., Bland J., Axon D. J., Davies R. D., Sharples R. M., 1990, ApJ, 364, 23

Staveley-Smith L., Kim S., Putman M., Stanimirovic S., 1998, in Reviews in Modern Astronomy, Vol. 11, on behalf of the Astronomische Gesellschaft Universitats-Sternwarte Jena S., ed, Stars and Galaxies. Astronomical Society of the Pacific, Germany, p. 117

Staveley-Smith L., Sault R. J., Hatzidimitriou D., Kesteven M. J., McConnell D., 1997, MNRAS, 289, 225

Stewart R. T., Caswell J. L., Haynes R. F., Nelson G. J., 1993, MNRAS, 261, 593

Tenorio-Tagle G., 1981, A&A, 94, 338

Thompson A. R., Moran J. M., Swenson G. W. J., 1986, Interferometry and synthesis in radio astronomy. John Wiley & Sons, New York, USA, p. 265

Tomisaka K., Habe A., Ikeuchi S., 1981, A&AS, 78, 273T

Tomisaka K., Ikeuchi S., 1987, PASJ, 38, 697

Toomre A., 1964, ApJ, 139, 1217

Torres G., Carranza G. J., 1987, MNRAS, 226, 513

Tsvetkov T. G., 1980, Sov. Astron. Lett., 6, 400

van der Hulst J. M., Kennicutt R. C., Crane P. C., Rots A. H., 195, A&A, 38, 20

van der Hulst J. M., Terlouw J. P., Begeman K., Zwitser W., Roelfsema P. R., 1992, in ASP Conference Series, Vol. 25, Worall D. M., Biemesderfer C., Barnes J., ed, Astronomical Data Analysis Software and Systems I. Astronomical Society of the Pacific, San Francisco, p. 131

van der Hulst T., Kamphuis J., 1991, in Bloemen H., ed, The Interstellar disk-halo connection in galaxies, I.A.U. Symposium No. 144. Kluwer, Dordrecht, p. 201

van der Kruit P. C., Searle L., 1981, A&A, 95, 105

van der Kruit P. C., Searle L., 1982, A&A, 110, 61

Viallefond F., Goss W. M., 1986, A&A, 154, 357

Viallefond F., Goss W. M., Allen R. J., 1982, A&A, 115, 373

Vogelaar M. G. R., Wakker B. P., 1994, A&A, 291, 557

Volgel S. N., Wright M. C. H., Plambeck R. L., Welch W. J., 1984, ApJ, 283, 655V

Walker M., Wardle M., 1998, ApJ, 498, L125

Walter F., 1999, Proc. Astron. Soc. Aust., 16, 106

Walter F., Brinks E., Duric N., Kerp J., Klein U., 1998, in Richtler T., Braun J., ed, The Magellanic Clouds and Other Dwarf Galaxies. Shaker Verlag, Aachen, p. 221

Walterbos R. A. M., Schwering P. B. W., 1987, A&A, 180, 27

Weaver R., McCray R., Castor J., Shapiro P., Moore R., 1977, ApJ, 218, 377

Welch D. L., McLaren R. A., Madore B. F., McAlary C. W., 1987, ApJ, 321, 162

Westerlund B. E., 1997, The Magellanic Clouds. Cambridge University Press, Cambridge, United Kingdom, p. 32

Westpfahl D. J., Coleman P. H., Alexander J., Tongue T., 1999, ApJ, 117, 868

Wheelock S. L. et al., 1994, IRAS Sky Survey Atlas Explanatory Supplement, Jet Propulsion Lab., California Inst. of Tech., Pasadena, California, JPL Publication 94-11

Williams D. R. W., 1973, A&AS, 8, 505

Wilner D. J., Welch W. J., 1994, ApJ, 427, 898

Wynn-Williams G., 1992, The fullness of space. Cambridge University Press, Cambridge, England, p. 87

Ye T., Turtle A. J., 1991, MNRAS, 249, 722

Young E. T., Neugebauer G., Kopan E. L., Benson R. D., Conrow T. P., Rice W. L., Gregorich D. T., 1985, A user's guide to iras pointed observation products, Technical report, IPAC

Yuen C. K., Fraser D., 1979, Digital Spectral Analysis. CSIRO/Pitman, Adelaide, Australia, p. 59

Zhou S., Evans N. J., Wang Y., 1996, ApJ, 466, 296

Zubko V. G., 1999, ApJ, 513, L29